



HAL
open science

Microstructural and micromechanical study of ODS steel tubes transformed by cold pilgering

Elena Vakhitova

► **To cite this version:**

Elena Vakhitova. Microstructural and micromechanical study of ODS steel tubes transformed by cold pilgering. Materials and structures in mechanics [physics.class-ph]. Université de Technologie de Troyes, 2018. English. NNT : 2018TROY0040 . tel-03596727

HAL Id: tel-03596727

<https://theses.hal.science/tel-03596727v1>

Submitted on 3 Mar 2022

HAL is a multi-disciplinary open access archive for the deposit and dissemination of scientific research documents, whether they are published or not. The documents may come from teaching and research institutions in France or abroad, or from public or private research centers.

L'archive ouverte pluridisciplinaire **HAL**, est destinée au dépôt et à la diffusion de documents scientifiques de niveau recherche, publiés ou non, émanant des établissements d'enseignement et de recherche français ou étrangers, des laboratoires publics ou privés.

Thèse
de doctorat
de l'UTT

Elena VAKHITOVA

Microstructural and Micromechanical Study of ODS Steel Tubes Transformed by Cold Pilgering

Champ disciplinaire :
Sciences pour l'Ingénieur

2018TROY0040

Année 2018

THESE

pour l'obtention du grade de

DOCTEUR

de l'UNIVERSITE DE TECHNOLOGIE DE TROYES

EN SCIENCES POUR L'INGENIEUR

Spécialité : MATERIAUX, MECANIQUE, OPTIQUE, NANOTECHNOLOGIE

présentée et soutenue par

Elena VAKHITOVA

le 26 novembre 2018

**Microstructural and Micromechanical Study of ODS Steel Tubes
Transformed by Cold Pilgering**

JURY

M. R. LOGÉ	PROFESSEUR	Président
Mme. S. BERVEILLER	MAITRE DE CONFERENCES - HDR	Rapporteure
M. D. FABRÈGUE	PROFESSEUR DES UNIVERSITES	Rapporteur
Mme. M. GASPÉRINI	PROFESSEURE DES UNIVERSITES	Examinatrice
Mme. N. OONO-HORI	ASSISTANT PROFESSOR	Examinatrice
M. M. FRANÇOIS	PROFESSEUR DES UNIVERSITES	Directeur de thèse
M. D. SORNIN	DOCTEUR	Directeur de thèse

Dedicated to my family

Acknowledgments

I give my sincere thanks to everybody who contributed during my PhD research for their constant encouragement, support and help. I would like to express my gratitude to the direction of CEA Saclay for a conferred opportunity to realize this PhD project and to welcome me to the LTMEx research team. I thank **Laurence Portier**, **Laurent Chaffron** and **Cedric Sauder** for helping me with every organization steps toward graduation.

I especially thank my research supervisors **Dr. Denis Sornin** and **Pr. Manuel François** for their invaluable guidance, patience and strong encouragements throughout the whole PhD period. They shared with me their profound knowledge and experience in the field of materials and processing, that certainly widened my horizons and will have an important impact on my future. I would also like to thank the members of my defense committee, **Pr. Damien Fabrègue**, **Dr. Sophie Berveiller**, **Pr. Roland Logé**, **Pr. Monique Gasperini** and **Dr. Naoko Oono** for their precious suggestions to improve the quality of my work.

I am grateful to **Jonathan Wright** for his assistance in the realization of in-situ texture analysis using European Synchrotron Radiation Facilities and also in the post-treatment of a huge experimental data volume, that represent the essential results of this work. I sincerely acknowledge **Toshiro Tomida** for scientific exchange and the possibility to use in this study the DKS variant selection model developed by himself. I express my gratitude to **Francoise Barcelo** for technical assistance on EBSD analysis, **Joël Malaplate** for TEM observations, **Jean-Luc Fleman** for his assistance on mechanical testing, **Didier Hamon** for EPMA measurements, **Thomas Guilbert** for dilatometry experiments and **Jean-Baptiste Moussy** for magnetometric studies. Their technical supports and collaboration are greatly appreciated.

In addition, many thanks go to my colleagues **Nicolas Locher**, **Lucas Domergues**, **Yann de Carlan**, **Jean-Christophe Brachet**, **Eric Bouaravong**, **Cathy Vidal**, **Patrick Olier**, **Pierre-François Giroux**, **James Braun**, **Clémentine Fellah**, **Esther Simondon**, **Frederique Bourlet**, **Nassim Bouchoul**, **Hiroki Kurita**, **Didier Bossu**, **Serge Zarembowitch**, **Philippe Bertrand**, as well as **the international group of PhDs, postdocs and permanents at CEA** and others. Thanks for all the help and happy distraction provided during my graduate study.

I'm also very thankful to my russian colleagues and friends **Evgeny Trofimov, Andrey Dildin, Vladimir Gerasimov, Alexandre Zmanovsky, Darya Pakharukova, Regina and Irina Groisman, Guéorgui Kratassiuk, Ekaterina Boldyreva** and others that were always interested in my project advancements and gave me valuable advices up to the defence. I would like to give my kind regards to the **professors** I have met during my professional education at **South Ural State University, l'Ecole d'ingénieurs de Saint Etienne** and **Centre de Mise en Forme d'Ecole des Mines de Paris** who gave me a good knowledge and open my mind to the field of material science.

Last, but not the least... I am greatly indebted to my **Russian** and **French families** for their complete, continued, and undoubted support. I would not have made it where I am today without their encouragement, help and understanding. Thanks a lot to my parents and my husband for their inlimited love and sharing with me both difficult and happy moments of my PhD life.

General introduction

Nowadays nuclear power is a significant part of electricity production in the world. Many countries forecast an important growth of capacities of nuclear power units, keeping in mind the reduction of a final production cost and insurance of an improved safety. Nuclear material studies focus on the development of materials that are able to withstand high thermomechanical loadings under strong irradiation flux.

Various international programs aim to develop the construction materials for advanced type reactors [ESNII, 2010]. Throughout these programs, it is required to find and approve materials for the working conditions of the coming generation (GEN IV) of fission reactors. More specifically the sodium cooled fast reactors, mostly supported by Commissariat à l'Énergie Atomique et aux Énergies Alternatives (CEA), suppose a strong increase of radiation flux and temperature compared to conventional reactors. The red rectangle on Fig. 1 illustrates the core of a nuclear reactor. At this specific location, conditions of irradiation and temperature are very severe and require resistant materials with adapted properties. Research of [Kimura, 2005; Yvon and Carré, 2009] indicated that ODS ferritic-martensitic stainless steels are good candidates due to their ability to be used in severe conditions. Indeed, they are characterized by low vacancy swelling, high creep resistance and corrosion resistance. Fig. 2 illustrates the potential of the ODS steels in regards to the Austenitic (316, 304) and the Ferritic/Martensitic steels. It provides a workability at irradiation doses not less than 100...200 dpa and at temperatures about 650...750°C [Kaito *et al.*, 2003].

A wide study of the ODS ferritic-martensitic steel is currently carried out at CEA. Main attention is paid to the materials processing development and determination of their behavior under thermal, radiation, mechanical and corrosion loading. Due to its specific cubic lattice structure with the presence of strengthening nano-particles of yttrium oxides, this material shows a high performance in industrial use.

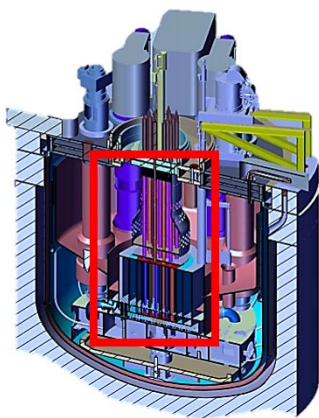


Fig. 1 Concept of sodium cooled fast reactor of IV Generation [Rodriguez, 2018]

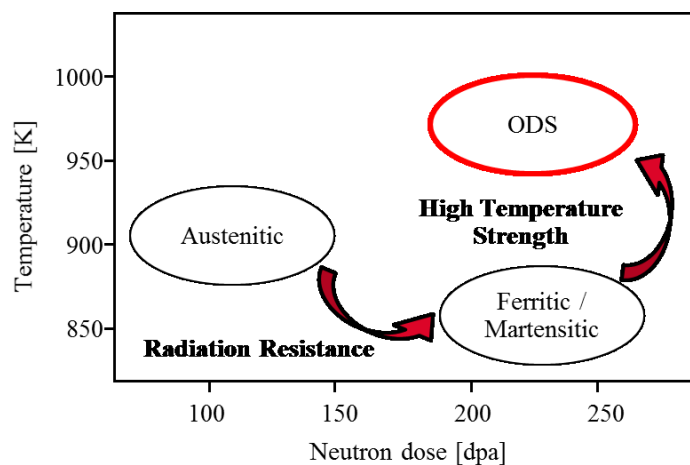


Fig. 2 Mechanical performance of several materials as a function of neutron dose and temperature [Sakasegawa *et al.*, 2007]

Context of the study

This project is related to the study of the metallurgical and mechanical properties of ODS tubes, which are foreseen to be used under the severe conditions present in reactor cores. Their manufacturing process includes a hot extrusion of seamless tubes made from the mechanically alloyed powder mixture and further cold rolling passes into cladding tubes at the **industrial scale**. For this project the first set of ODS tubes was produced by Vertikaler Massenausgleich Ringwalzei technology (VMR). During VMR pilgering process, severe plastic deformation (on the order of several hundred percent) is applied on the material. In the present work, it is proposed to study in details the physical and mechanical properties of received tubes with a polycrystalline structure that has undergone high deformation loadings and specific heat treatments.

The major points in this research work are the following:

- Analysis of the microstructure and mechanical properties evolutions using experimental techniques
- Detailed analysis of phase transition properties of ODS steels
- Prediction of the texture formation and anisotropy of mechanical properties by simulation of pilgering sequences in polycrystalline model
- Recommendations for design and qualification of new set of ODS tubes based on the obtained results

The motivation of this project is to demonstrate the **feasibility** of industrial manufacturing for ODS cladding tubes by means of experimental and numerical studies. The overall objective is to identify the paths towards process optimization, looking in particular at the risk of mechanical properties degradation and the possibility to reduce the total production costs by minimizing the number of rolling passes and the duration of heat treatments.

Thesis outline

The following key points are formulated to introduce the state-of-the-art in theoretical and experimental studies for ODS steels, as well as the results of the present work. They are presented through the 6 chapters of this manuscript:

- **Chapter I** provides the acquired knowledge about nanostructured ODS steel properties and the features of its production, where the role of oxides particles is explicitly presented. The choice of manufacturing process is also addressed here.
- In **Chapter II**, the materials investigated in this thesis are introduced with detailed information on manufacturing process. The design of the experiments and the used experimental techniques are explained here, taking into account the thesis objectives.
- In **Chapter III**, the microstructural evolution of 9%Cr ODS steel tubes produced by VMR process is presented. Influence of processing parameters on the microstructural, mechanical and magnetic properties is described. The first observation of texture memory effect in ODS steel is discussed.
- **Chapter IV** is then focused on the detailed study of texture memory and the theory of variant selection during diffusive and displacive transformations. A synchrotron in-situ analysis is used to follow the texture evolution during the thermal cycle. Observation of the texture in the austenite domain is performed.
- In **Chapter V** based on the obtained investigations on texture evolution, a set of experiments was realized in order to identify the particular behavior of ODS steels during phase transition process and to propose an optimized method for intermediate and final heat treatment.
- In **Chapter VI**, a modeling of texture and mechanical behavior for ODS pilgered tubes is realized using Visco-Plastic Self-Consistent (VPSC) code. The results of simulations were compared to experimental data from the present work and the literature.

Finally, conclusions and perspectives about optimization of the pilgering process of ODS tubes are given in the last chapter of this manuscript.

Table of Contents

Acknowledgments	5
General introduction	7
Context of the study	8
Thesis outline	9
Chapter I. Development of Oxide Dispersion Strengthened steels.....	15
I.1. Development of ferritic/martensitic ODS steels	15
I.2. Microstructure of ferritic/martensitic ODS steels	17
I.3. Influence of cold working and annealing on the microstructure.....	21
I.4. Critical temperatures and hardness in ODS steels	22
I.5. Mechanical properties of ODS steels.....	26
I.6. Choice of cold forming method for ODS tube manufacturing.....	28
Conclusions for Chapter I.....	30
Chapter II. Materials and Observation Methods	33
II.1. Manufacturing routes from powder state to pilgered tubes	33
II.2. Experimental details	37
II.2.1. Microstructural observations.....	37
II.2.2. HKL and MTEX software for images post-treatment.....	40
II.2.3. TEM observations	40
II.2.4. Hardness and traction tests.....	41
II.2.5. Dilatometric measurements.....	42
II.2.6. Magnetometry observations	42
Conclusions for Chapter II	43

Chapter III. Impact of pilgering sequence on microstructure and properties of ODS pilgered tubes	45
III.1. Grains morphology and their internal misorientation.....	45
III.2. Texture evolution after pilgering and applied heat-treatment	48
III.3. Evolution of mechanical properties: hardness and traction tests.....	53
III.4. Evolution of chemical composition.....	56
III.5. Dilatometric measurements of phase transformations.....	59
III.6. Particles distribution and the evolution of particles size	60
III.7. Mechanical properties observed by tensile tests.....	62
III.8. Internal stresses	65
III.9. Evolution of magnetic properties	67
Conclusions for Chapter III	69
Chapter IV. Phase transition and Texture memory effect in ODS steel pilgered tubes	73
IV.1. Texture memory effect in deformed steels.....	73
IV.2. Experimental Method and Data processing for <i>in-situ</i> synchrotron analysis.....	74
IV.2.1. Materials and samples preparation	74
IV.2.2. Synchrotron setup.....	74
IV.2.3. Test conditions	75
IV.2.4. Data Post-treatment	76
IV.3. Texture evolution during the thermal cycle	77
IV.4. Crystallite size and lattice distortion determination	80
IV.5. Prediction of transformation texture in cold-rolled ODS by Double Kurdjumov-Sachs relation.....	84
Conclusions for Chapter IV	93

Chapter V. Influence of heat-treatment parameters on phase transition.....	97
V.1. The objectives for the study of phase transition processes.....	97
V.2. Influence of holding temperature on texture formation.....	98
V.2.1. The Sellars model for ferrite grain growth	100
V.3. Mechanism responsible for ferrite nucleation / growth - Isothermal treatments.....	103
V.4. Impact of initial microstructure on the final one - Double step treatment.....	105
V.5. Estimation of parent γ grains shape and size – Inter-critical treatments	106
V.6. Effect of heating rate on the phase transformation kinetics	107
V.7. Discussion on the selective nucleation and growth and the role of the particles on the texture formation	108
Conclusions for Chapter V	110
Chapter VI. Modelling of texture and mechanical properties of ODS pilgered tubes	113
VI.1. Introduction of texture prediction using polycrystalline models.....	113
VI.2. VPSC formulation.....	115
VI.3. Viscoplastic constitutive law.....	116
VI.4. Parameters identifications and sensibility analysis	117
VI.5. Representative Volume Element for modeling of the pilgering sequence	122
VI.6. VMR modelling	123
VI.7. HE-R1-R2 pilgering sequence	125
VI.7.1. Texture simulation.....	125
VI.7.2. Mechanical anisotropy prediction	128
VI.8. Conclusions for Chapter VI.....	129
General Conclusions and Perspectives.....	131
Résumé en français	137
References.....	161
Annex 1	173
Annex 2	174
Annex 3	175

Chapter I. Development of Oxide Dispersion Strengthened steels

Introduction

In this Chapter, the development of Oxides Dispersion Strengthened steels is detailed. It includes information about the current knowledge about the features in chemical composition, structure and mechanical properties of ODS steels. These data are studied in order to explain the choice of the grade and processing routes for the present study, as well as the comparison of this study results with the reference materials.

I.1. Development of ferritic/martensitic ODS steels

Steel strengthening mechanism by dispersion of nano-particles (oxides, carbides, nitrides, etc.) is explored at the beginning of XXth century [Fink, 1910]. It was shown that the particles of the dispersed phase act as an obstacle to the dislocations movement in the crystal lattice and increase the mechanical resistance of the material, especially at the high working temperatures. The first ODS steels were manufactured for Al, Ni, Fe and W-based alloys.

Various commercial and experimental ODS chromium ferritic/martensitic (F/M) steels, found in the literature, were continuously developed, showing out their performance in nuclear application. Many articles and manuscripts were focused on the behavior of these steels under thermal, thermomechanical and irradiation conditions. A huge bulk of work was done by **Japanese** research teams [Ukai *et al.*, 1998], [Ukai *et al.*, 2002], [Kaito *et al.*, 2003], [Kimura *et al.*, 2007], [Narita *et al.*, 2013], [Ohtsuka *et al.*, 2013], **European** and **American** researchers [Carlan *et al.*, 2009], [Béchade *et al.*, 2012], [Dubuisson *et al.*, 2012], [Stoica *et al.*, 2014], [Toualbi *et al.*, 2013], [Dadé, 2014], [Hoelzer *et al.*, 2012], [Fazio *et al.*, 2009], [Zinkle *et al.*, 2017]. Detailed review on a historical contribution of each country in ODS steel development is given in the thesis of [Laurent-Brocq, 2010].

The evolution of F/M alloys can be divided into five generations from 0 to IV, presented on Fig.I.1. The transition from one generation to another is classified by increasing of reactor power capacity and, consistently, the requirement of more resistant materials with advanced microstructure. The first generation of F/M ODS steels was initially designed for the conventional fossil fuel power plants, and then, in the 1970s, they were studied for the application in the core part of fast neutron reactors [Fischer, 1976]. In the middle of 1980s, the idea of low-activation materials was proposed for the international fusion programs with the objective to build reactors from materials that are not activated by neutrons irradiation or low-activated, allowing to improve the safety. The research results allowed to determine that such elements as Mo, Nb, Ni, Cu, and N must be minimized to obtain the reduced activation in conventional Cr-Mo steels.

It was proposed to replace molybdenum steels by tungsten and/or vanadium. Steels with 7–9% Cr were preferred, because of the difficulty of eliminating δ -ferrite (giving a lower toughness and brittle precipitations formation) in a 12% Cr steel without increasing carbon or manganese for austenite stabilization.

F82H and JLF-1 steels were chosen in Japan and in Europe, based on the previous work on the reduced-activation steels, and a new composition EUROFER was more recently studied. These new compositions of reduced activation steels in GEN IV present an interest in the future development of international fusion programs.

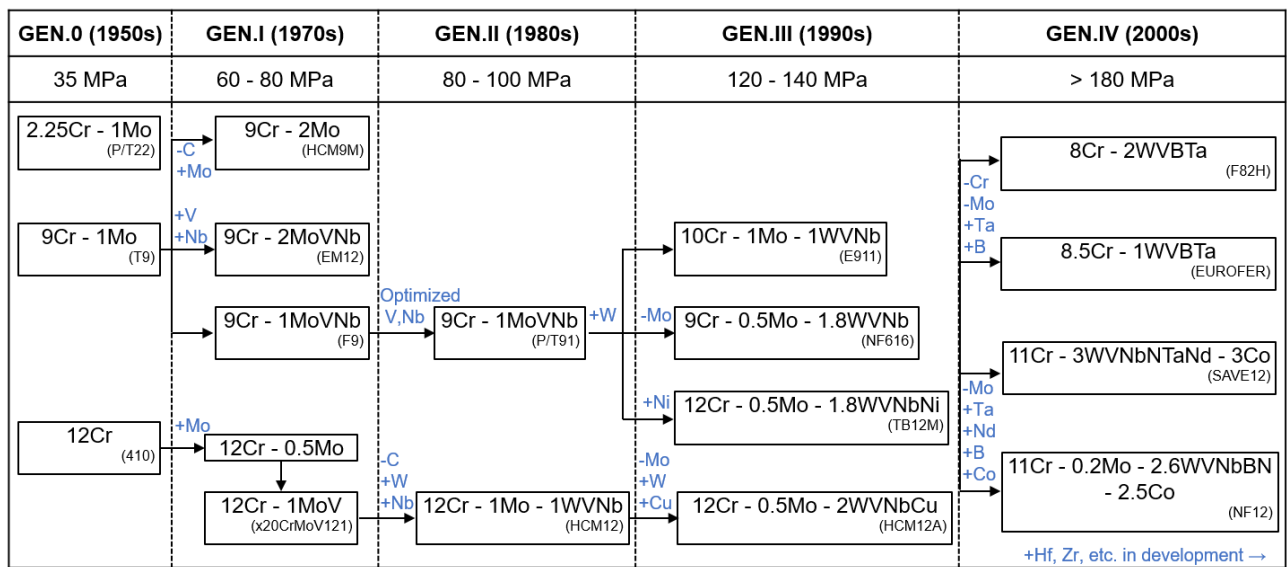


Fig.I.1 Progress in chromium stainless steel designs with corresponding predicted long-term creep properties at 600°C for 10⁵h (adapted from [Hald, 1996])

First ODS steels were initially manufactured by traditional powder metallurgy. This technique could not allow to obtain homogeneous distribution of oxide particles in the matrix. That is why a new method of mechano-synthesis was developed. With this method, the metal powder is ground with the oxides powder, finally giving a homogeneous distribution of oxides particles in the metallic matrix.

But the main issue of these steels is their tendency to form a strong texture during the rolling process that leads to an anisotropy of mechanical properties. Implementation of heat treatment allows to reduce the internal stresses inside the tubes and to achieve a more homogeneous structure, as well as to restore the isotropic microstructure by a phase transformation process [Kaito *et al.*, 2003]. However, the nature of some processes, such as recrystallization and phase transformation, which are responsible for formation of such structure, are still unclear [Lambard, 1998; Toualbi *et al.*, 2013; Hary, 2017]. In the framework of this research, it is tried to formulate the basic mechanisms of material response in the thermomechanical processes, which plays the main role in the formation of microcrystalline structure, and its effect on the overall mechanical properties under severe deformation loadings. To reply to this challenge it is proposed to investigate the microstructural properties of ODS steel.

I.2. Microstructure of ferritic/martensitic ODS steels

Initially the microstructure depends on the manufacturing **process**, operating **temperature** of the process and **chemical composition**. ODS steels are manufactured from a powder mixture. Milling, enable to introduce a large amount of oxygen in the material. Subsequently, this oxygen will react with metallic elements like yttrium or titanium to form the oxides. Grain size is directly dependent from Zener pinning effect, which is defined by the number and size of precipitates [Boulnat et al., 2015]. Thus, nano-particles affect the mechanism of grain growth, depending on the temperature and holding time.

The manufacturing process also plays an important role. There are two main methods applied for the production of rough tubes: Hot Isostatic Pressing (HIP) and Hot Extrusion (HE). In the first case, the grains will be equiaxed and have a bigger size, in the second, they will be elongated in the direction of extrusion.

The influence of alloying elements in the composition of ODS steels can change significantly the microstructure in the following way:

▪ Chromium (α -stabilizer)

As can be seen on the phase diagram for ODS steel on Fig.I.2, two main series can be obtained depending on chromium content: ferritic-martensitic steels with a relatively low chromium content (from 9 to 12 wt%) and ferritic steels with a high chromium content (12 to 20 wt%). The crystallographic structure of these steels will have a **body centered cubic lattice**. This structure with additional presence of yttrium nanosized precipitates will create a stable structure avoiding the formation of vacancies and interstitial atoms under irradiation [Klueh, 2018]. Therefore, the cavity formation due to void coarsening will be lower. It allows to limit **swelling phenomenon**, the **irradiation resistance** and consequently the burn-up of fuels.

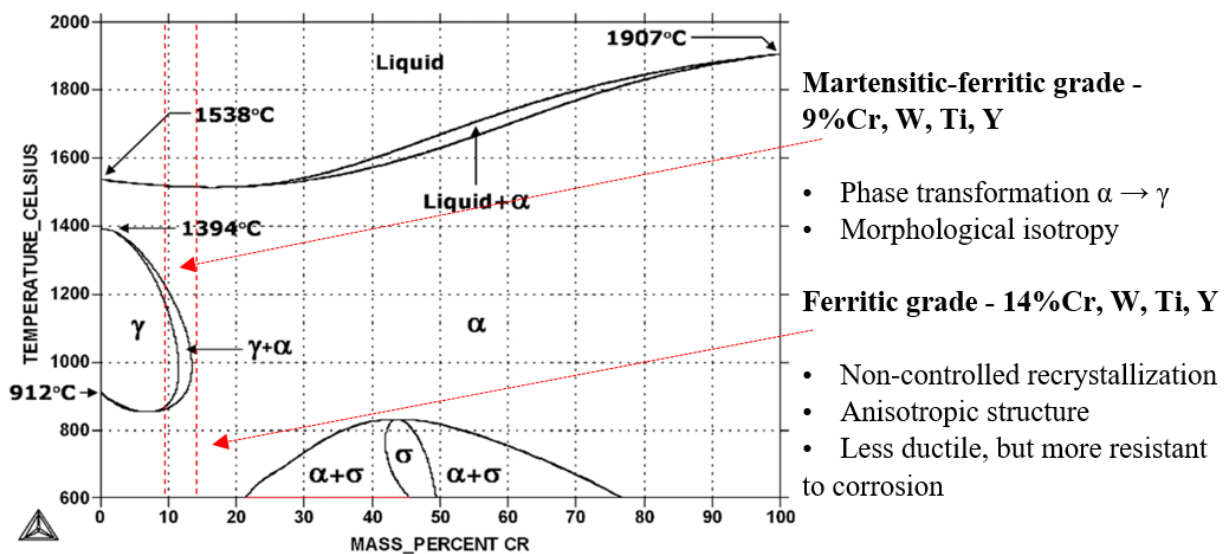


Fig.I.2 Fe-Cr phase diagram describing the phases that develop in stainless steels based on the chromium content. The ferritic-martensitic and the ferritic domains are limited with red lines

Two grades of ODS steel with different contents in chromium, 9 wt% and 14 wt%, present a big interest for research. Martensitic steels undergo α/γ phase transformation around 900°C. This transformation is used to obtain a microstructure with **isotropic creep properties** after cold-rolling. Nevertheless, this phase transformation will induce some dimensional variations in the lattice, which is undesirable under irradiation. Ferritic alloys, due to their higher chromium content, will be more **resistant to corrosion**, but, since there is no possibility for martensitic phase transformation, they will have a strong anisotropic structure. Moreover, they are more sensitive to the α/α' decomposition under irradiation and thermal ageing [Ukai, 2008]. The process of their recrystallization is rather complex due to the very high precipitation density that prevent boundary migration. Therefore, the forming sequence will be more complex to control due to the difference of properties in longitudinal and transverse directions associated with the heterogeneous anisotropic microstructure with a preferred grain orientation $\langle 110 \rangle$ α -fiber parallel to the rolling direction [Hary, 2016].

- **Nano-precipitates of oxides**

These nano-precipitates contained in steel are particles of different composition: $Y_2Ti_2O_7$, Y_2TiO_5 , TiO and AlO with a volume density of 10^{22} to 10^{24} m⁻³ and an average size of 1-100 nm for YTiO particles and 1000 nm for AlO particles, which are harmful impurities [Sakasegawa *et al.*, 2007]. Undesirable agglomerates of TiO with a size of about 100 nm were discovered [Kasada *et al.*, 2011]. Located at the grain boundaries, they reduce the ductility of the material during deformation. Their formation occurs during the first heating of the powder and is related to the oxidation of titanium on the surface of the powder particles. The presence of both too small (less than 1 nm) and too large particles (more than 100 nm) is not desirable for hardening, since too small particles are not effective to decrease the dislocations movement and too large ones may facilitate damage [Steckmeyer, 2012]. Thus, the average effective particle size is in the range of 1-35 nm. They can be located both inside the grain and at its borders, as shown on Fig.I.3.

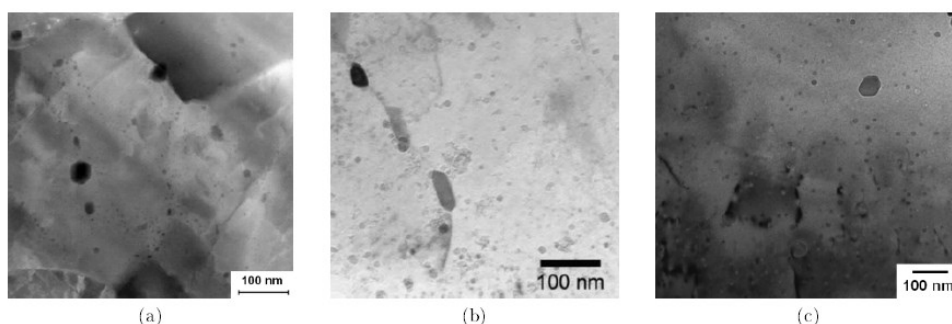


Fig.I.3 Nano-particles observed by electron transmission microscope in different ODS steels

(a) 14YWT (14Cr) [Brandes *et al.*, 2012]; (b) J1 (9Cr) [Shinozuka *et al.*, 2009]

(c) K3 (16Cr) [Kimura *et al.*, 2007]

Yttrium oxides are represented by two types $Y_xTi_yO_z$ (with titanium) or Y_xO_z (without titanium). Almost all existing ODS steels have in their content between 0.25% and 0.35% of yttrium oxides Y_2O_3 . Yttrium oxides have a very high thermal stability due to a very low enthalpy of formation [Zhong *et al.*, 2012]. Strengthening by yttria (Y_2O_3) is better than with titanium oxide (TiO_2) or aluminum oxide (Al_2O_3) since this oxide is more resistant at high temperature [Kang *et al.*, 1996].

The coherence of these particles with the matrix plays a special role in the hardening effect. It influences the mechanism of interaction between particles and dislocations, and in general it defines the mechanical properties of the material. Particles can be coherent, semi-coherent (partially) or incoherent with the cubic lattice of the matrix. This phenomenon was first discovered [Klimiankou *et al.*, 2003] in the steel with 9% chromium (EUROFER) and subsequently studied by [Yamashita *et al.*, 2004; Zhang, 2015]. The degree of coherence is determined by the particle size, shape, its chemical composition and shear modulus.

In the case of small particle size, they can be **sheared** during dislocations movement. The larger particles are characterized by a greater rigidity and a greater distances between themselves, significantly exceeding their diameter. Under the loading, dislocations will **bend** between these particles and pass on, leaving a dislocation loops around the particles, this is the Orowan mechanism. Two types of dislocation-particles interactions can co-exist depending on particles size and chemistry, applied stress and coherency with matrix [François *et al.*, 1991]. Mechanical strength depends on the efficiency of particles dispersion, the smaller the distance between the dispersed particles, the higher the material resistance [Reppich, 1998].

- **Tungsten (α -stabilizer)**

The presence of tungsten has the main role in strengthening by substituted solid solution [Kim *et al.*, 2003]. Tungsten additions are limiting the concentrations of titanium and oxygen, which promotes a **homogenous dispersion of the oxides** as $Y_2Ti_2O_7$ for larger oxides and a non-stoichiometric cluster of Y-Ti-O for oxides approximately less than 15 nm. For fusion application, tungsten also has an additional benefit of producing less active fission daughters following **neutron absorption**. According to [Narita *et al.*, 2011], an excess of tungsten can trigger laves brittle phase formation. This is why the authors suggest a tungsten content of about 2 % mass.

- **Nickel (γ -stabilizer)**

In order to balance the effect of the addition of ferrite stabilizer, austenite stabilizers such as nickel or carbon are added (0.2% C and 0.5% Ni). It allows to ensure 100% austenite formation (no δ -ferrite) during the austenitization treatment, thus ensuring 100% martensite when cooled. It also improves corrosion resistance, strength and toughness [Gaffard, 2004].

- **Titanium (α -stabilizer)**

Addition of Ti in ODS steels is the most effective method for making **uniformly distributed ultra-fine oxide particles** and significantly improves its **high temperature strength**. High temperature strength is dominated by the size and distribution of dispersoids. The structure with $Y_2Ti_2O_7$ is shown to be very stable under thermal ageing and irradiation. Ti also helps in stabilization of martensitic ODS steel grades [Dade, 2015].

- **Carbon (γ -stabilizer)**

Carbon plays a role of austenite phase stabilizer at high temperatures. This element is also mandatory for martensite formation. However, the high content of carbon is not desirable because of brittle phase creation that reduces the properties of the steel. The manufacturing process makes it possible to have the lowest carbon content about 0.1wt% [Lambard, 2000].

The carbides of $M_{23}C_6$ type were previously observed at the grain boundaries of ODS steels with different content of Cr (9-19% Cr). Their presence in the structure can be observed at the mechanical alloying step during the manufacturing process. The application of an appropriate heat treatment can resolve this problem.

Hence, the manufacturing of ODS steel will allow to obtain the very complex structure with a dispersion of nanosized oxide particles and a grain size of few micrometers. The choice of consolidation and deformation methods will also play a role in texture and morphology formation. The role of heat treatment on the microstructure and mechanical properties of ODS steel is studied in the next part of this work.

I.3. Influence of cold working and annealing on the microstructure

The various structural states will bring different properties to the same material. It can be achieved by applying a special heat treatment. During plastic deformation, dislocations are generated throughout the material. These dislocations induce distortions of the crystal lattice which results in an unstable state of the metal structure. During heating, due to the increase of atoms mobility, the metal structure can go back to its equilibrium state. Two main driving forces of these processes can be determined. First one is the deformation energy that appears in heavily deformed materials. And another one is the diffusion and solubility of interstitial elements. This thermally activated process will reduce the number of dislocations and form new grains. The different stages of microstructure evolution are presented on Fig.I.4.

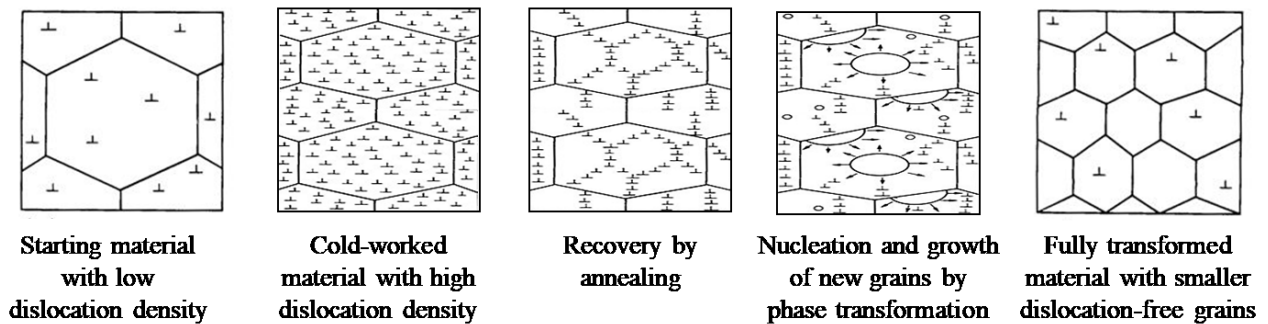


Fig.I.4 Microstructure evolution during cold working and thermal treatment
(adapted from [Rich, 2015])

The process in which the number of dislocations is reduced is called recovery. During **recovery**, the system lowers its energy by rearranging the dislocations into structure sub-boundaries. Increasing the temperature up to some critical point will result in phase transformation due to the diffusion and solubility of interstitial elements like carbon. During **phase transformation**, new phase **nuclei** are formed with their following growth [Savran, 2010]. During **growth**, grains increase their size until the end of transformation process. At high temperature in the formed phase, the grain growth become possible with carbides dissolution. In the case, when the nucleation and growth of new grains are determined by the gradient of the stored deformation energy, the process is controlled by **recrystallization** that can also occur at the high temperature [Humphreys, 1997]. Like this, the boundary features, namely the mobility, curvature and energy boundaries will monitor the grain growth [Doherty et al., 1997].

Some alloying elements can reduce the tendency of new grains to grow. For instance, the elements that do not form carbides (like nickel) will have little effect on the grain growth. But such elements as chromium, tungsten and titanium can heavily reduce the grain growth. The formed carbides of these elements cannot be fully dissolved in the new structure and prevent the growth of new grains. Therefore, the steel retains a fine-grained structure up to high heating temperatures.

I.4. Critical temperatures and hardness in ODS steels

Thermal processes are actively applied for ODS steels for the following reasons:

- 1) To recover the texture and consequently the isotropy of mechanical properties.
- 2) To increase the ductility, since the deformed material can be very hard and brittle, which presents a problem to continue the deformation process and even installation in service conditions.
- 3) To homogenize the chemical composition: the distribution of carbides and oxides particles.

In previous experiments, it was found that the level of hardness required to ensure a possible deformation should be lower than 400 HV1 [Inoue *et al.*, 2008; Toulbi *et al.*, 2013]. Compared to zirconium alloys, ODS alloys have a higher hardness and a lower ductility at room temperature. Therefore, intermediate heat treatments between rolling passes should be much more frequent than for zirconium alloys.

The intermediate heat treatments performed during the fabrication are strongly linked to the chemical composition and have a crucial influence on the microstructural and mechanical properties of the final tube. The alternate heat treatments and deformation steps have to be adjusted to determine a robust fabrication route which allows ODS cladding tubes manufacturing with limited crystallographic and morphological anisotropies.

As mentioned before, for ferrite/martensite grade there is a possibility to recover the texture by phase transformation from alpha to gamma domains. For ferritic grains this operation is not possible and structure changes can only be achieved by recrystallization.

The 3 main parameters of heat treatment that characterize the material final structure are: holding **temperature**, holding **time** at high temperature and cooling **rate**.

In the work of [Toulbi *et al.*, 2013], the critical cooling rates for phase transformations in 9Cr-1W ODS steel (the same grade as we use in this work) were determined by dilatometry measurements. On Fig.I.5 it can be seen, that the first nuclei of austenite were observed at 850°C and complete transformation was achieved at 900°C. In order to obtain a fully martensitic structure, it is necessary to apply a cooling rate of more than 1 °C/s (or 60°C/min), with a cooling slower than 0.1 °C/s (or 6°C/min) the structure will be fully ferritic.

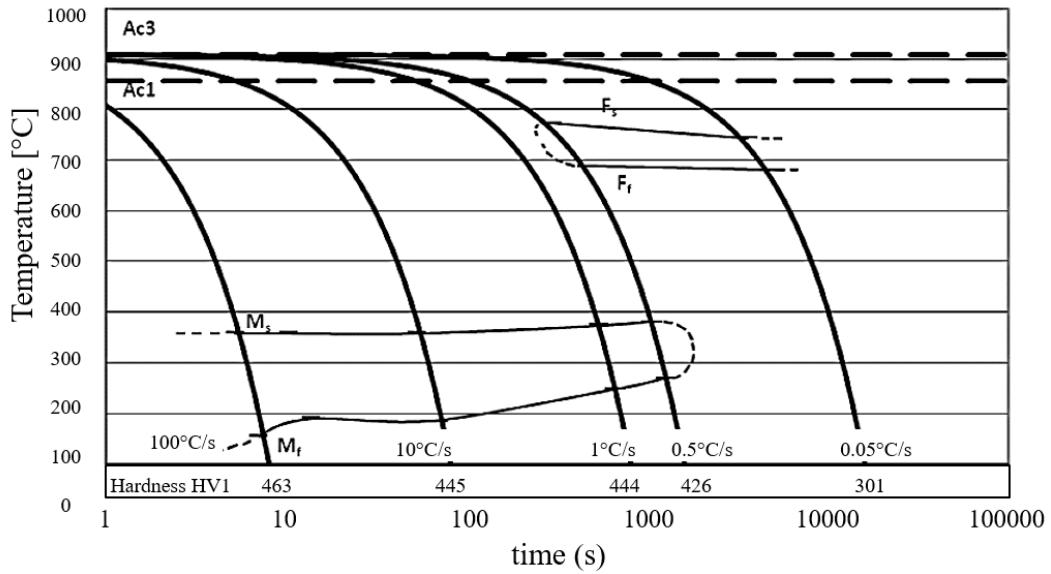


Fig.I.5 CCT diagram characterized martensitic Fe-9Cr-1W ODS steel [Toualbi et al., 2013]
 Holding at 1050°C / 20 min (Powder AUBERT & DUVAL 9048 with size of the precipitates about 10 nm and the density of 10^{22} - 10^{23} m⁻³)

Another data exist on the critical temperatures for the tubes made from the powder AUBERT& DUVAL 9073 with bigger size of precipitates (Fig.I.6). Both CCT diagrams show that the fully martensitic structure could be obtained at a cooling rate more than 0.5°C/s (or 30°C/min).

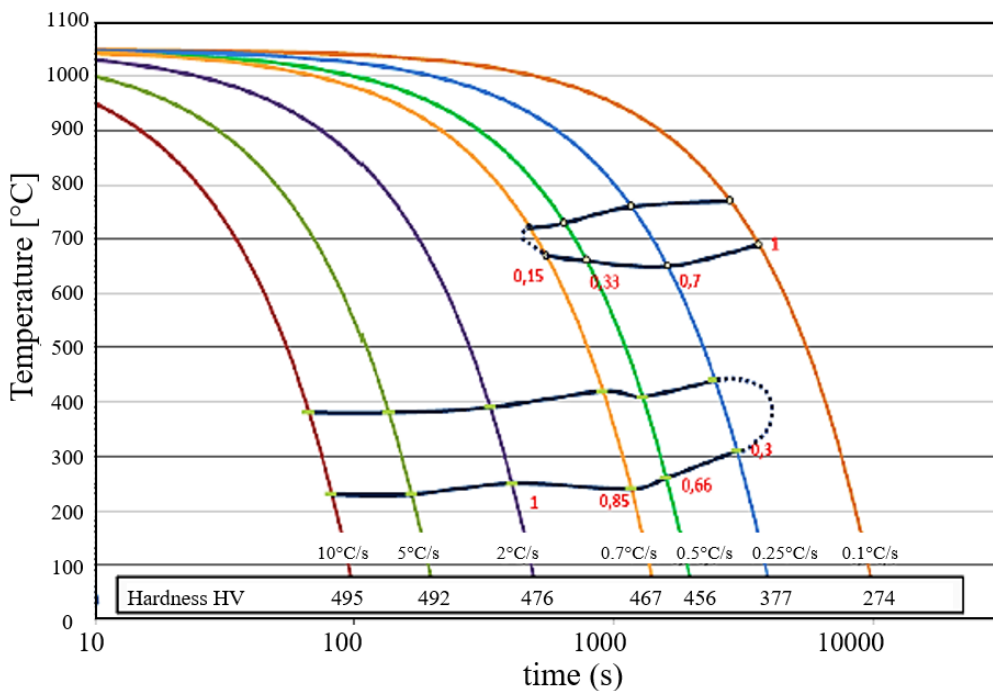


Fig.I.6 CCT diagram characterized martensitic Fe-9Cr-1W ODS steel (K30_M1).
 Holding at 1050°C / 1min [Vaugoude, 2016]

In the literature different approaches on the intermediate and final heat treatment for ODS steels were found. One of them was proposed by Japan Atomic Energy Agency (JAEA). They performed an Intermediate Heat Treatment (IHT) of 30 min at 1050°C carried out every 3 or 4 passes, reducing the hardness of around 50 HV1 [Ukai *et al.*, 2004]. And for the final treatment, they typically heat-treated with a standard normalization (1050°C / 1h with air cooling) and tempering process (800°C / 1h with fast cooling). The normalization or austenitization temperature is selected at 1050°C to dissolve alloying carbides and prevent significant coarsening of austenite grains [Van Den Bosch *et al.*, 2013]. This treatment shows its efficiency on the recovery. It gives a hardness allowing to apply a high reduction rates per rolling pass (in the order of 45%), but can be limiting during the cold forming and cause in material fragility. After final heat treatment, the hardness level is about 400HV (Fig.I.7).

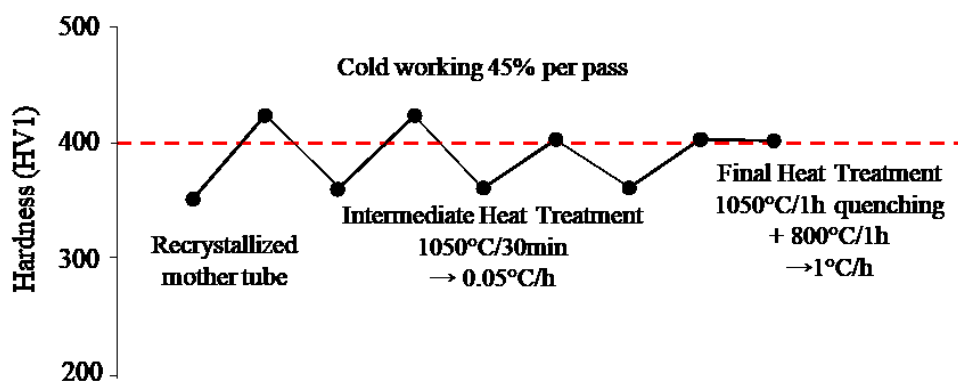


Fig.I.7 Hardness evolution during cold rolling and applied heat treatments [Ukai *et al.*, 2004]

During a collaboration of JAEA with CEA, it was proposed to make an intermediate heat treatment of 2h at 800°C after every 2 passes, allowing a reduction in hardness of about 20 HV1 (Fig.I.8). This annealing temperature corresponds to the higher temperature part of ferritic domain without inducing any phase transformation. In results the hardness decrease is too small, which implies the use of moderate reduction rates to remain below the critical value of 400HV1. Finally, this treatment was not really interesting regarding microstructure recovery [Ukai *et al.*, 2002].

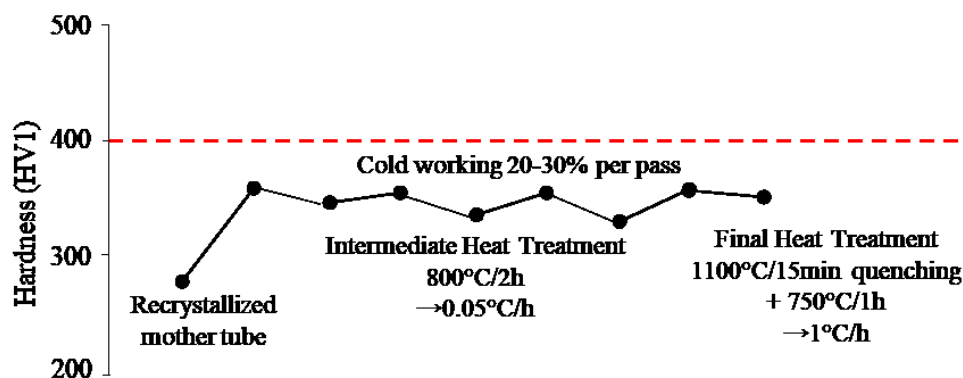


Fig.I.8 Hardness evolution during cold rolling and applied heat treatments [Inoue *et al.*, 2008]

An additional approach was proposed in CEA [Toualbi *et al.*, 2013], where the intermediate HT was realized at 1050°C/1h with slow cooling after each 2 rolling passes. For the final treatment, normalization at 1050°C / 30min with air cooling and tempering process at 750°C / 1h with fast cooling was applied (Fig.I.9). The results shows that thermomechanical treatment allows to complete recovery of the deformed microstructure and obtain higher mechanical properties in comparison with the first approach ($R_m=1200$ MPa instead of $R_m=1000$ MPa). This happens probably thanks to the holding time reduction at high temperatures (30min instead of 1h).

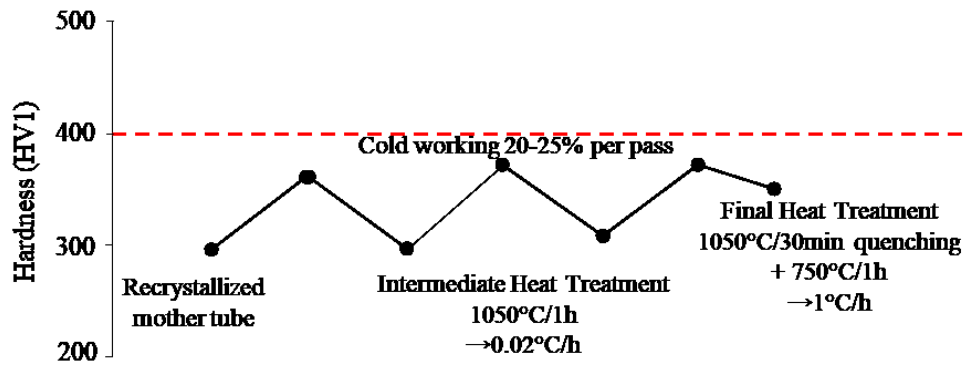


Fig.I.9 Hardness evolution during cold rolling and applied heat treatments [Toualbi *et al.*, 2013]

As shown on Fig.I.10 (a and b), successful recovery from elongated textured grains into fully equiaxed and non-orientated grains is possible for 9% chromium ODS steels. Using a high cooling rate, the grains will have a needle shape of disoriented crystals typical of martensitic structures, as shown on Fig.I.10c).

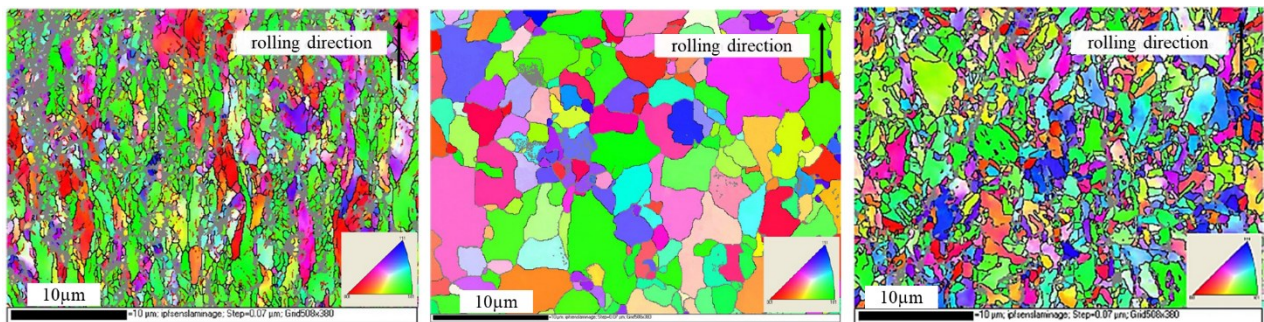


Fig.I.10. EBSD cartography of Fe-9Cr-1W ODS tube [Toualbi *et al.*, 2013]

a) after 40% reduction; b) after 40% reduction and treated at 1050°C/1h;

c) after 150% reduction and treated at 1050°C/30 min + fast cooling + 750°C/1 h

I.5. Mechanical properties of ODS steels

Creep resistance

Different generations of ferritic-martensitic steels are characterized by their creep strength at 600°C up to 10⁵ h, which is an important property for practical applications. The creep strength of the first generation of ODS steel is below 40MPa, and the maximum application temperature is below 540°C. The creep strengths of steels of following generations are 60, 100, 140, 180 MPa at 600°C for 10⁵ h and the upper bound applicable temperatures are 565, 592, 620 and 650°C, respectively.

Life duration of ODS steels is given on Fig.I.11 with comparison with non-ODS steels HT9 (Fe-12Cr-0,2C-1Mo-0.5W-0.25V) and PNC 316 (Fe-16,5Cr-13,8Ni-2,5Mo) by applying an internal pressure in the tubes. It is recognized that ODS steels have a better performance in terms of creep resistance at high temperature.

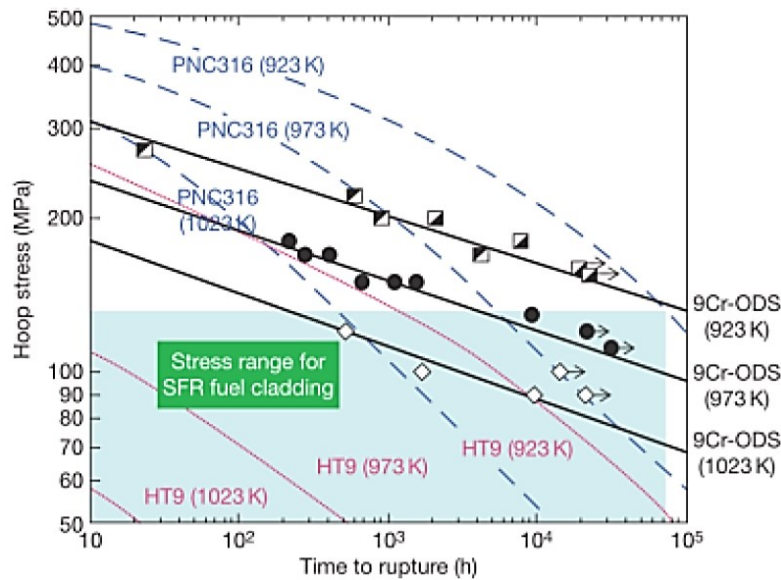


Fig.I.11 Creep resistance under internal pressure of 9Cr-2WTi-ODS steel with martensitic structure at 650, 700, and 750°C, compared to non-reinforced ferritic HT9 and austenitic PNC316 steels [Allen *et al.*, 2009]

Tensile strength

The problem of strong deformation texture is that it leads to anisotropic mechanical properties, detrimental to the biaxial creep-rupture conditions. Studies are looking for a process able to produce an isotropic grain structure. The austenite-to-martensite transformation has produced steels with excellent tensile properties and a significant decrease in the anisotropy at the ambient temperature. The maximum resistance for the grade 9Cr-1W is about 1200 MPa at room temperature and about 400 MPa with increasing of ductility at 650°C (Fig.I.12). However this state do not offer particular benefits regarding the creep properties at high temperatures.

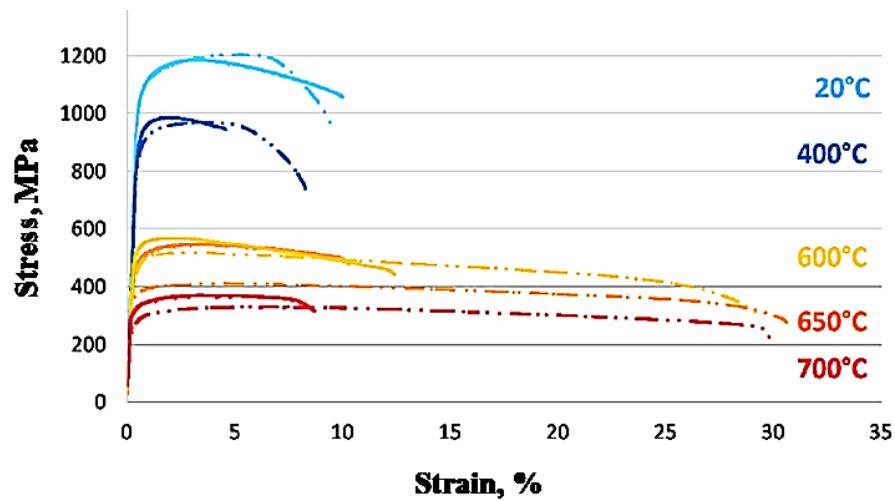


Fig.I.12 Traction curve at different temperatures for longitudinal (points) and orthoradial (line) directions for the tempered tube ODS Fe-9Cr-1W (SRMA J95-M3) [Toualbi, 2012]

I.6. Choice of cold forming method for ODS tube manufacturing

Plastic deformation is one of the main processes used to reduce the grain size of the metals. It is known that the most effective grain size reduction occurs when large plastic deformations are applied. Also, after hot consolidation, ODS bars must be transformed to reach the final geometry of the cladding tube with the external diameter of ~ 10 mm and wall thickness $\sim 0,5$ mm. Such high precision in geometrical dimensions can only be achieved by cold forming processes. The widely used methods of intensive plastic deformation, found in the literature, are: volume forging, rolling, drawing and pilgering.

The first ferritic ODS tubes were cold formed by drawing. It consists in a very low reduction rate (5% - 10%) with several drawing passes and annealing at 1050°C every 2 to 5 passes. Nearly 30 drawing passes are required to reach the final geometry. However, many defects (cracks, porosities) were detected (total efficiency 60%) and the mechanical properties were quite weak [De Bremaecker, 2012]. An attempt to cold form the ferritic industrial grade was done by forging and drawing [Hamilton, 2000]. Reduction rate stayed very low (of the order of 15%) and cracks were frequently observed as well.

At this time, it was tried to use pilgering rolling process [Parmentier, 2001]. This rolling process proved to be much more conservative in comparison with drawing, giving cumulative reduction rates of up to 70% without the appearance of cracks. Intermediate heat treatments can be carried out to relax the material between passes. By now, two types of pilgering process were studied for the deformation of ODS tubes: HPTR [Ukai *et al.*, 2004] and VMR [Inoue *et al.*, 2008]. The working principle for both of this techniques consists in the simultaneous reduction of the tube diameter and wall thickness with incremental forward (Fig.I.13 left) and backward motions (Fig.I.13 right) applied on the tube cross section between the dies and the mandrel.

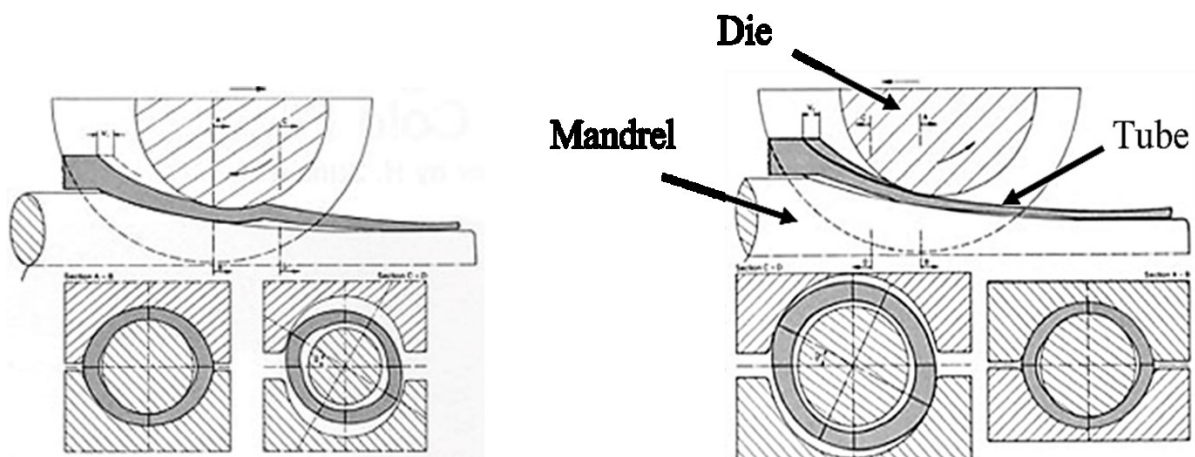


Fig.I.13 The principle of the pilgering process: (left) forward motion; (right) backward motion

Pilgering: VMR and HPTR

The specificity of VMR process, compared to HPTR, is related to the distribution of deformation value between normal and shear stresses [Vanegas-Marquez, 2011]. Although both VMR and HPTR dies reduce tubes via compression rather than tension, the complexity of tooling design and manufacturing varies greatly between these machine types. The difference lies in tools design (number of dies, types of mandrel, applied rotation angle) and in production speed. It will influence the distribution of the radial, longitudinal and tangential stresses and the work-hardening rate in tension/compression. In VMR process only two dies are used instead of three in HPTR (Fig.I.14) and the ratio between wall reduction and mean diameter reduction reach 300% after one rolling pass. This significant reduction will lead to non-homogeneous deformations in the tube section and can be dangerous regarding the crack opening due to the increase of all normal stresses with additional shear stresses in the axis zone.

The variable cross-sectional groove of a VMR die requires special expertise and equipment to be designed and manufactured, as does the matching conical mandrel. On the contrary, the cylindrical dies and mandrels of HPTR machine with constant cross-sectional grooves are relatively simpler to design and build. It gives more flexibility to users of HPTR dies on tool sourcing and modification of tool design.

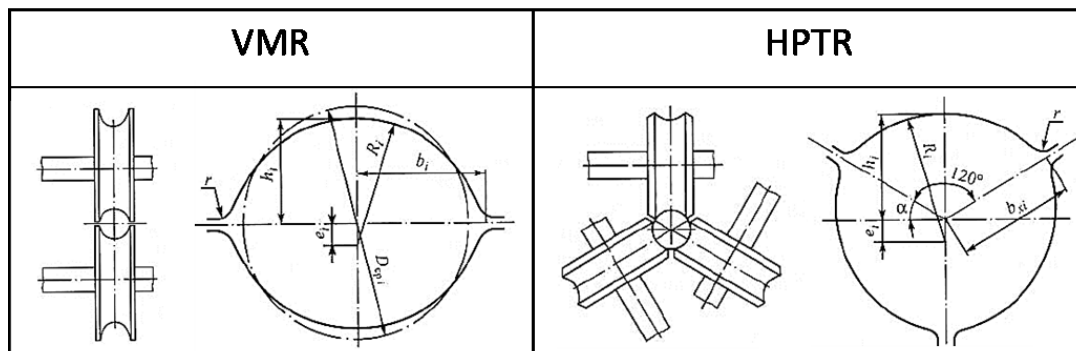


Fig.I.14 VMR and HPTR pilgering process comparison

While HPTR dies are simpler in design and operating than VMR dies, they cannot obtain the output rates of VMR. Modern and high-speed VMR pilgering machines overtake the role of HPTR pilgering machines, when production speed and quantity are important. However, HPTR pilgering machine sometimes is recommended for the last cold work passes because it guarantees non-cracking and very limiting thin wall thickness. The large number of small forming steps helps to ensure a constant wall thickness and nearly homogeneous material characteristics in the rolled tube.

Cold pilgering was already applied for tube fabrication mainly from zirconium alloys [Abe *et al.*, 1994], [Abe, 2000], [Girard *et al.*, 2001] and [Gaillac and Ly, 2018], as well as from austenitic, duplex and titanium alloys [Abe and Furugen, 2012]. For ODS material, successful experiences were found in the work of [Inoue *et al.*, 2008] for VMR and [Toualbi *et al.*, 2013] for HPTR.

Conclusions for Chapter I

The aim of the first chapter was to present the historical development of nano-reinforced ferritic-martensitic steels (less than 12wt%Cr) and the main challenge of its production, including powder metallurgy, cold forming and heat treatment processes.

It was noted that a homogeneous distribution of chemical elements must be achieved during mechanical alloying and hot extrusion steps to ensure high mechanical properties of the final product. Here, the consolidation temperature will affect the grains size. The choice of the consolidation process determines the possible anisotropy of the material. The chemical composition of the material is also essential to the nature of the nano-reinforcements.

The complexity of the ODS elaboration can be represented by three essential points: the distribution of the **nano-particles**, their size and coherency with the matrix; the size and morphology of the **grains**; and the crystallographic **texture**. Presently, it is possible to elaborate ODS steels that contain a very high density of nano-reinforcements of a few nanometers in diameter, distributed both in the grains and along the grain boundaries. The observed grain size varies from micron to submicron. ODS produced by hot extrusion can present a small anisotropy of microstructure in terms of grain morphology and crystallographic texture, that will be largely developed later during the cold forming process. This microstructural anisotropy leads to anisotropic mechanical properties of tubes, which are critical in particular for inner pressure creep conditions.

The mechanical properties of ODS steels were also presented. Compared to non-reinforced grades, they are very good in traction and creep resistance, and the primary role of nano-reinforcements in this stability was highlighted.

In terms of deformation methods, two pilgering processes of HPTR and VMR were compared, showing their advantages and drawbacks. VMR pilgering, under the interest in this study, shows great performances regarding productivity compared to HPTR. The overall view of tubes production process is presented in the Chapter II.

Chapter II. Materials and Observation Methods

Introduction

In this Chapter, the data about materials and applied processing routes associated with the present study are introduced. It includes presentation of the experimental equipment and protocols used in the following chapters.

II.1. Manufacturing routes from powder state to pilgered tubes

The development of ODS materials needs a precise control at each stage of the manufacturing process in order to obtain the expected microstructure. Production chain in ODS steel fabrication is shown on [Fig.II.1](#) and it includes:

- Pre-alloyed powder atomization under Ar gas atmosphere
- Milling of the alloy powder with the powder of oxides
- Consolidation of the material at high temperatures by Hot Extrusion (HE) or Hot Isostatic Pressing (HIP)
- Cold rolling by several passes until the desired tube dimensions are obtained

The rolling operation is used to modify the tube geometry by plastic deformation, where the diameter and thickness of the tube are simultaneously reduced. The rolling passes will induce an increase of hardness, so it is recommended to apply an annealing operation to restore the material and to avoid the risk of damage.

The tubes characterized in this study were produced by hot extrusion by CEFIVAL from powder materials delivered by PLANSEE. A pre-alloyed metallic powder Fe-Cr-W-Ni atomized by AUBERT&DUVAL was ball-milled with (0.25wt% Y_2O_3 + 0.3wt% TiH_2) powder under hydrogen protective atmosphere. The obtained average powder particle size was about 80 μm . The milled powder was embedded in a can made from an AISI430 ferritic stainless steel. After an outgassing step (2h at 400°C), the powder was heated at the temperature of 1100°C during 2h and hot extruded to form a seamless rough tube.

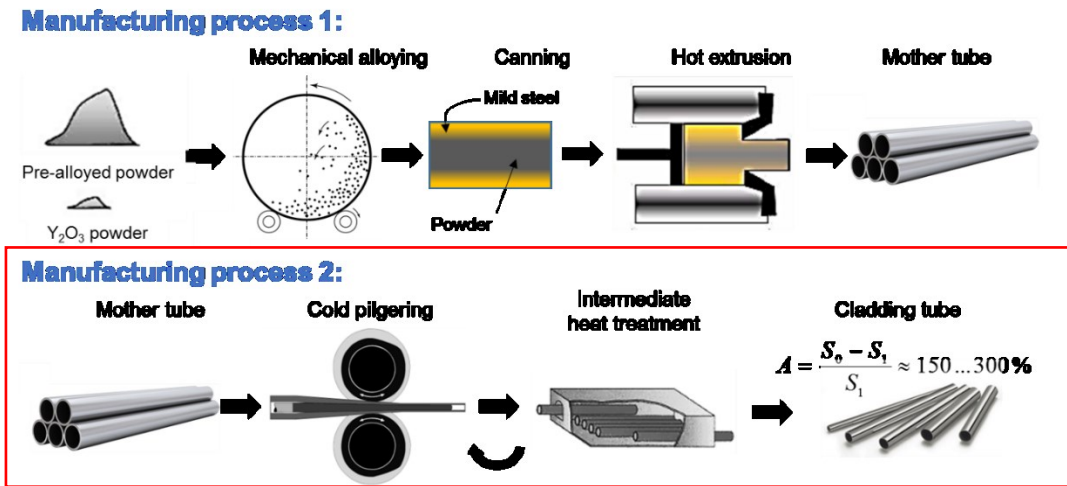


Fig.II.1 ODS alloy production chain by hot extrusion and pilgering
[Inoue *et al.*, 2007]

Pilgering was performed on VALINOX-NUCLEAIRE facilities in the framework of the STRATOTUBE ANR funding. The processing of the tubes consists of 2 pilgering steps. On Fig.II.2 two processing routes are presented. The first scheme joins the R1 pilgering step from the Hot Extruded (HE) state to the second pilgering step R2. The second scheme includes an intermediate heat treatment operated under Ar atmosphere. Final heat treatments were applied under $5 \cdot 10^{-2}$ mbar vacuum conditions on small sections. The dimensions of the tube, studied in this project, after hot extrusion, first and second rolling passes are given in Table.II.2. The dimensions of all produced tubes for this industrial campaign are given in Table.II.3. The strain tensor imposed during each pilgering step is obtained from the dimension evolutions of pilgered tubes. According to [Abe *et al.*, 2012], strain and Q factor (i.e. the ratio between thickness reduction and external diameter reduction) are estimated for each deformation step. Although, cold pilgering can introduce a significant shear component [Girard *et al.*, 2001], which is neglected in this work.

This study focuses on a 9%Cr ODS ferritic steel whose chemical composition is given in Table.II.1. This grade exhibits a ferrite-austenite ($\alpha \rightarrow \gamma$) phase transformation at high temperature as presented on Fig.II.3. Restoration by phase transformation in $\alpha + \gamma$ domain reduces both hardness and internal stresses accumulated during deformation. Two kinds of heat treatment were applied on samples R1 in laboratory furnace to investigate the influence of the heat treatment conditions on the ODS steel microstructure. The samples were heated, under vacuum, until 1050°C with a rate of 15°C/min and a 20 min holding time. Then, the tubes are submitted to 2 different cooling rates; a reference one at about 2 °C/min (IHT1) and a second one that mimics the industrial conditions at 0.4 °C/min (IHT6). Thus, the heat treatment time is almost 5 times longer in the case of industrial treatment. For the final treatment, both of the tubes R2 and R2 (HT) were exposed to the same cooling rate of 15°C/min.

Table.II.1 Chemical composition of ODS steel tubes (wt.%)

Cr	W	Ti	Ni	O	Y	C	Fe
9	0.9	0.2	0.2	0.1	0.1	0.08	Balance

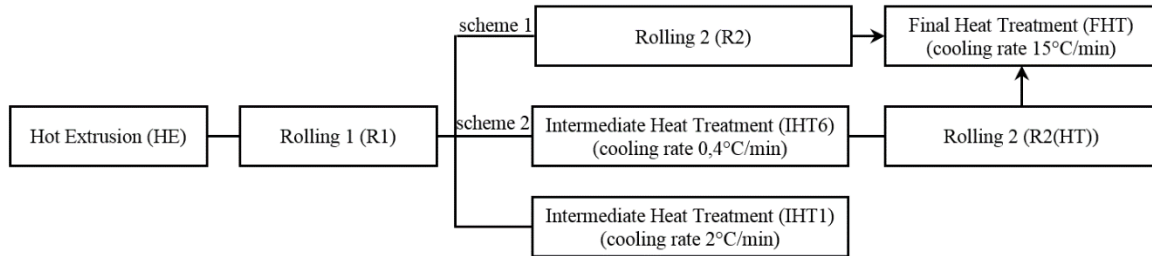


Fig.II.2 Processing route for the pilgering of ODS steel tubes

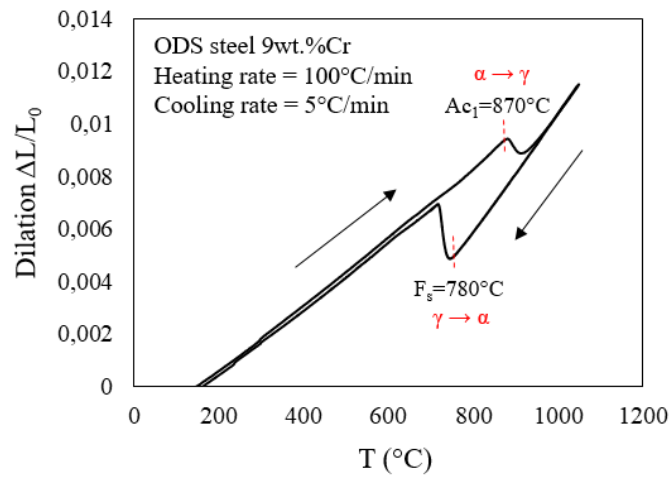


Fig.II.3 Dilation curve of ferrite-austenite phase transformation for 9wt% Cr ODS steel

Table.II.2 Tube dimensions obtained during pilgering (including the stainless steel cladding)

Step	Diameter (mm)	Thickness (mm)	Elongation (%)	Total deformation ϵ_p (%)	Q factor
HE	44,3	7,86	-/-	-/-	-/-
R1	28,3	3,98	300	110	1,4
R2	17,6	1,55	385	140	1,6

Table.II.3 Rolling process details of ODS tubes by VMR process performed by Valinox Nucleaire. The tubes taken for this study are in the red boxes.

Raw tubes	L_i, mm	ϕ_i, mm	Ep_i, mm	1 st pass	L_1, mm	ϕ_1, mm	Ep_1, mm	A 1, %	Treatment SOTEP	L^1, mm	2 nd pass	L_2, mm	ϕ_2, mm	Ep_2, mm	A 2, %				
11 (77.1 mm x 14.59mm)	19005	44.32	7.86	11.0	19.7	28													
				11.1	1995	28.31	3.98	296											
12	1903	44.37	7.89	12.1	3090														
				12.2	1300														
				12.3	1300 (1000)	30													
				12.4	40														
21	2001	44.3	7.79	21.1	3985														
				21.2	940														
22	1992	44.31	7.78																

II.2. Experimental details

II.2.1. Microstructural observations

Scanning Electron Microscopy (SEM) is a technique used for microstructural observation. This method is based on the interaction of electrons, emitted from incident beam, with the atoms of the sample surface. Depending on the interaction volume within the sample, various types of signals can be produced including secondary electrons (SE), reflected or back-scattered electrons (BSE), characteristic energy-dispersive X-rays (EDX) and others, presented on Fig.II.4. Each of these signals can be detected by specialized detectors.

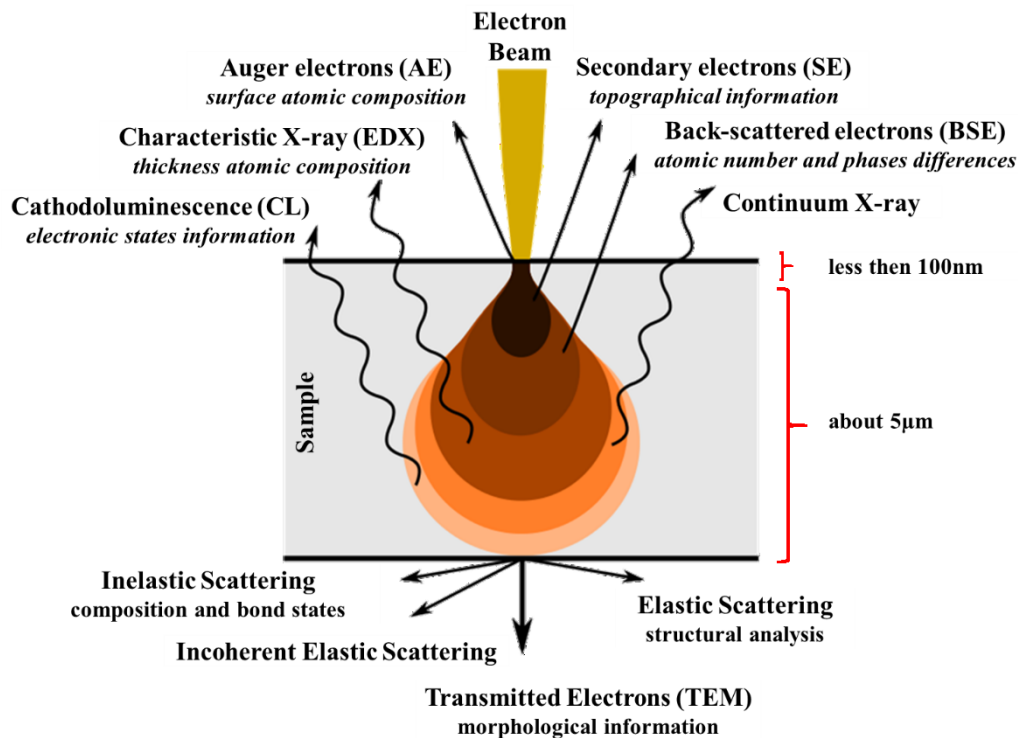


Fig.II.4 Interaction volume of various signals between the electron beam and sample surface [Goldstein et al., 1992]

In this work, we used three main signals: SE, EDX and BSE to obtain information corresponding to topography, composition and grain morphology in the sample.

The **secondary electrons (SE)** are emitted by inelastic scattering interactions with beam electrons from very close to the specimen surface ($\sim 10\text{nm}$). Consequently, they can produce very high-resolution images of a sample surface, revealing details less than 1 nm in size. For example in this work, it is applied to study the **fracture surfaces** of the samples in order to characterize in details the morphology of dimples. The voltage is set at 10 kV and the working distance is about 9.2 mm for SE observations.

Characteristic X-rays (EDX) are emitted when the electron beam removes an inner shell electron from the sample ($\sim 5\mu\text{m}$), causing a higher-energy electron to fill the shell and release energy. The measured X-ray signals are used to plot maps of the distribution of elements in the sample. The voltage is set at 15 kV and the working distance is about 10.5 mm for EDX observations. In this project, EDX is used for chemical analysis of the specimens. It can detect the presence of elements, their **distribution** and their concentration. However, for light elements (like O, C) EDX is not really suitable for quantitative analysis, but can be used at least for qualitative characterization. Electron Probe Micro-Analyzer (**EPMA**) is the ability to acquire precise, quantitative elemental analyses at very small "spot" sizes, primarily by wavelength-dispersive spectroscopy (WDS). This technique identifies the elements present and measure their concentration with a small degree of error. It allows to analyze the **lower Z elements** (C, N, O) [Goldstein et al., 1992].

Back-scattered electrons (BSE) are beam electrons that are reflected from the sample by elastic scattering. They emerge from deeper locations within the specimen and consequently the resolution of BSE images is lower than SE images. Backscattered electrons is also used to form electron backscatter diffraction (EBSD) images that determine the crystallographic structure of the sample. The latter collects the information about the size and shape of grains, grains misorientation, the crystallographic texture, etc. To realise EBSD observation, the sample should be tilted at approximately 70° relatively to the incidence of the electron beam to optimise both the contrast in the diffraction pattern and the fraction of electrons scattered from the sample. If the tilt angle is smaller, the contrast in the diffraction pattern will decrease. The voltage is set at 20 kV and the working distance is about 14.5 mm for BSE mapping.

The study of crystals orientation and textures by EBSD allows to work only at the local **microscale of observed 2D** surface. In order to obtain information about texture at **macroscale in volume**, we have to use another technique, such as X-ray or neutron diffraction. Since the information depth of EBSD and XRD differ by a factor 2-3, it is clear that statistically XRD has certain advantages. X-ray diffraction can measure more grains than EBSD scans. But, if the EBSD map has more than about 1000 grains then we can compare the results and obtain very similar textures.

In this work we use both of these techniques in order to extract the maximum of information about microstructure: orientation distribution and texture (XRD and EBSD) and misorientation between the grains (EBSD).

Synchrotron X-ray diffraction. In addition to EBSD and XRD texture analysis, it was needed in this work to obtain the information on the kinetics of texture evolution during phase transformation at the different stages of heat treatments. For this, the measurements must be done in-situ to follow quantitatively $\alpha \rightarrow \gamma \rightarrow \alpha$ transformation with a time resolved method. Synchrotron radiation facilities are used to realize this study. Detailed description of the set up and sample preparation are given in [Chapter V](#).

Sample surface preparation for EBSD and XRD texture analysis

Samples preparation is based on a 6 steps mechanical polishing and final colloidal silica oxide polishing suspension (OPS) polishing on a Vibromet equipment to perform surfaces suitable for EBSD analysis. Specimen parts are sampled in longitudinal and transverse directions of the tube named as RD and TD directions.

EBSD and XRD operating modes

Grains morphologies and their crystallographic orientations are measured by Scanning Electron Microscopy (SEM) JEOL 7001-FLV coupled with EBSD using a Bruker QUANTAX system (Esprit software). The voltage is set at 20kV and the working distance is about 14.5mm. EBSD maps are realized on an area of $60\mu\text{m} \times 45\mu\text{m}$ with a step size of 52 nm that is consistent with the grain size. An exception was done for sample R2 where the grains size is very small, so the step size was reduced by a factor 2 to 26 nm whereas the map is $30 \times 22.5 \mu\text{m}^2$. The orientation maps for all samples presented in this report were taken with the vertical direction parallel to the rolling direction. The illustration of the sampling scheme for EBSD and XRD analyses is given on Fig.II.5.

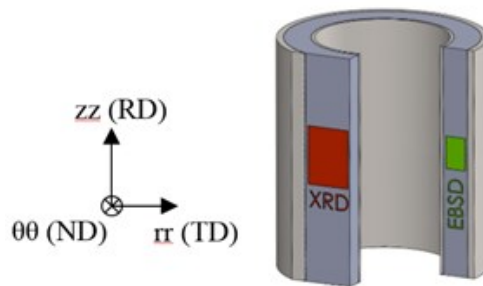


Fig.II.5 Sampling scheme for EBSD and XRD analyses

Textures are also analyzed by X-ray diffraction on a Bruker D8 Discover A25 with a $\text{Cu-K}\alpha$ radiation and it is plotted as pole and inverse pole figures using Labotex software. The measurement was done in the orthoradial plane parallel to the rolling direction and represents the macro texture of the samples. A method of Arbitrary Defined Cell (ADC) was used to determine the complete Orientation Distribution Function (ODF) from the incomplete pole figures. X-ray analysis is realized using a PANalytical X'Pert Pro diffractometer. To calculate the micro-stresses and the average crystallite sizes, the diffraction patterns were fitted by a Thomson-Cox-Hastings pseudo-Voigt function [Thompson et al, 1987].

II.2.2. HKL and MTEX software for images post-treatment

Channel 4 HKL software is used for post treatment of EBSD maps. The post treatment starts from noise reduction, when non-indexed points are replaced by the orientation of the closest neighbors. Then, Inverse Pole Figures (IPF) maps are plotted consistently with the color code presented on Fig.II.6. Boundaries with misorientations between 3° and 10° were defined as low angle grain boundaries (LAGB) and the misorientation higher than 10° as high angle grain boundaries (HAGB).

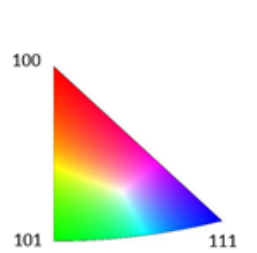


Fig.II.6 Colour code used for EBSD cartography analysis

MTEX (Matlab toolbox) is used in this work in order to construct the orientation distribution from EBSD or XRD measurements, as well as to analyze and model crystallographic textures by means of EBSD or pole figure data.

II.2.3. TEM observations

Transmission Electron Microscope (TEM) is an observation instrument used to study the internal microstructures of the samples at high magnification. In this technique, the beam of accelerated electrons is transmitted through a specimen to form an image, showing the distribution of **nano-precipitates** and **dislocations** networks in the sample.

For observation by TEM, the ODS samples were thinned by mechanical polishing to $100\ \mu\text{m}$. Then the discs of 3 mm diameter were cut from these thin membranes and electropolished at -10°C in a solution of 10% perchloric acid and 90% ethanol. Samples, presented in this work, are taken from the surface perpendicular to the orthoradial axis of the tube (as for XRD analysis on Fig.II.5).

II.2.4. Hardness and traction tests

Vickers hardness tests were carried out using a hardness testing machine applying a loading of 1kg not less than at ten points for each polished samples. Vickers microhardness profiles were realized under 0.1kg/10s loading on thousands of points using an automated system.

The tensile tests were carried out on an INSTRON electromechanical machine installed at the Laboratoire d'étude du Comportement Mécanique des Matériaux (LC2M). The experimental procedures were performed using the same methodology adopted for 9%ODS steel reported in [Toualbi, 2012] with the possibility to compare the obtained results later. Thus, for traction tests two geometries of tile and ring were used in order to measure stress/strain resistance in longitudinal and transversal directions. The tensile specimens dimensions are given on Fig.II.7. Force measurements were made using a 2 kN force cell. The sensitivity of the stress to the strain rate were estimated by using three strain rates 10^{-2} , 10^{-3} and 10^{-4} s^{-1} . The post-treatment analysis of the tensile tests were done to correct the conventional deformation/stress curves by correcting the rigidity of the machine. The elastic slopes are recalibrated from the Young's modulus for 9%Cr ODS material, assumed to be known as 228 GPa [Note d'essai DMN/SRMA/LTMEEx/NE-2013-24].

During the cold pilgering, the tubes have a triplex structure. It means that ODS material was covered from the external and internal sides by F17 steel with a lower hardness to facilitate the deformation and prevent the material and equipment from damage. For the traction tests these F17 layers were completely removed by roughing from the ODS tube surface to provide the data concerning only ODS material.

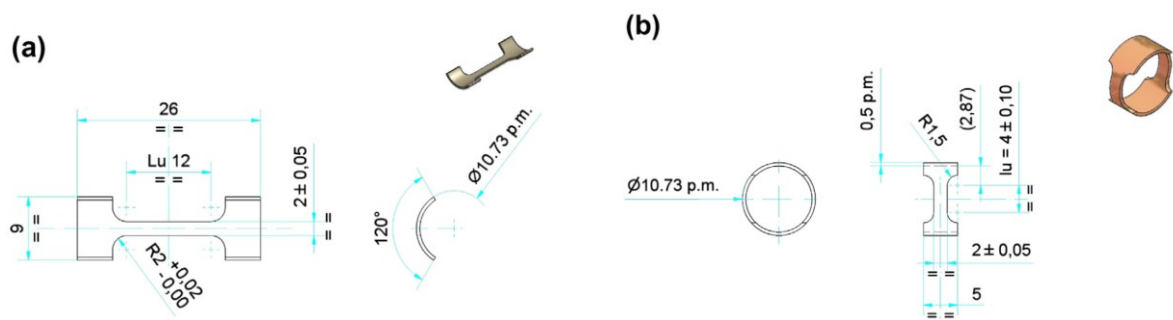


Fig.II.7 Tensile specimens: (a) in longitudinal direction (tile) and (b) in transversal direction (ring)

II.2.5. Dilatometric measurements

In order to evaluate phase transformations during heating and cooling, dilatometry tests are carried out on a dilatometer DT1000 ADAMEL-LHOMARGY. This thermal analysis technique consists in monitoring the sample expansion as a function of temperature and time. These variations are characteristic of a phase transformation. The dilatometry curves make it possible to determine the start and the end of phase transformation temperatures, as well as the transformed phase ratio. This information is then plotted on the Time-Temperature-Transformation (TTT) diagram. For dilatometry measurements, the samples with a size 12x2x2 mm are cut by metallographic cut-off saw in the rolling plane of the tubes. ThermoCouples type K (NiCr-Ni) are spot welded along the sample surface. The sample is installed in the furnace and heat treated in He atmosphere.

II.2.6. Magnetometry observations

The evolution of the magnetic properties reveals information about the internal structure of the material. This structure will depend on the applied thermomechanical treatments. Therefore, our study is conducted to find out what can be revealed by the evolution of the magnetic properties on the microstructures of the ODS steel. In particular, it can highlight the specificity of ODS steels compared to similar materials without precipitates (like Fe-Si electrical steel). It can also elucidate at which conditions the material will have enhanced magnetic properties and if there is any parallel between metallurgical states and magnetic properties in ODS rolled steel.

Magnetometry observations were realized in laboratory of "Nanomagnetism and oxides" (SPEC, CEA Saclay) using VSM machine (Vibrating Sample Magnetometry). The objective was to determine the evolution of magnetic properties for small ODS steel pieces (2x1x1 mm) at different elaboration states. The method consists in measuring the induced flux Φ during a periodic displacement of the sample submitted to an evolving global magnetic field. Thus, the voltage induced in the detection coils by a magnetic moment sample μ is obtained. The tests were realized with a maximum magnetic field of 2.8 T, ambient temperature and argon controlled atmosphere of measurements.

Conclusions for Chapter II

This chapter presents a summary of manufactured ODS tubes with the codes corresponding to their metallurgical states appearing in the next chapters of this manuscript. It introduces also the various experimental techniques that were used to characterize the microstructure of the ODS tube at a multi-scale starting from nano-precipitate by TEM and finishing by tensile tests for macroscopic mechanical properties. SEM coupled with EBSD, X-ray Diffraction and magnetometry techniques make it possible to follow microstructural evolutions at different production steps. The techniques of dilatometry and Synchrotron X-ray diffraction are complementary in the study of phase transformations of ODS cold-rolled steels. Finally, some measurements using VSM machine will show the impact of texture and heat treatment on the magnetic properties of ODS steels.

Chapter III. Impact of pilgering sequence on microstructure and properties of ODS pilgered tubes

Introduction

In this Chapter, the evolution of microstructure, crystallographic texture, physico-mechanical properties is studied for all pilgering steps considering two processing routes: with and without intermediate heat treatment between rolling steps. The present study highlights the effects of severe cold working and intermediate/final heat treatments. The understanding of the observed mechanisms can help to find the limiting parameters of the process and suggest improved processing sequences.

III.1. Grains morphology and their internal misorientation

In this section 9%Cr tubes are cold formed with various thermomechanical sequences. All sequences are obtained from an initial Hot Extruded (HE) material. The initial hot extruded structure, presented on [Fig.III.1](#), can be characterized as slightly elongated grains with almost morphological isotropy and no preferential orientation. The average grain size is 800 nm.

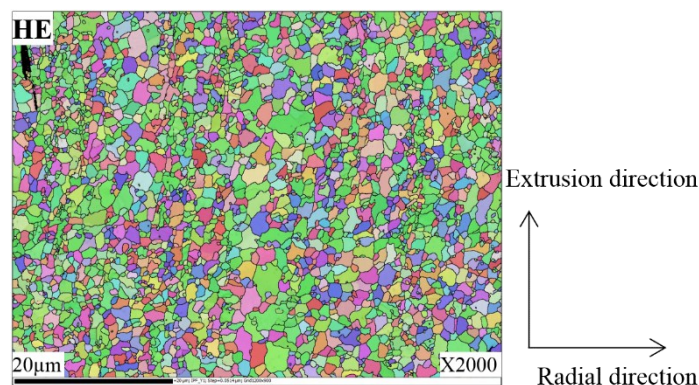


[Fig.III.1](#) Inverse pole figure map of the hot-extruded 9%Cr ODS sample

[Fig.III.2](#) presents EBSD maps of longitudinal cross-sections of the tubes at various stages of the pilgering process and heat treatment. After the first pilgering step (R1), the grains present elongated shapes with a preferential α -fiber texture collinear to the pilgering direction. During the Intermediate Heat Treatment (IHT) the morphology is changed to almost equiaxed grains and it still shows a high texture intensity. The second pilgering step (R2 and R2(HT)) will again rearrange the microstructure into elongated grains, until final heat treatment (FHT) that will create a highly textured material constituted of equiaxed grains.

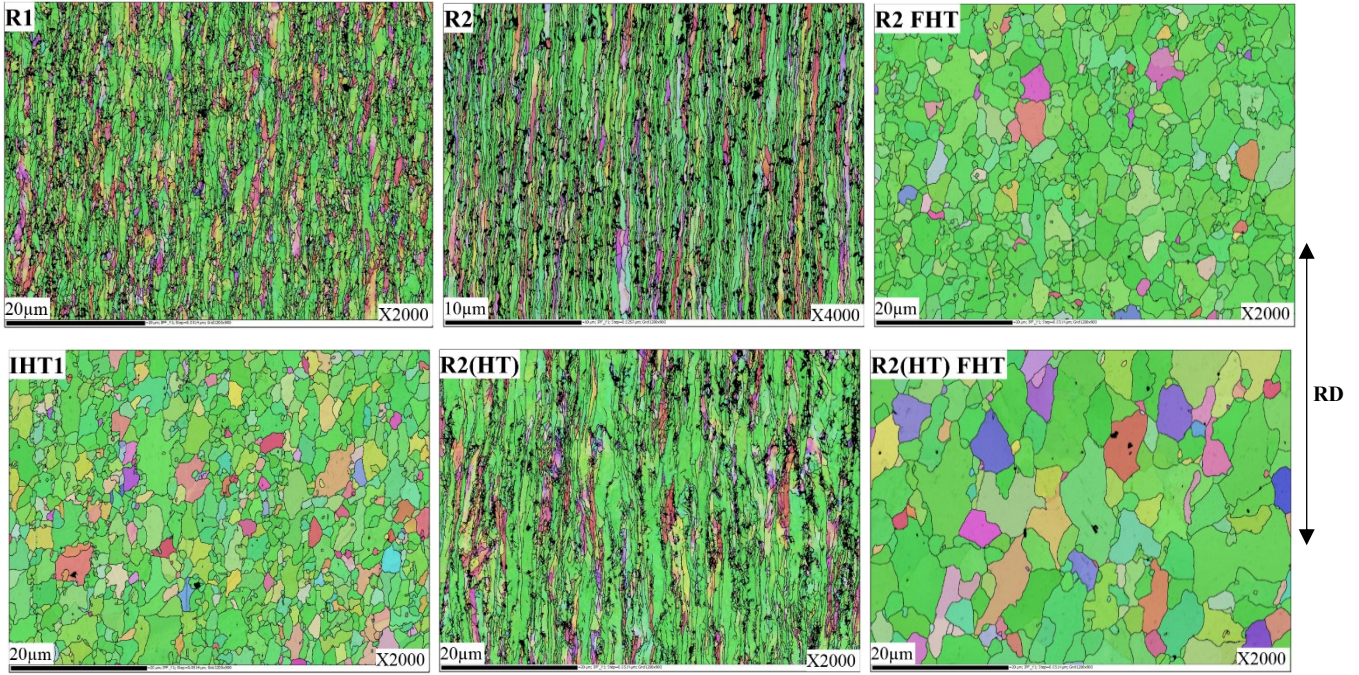


Fig.III.2 IPF maps with grain boundaries pattern at each pilgering step of ODS tubes (RD-TD plane)

Pilgering operations and Intermediate Heat Treatment (IHT) were driven in industrial conditions on Valinox-Nucleaire facilities. This IHT was realized at 1050°C with 20 min of holding time followed by slow cooling at 0.4°C/min under argon atmosphere. In order to characterize this state, a R1 sample has been treated in CEA laboratory furnace in the same conditions and this sample is called IHT6 (cf. the heat treatment details in Annex 1). Additional heat treatment in the ferritic domain was realized at 1050°C with 1h of holding time, but with a faster cooling rate (15°C/min), called IHT1. The same operation was done for the final heat treatment FHT. On Fig.III.3 those longer final treatment R2 FHT6 and R2(HT) FHT6 exhibits microstructures with larger grains.

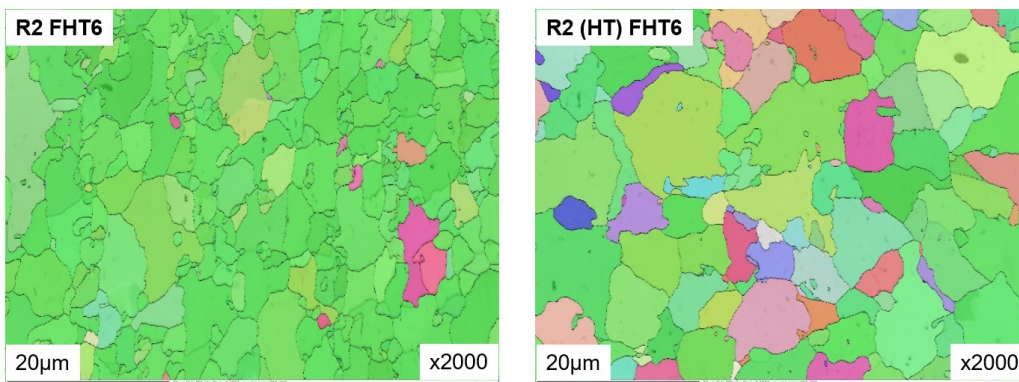


Fig.III.3 IPF Y maps with grain boundaries pattern for tubes R2 FHT6 and R2(HT) FHT6 (RD-TD plane)

Grain size distribution (based on equivalent circle diameter) and average aspect ratio (the ratio between the largest to the smallest orthogonal grain dimension) computed from EBSD maps are presented on Fig.III.4. The higher grain refinement was achieved at about 140% equivalent straining (R2). At the same time, the intermediate heat treatment makes it possible to recover the grain shape after the first pilgering step to the initial non-rolled HE state with an isotropic and homogeneous morphology. Moreover, the fraction of small grains after the second pilgering step (R2 HT) is similar to the one after the first step (R1) (see Fig.III.4b).

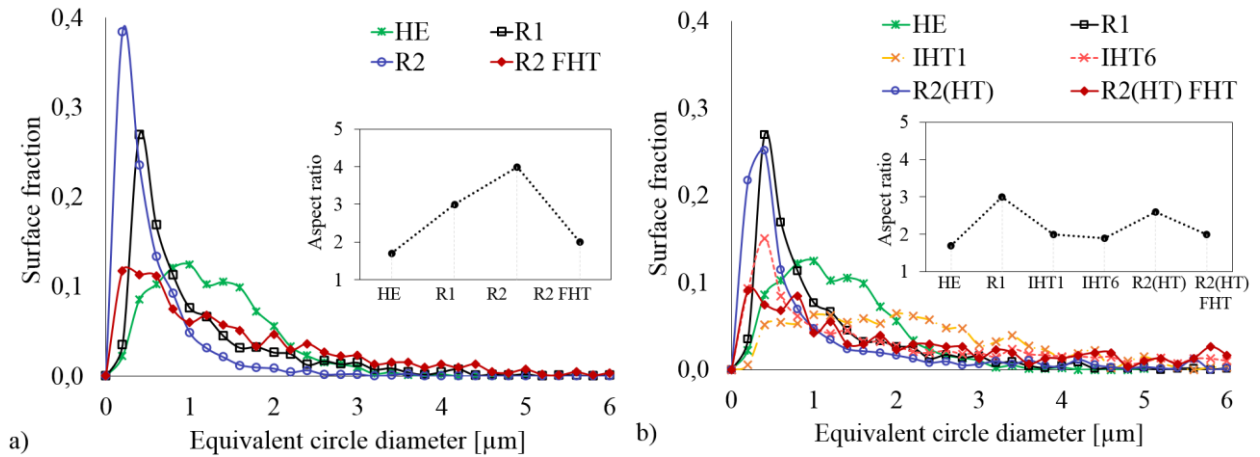


Fig.III.4 Grain size distribution and average aspect ratio: (a) scheme 1, (b) scheme 2

Fig.III.5 shows the grain boundary misorientation distribution diagram. Low Angle Grain Boundaries (LAGB) frequency increases with deformation. After annealing, a peak at 50-55° is detected that corresponds to the formation of High Angle Grain Boundaries (HAGB). In pilgered samples, the HAGB fraction is very low. This transformation of LAGB into HAGB during annealing is characteristic of recovery associated to phase transformation. In this scheme LAGB are progressively transformed into HAGB without formation of new nuclei. This phenomenon monitors the grain size evolution [Jazaeri and Humphreys, 2004].

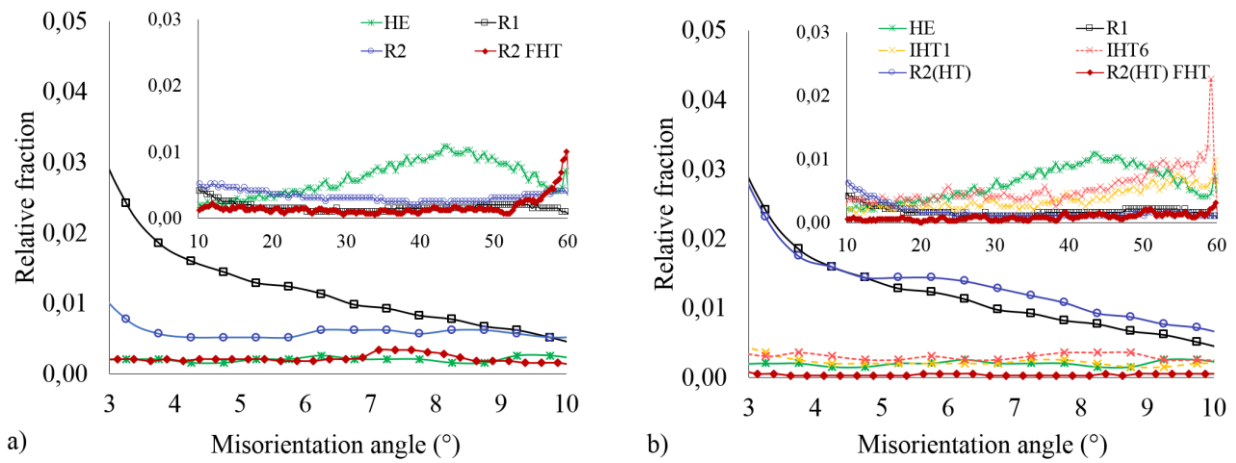
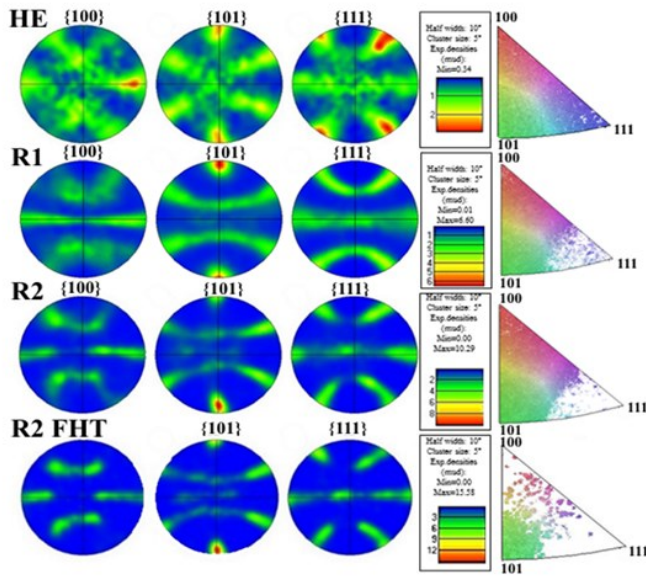


Fig.III.5 Misorientation distribution of pilgered samples: (a) scheme 1, (b) scheme 2

III.2. Texture evolution after pilgering and applied heat-treatment

On Fig.III.6 the evolution of crystallographic texture is illustrated for the two production schemes by the pole figures and inverse pole figures obtained by EBSD. At each manufacturing step all pilgered samples showed a similar α -fiber texture parallel to the rolling direction. For initial HE state it is observed that the $\langle 001 \rangle$, $\langle 110 \rangle$ and $\langle 111 \rangle$ lattice orientation distribution is homogeneous. Nonetheless, it should be noted that the $\langle 111 \rangle$ lattice orientation is slightly less represented. For R2 (HT) FHT sample the large grain size results in a few amount of grains on the EBSD map. This may explain the spreading of the inverse pole figure (IPF).

□ Scheme 1



□ Scheme 2

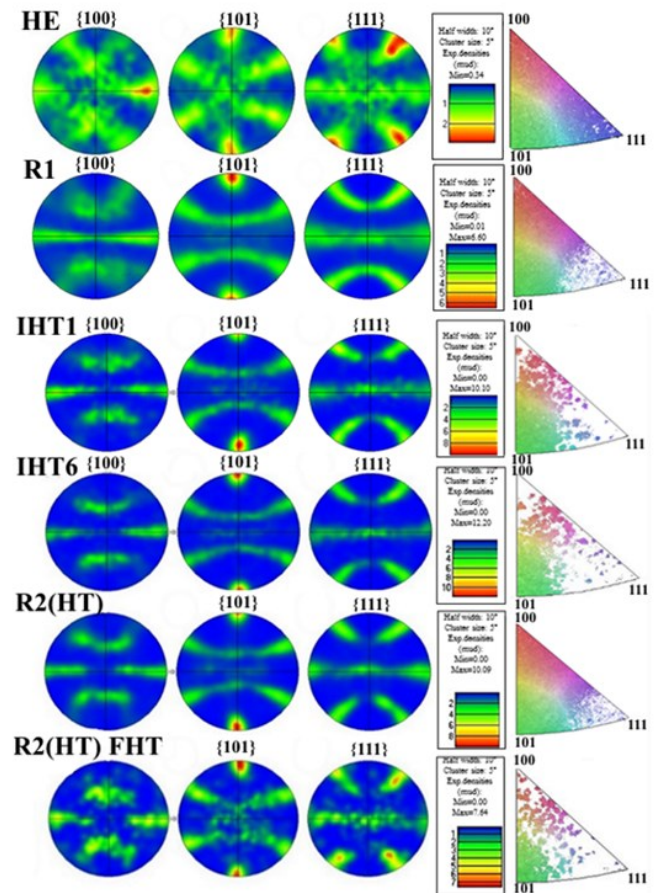


Fig.III.6 Pole figures and inverse pole figures of 9%Cr ODS samples during different rolling steps

Fig.III.7 presents a quantitative estimation of the surface fraction for three fibres that are dominant in BCC materials. Subset selection for each texture component was done for a maximum deviation of 15° from the ideal fibre orientations. The value ‘others’ presents all non-indexed zones (porosity, precipitates, etc.). It can be clearly seen on Fig.III.6 and Fig.III.7 that during pilgering processing the surface fraction of $\langle 111 \rangle$ oriented grains decreases progressively to the benefit of $\langle 110 \rangle$ oriented grains parallel to RD. The following process of heat treatment (IHT1 and IHT6) will additionally remove the $\langle 001 \rangle$ oriented grains and transform them to the dominant $\langle 110 \rangle$ component. The longer the heat treatment the higher the fraction of grains that will take the orientation $\langle 110 \rangle$. However, during the second pilgering step R2 and R2 (HT), the $\langle 001 \rangle$ oriented grains are maintained, only the $\langle 111 \rangle$ oriented grains are still not present in the structure.

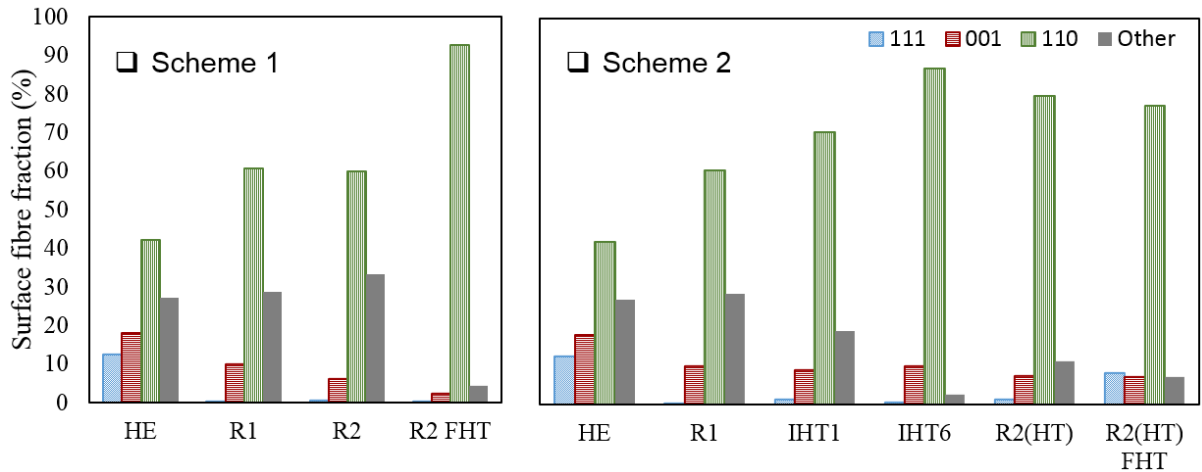


Fig.III.7 Surface fraction of <111>, <001> and <110> lattice orientation components

The texture intensity evaluated by multiples of the uniform density (m.u.d.) is presented on Fig.III.8 using both EBSD and XRD techniques. Also the texture indexes were computed from an interpolated ODF using the coefficients of the series expansion method and presented on Fig.III.9. It appears clearly that the texture index is significantly increased after heat treatments. This kind of texture memory effect can be explained by a specific variant selection during direct $\alpha \rightarrow \gamma$ or reverse $\gamma \rightarrow \alpha$ transformation according to a Kurdjumov-Sachs relation [Kurdjumow and Sachs, 1930]. However, looking to IHT1 and IHT6 samples (Fig.III.8 and Fig.III.9) the texture index keeps increasing with heat treatment holding time contradicting the results observed, for instance, for IF steels [Yoshinaga et al., 2007]. This seems to indicate that austenitic grains with a preferential orientation (along fiber) are growing to the detriment of others grains more distant from the fiber in terms of orientation.

Unexpectedly, pilgering sequences operated on the same material but with a lower cold working straining (in the laboratory reference system) do not exhibit such behavior [Toualbi et al., 2013]. In such cases, the pilgered texture index is slightly reduced by heat treatments between pilgering sequences [Ukai, 2011]. More information about crystallographic texture of the austenitic grains seems necessary to elucidate this phenomenon apparently sensitive to the amount of cold working, texture and/or total holding time at high temperature. A specific insight of this phenomenon is proposed in Chapter IV.

The recovery effect observed during heat treatment is consistent with microstresses evolution (see Fig.III.8) computed from X-ray diffraction measurements (identification on simplified Gaussian contribution with Stokes equation). Thus, the value of microstresses are decreased by factor 3 for the heat treated sample IHT6.

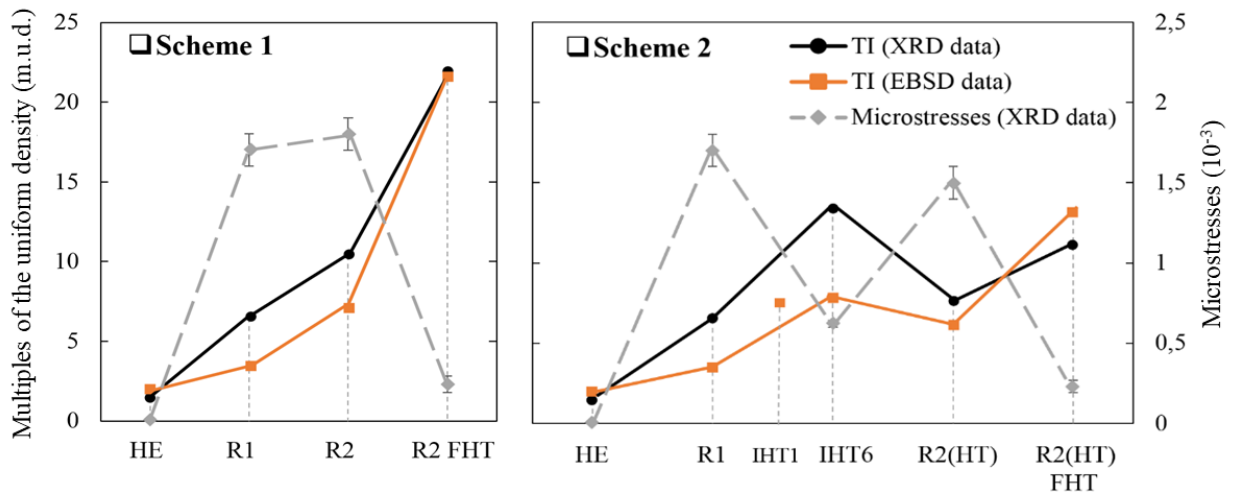


Fig.III.8 Multiples of the uniform density and microstresses level at various step of the processing sequence

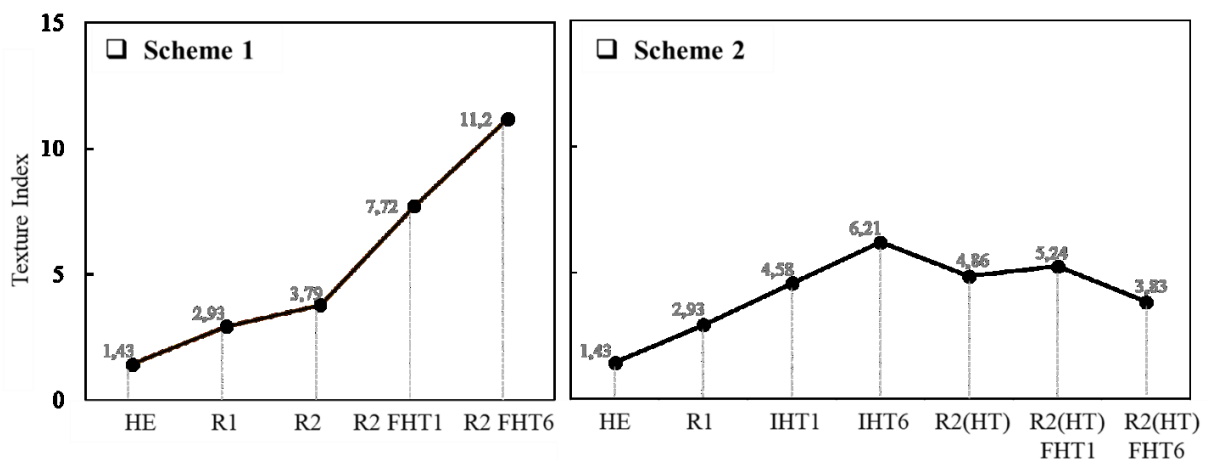


Fig.III.9 Texture index at various step of the processing sequence

On Fig.III.10 experimental ODF plots in the $\phi_2=45^\circ$ section are presented for the samples R2 FHT (left) and R2 (HT) FHT (right). The appearance of a double-pole α -fiber was observed during the final treatment of the R2 HT tube, while the tube R2 FTH has only one pole corresponding to the α -fiber.

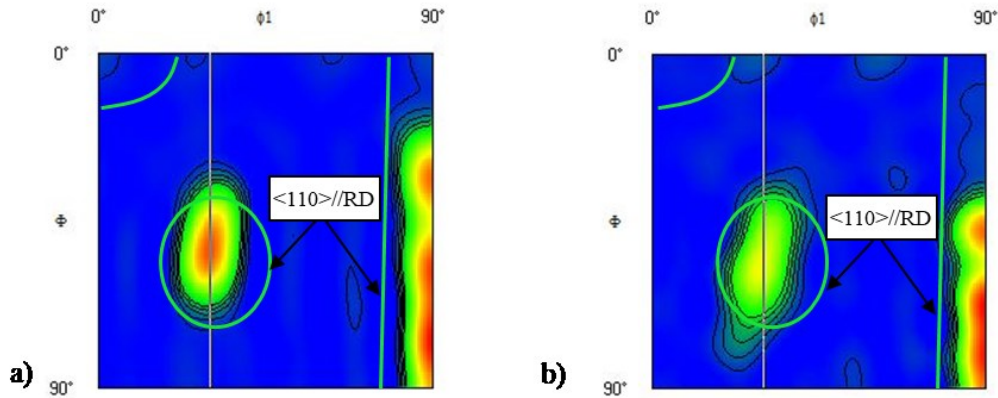


Fig.III.10 Experimental Orientation Distribution Function (ODF) figures ($\varphi_2=45^\circ$ section of ODF) for R2 FHT (a) and R2(HT) FHT (b) with ideal crystallographic fibres in green line

It is demonstrated on Fig.III.11 with the ODF section plots in $\varphi_2=45^\circ$, $\varphi_1=30^\circ$. The figure on the left, corresponding to production scheme 1, contains a pure α -fiber with a maximum at $\Phi = 55^\circ$ after the second rolling pass R2 and its heat treatment R2 FHT. For production scheme 2, this maximum is split into two components at $\Phi = 45^\circ$ and 60° respectively, which means that the α -fiber is rearranged with 15° difference during the second rolling pass R2 (HT). This double pole could be explained by the combination of the α -fibre pole generated by cold working and also another one inherited from nucleus selection during phase transformations. A similar mechanism was observed during recrystallisation of cold-rolled titanium [Wronski et al., 2016].

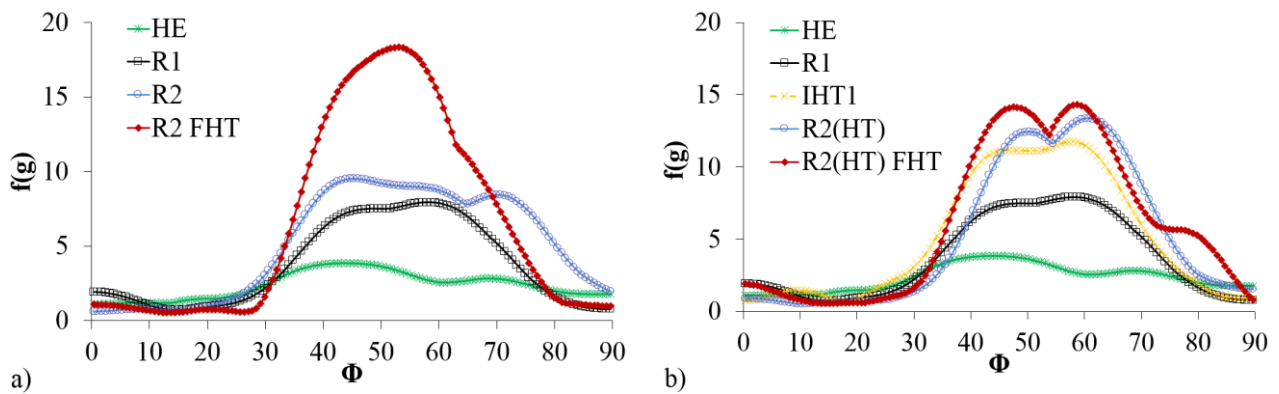


Fig.III.11 Texture fiber plots in $\varphi_1=30^\circ$; $\varphi_2=45^\circ$ section of ODF: (a) scheme 1 and (b) scheme 2

III.3. Evolution of mechanical properties: hardness and traction tests

Hardness is measured on tubes in RD section using a Vickers indenter. The measurements are performed for various positions along the tube thickness and the average value is computed over 500 points and their profiles are presented on Fig.III.12. It can be seen that the recovery of hardness after heat treatment is not complete: the outer layers of the material remain slightly harder than the core.

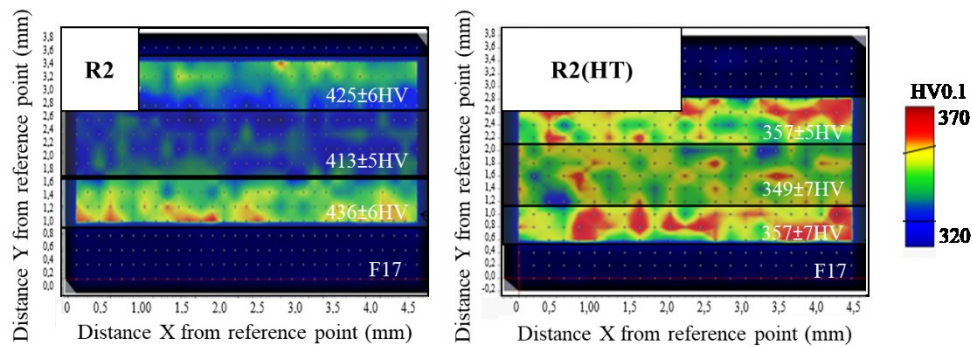


Fig.III.12 Hardness map in the ODS tubes thickness for R2 and R2(HT) states (F17 steel on the outer layer of tube are plotted in blue)

Microhardness evolutions during manufacturing process are shown on Fig.III.13 for schemes 1 and 2. The highest hardness level was achieved after the two rolling passes following the Scheme 1 with a value higher than 400 HV. For Scheme 2, it is seen, after R1, that applied thermal treatment softens the ferritic structure from 350 ± 7 HV to 250 ± 6 HV (IHT1/IHT6). The hardness after the second rolling pass R2 (HT) 345 ± 6 HV is almost equal to the hardness after the first pass R1 which comes from the recovery of the microstructure. For the last step of pilgering process two different heat treatments were applied in order to obtain, a ferritic structure R2(HT) F and a tempered martensite structure R2(HT) MR. Both samples were heated, under vacuum, until 1050°C with a $15^\circ\text{C}/\text{min}$ rate and were held at this temperature for 1 hour. Then, the first sample R2(HT) F was cooled at $2^\circ\text{C}/\text{min}$ and the second one R2(HT) MR was quenched by Ar gaz at $50^\circ\text{C}/\text{s}$ before tempering at 750°C during 15 min. Thus, these two states present respectively the properties of tubes ready for the next pilgering step and the service conditions.

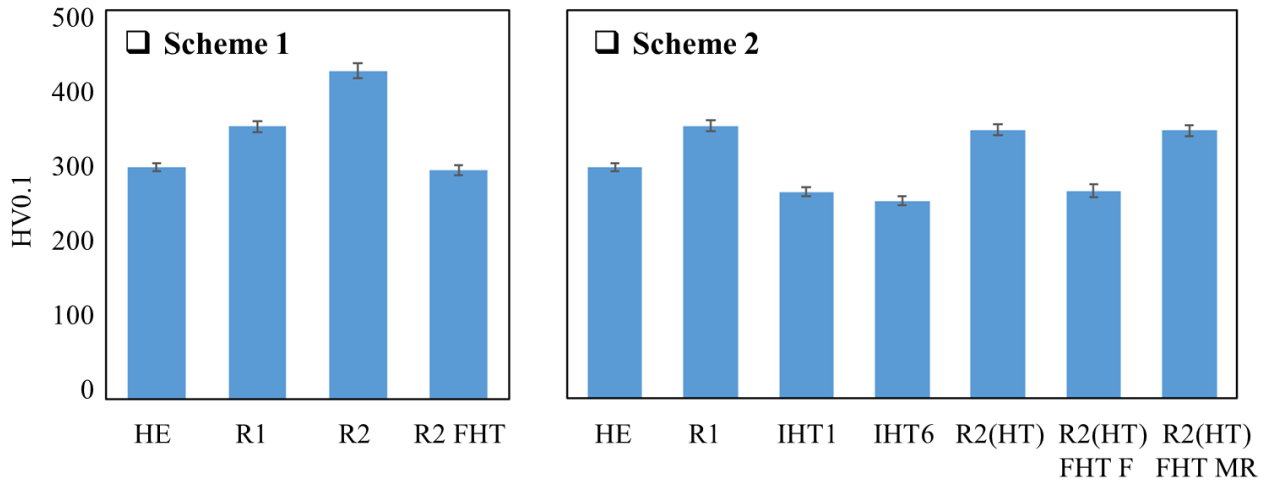


Fig.III.13 Hardness evolution for each production step

To analyze the macroscopic mechanical response of the material, the yield strength is recalculated from hardness with the semi-empirical relation $\sigma_y = 3.5HV$ [Courtney, 2000]. The relation between the flow stress and grain size in polycrystals under monotonic deformation has been investigated using a Hall–Petch-type plot. This plot exhibits linear relations between the flow stress and the inverse of the square root of the grain diameter $d^{-1/2}$ [Hall, 1951], [Petch, 1953].

$$\sigma_y = \sigma_0 + K \cdot d^{-\frac{1}{2}}$$

where σ_y is the yield stress, σ_0 is a frictional stress required to move unlocked dislocations along a glide plane, d is the grain size and K is a constant. It is considered that in Hall-Petch dependence frictional stress σ_0 includes several mechanisms of material strengthening such as strain hardening, precipitate strengthening and solid solution strengthening, whereas the constant K characterizes a grain boundaries strengthening due to interactions between dislocations and grain boundaries [Li et al., 2003].

In this work we used this simplified model to summarize the results of the hardness measurements for the first approximation, assuming a technological application. However, the contribution of various phenomenon, including solide solution, precipitation, dislocation densiy and grain size, is important. For HIPed ODS material, their respective influences were studied in the work of [Dadé et al., 2017].

On Fig.III.14 the macroscopic mechanical response of the material is analysed as a function of grain size. Data analyzed here are related to both cold-rolled (strain of 1.40 per pass) and heat treated ODS samples described above. The results of the present work are compared with representative results for Ultra Fine Grains or Nanocrystallized (UFG/NC) steels exclusively obtained by severe plastic deformation and a subsequent heat treatment: 12wt.%Cr ODS steel produced by Equal Channel Angular Extrusion (ECAE) process (strain of 1.15 par pass) [Song et al., 2013], interstitial-free (IF) steel after plastic deformation by Equal Channel Angular Pressing (ECAP) (total strain between 1.15 to 9.2) [De Messemaeker et al., 2004] and IF-steel after cold rolling (total strain between 0.1 to 0.9) [Li et al., 2003]. It can be seen that a higher fraction of grain boundaries and dislocation density, induced by intensive plastic deformation, will increase the yield stress following the Hall-Petch strengthening effect.

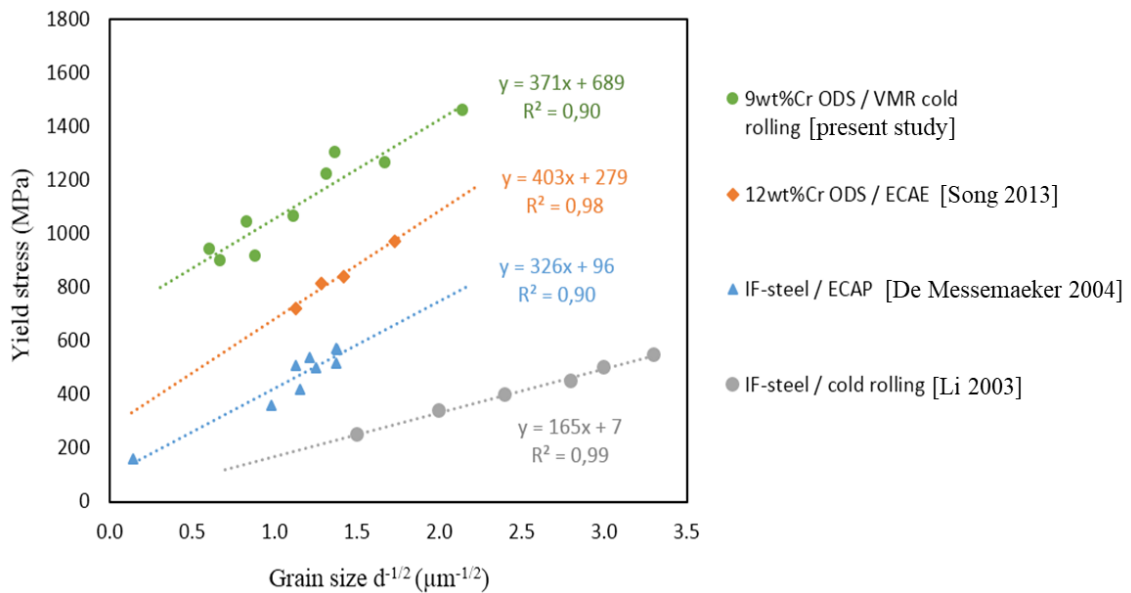


Fig.III.14 Hall-Petch plots in UFG steels with comparison to ODS steel

It is interesting to note that the slopes for the two ODS steels are quite similar, that demonstrates the effective grain refinement provided by both forming processes on ODS steel. It also shows that the physical mechanisms of grain boundaries hardening are the same in the two steels. However, it is seen that the larger deformation level (VMR process in comparison with ECAE), the higher the dislocation density produced in the matrix and consequently the higher the measured frictional stress. The same tendency was observed for IF-steels produced by ECAP and cold rolling processes respectively. The efficiency of the dispersed oxides is shown by comparing ODS steel and IF-steel. By decreasing dislocation mobility, these oxides significantly improve the material strength [Feaugas et al., 2003]. The high microstructural anisotropy in VMR ODS steel can play an important role in this strengthening mechanism and should be studied in future.

III.4. Evolution of chemical composition

EPMA measurements were realized in order to characterize the possible diffusion of chemical elements from the F17 cladding into ODS steel during rolling and heat treatment and to link it with the hardness evolution mentioned above. Polished sample surface was used for the measurements, where the composition was measured along lines in three zones as shown on Fig.III.15: (1) on the border of F17 and ODS on the external tube side, (2) in the center and (3) on the internal side. Each line consists of 15 measurement points with 2 μ m step size.

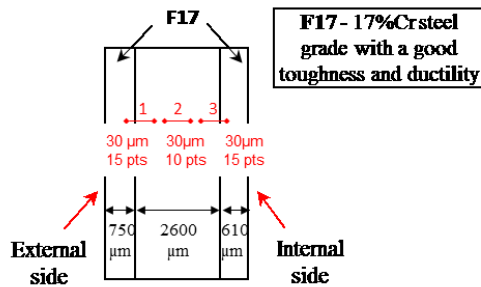


Fig.III.15 EPMA measurement profile on the tube wall thickness

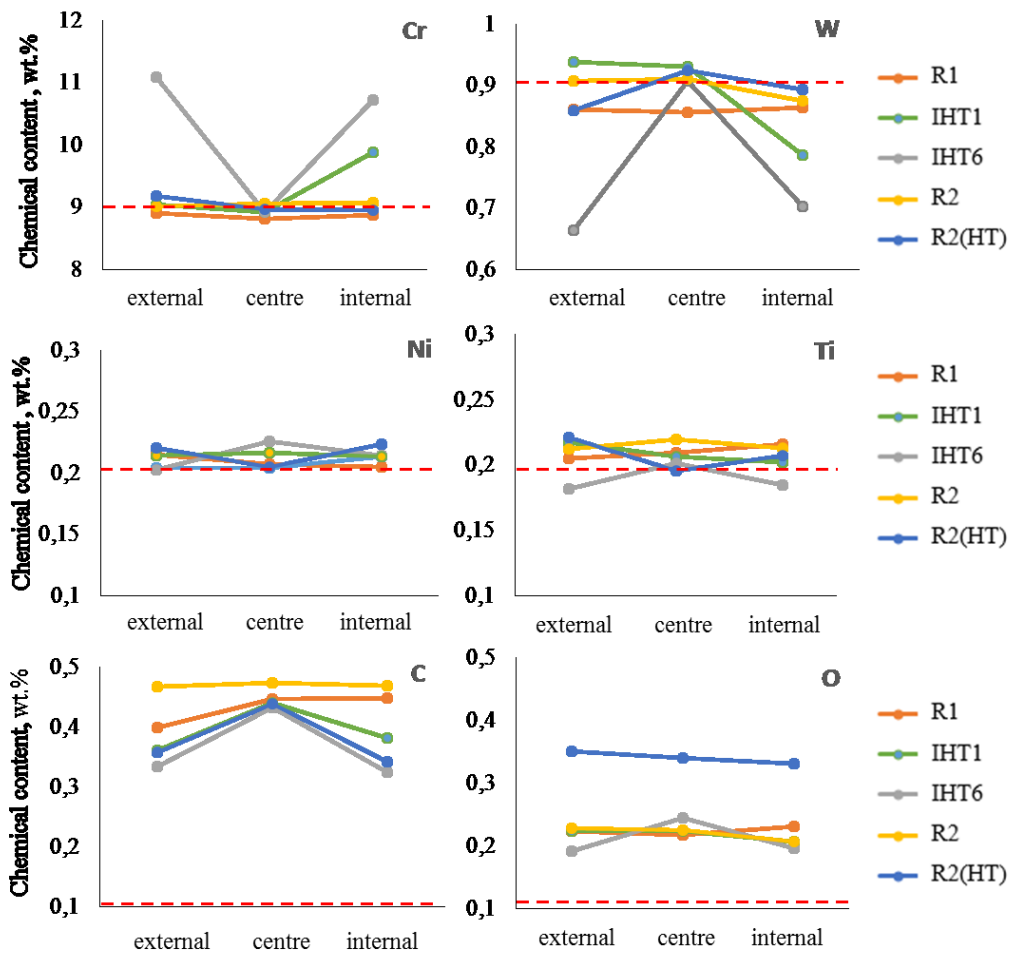


Fig.III.16 EPMA measurement profile for the 6 main grade elements: Cr, W, Ni, Ti, C and O at each production step. The red dashed lines indicate the nominal chemical composition of 9%Cr ODS steel

The results of EPMA analysis are presented on Fig.III.16. It was observed that:

- **Cr** is diffused from F17 to ODS during TTH, increasing its value from 9wt.% to 11wt.%, making the ODS boundary layer rich in Cr.
- **W** is diffused from the center of ODS bulk to the F17 layer during TTH, making the ODS boundary layer poor in W.
- There is no evolution for **Ni** between the measurement zones and production steps, it keeps values between 0.20wt.% and 0.24wt.%
- **Ti** is quite stable and keeps values between 0.18wt.% and 0.22wt.%
- **C** content is much higher than the nominal value of 0.1wt.%, this increasing could be a result of carbon contamination inside of SEM chamber.
- **O** has a high level for R2(HT) step probably due to the production drawback; but for the rest of the steps it stays almost stable between 0.20wt.% and 0.25wt.%. It should be noted that the measured values are much higher than the nominal value of 0.1wt.%. The preparation of samples based on OPS may have an impact on the total amount of O measured.

The concentration profiles presented on Fig.III.17 show that the penetration depth between F17 and ODS layers is about 30 μm for heat treated samples. In the centre of the sample the elements concentration is quasi-constant.

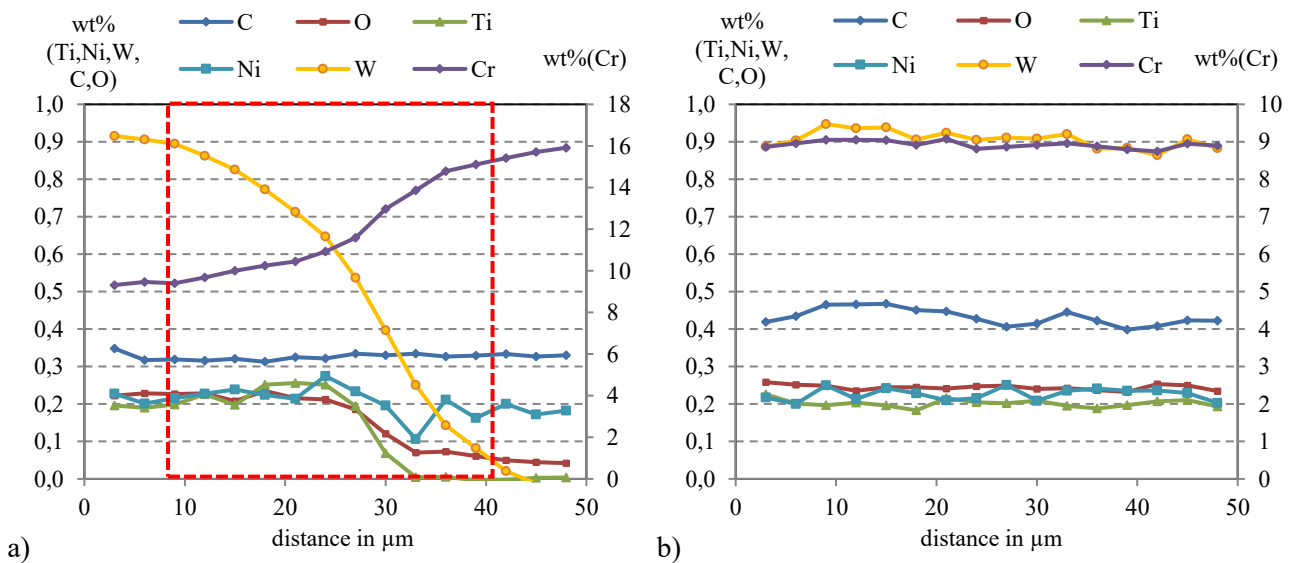


Fig.III.17 EPMA concentration profiles at (a) internal tube side and (b) in the centre of the tube for the sample IHT6.

In conclusion to EPMA measurements, we noted that if there is no heat treatment step, the chemical composition stays stable almost for all chemical components, i.e. the rolling step does not influence on the chemical composition. However, we suppose that the diffused carbon, in addition to the deformation strengthening, reinforces the surface layer of ODS which is reflected in the hardness measurements presented above.

EDX measurements on the rolled and heat treated samples show two types of precipitations in the microstructure. The first one is the precipitation of titanium oxides (probably Ti_3O as was observed in [Hary, 2017]), which were found in the cavities of the microstructure, they do not have a specific location and could be found both inside the grains and at the grain boundaries on Fig.III.18. Their size is increased after the rolling and heat treatments in comparison with the hot extruded state.

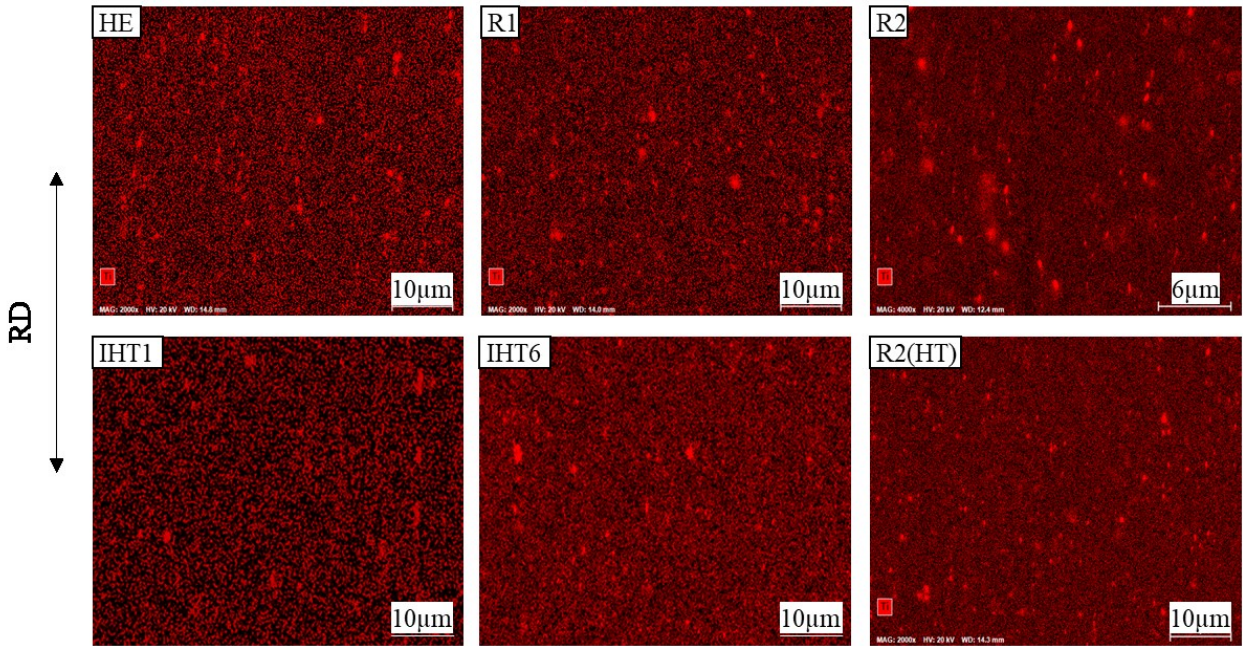


Fig.III.18 Ti distribution at each production step

The second type of precipitates is chromium carbides that segregate after rolling and heat treatments at the grain boundaries. These precipitates are elongated parallel to the rolling direction as can be seen on Fig.III.19.

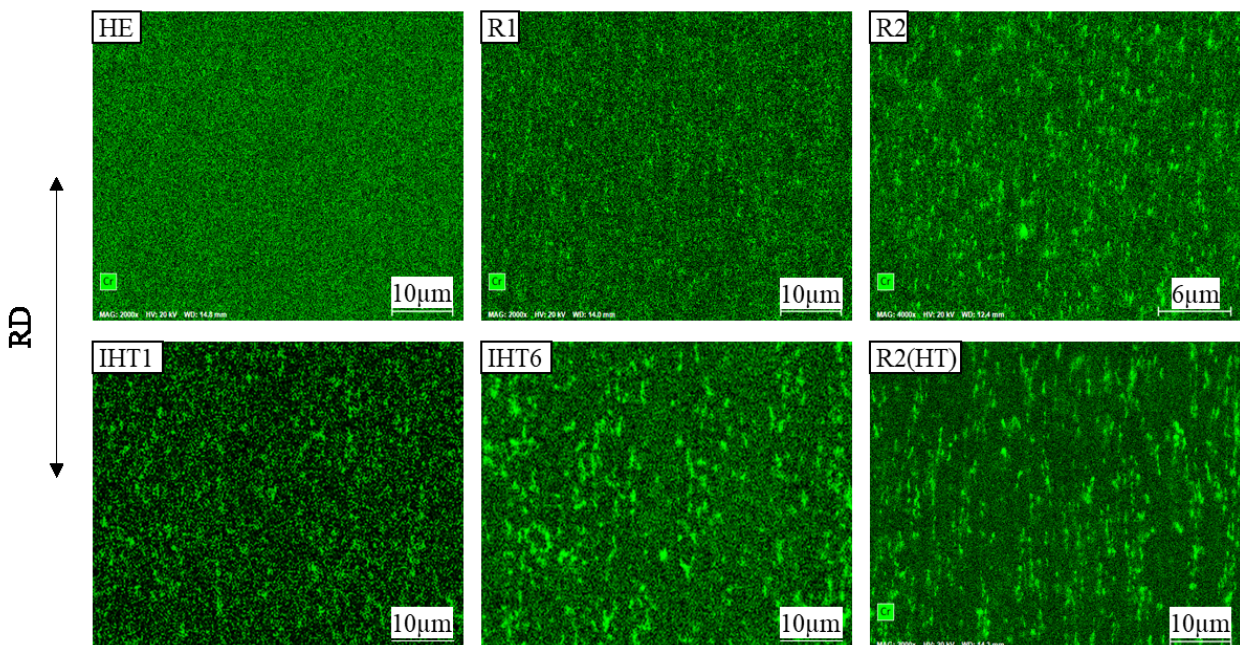


Fig.III.19 Cr distribution at each production step

III.5. Dilatometric measurements of phase transformations

The critical points during phase transformation were determined by dilatometric measurements and they are presented in Table III.1. These measurements were done for the HE, R1 and R2 (HT) states in order to identify the impact of deformation and intermediate heat treatment on the evolution of phase transformation temperatures. Two cooling rates of $v_c = 120^\circ\text{C}/\text{min}$ (orange part of Table III.1) and $v_c = 1.2^\circ\text{C}/\text{min}$ (blue part of Table III.1) were applied to obtain martensitic and ferritic structure respectively. One remark should be done here: the samples (R1 and R2 (HT)) used for the measurements were collected from the tube and they contained the ODS steel (in the bulk) and some amount of F17 steel on the borders. That is why the cooling rate of $120^\circ\text{C}/\text{min}$ was not enough to form a 100% martensite structure, in comparison with a pure ODS steel, where the 100% martensite structure was obtained with the cooling rate of $50^\circ\text{C}/\text{min}$ (see Chapter V).

Table III.1 Phase transformation temperatures and the formed phases fraction

Samples	Phase transformation temperatures ($^\circ\text{C}$)						Martensite	Ferrite
	Ac_1	Ac_3	F_s	F_f	M_s	M_f	%	%
HE	870	930	750	670	370	320	0,71	0,29
	-/-	-/-	810	750				
R1	870	910	730	680	380	320	0,73	0,27
	-/-	-/-	780	740				
R2 (HT)	880	930	720	680	410	340	0,55	0,45
	-/-	-/-	780	740				

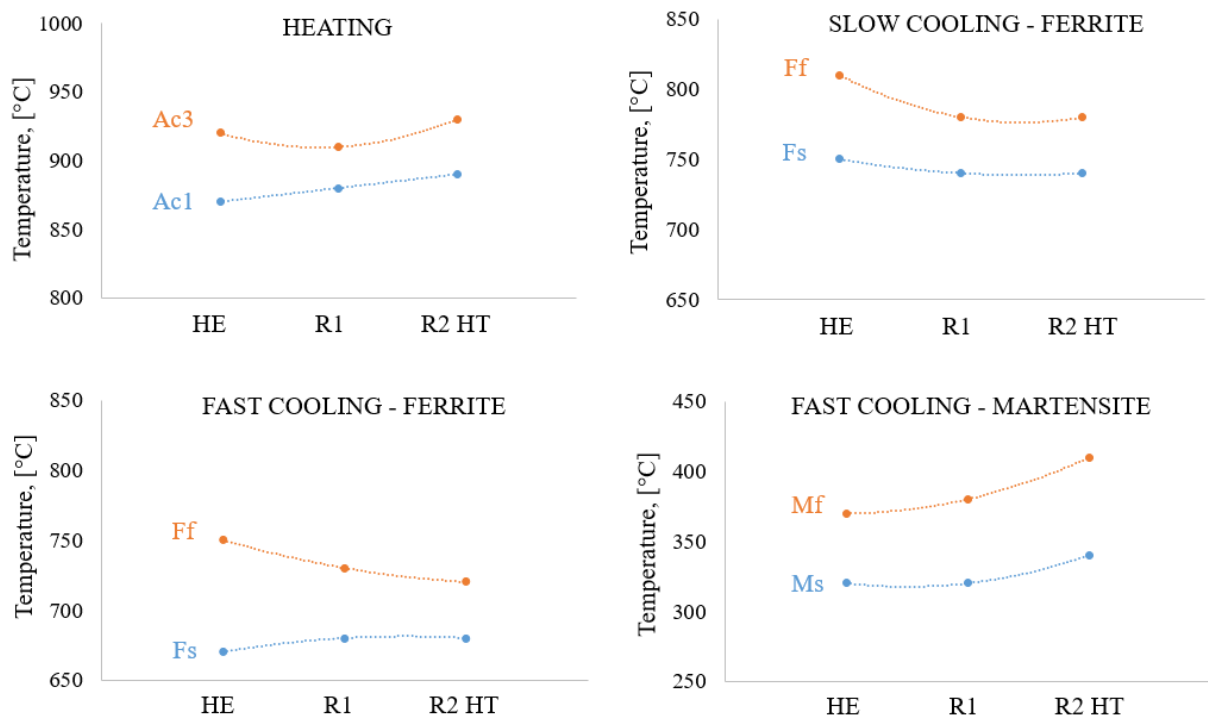


Fig.III.20 The evolution of critical temperature points as a function of metallurgical state

The temperature of the beginning Ac_1 and the end of austenitization Ac_3 almost for all samples are equal at 870° and 930°C respectively, with a standard deviation $\pm 10^\circ\text{C}$. These values are 20°C higher than in the work of [Toualbi, 2012] probably due to the difference in chemical compositions. Indeed, powder slot were not exactly the same.

The evolution of critical temperature points (Ac_1 and Ac_3 ; F_s and F_f ; M_s and M_f) was studied as a function of metallurgical state (HE, R1 and R2(HT)) on Fig.III.20. The variation of the critical temperatures is low regarding the metallurgical states of studied samples HE, R1 and R2(HT). This variation is in the range of 5-10%. Some tendencies can be explained by the difference of the dislocation density increasing with deformation or the Cr segregations that promote the earlier phase transition process.

III.6. Particles distribution and the evolution of particles size

TEM observations were realized for the samples R1, R2, IHT6 and R2(HT). The objective is to analyze the impact of deformation and intermediate heat treatment on the distribution and the size of the particles in the matrix for the studied samples. The TEM patterns are given on Fig.III.21(a) at a low scale and Fig.III.21(b) at a larger scale. It was observed that the dislocation density is high in the rolled samples, their microstructure presents elongated grains with dislocations distributed inside the grains and at the grain boundaries. On Fig.III.22 the particles size was measured by TEM images analysis. The average size of oxides particles is equal to 10-15 nm for all samples. More specifically for observed regions:

- **R1** has particles of various sizes from 5nm to 25nm
- **IHT6** exhibits less particles with very small or very large size, most of the particles are about 15nm
- **R2** presents almost no small and large particles, the majority of the particles are about 15nm
- **R2(HT)** : no particles with small or large size, mainly 10 and 15 nm

In conclusions, it can be said that there is no significant evolution of the particle size between the production stages. The impact of deformation on the particles size is not evident. In the case of large deformation by Scheme 1 (R1→R2) the particle size is increased. For the Scheme 2 with intermediate heat treatment (R1→IHT→R2(HT)) the particle size is decreased. The tendency found in the work of [Toualbi, 2012] shows that the particles size was increased from 10 nm until 11.4 nm between HE and rolled state. So, it confirms the results obtained for Scheme 1.

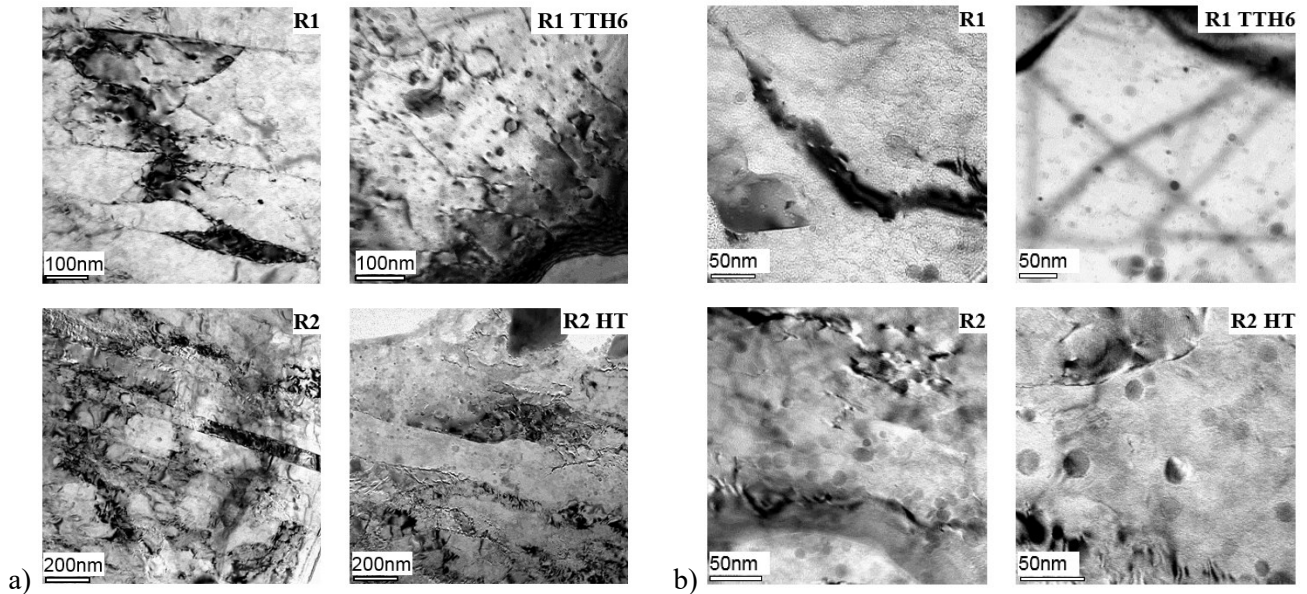


Fig.III.21 TEM patterns with the nano-particles for the samples R1, R2, IHT6 and R2(HT)

a) scale 100-200nm, b) scale 50nm

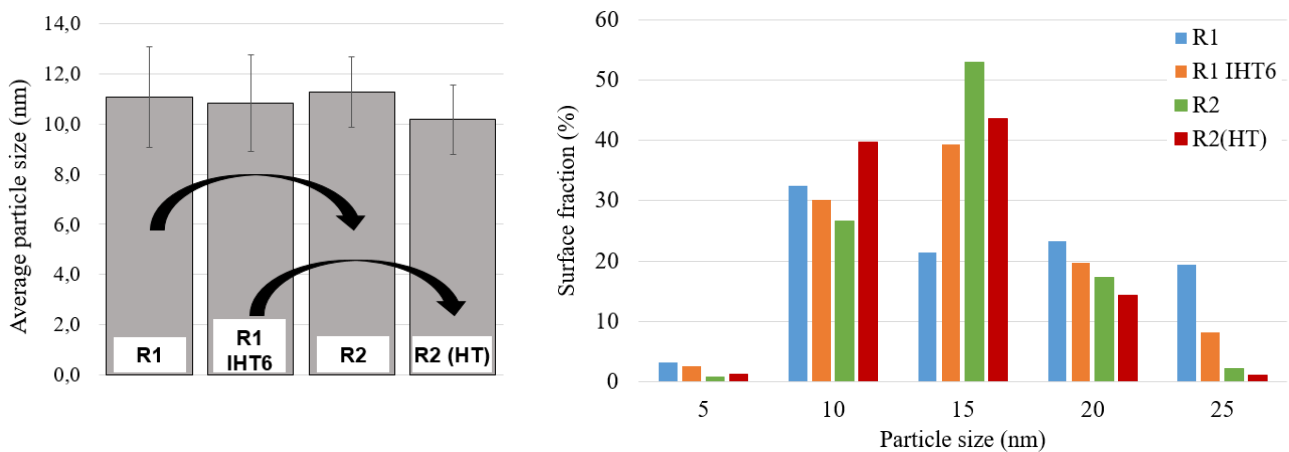


Fig.III.22 Particles size distributions by TEM measurements

These measurements did not have a reliable resolution and some of the structures were distorted because of high dislocations density and anisotropy level. The observed tendency should be confirmed by statistically more representative techniques, for example Small-angle Neutron Scattering (SANS) or Small Angle X-rays Scattering (SAXS). The first measurements by SAXS are in the progress, but the results are not yet analyzed.

III.7. Mechanical properties observed by tensile tests

The mechanical properties of ODS rolled tubes R2 and R2(HT) and their treated state (ferrite state and tempered martensite state) have been characterized by uniaxial tensile tests. Two geometries of tile and ring were used in order to measure stress/strain resistance in longitudinal and transversal directions (cf. [Chapter II.2.4](#)). These tests were realized at three strain rates 10^{-2} s^{-1} , 10^{-3} s^{-1} and 10^{-4} s^{-1} in order to investigate the rate sensitivity of the ODS material. The results of the traction tests are shown on [Fig.III.23](#).

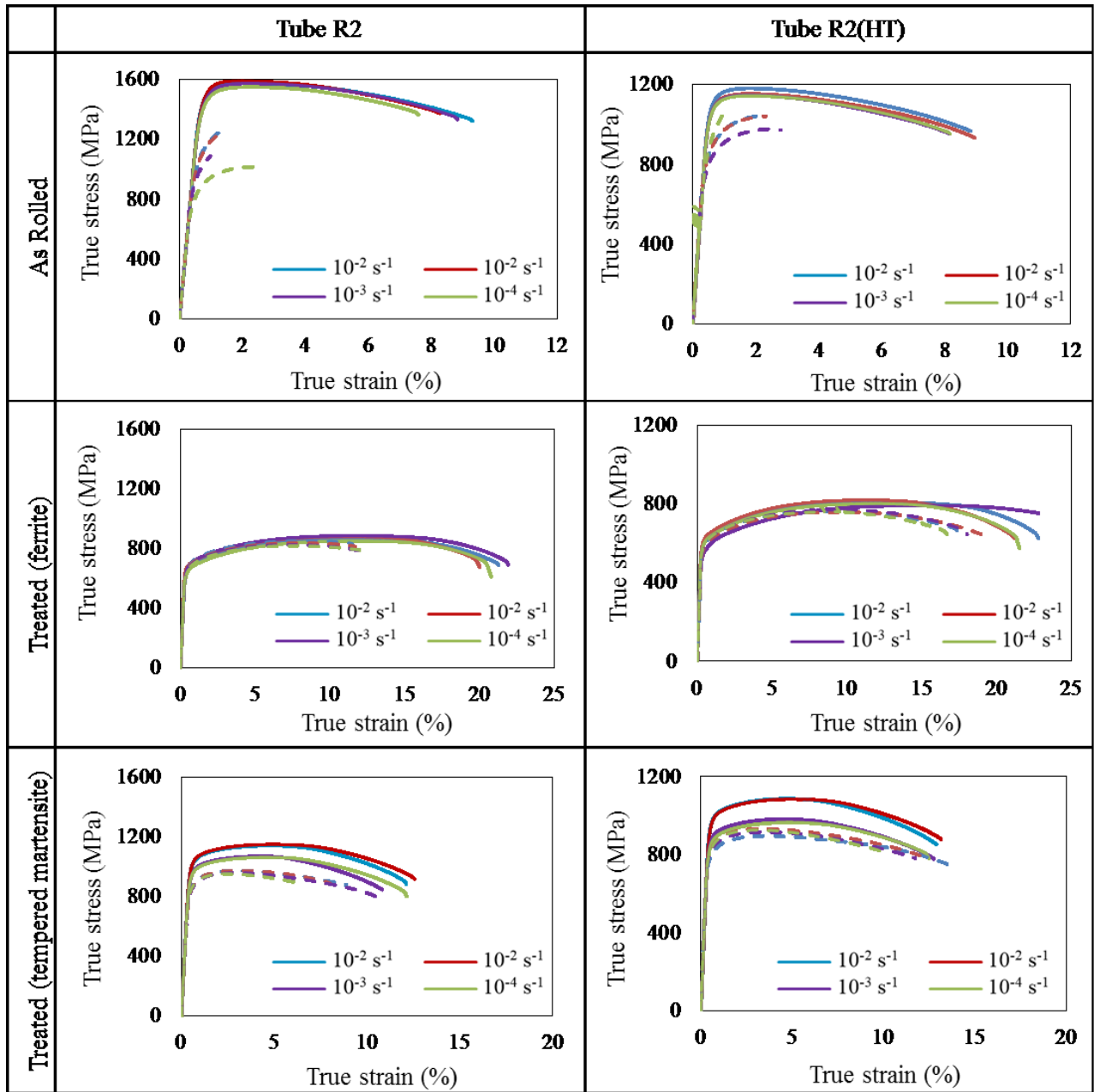


Fig.III.23 The results of the traction tests for rolled R2 and R2(HT) tubes and their treated state
 Continuous line for tiles; dashed line for rings

The summary of R_m elasticity limits and elongation $A\%$ are given on Fig.III.24, where also the results obtained by [Toualbi, 2012] are mentioned for the tempered martensitic structure.

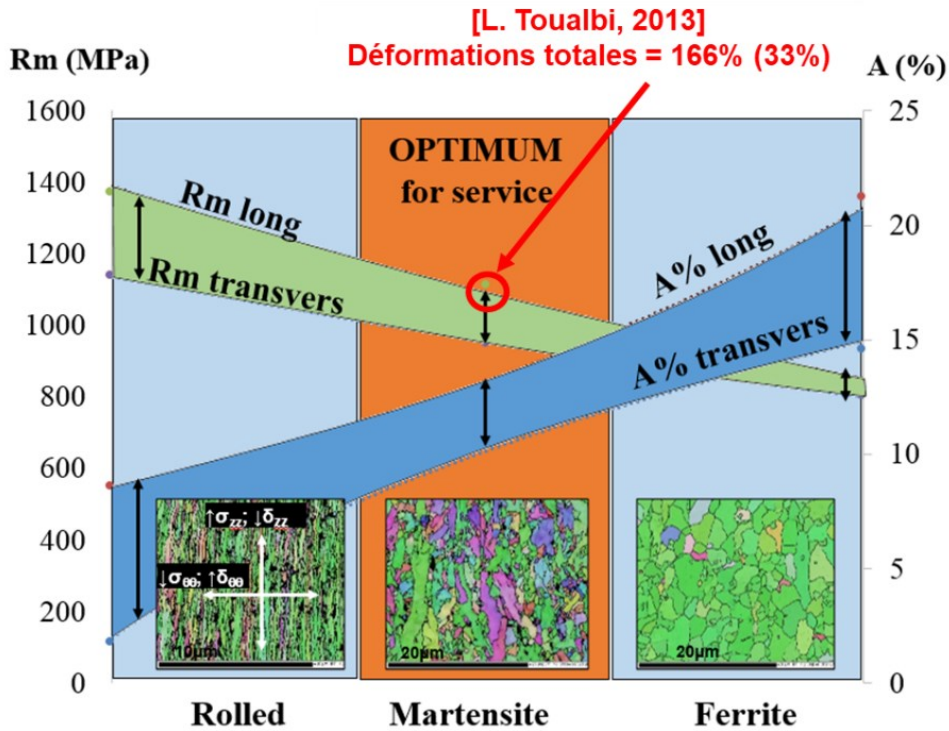


Fig.III.24 Summary of elasticity limits R_m and elongations $A\%$

In the rolled state the material is very brittle in the transversal direction, which confirms the need for an intermediate heat treatment between the rolling passes to avoid cracking of the material during deformations. An intermediate heat treatment with slow cooling is recommended at this stage. It allows to obtain a ductile material that can be easily deformed, despite the **anisotropy brought by texture**. It was seen for the samples in ferritic state that the texture memory effect provoke the anisotropy development, especially for R2 sample that was not undergone IHT. Thus, the more severe the applied strain, the higher anisotropy of ferritic structure is measured.

For the final heat treatment, it is mandatory to apply a fast cooling to restore the texture and obtain isotropic microstructure and properties. Finally, the tempered martensite structure presents a good compromise between mechanical strength and ductility, which is consistent with the mechanical properties obtained for HPTR tubes with total deformation after rolling at total strain 166% [Toualbi, 2012]. Indeed, the martensitic states enhance the toughness compared to the ferritic state at room temperature. The EBSD maps of tempered martensitic states are given on Fig.III.25, where it can be seen that R2(HT) state is more homogeneous than R2 state, without remaining columnar structure.

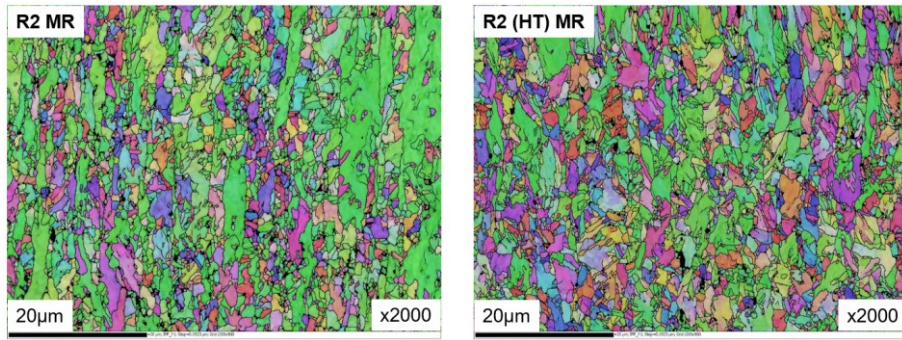


Fig.III.25 EBSD maps of tempered martensite states for R2 and R2(HT) samples

Study of the rupture surface shows on Fig.III.26 that the cold-rolled material (R2 and R2(HT)) has a significant amount of cracks that identify a high level of internal stresses. The thermal treatment reduces these stresses and less crack will be found on the rupture surfaces of treated samples (ferritic or martensitic ones). The dimples on each of studied surfaces indicate that the material has a ductile ruptures.

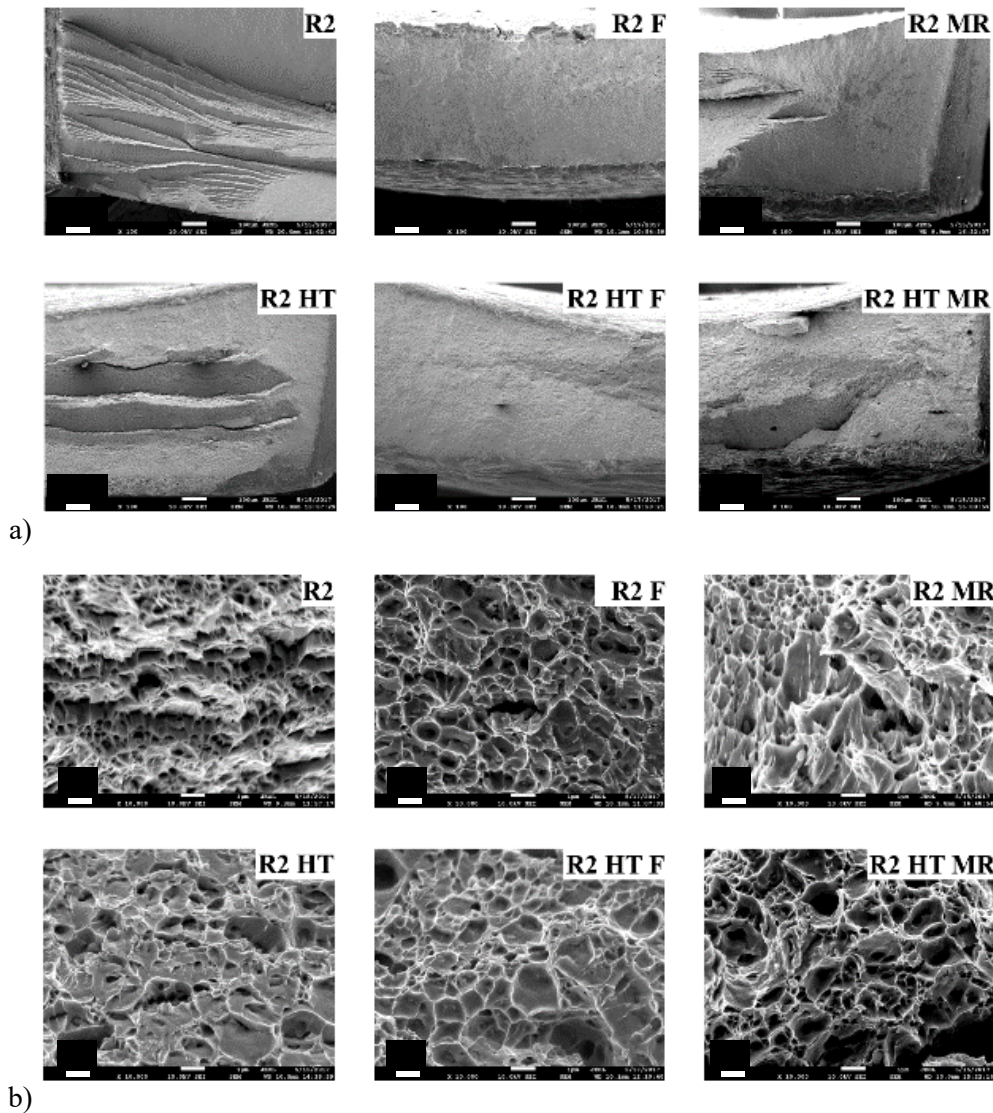


Fig.III.26 Rupture surfaces for the tubes R2 and R2(HT) at the cold-rolled, ferritic and tempered martensitic states. Scale 100µm (a) and scale 1µm (b)

III.8. Internal stresses

These measurements allow us to evaluate the macroscopic internal stresses introduced by deformation, efficiency of heat treatment to relax the internal stress of the ODS tubes is also prospected. The measurements were realized using a tube with the geometry presented on Fig.III.27.

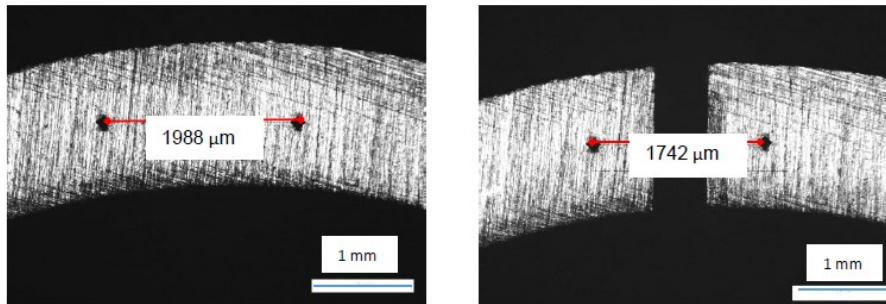


Fig.III.27 Specimen for measurements of internal stresses in orthoradial direction (before and after the test)

Tested tubes have a triplex structure F17-ODS-F17 and present the states R2(HT), R2(HT) FHT and R2 FHT. These tubes were cut in the orthoradial directions. Measuring the deviation from the initial dimensions (as shown on Fig.III.28), it is possible to calculate $\sigma_{\theta\theta}$ (MPa) using following equations

$$\sigma_{\theta\theta} = E \frac{e}{2} \left(\frac{1}{R} - \frac{1}{R_0} \right)$$

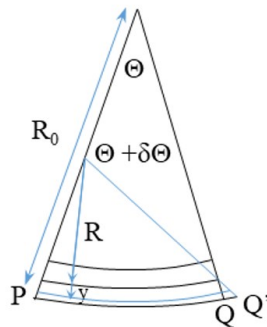


Fig.III.28 Scheme of the sample sections before and after relaxation of stresses in orthoradial direction

In [Table.III.2](#) the results of these measurements show that for the **rolled** material in the orthoradial direction there is the compressive internal stresses. Such results are contradictory to the measurements provided by [\[Toualbi, 2012\]](#) in [Table.III.3](#). In their case, the tensile stresses were observed both for orthoradial direction. It can be supposed that this variation is presented by a different distribution of applied loading during HPTR and VMR process. After the **thermal treatment** at 1050°C/1h and slow cooling the residual stresses become negligible in orthoradial direction.

[Table.III.2](#) The internal stresses in the rolled and heat treated tubes

	R2 (as rolled)	R2 FHT (ferrite)	R2(HT) (as rolled)	R2(HT) FHT (ferrite)
$\sigma_{\theta\theta}$ (MPa)	-112	-3	-45	-14

[Table.III.3](#) The internal stresses in the rolled (40%) and heat treated tubes in [\[Toualbi, 2012\]](#)

	J95-M1 (as rolled)	J95-M5 (ferrite)	J95-M3 (tempered martensite)
$\sigma_{\theta\theta}$ (MPa)	165	-5	0

III.9. Evolution of magnetic properties

ODS ferritic steels are ferromagnetic materials. Therefore, magnetic properties may evolve depending on microstructural evolution involved by forming sequences. In this section, the microstructural changes are followed by magnetic measurements, in particular the corresponding variations of the coercive field H_c (Oe), as a function of both mechanical and thermal treatments [Renzetti et al., 2011]. This type of measurements presents a special interest since it allows to detect microstructural changes (like recovery and phase transformation) by high sensitive non-destructive analysis of magnetic properties.

The evolution of magnetic properties for ODS samples are determined at different elaboration states:

- Reference material after HE **without precipitations** in order to identify the particles impact
- R1 state after first **rolling** pass with $\epsilon=110\%$
- R2(HT) state after second **rolling** with $\epsilon=140\%$
- R2(HT) state with **ferrite** structure
- R2(HT) state with tempered **martensite** structure

The measurements were realized on the samples taken in two directions: longitudinal (RD) and transversal (TD) in order to see the impact of microstructural anisotropy on the magnetic signal. The magnetic field is applied parallel to the rolling direction. The maximum applied field was 10 kOe. The H values for all studied samples are displayed on Fig.III.29. We could see that there is no significant difference concerning the coercive field values between the different states and sampling directions.

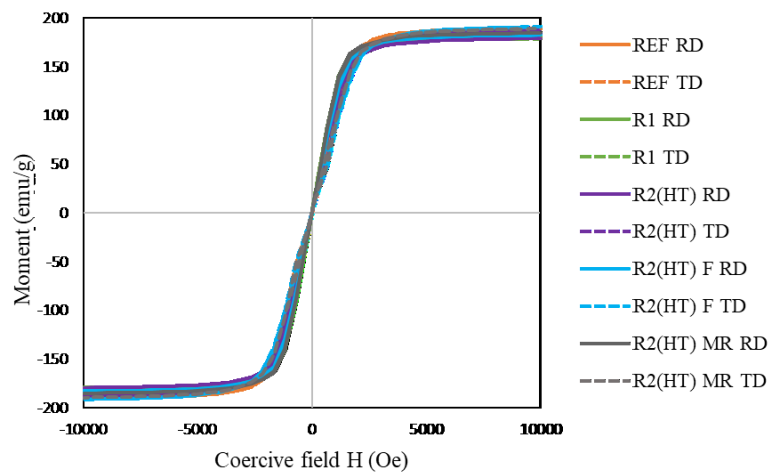


Fig.III.29 Hysteresis loop obtained for the 9%Cr-ODS steel with applied field parallel to the rolling direction

However, zooming the center of the hysteresis loop on Fig.III.30, we observed that the values of coercive field H_c in TD direction is lower than in LD one, but the effect is rather weak. The lowest value was measured for tempered martensitic state. We could observe that the coercive field is dependent on microstructural parameters such as grain size and dislocation density. For instance, for the state R2(HT) the H_c is increasing in the following order: Tempered Martensite \rightarrow Rolled \rightarrow Ferrite.

No influence was observed compared to the reference material without particles. These results are quite surprising, since according to [Arzt, 1998] all kinds of microstructural defects existing in a crystal such as vacancies, solutes, second-phase particles, twin boundaries and others have an influence on the magnetic permeability.

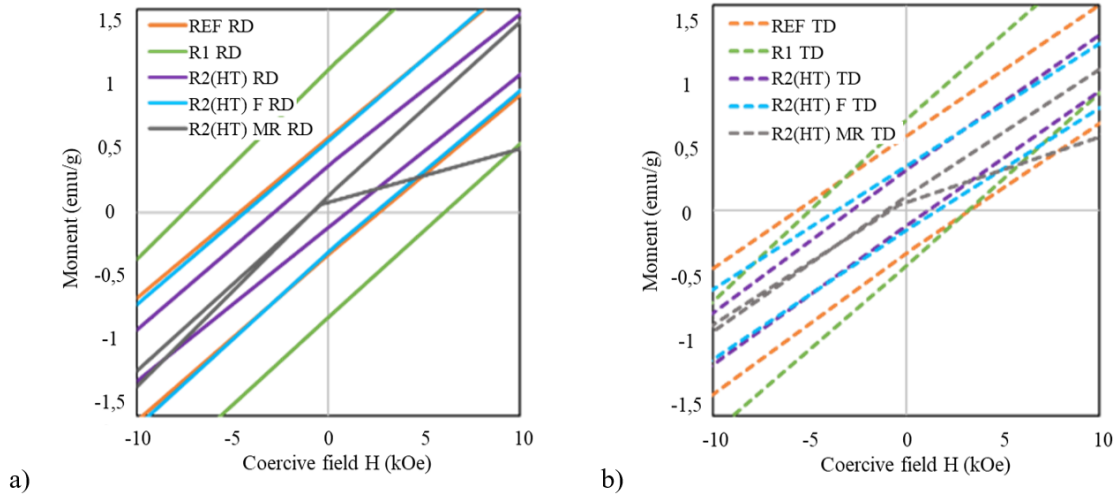


Fig.III.30 The centre of the hysteresis loop: a) RD, b) TD

Similar measurements were found in the literature [Oliveira et al., 2013] for **Eurofer-97** (9Cr–1.1W–0.125Ta–0.25V–0.105C–0.6Mn–0.036N (wt.%)) and **ODS-Eurofer** steel (9Cr–1W–0.08Ta–0.2V–0.07C–0.4Mn–0.0278N–0.3Y2O3 (wt.%)). On Fig.III.31 it can be seen that, over the Curie temperature, the values of H_c are a bit higher than for our ODS samples in as-rolled state, that can be explain by the difference in composition and production (only 80% of cold reduction). But in general, these values are in the same order of magnitude with the results obtained in this work.

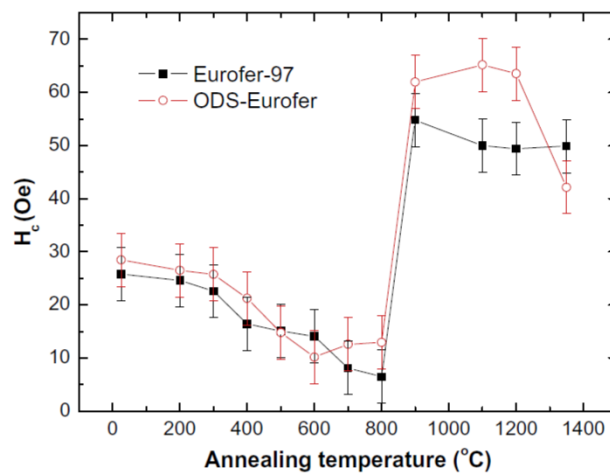


Fig.III.31 H_c values obtained for Eurofer-97 and ODS-Eurofer for as-rolled and annealed conditions [Oliveira et al., 2013]

Therefore, this study shows that magnetic properties of ODS ferritic steels are poorly affected by various microstructural conditions. This tends to prove that magnetic properties cannot be used for processing monitoring and control during ODS steel cold forming sequences.

Conclusions for Chapter III

The evolution of microstructure, crystallographic texture and mechanical properties during pilgering of 9%Cr ODS tubes is studied with the help of EBSD, X-ray diffraction and hardness measurements. The evolution of texture was measured at each deformation step and the main conclusions are:

1. All pilgered samples present elongated grains shape and show a strong texture formation with a preferential α -fiber orientation along the rolling direction.
2. The applied heat treatment restores the grain shape to almost equiaxed grains. However, texture intensity increases unexpectedly and only the α -fiber orientation along the rolling direction is preserved. Most of the grains with $\langle 100 \rangle$ and $\langle 111 \rangle$ oriented along the rolling direction are eliminated. This heat treatment decreases the internal stresses and allows to recover the grain size and the ductility of the material after the pilgering passes.
3. The heat-treated samples textures of this study differ from the ODS steel produced by HPTR technology presented in [Toualbi et al., 2013], where the material is almost recovered in term of morphology and grain orientation. This difference seems to be related to the amount of cold working.
4. A double pole in ODF section was identified after final treatment of the sample R2 (HT) FHT. It was not observed for the tube which was not submitted to an intermediate heat treatment. This double pole could be explained by combination of the α -fiber pole generated by cold-working and another one inherited from variant selection during phase transformations.
5. Strong grain refinement is observed for the final step of the pilgering process. Increase of the hardness values is consistent with the Hall-Petch relation. Large deformation, induced by VMR cold pilgering, produces a high dislocation density and grain refinement in this ODS steel and improves its mechanical properties.
6. Comparison of mechanical behavior at different metallurgical state, namely as-rolled, ferrite and tempered martensite, showed that the ferritic structure is favorable for being applied as intermediate heat treatment, based on the values of high ductility in a ferritic state. However, it should be noted that the ferritic structure has a crystallographic anisotropy that is linked with the texture memory effect. In perspectives, another heat treatment route should be found with the objective to obtain a ferritic structure keeping a good ductility, but with more isotropic properties.

For the final heat treatment, the tempered martensite structure showed a good compromise between stress resistance and ductility. In addition, the texture for this state is the lowest one with an almost completely restored structure.

The as-rolled state presents extremely high mechanical resistance and, at the same time, quasi brittle behavior in the transversal direction. It is also characterized by a high level of anisotropy and shows the necessity of intermediate heat treatment between the rolling passes. In addition the heat treatment demonstrates the decreasing of internal stresses introduced by cold working.

7. Magnetic measurements were performed for the samples presenting various metallurgical states. It was confirmed that the magnetic signal is weakly dependent on microstructural parameters such as grain size and dislocation density. However, the impact of the nano-precipitates was not evidenced and have to be studied later in details.

In the following chapter, the texture memory effect will be analyzed during phase transformation process by following texture evolution during a heating-cooling path. Such kind of experiment will be realized in-situ using X-ray synchrotron diffraction. Those results may help to quantify both the phase transformation kinetic and the crystallographic texture of phases.

Chapter IV. Phase transition and Texture memory effect in ODS steel pilgered tubes

Introduction

In this Chapter, the study of phase transformation in ODS steel is presented, taking into account the main factors that influence the microstructure development. The objective is to understand how the microstructure after high deformation can be controlled in order to obtain the best service properties. The texture memory effect, observed previously, is studied in details using in-situ synchrotron facilities during heating and cooling operations. The theory of variant selection and, in particular, Double Kurdjumov-Sachs relations is prospected to explain the observed phenomenon.

IV.1. Texture memory effect in deformed steels

In previous chapter, the influence of the Mannesmann (VMR) cold pilgering process parameters and the intermediate heat treatment on the microstructure evolution has been studied. Pilgered tube samples showed a strong crystallographic texture according to the well-known α -fiber preferential orientation along the rolling direction. Unexpectedly, after recovery heat treatment, a strong inherited texture fiber was still observed even for very long holding time at high temperature, resulting in an even stronger texture than before the annealing. Although some texture memory effects have been known in various materials such as Quartz [Wenk et al., 2009], Ti-alloys [Mulot et al., 1996; Bhattacharyya et al., 2006] and hot-rolled [Tomida et al., 2008; Tomida et al., 2012; Tanaka et al., 2015], cold-rolled [Wenk et al., 2007; Tomida et al., 2015] and ECAP (equal channel angular processing)-processed steels [Tomida, 2018], the resulted textures are in general weaker than the initial ones. Therein exists a motive to investigate the phenomenon observed in the pilgered ODS tube, which is not simply a texture memory but a ‘texture enhancement’. This remarkable thermal stability of the $\langle 110 \rangle$ fiber was assumed to be linked to the very dense distribution of nano-oxides precipitates that could promote variant selection or selective growth of specifically oriented grains during phase transformation. This peculiar inheritance of specific crystallographic orientation can be either achieved during the heating stage (ferrite to austenite (α/γ) transformation) and/or the cooling stage (austenite to ferrite (γ/α) transformation).

Commonly, this kind of phenomenon is explained by variant selection during phase transformation. Widely used for analysis of martensitic transformation all those models are based on specific orientations between a parent and a daughter phase linked by their specific lattice properties and orientation. More recently, in the study of texture memory in steel, it was found that the observed texture change during the texture memory cycles can be predicted based on the so-called Double K-S Relation (DKS), in which variants having the Kurdjumov-Sachs (K-S, $\{111\}_{\gamma} // \{110\}_{\alpha}$ and $\langle 110 \rangle_{\gamma} // \langle 111 \rangle_{\alpha}$) or near-K-S relation to two adjoining parent grains should be preferentially chosen. It has been also reported by many researchers that

the variant selection on heating is weaker than that on cooling [Yoshinaga et al., 2007; Tomida et al., 2013]. However, it is not evident whether the texture memory in the pilgered ODS steel could be attributable to the same mechanism.

IV.2. Experimental Method and Data processing for *in-situ* synchrotron analysis

IV.2.1. Materials and samples preparation

The *in-situ* test was realized on the 9%Cr ODS pilgered tubes presented in Chapter II. This grade exhibits a ferrite-austenite ($\alpha \rightarrow \gamma$) phase transformation at high temperature. The critical temperatures A_{c1} , A_{c3} , F_s , F_f , M_s , M_f , related to phase transformations, are identified by dilatometry measurement and listed in Table.IV.1.

Table.IV.1 Critical temperatures related to phase transformations for 9%Cr ODS tubes

Cooling rate / T_{crit} , [°C]	A_{c1}	A_{c3}	F_s	F_f	M_s	M_f
$V_c = 120$ °C/min	870	910	730	680	380	320
$V_c = 1.2$ °C/min			780	740	-	-

Cylindrical samples are cut by Electrical Discharge Machining (EDM) technique with the axis parallel to the rolling direction of the R1 and R2 tubes with a size of 1 mm in diameter and 10 mm in length. After cutting, samples were polished with carbide papers to remove the oxides from surface that could influence the signal. It is assumed that this process, operated at low temperature does not affect significantly the microstructure and the microstrains in the bulk of the samples. Pt/PtRh ThermoCouple (TC) are spot welded along one side of sample surface. The TC wires diameter is 0.5 mm.

IV.2.2. Synchrotron setup

Synchrotron X-Ray diffraction measurements were carried out on ID-11 beamline at the European Synchrotron Radiation Facility (ESRF), Grenoble, France. The measurements were done in transmission mode operating with a 200x200 μm monochromatic incident beam of 80.005 keV energy. During heat treatment, complete Debye-Scherrer diffraction rings were obtained using a 2048x2048 pixels CCD detector (Fig.IV.1).

Samples are set up in quartz tube of 3 mm internal diameter. The heating furnace reaches temperatures up to 1050°C with the sample inside. The Rolling Direction (RD) is parallel to the vertical axis and normal to the incident beam (Fig.IV.1). Argon purge and vacuum atmosphere were used to protect the sample from oxidation during heating. Before each measurement, the sample axis was centered on the beam, and aligned on the vertical rotation axis (ω -tilt). During heating, the sample was rotated stepwise along ω axis (i.e. RD)

by 180 degrees and a 2D pattern is collected every 2.5 degrees. The acquisition time is equal to 48 s per diffraction pattern. Cooling rates were controlled by using a variable flow of cold Ar gas.

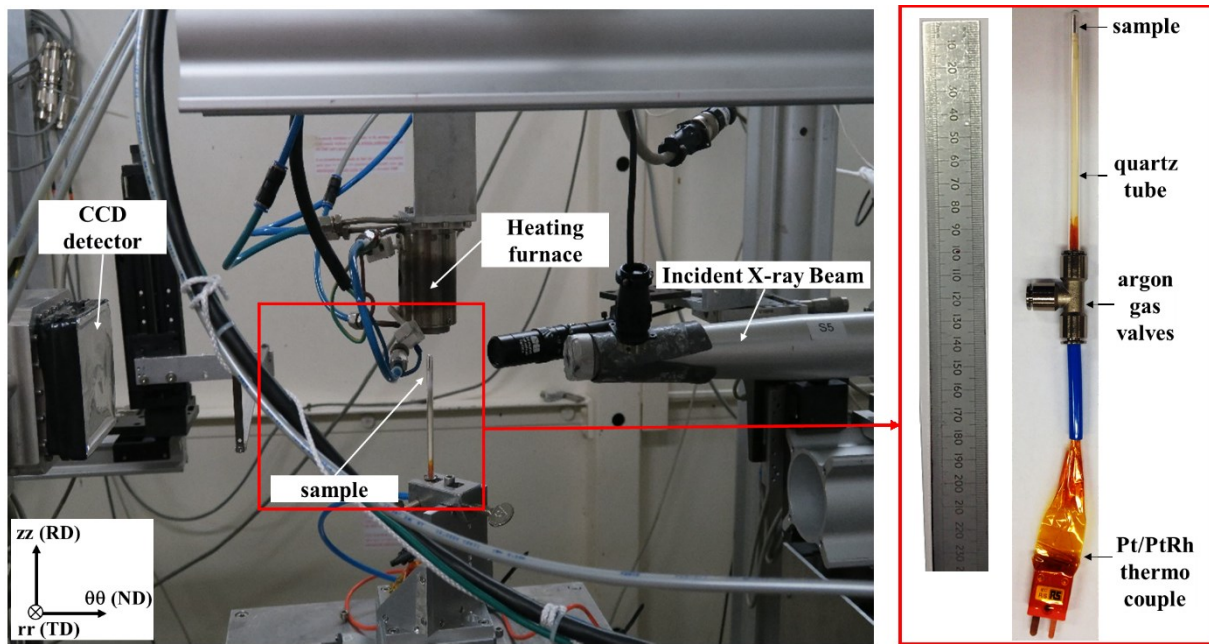


Fig.IV.1 Sample setup composed of the X-ray source, the X-ray detector and the heating furnace. The sample is rotated vertically (tilt angle) with 2.5° steps

IV.2.3. Test conditions

The sample selection was based on factors which are likely to influence the texture evolution [Wenk et al, 2003; Hutchinson et al, 2005]: (1) Initial microstructure; (2) Holding time in furnace at austenizing temperature; (3) Applied cooling rate. To study this effect, it was decided to observe:

- **For martensite transformation on cooling**, two samples with different level of cold working, after 1st rolling pass R1 of $\epsilon_p=110\%$ and 2nd rolling pass R2 of $\epsilon_p=250\%$ (cf. Chapter II), were heated at the rate of 100°C/min to 1050°C, held for 60 min, and cooled at the rate of 50°C/min as shown on Fig.IV.2a.
- **For ferrite transformation on cooling**, two samples after R1 of $\epsilon_p=110\%$ and R2 of $\epsilon_p=250\%$, were heated at the rate of 100°C/min to 1050°C, held for 20 min, and cooled at the rate of 2°C/min from A_{c3} to below 500°C as illustrated on Fig.IV.2b. By these heat treatments, the influence of increase in holding time from 20 to 60 min on austenite structures was also studied.

To identify the texture memory effect, the crystallographic texture was measured for initial deformed ferritic structures, ferritic structures before transformation at 850°C, austenitic structures at 1050° and final ferritic structures after cooling. Experimental conditions are illustrated on Fig.IV.2.

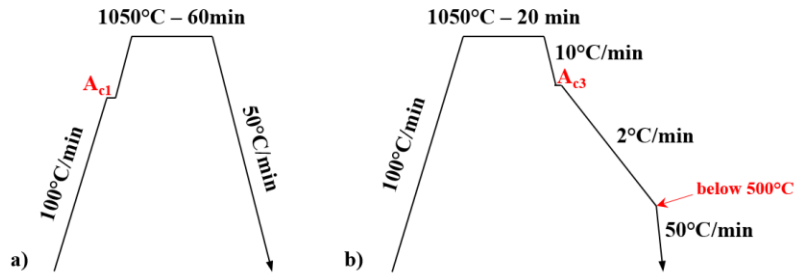


Fig.IV.2 Experimental conditions applied to obtain $\alpha \rightarrow \gamma \rightarrow \alpha$ transformation:
 a) fast cooling leading to a martensitic structure; b) slow cooling leading to a ferritic structure

IV.2.4. Data Post-treatment

To evaluate the texture, integrated intensities were acquired every 2.5 degrees. The examples of obtained diffraction patterns for ferritic and austenitic domains are given on Fig.IV.3. The resulting 72 patterns were refined using FabIO Python module [He et al., 2000]. The data taken as a function of a sample tilt angle (ω) and Debye ring azimuthal angle (χ) were converted into more classical pole figures with inclination angle ρ and azimuth angle φ . For the present sample setting and the incident beam in the center of the pole figure this conversion is straightforward ($\varphi = \omega$ and $\rho = \chi - 90^\circ$) [Jung et al., 2017]. It can be considered that χ and ρ angles are linked directly because the diffraction angles 2θ are very small. Three pole figures were computed from the 3 first rings corresponding to (110), (211) and (200) diffraction peaks in ferrite and martensite and (111), (200) and (220) diffraction peaks in austenite, presented on Fig.IV.4. The Orientation Distribution Function (ODF) was calculated from the 3 poles figures via a 5° half-width kernel function in MTEX toolbox. Texture index was calculated as a mean square value of the ODF. For transformation texture calculation, the ODF was calculated using the harmonic method [Inoue et al., 1994; Tomida et al., 2008].

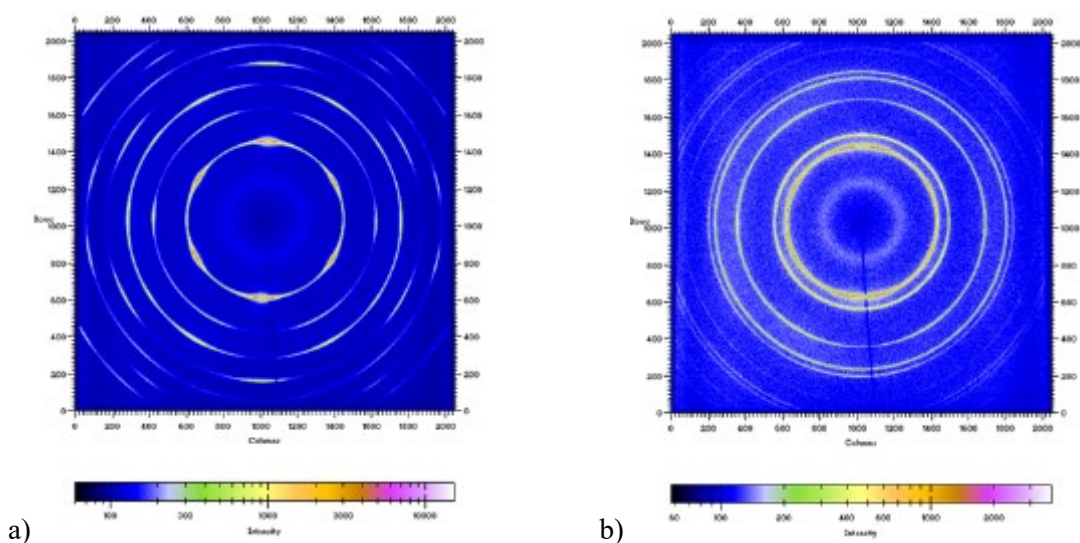


Fig.IV.3 Diffraction pattern: a) ferritic domain b) austenitic domain

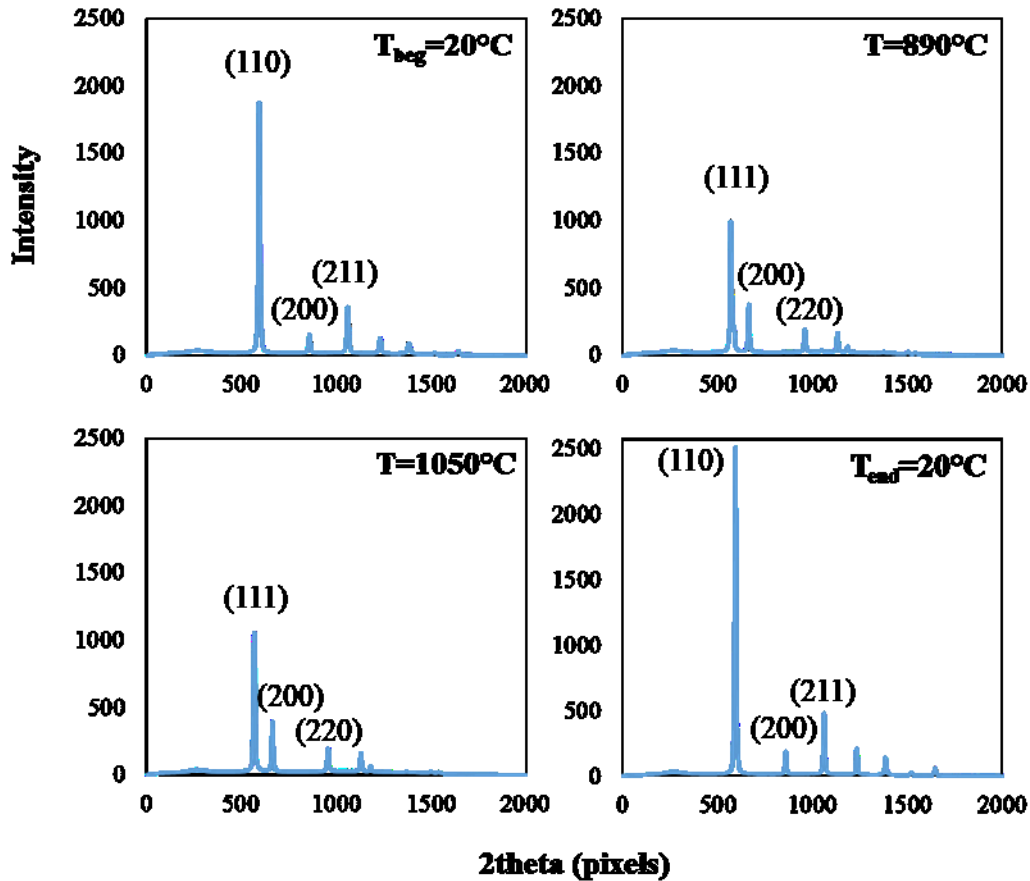


Fig.IV.4 Diffraction patterns evolution during thermal cycle (sample R1 with slow cooling). The patterns are integrated on 360° along the rings (along χ angle)

IV.3. Texture evolution during the thermal cycle

The evolution of textures during thermal processing for low and highly deformed sample after slow and fast cooling is presented on Fig.IV.6. A texture analysis is summarized in the form of ODF maps (Euler angles following Bunge's convention) with a cross section at ϕ_2 angle = 0° (Fig.IV.6a) and at ϕ_2 angle = 45° (Fig.IV.6b). The texture index is given in the right bottom corner at $\phi_2 = 45^{\circ}$ (Fig.IV.6b). A reference map for $\phi_2 = 0^{\circ}$ and 45° sections of an ODF with common texture components is given on Fig.IV.5. Experimental data for all samples are joined in Annex 3.

The original texture represents the well-known alpha-fiber, which slightly decreases in intensity during heating. After the phase transformation into the face cubic centered structure, the texture consists in two components close to copper component (112)[111] and P-component (110)[122] [Hutchinson et al., 1998; Saleh et al., 2014; Masoumi et al., 2017]. During holding at 1050°C , these fibers retain their intensity and do not show any significant evolution in austenite domain. Increasing the holding time up to 60 min does not change the texture intensity as well.

Fig.IV.5 Reference map for $\phi_2 = 0^\circ$ and 45° sections of Euler's space with common texture components [Jung *et al.*, 2017]

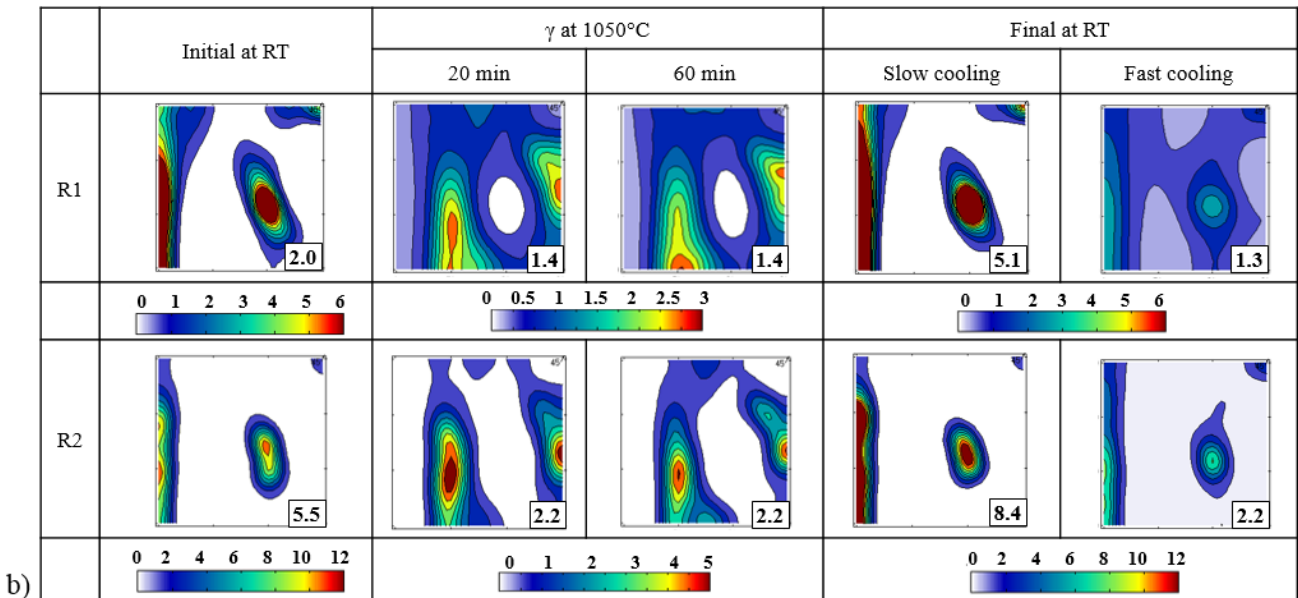
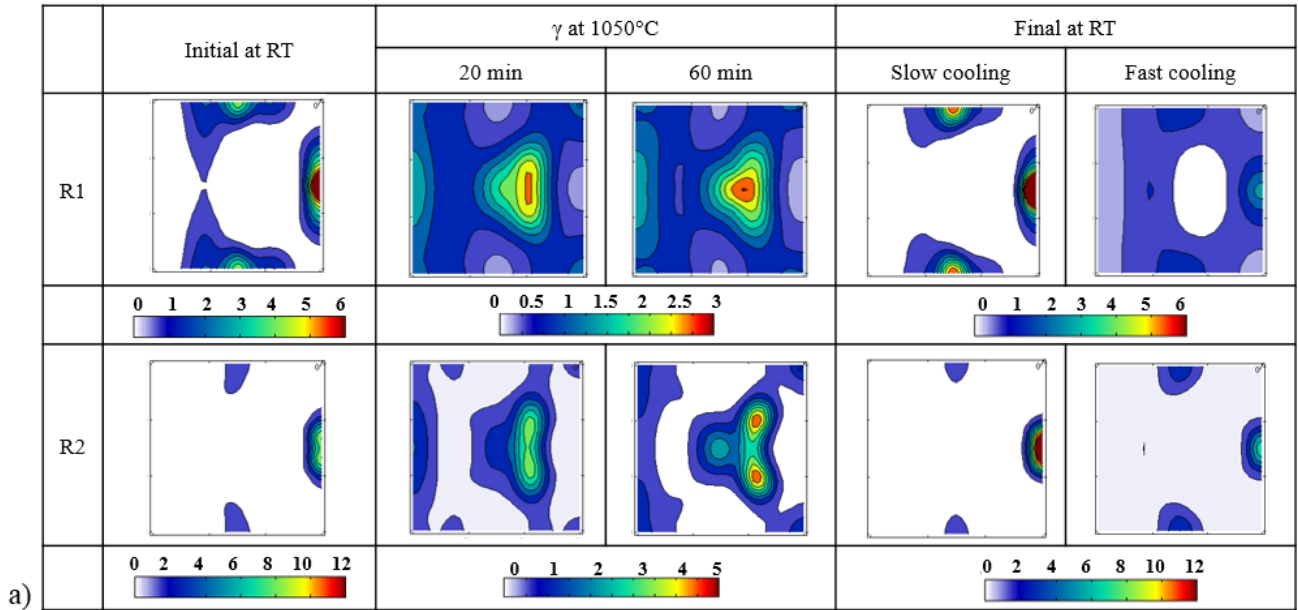
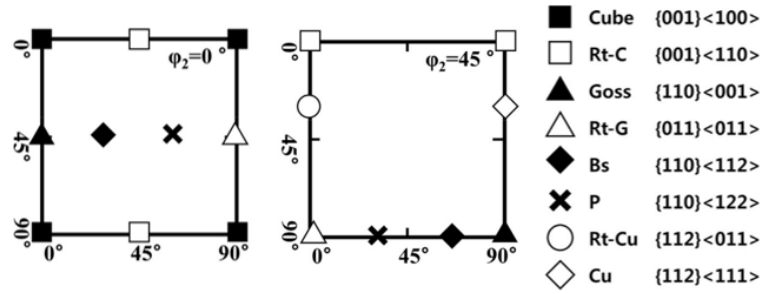


Fig.IV.6 Measured texture evolution during the thermal cycle for sample R1 ($\epsilon_p=110\%$) and sample R2 ($\epsilon_p=250\%$) at slow and fast cooling: a) $\phi_2 = 0^\circ$ and b) $\phi_2 = 45^\circ$

(Texture index is in the right bottom of each ODF map)

On Fig.IV.7 analysis of the texture evolution is presented as a function of initial texture level and the applied cooling rate. The highly deformed sample (R2) with the sharper initial texture, in comparison with R1 sample, showed a more intense texture in the austenitic domain, with a small deviation from Copper and P-components (Fig.IV.6). During slow cooling, increase in the intensity of alpha-fiber for both samples was noticed in the ferritic structure: it is almost twice higher than the initial one. However, increasing of the cooling rate (quenching) shows that the resulting martensite texture index is very weak and can be characterized as a nearly non-textured state. Quenching of R2 sample also results in a low texture index, but more intense compared to the low deformed sample. These results show that, during displacive martensitic transformation, much weaker variants selection takes place than during diffusive ferrite transformation in which a strong memory effect occurs.

Previous studies related to heat treatments of similar material but with significantly lower straining did not report large texture memory effect [Toualbi et al., 2012]. The initial microstructure (R1 or R2 state) seems to play a crucial role on both occurrence and intensity of the texture memory effect. It was not clear if only texture or also grain size and stored energy were involved in the phenomenon. However, this property of ODS steel must be taken in consideration for highly strained material obtained by Mannesmann (VMR) pilgering. Indeed, strongly textured materials are prone to exhibit mechanical anisotropy in particular in creep conditions. Because, this texture memory effect has not been reported in commercial 9wt%Cr steels like T91 grade, it is assumed that nanoprecipitation may play a role in variants selection during the ($\gamma \rightarrow \alpha$) phase transformation.

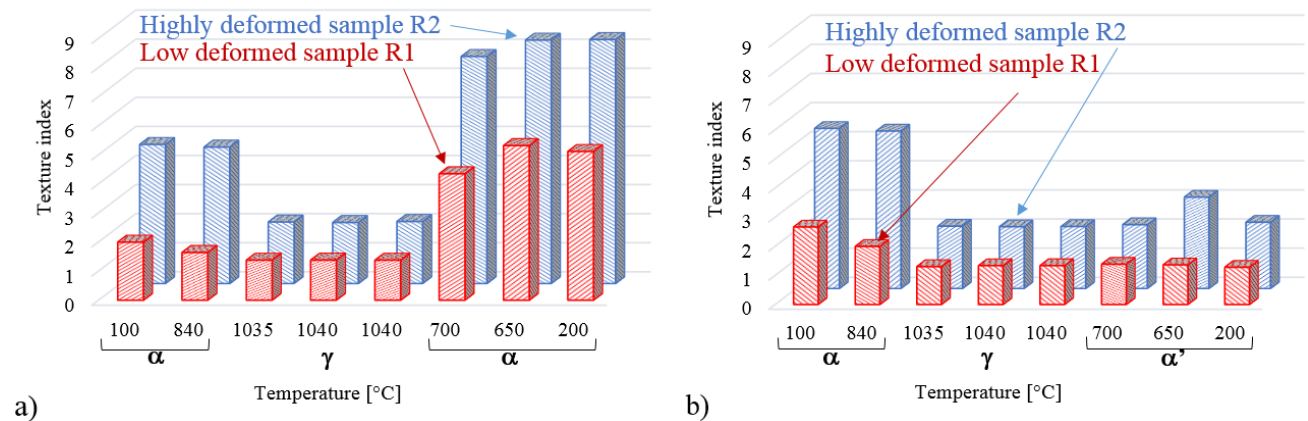


Fig.IV.7 Texture index value as a function of temperature during heating and cooling:

a) slow cooling; b) fast cooling

IV.4. Crystallite size and lattice distortion determination

This study presents the first characterization of austenitic strain state in ODS steel. By strain state, it is meant here the root-mean-square (rms) strain $\langle \varepsilon^2 \rangle$ of the crystallites, also sometimes called microstrains or type III strains. During heat treatments, the powder diffraction patterns are computed as the mean value over the azimuthal direction χ of diffraction patterns. On Fig.IV.8 those patterns are plotted for low deformed sample R1 ($\varepsilon_p=110\%$) at slow cooling. On Fig.IV.8a, it appears that the peak widths evolve slowly during the whole heat treatment. Therefore, both diffraction volume and lattice distortion are assumed to be weakly impacted during the heat treatment. However, microstructural characterizations show that grain size is strongly increased after heat treatments [Vakhitova et al., 2017]. Comparing the peak width during the holding time at high temperature on Fig.IV.8b it appears that in austenitic domain the diffraction peaks do not evolves. Therefore, it can be assumed that austenite has not recrystallized at any time during the treatment.

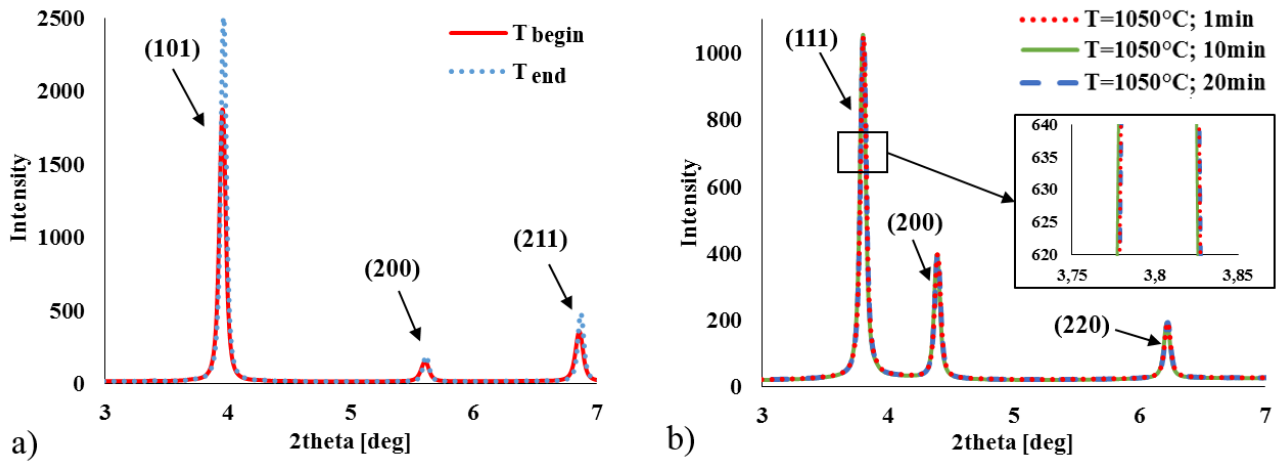


Fig.IV.8 a) Evolution of diffraction peaks (101), (200), (211) at the beginning and at the end of heat treatment; b) Evolution of diffraction peaks (111), (220), (200) at the high temperatures

The average crystallite size and strain for the low deformed sample R1 before and after heat treatment were studied by the Williamson–Hall method [Williamson and Hall, 1953]. It is based on the principle that the size broadening β_L and strain broadening β_e vary differently with respect to Bragg angle θ and can be calculated from the following Scherrer and Stokes equations:

$$\beta_L = \frac{K\lambda}{D \cos\theta} \quad \text{and} \quad \beta_e = 4 \langle \varepsilon^2 \rangle \tan\theta$$

$$\beta_{tot} = \beta_L + \beta_e = \frac{K\lambda}{D \cos\theta} + 4 \langle \varepsilon^2 \rangle \tan\theta$$

where β_{tot} is the total width of the peaks, $\langle \varepsilon^2 \rangle$ is the mean quadratic strain along the normal to diffracting planes, D is the average crystallite size, λ is the X-ray wavelength equal to 0.155 Å, K is the Scherrer constant, taken here equal to 1.

Finally, this equation can be written as:

$$\beta_{tot} \cos\theta = \frac{\lambda}{D} + 4\langle \varepsilon^2 \rangle \sin\theta$$

The calculations of the peak widths and of the Williamson-Hall diagram were realized in a Wolfram Mathematica notebook. Diffraction peaks were fitted by pseudo-Voigt functions that are defined by a weighted average between Gaussian and Lorentzian functions. The instrumental contribution was not taken into account since the measurements were realized at the same conditions before and after austenitization, so only relative variation will be analyzed.

Two examples of diagrams for ferrite before austenitization T_{beg} and after austenitization T_{end} , back to room temperature after slow cooling, are plotted on Fig.IV.9 for the sample R1 at slow cooling. It presents the first 7 diffraction peaks: (110), (200), (211), (220), (310), (222) and (321). An example of diagram for austenite at 1050°C for R1 sample is also shown on 8 diffraction peaks.

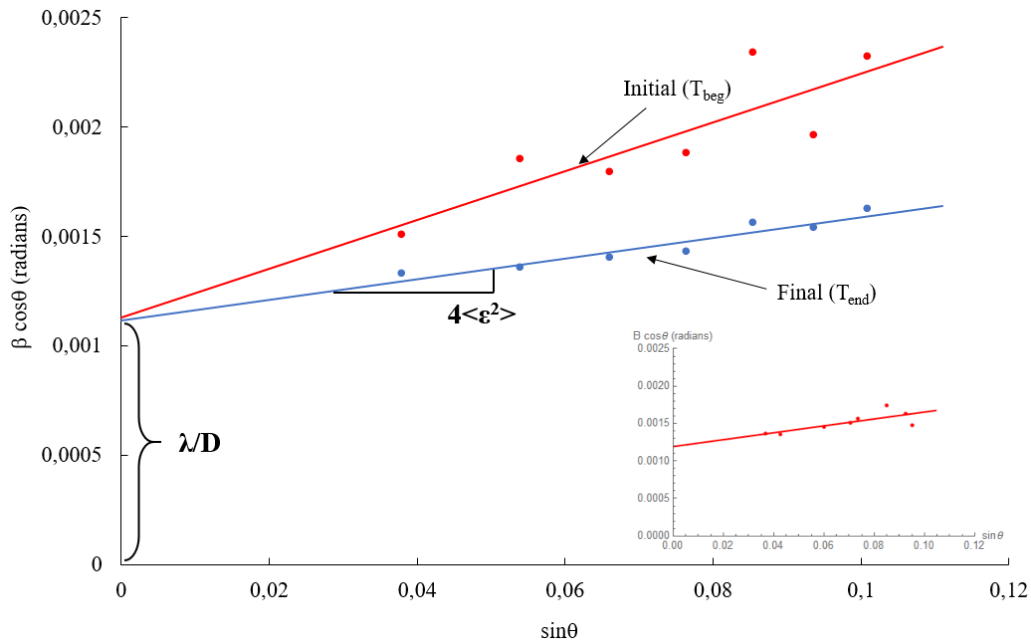


Fig.IV.9 Williamson-Hall analysis of ODS R1 sample at slow cooling before and after austenitization. Strain is extracted from the slope and crystalline size is extracted from y-intercept of the least-squares fit. The inset shows the Williamson-Hall diagram at 1050°C for 8 peaks of the R1 sample.

Williamson–Hall analysis was realized for the samples R1 and R2 with slow and fast cooling at different times of the thermal cycles. It was noted that the crystallite size is the same for all the specimens and it remains unchanged during the whole heating/cooling cycle. It is the same in the ferrite phase, the martensite phase and the austenite phase. To interpret the sizes, it must be recalled that, for diffraction, crystallites correspond to coherently diffracting domains (CDD) which are crystalline domains much smaller than the grains and which are bounded by defects. In given material, these defects can be the precipitates. Indeed, if the precipitate density is $\rho = 10^{22}$ to 10^{24} m^{-3} , the mean distance between two precipitates is $\rho^{-1/3}$ [Toualbi,

2012]. It corresponds to 10 to 46 nm. This length is consistent with the crystallite size found: 11 to 16 nm. This means that the crystallite size is probably controlled by the precipitates distribution. This distribution does not change during austenitization as the precipitates are unlikely to dissolve at 1050°C.

The results of calculations by Williamson-Hall method for crystallite size and strain evolutions are presented in the Table.V.2. Similar results were obtained using MAUD software with Rietveld refinement [Lutterotti, 2006] in which the “isotropic Delft” microstructural model was chosen.

Table.V.2. Evolutions of crystallite sizes and rms strains during the experiments

Temp.(°C)	D_{α} (nm)	$\langle \varepsilon^2 \rangle_{\alpha}$ (%)	D_{γ} (nm)	$\langle \varepsilon^2 \rangle_{\gamma}$ (%)
R1 Slow Cooling				
R.T.	12.2 ± 2.5	0.209 ± 0.088		
849	11.2 ± 2.1	0.002 ± 0.118	12.1 ± 0.6	0.076 ± 0.021
936			12.6 ± 1.4	0.102 ± 0.046
1050			13.6 ± 1.5	0.137 ± 0.042
1050			13.0 ± 1.3	0.115 ± 0.040
1050			12.9 ± 1.3	0.110 ± 0.041
830			13.4 ± 0.9	0.124 ± 0.026
727	12.2 ± 0.1	0.052 ± 0.005	11.9 ± 3.0	0.047 ± 0.112
516	12.4 ± 1.0	0.068 ± 0.033		
135	12.8 ± 0.7	0.079 ± 0.020		
R2 Slow Cooling				
R.T.	12.9 ± 3.9	0.265 ± 0.117		
853	14.4 ± 4.2	0.191 ± 0.13	12.5 ± 0.4	0.081 ± 0.014
938			11.4 ± 0.9	0.042 ± 0.038
1050			12.5 ± 0.9	0.084 ± 0.033
1050			12.4 ± 0.9	0.081 ± 0.031
1050			12.6 ± 0.7	0.093 ± 0.024
652	12.4 ± 1.1	0.078 ± 0.038		
340	12.9 ± 0.9	0.087 ± 0.028		
145	12.7 ± 0.8	0.075 ± 0.026		
R1 Fast Cooling				
R.T.	12.2 ± 2.5	0.219 ± 0.085		
853	13.4 ± 4.9	0.182 ± 0.175	12.5 ± 0.4	0.087 ± 0.013
1050			12.7 ± 1.0	0.090 ± 0.033
1050			12.1 ± 0.7	0.071 ± 0.028
1050			12.3 ± 0.8	0.075 ± 0.030
652	16.1 ± 4.2	0.187 ± 0.095	14.2 ± 2.1	0.139 ± 0.056
340	11.8 ± 4.0	0.299 ± 0.181	11.4 ± 1.6	0.118 ± 0.084
145	11.1 ± 3.4	0.326 ± 0.175	8.9 ± 1.9	0.181 ± 0.127
R2 Fast Cooling				
R.T.	14.4 ± 3.8	0.270 ± 0.092		
838	12.0 ± 1.9	0.107 ± 0.083	12.4 ± 0.2	0.065 ± 0.008
926	13.2 ± 5.4	0.124 ± 0.197	12.5 ± 0.6	0.079 ± 0.021
1050			12.5 ± 0.8	0.084 ± 0.029
1050			12.2 ± 0.7	0.072 ± 0.027
1050			12.2 ± 0.7	0.072 ± 0.027
656	16.1 ± 4.5	0.202 ± 0.101	13.8 ± 1.1	0.145 ± 0.030
361	11.8 ± 2.9	0.234 ± 0.132	13.3 ± 6.5	0.199 ± 0.197
310	11.6 ± 3.1	0.305 ± 0.147	12.0 ± 7.6	0.335 ± 0.281

It can be observed that, for slow cooling (R1 and R2), the distortion in the final ferrite is lower after austenitization. The interpretation is straightforward: it is certainly linked to the dislocation density. Dislocations were created during cold rolling, creating a high lattice distortion. During austenitization, a significant fraction of these dislocations was annihilated, reducing the distortion after slow cooling. As can be seen the rms strain already started to decrease even before reaching the austenitization temperature, probably because of dislocation annihilation or rearrangement.

For rapid cooling (R1 and R2), the distortion in the martensite increases during cooling and the final values attained are higher ($>0.3\%$) than in the initial ferritic state. It can also be seen that, during cooling, the distortion in austenite is also increasing strongly, from 0.08% at 1050°C to 0.2% or 0.3% at room temperature. It can be explained by a progressive plastification of austenite during the transformation and also by the growth of neighbouring martensitic domains

Furthermore, it is seen on Fig.IV.10 that ferrite does not completely disappear at high temperature. This residual ferrite remains visible after 20 min of holding at 1050°C . It is more pronounced for R2 sample than for R1. For the holding time of 60 min, the peaks of residual ferrite are no longer visible. The existence of this residual ferrite may also contribute to the texture memory effect by acting as germs for the transformation of austenite into ferrite during cooling. Further investigation on the size, the localization and the orientation of the residual ferrite, for instance by TEM, would be necessary to support this hypothesis.

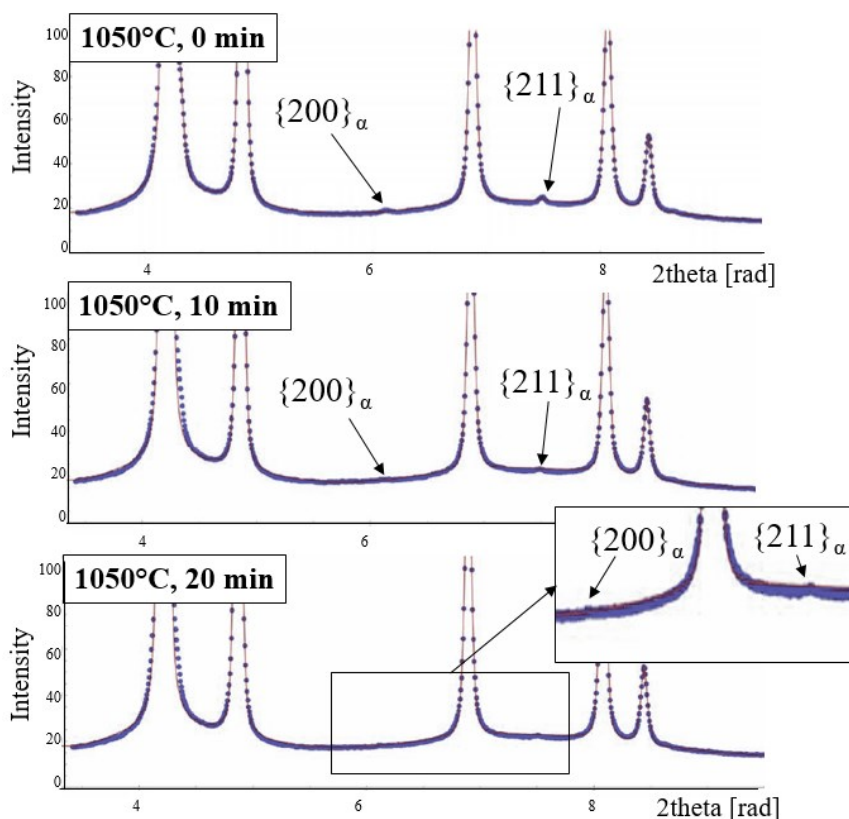


Fig.IV.10 Diffraction patterns for R2 sample at 0, 10 and 20 min at 1050°C

IV.5. Prediction of transformation texture in cold-rolled ODS by Double Kurdjumov-Sachs relation

Texture memory effect is commonly explained, in bibliography, by a phenomenon of variant selection during phase transition. First attempt to catch this phenomenon were presented by Kurdjumov and Sacks in 1930 [Kurdjumow and Sachs, 1930] and further developed by many authors. All the proposed model aims to predict the obtained texture of the transformed phase taking into account the lattice structure and the initial texture of parent phases. Martensitic transformation is widely studied using those models [Hutchinson et al., 2005; Tomida et al., 2010; Tomida, 2018]. All the proposed models are based on an orientation relation between the parent phases and the resulting transformed phase. Depending on the lattice structure and the concerned phases, different orientation relation are identified (Burgers for hcp lattice, Kurdjumov-Sachs or Nishiyama-Wassermann for cubic lattice). For cubic structures and alpha/ gamma transition the K-S relation is the widely used. Recently, T. Tomida proposed the Double Kurdjumov-Sachs (DKS) relation [Tomida et al., 2012; Tomida et al., 2013; Tanaka et al., 2015] as an extension of the standard K-S relation. This approach is shown as to be correctly estimated for texture formation in many materials. Not only during displacive martensitic transformation but also during diffusive alpha-gamma and gamma-alpha transition. Section below, present the DKS model theory that effectively helps to predict texture memory effect in steels [Tomida et al., 2013].

In DKS model, the variants having K-S or near K-S relations with two or more neighboring parent grains at the same time are preferentially selected. Under this modeling, since the operation of the i -th K-S variant of ferrite in the parent austenite grain γ_1 requires the presence of γ_2 on the opposite side of the grain boundary, with which the i -th variant can have K-S or near-K-S relationship as well, the probability for the i -th variant to be chosen, $\rho_i(g)$ may be proportional to the orientation density of γ around $\Delta g_k^{-1} \cdot \Delta g_i \cdot g$ that is the orientation of such KS-related γ_2 (see Fig.IV.10),

$$\rho_i(g) \propto \sum_k f(\Delta g_k^{-1} \cdot \Delta g_i \cdot g).$$

Here, g and Δg are the orientation of γ_1 and the crystal rotation due to K-S relation, respectively, and $f(g)$ is the ODF of austenite. The numbers k and i represent variants of K-S relation.

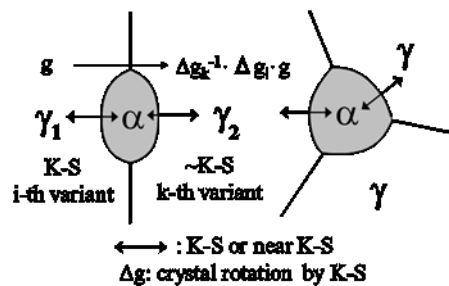


Fig.IV.10 Schematic representation of Double K-S relation

Introducing the variable ω that determines the intensity of variant selection and the material conservation law, the probability function shown below can be derived,

$$\rho(g) = \frac{\omega}{N} \sum_k f(\Delta g^{-1} \cdot g_k^c \cdot \Delta g \cdot g) + \rho_C(g),$$

$$\rho_C(g) = 1 - \frac{\omega}{24 \cdot N} \sum_{i=1}^{24} \sum_k f(\Delta g_k^{-1} \cdot \Delta g_i \cdot g).$$

Here, g_k^c and N are the rotational operators for the cubic crystal symmetry and the number of possible orientations of K-S related γ_2 , respectively; $N=21$ for this study to exclude the same orientation as γ_1 and two close orientations (10.6 degrees from γ_1). Therefore, $g_k^c \cdot g$ represent the equivalent orientations to g for cubic crystals.

The value of ω that determines the strength of the variant selection by DKS should depend on microstructures of materials and is known to be from about 0.5 to unity for transformation from austenite to ferrite in hot-rolled low-carbon steel. When $\omega=0$, there is no variant selection. Mathematically, the upper limit of the ω value is around unity for strong parent textures, since $\rho_c(g)$ as well as $\rho(g)$ may become negative for strong textures, which is physically undesirable. For weak textures, the upper limit would be around 2 to 3.

With the probability function of variant selection being expanded as

$$\rho(g_\gamma) = \sum_{\lambda=0}^{\infty} \sum_{m=-\lambda}^{\lambda} \sum_{\nu=1}^{N(\lambda)} \rho_{\lambda}^{m\nu} T_{\lambda}^{m\nu}(g_\gamma),$$

the transformation texture can be calculated using the following equations [Bunge et al.,1984],

$$\alpha C_{\lambda}^{\mu\nu} = \sum_{\lambda_1=0}^{\infty} \sum_{\mu=1}^{M(\lambda_1)} \sum_{\nu_1=1}^{N(\lambda_1)} \gamma C_{\lambda_1}^{\mu\nu_1} \left[\sum_{\lambda_2=0}^{\infty} \sum_{\nu_2=1}^{N(\lambda_2)} \sum_{m=-\lambda}^{\lambda} \sum_{s=-\lambda}^{\lambda} \rho_{\lambda_2}^{r\nu_2} A_{\lambda_1}^{m\mu} (\lambda_1 \lambda_2 m r | \lambda s) \{ \lambda_1 \lambda_2 \nu_1 \nu_2 | \lambda \nu \} T_{\lambda}^{\mu s*} (\Delta g) \right]$$

The A 's are the coefficients for the symmetries of crystals, $(\lambda_1 \lambda_2 m r | \lambda s)$'s are the Clebsch-Gordan coefficients, $\{ \lambda_1 \lambda_2 \nu_1 \nu_2 | \lambda \nu \}$'s are generalized Clebsch-Gordan coefficients defined by Bunge, Δg represents the rotation of a crystal lattice due to phase transformation, $s=m+r$, and $|\lambda_2 - \lambda_1| \leq \lambda \leq |\lambda_2 + \lambda_1|$. $\gamma C_{\lambda}^{\mu\nu}$ and $\alpha C_{\lambda}^{\mu\nu}$ are the expansion coefficients of ODFs of austenite and ferrite, respectively, and $T_{\lambda}^{\mu\nu}$ are spherical harmonics with Bunge's convention [Bunge, 1982]. Therefore, the variant selection is statistically determined by the texture of parent phase in the DKS modelling. The reverse transformation from ferrite to austenite can also be calculated in the same fashion, hence the texture memory can be modelled. In this study, the deformed texture before heat treatment was chosen as the initial texture for prediction, since the

measured ferrite texture at 850°C on heating was little different from the as-deformed texture having a poor signal-to-noise ratio due to short time measurement.

On Fig.IV.12, the results of synchrotron measurements are presented by ODF cross-sections in **new coordinates** without rotation around Z axis (in comparison with ODFs presented above), so the fiber axis is located at the center of pole figures with $\langle 011 \rangle // RD$ and $\langle 111 \rangle // RD$ is parallel to Z-axis. Fig.IV.11 presents a new reference map with the rolling components parallel to Z-axis. These references were used for the DKS model on the texture prediction, described in the next section.

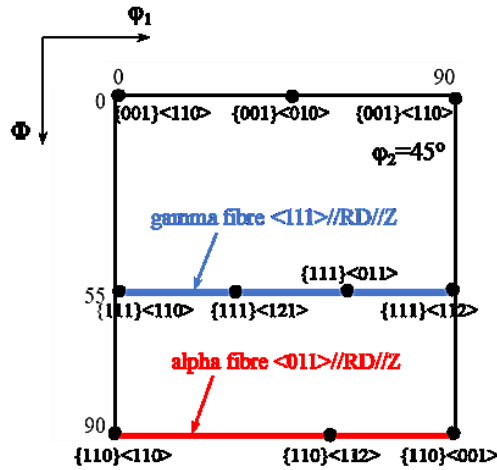


Fig.IV.11 Reference map for $\phi_2 = 45^\circ$ sections of an ODF with common texture component

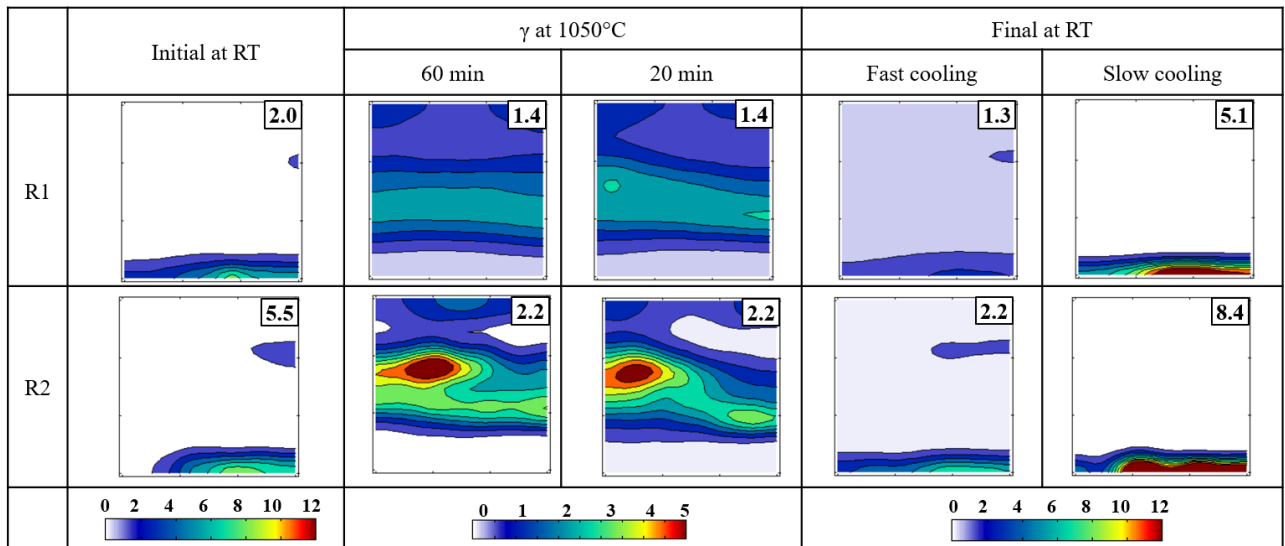


Fig.IV.12 Measured texture evolution during the thermal cycle for low deformed sample R1 ($\epsilon_p=110\%$) and high deformed sample R2 ($\epsilon_p=250\%$) at slow and fast cooling at $\phi_2 = 45^\circ$

(Texture index is in upper right side of ODF map)

On Fig.IV.13 and Fig.IV.14, the prediction results via DKS modelling as well as observed textures are presented as ODF cross-sections at $\varphi_2 = 45^\circ$ for R1 samples. The austenite textures on Fig.IV.13(d) and Fig.IV.14(d) were calculated from the experimental initial textures on Fig.IV.13(a) and Fig.IV.14(a), respectively, “without variant selection”, i.e., $\omega=0$, since the averaged deviation between the predicted and experimental ODFs was indeed minimized at $\omega=0$ when altering the value of ω (see Fig.IV.15). On the other hand, the final martensite texture on Fig.IV.13(e) was calculated (from the experimental austenite texture on Fig.IV.13(b) at $\omega=1.0$, which was also determined to minimize the averaged deviation as shown on Fig.IV.15. Note that this averaged deviation between the experimental and predicted textures for martensite is only about 0.09 in ODF values. The former result evidently shows that there is absolutely no variant selection operating in the phase transformation from ferrite to austenite on heating, which has been seldom mentioned in previous studies [Tomida et al., 2013, 2015; Tomida, 2018]. It can indicate that the nucleation of austenite on heating has probably occurred inside of ferrite grains around the oxide particles, where DKS can never be fulfilled. It may be caused by the severely deformed regions around the oxide particles formed during cold working, where the nucleation of austenite becomes more pronounced than on austenite grain boundaries on the heating [Bay and Hansen, 1979].

In contrast, on cooling, austenite transforms into martensite, with a small amount of ferrite, under the strong influence of DKS. The value of $\omega=1.0$ is comparable or a little larger than that for the low carbon hot-rolled steel [Tomida et al., 2008; Tomida et al., 2012; Tanaka et al., 2015] and slightly smaller than that for the cooling process of texture memory in low-carbon and IF (interstitial free) steel [Tomida et al., 2013, 2015]. Hence, although the texture intensity in a macroscopic scale increases only slightly as seen in Fig.IV.13(b) to (e) because of the weak texture in austenite, the martensite in the ODS steel is microscopically expected to obey DKS at a large probability. In a previous work [Tomida, 2018], an elastic anisotropy of the parent phase as well as the martensite itself was integrated in DKS model in order to model the variant selection in martensite transformation in low-carbon hot-rolled steel. However, whereas the elastic anisotropy of the austenite texture was also introduced in this work as well, its contribution was found as very small so that only the double K-S should be applied to the martensite transformation. The reason is could be that the rolled ODS steels cannot be readily quenched into martensite, and thus, quenched microstructure is often presented with a mix of small amount of ferrite and martensite. In this case, the ferrite is already nucleated on grain boundaries fulfilling Double K-S and orientation of martensite will align to the orientation of formed ferrite.

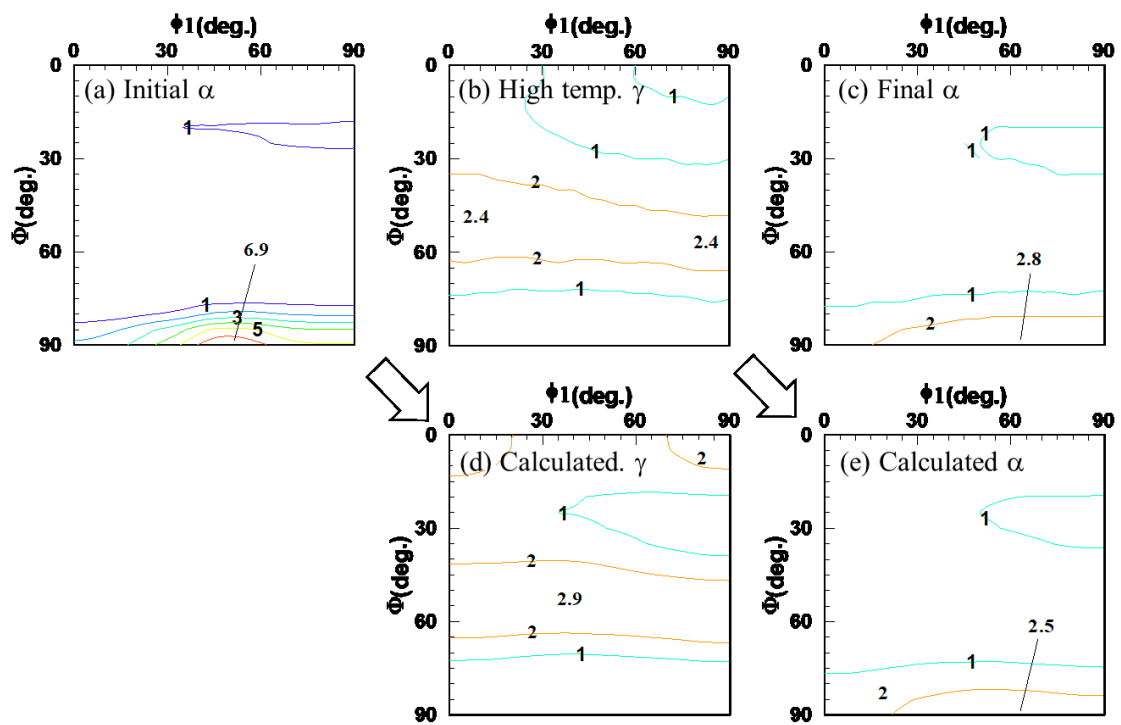


Fig.IV.13 Comparison of textures between (a to c) experiment and (d and e) prediction for R1 in the memory cycle with fast cooling, (d) austenite texture was calculated without variant selection, whereas (e) final martensite texture was calculated with DKS with $\omega=1$.

ϕ_2 is 45 degrees and levels are 1, 2, 3...

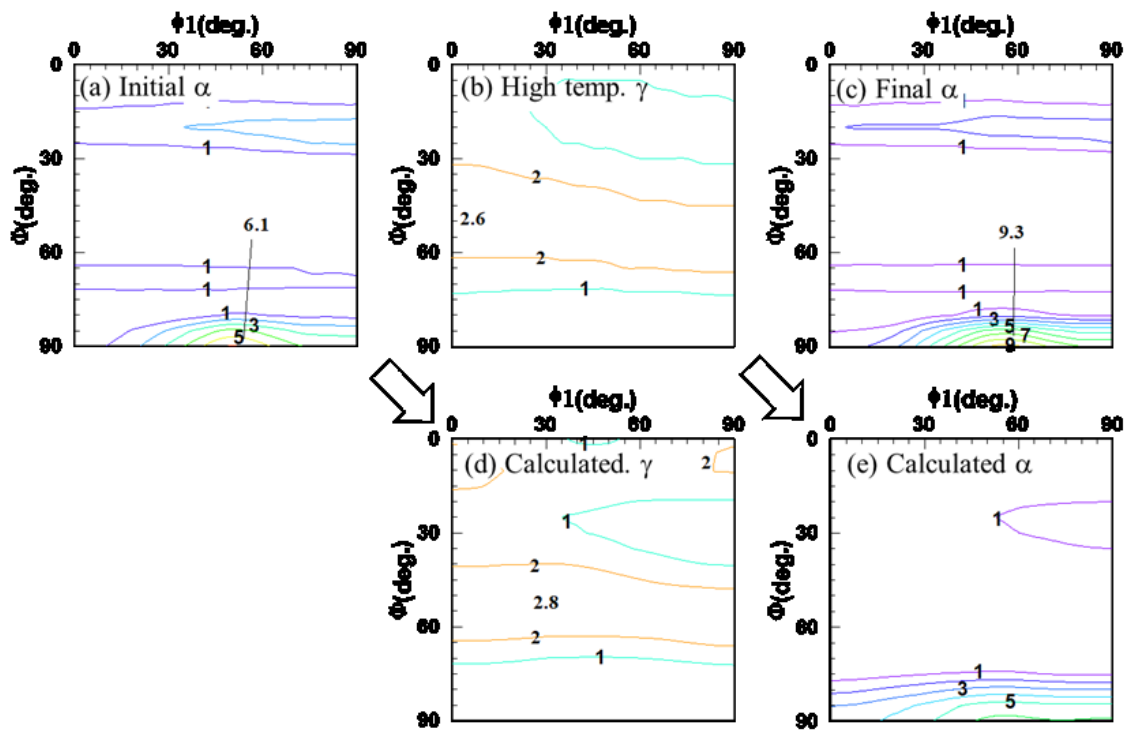


Fig.IV.14 Comparison of textures between (a to c) experiment and (d and e) prediction for R1 in the memory cycle with slow cooling. (d) Austenite texture was calculated without variant selection, whereas (e) final ferrite texture was calculated with DKS with $\omega=5$.

ϕ_2 is 45 degrees, and levels are 1, 2, 3...

Even more interesting in this study is the texture enhancement during slow cooling. On Fig.IV.14(e), a ferritic texture was calculated from the experimental austenite texture at $\omega=5.0$, which far exceeded the upper limit of the value of ω (2 to 3 for weak parent textures as abovementioned), to minimize the averaged deviation between the predicted and experimental textures. Because of the large value of ω , there were large areas of negative values both in $\rho(g)$ and ODF (not shown on Fig.IV.14(e)). However, despite the problems, the major characters of the experimental ODF on slow cooling is mostly well reproduced, although only a half of the peak intensity is reproduced. It suggests that the strong $\langle 110 \rangle$ fiber texture appearing on slow cooling should originate from the DKS mechanism as well. The question is why it is so strong that the value of ω exceeds the limit of the present modeling.

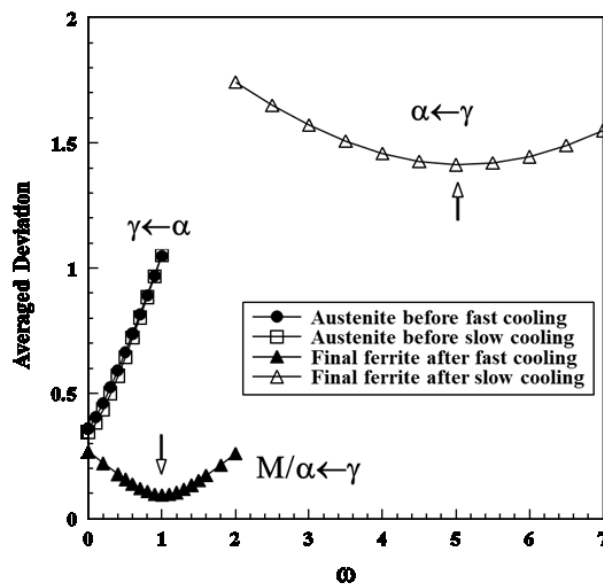


Fig.IV.15 Averaged deviation of textures between experiment and prediction for R1 samples as a function of the value of ω . Square root of squared deviation, averaged over an Euler angle space in which the value of experimental ODF was more than 0.5, is shown.

A possible mechanism is an intensive grain growth after the phase transformation, in which ferrite grains of the $\langle 110 \rangle$ fiber can selectively grow. To investigate this possibility, the martensite structure, characterized by EBSD on Fig.IV.16(a), was used for the reconstruction of parent austenite grains by K-S orientation relationship using ARPGE software [Cayron, 2007]. The reconstructed austenite grains of an elongated shape are shown on Fig.IV.16(b), in which boundaries have a zig-zag lines, indicating an error in the reconstruction probably related to DKS. It is also seen that the grain size of the reconstructed austenite grains is about 8 μm . Considering this first estimation of gamma grain size and by comparison with the microstructure of the ferrite after slow cooling (on Fig.IV.16(c)) that is less than 3 μm in grain size, a scenario of the intensive grain growth is improbable. It must be noted that due to the very fine microstructure and the remaining strong intragranular misorientation, there is no warranty that the results of ARPEG reconstruction of gamma grains is consistent with experience. To confirm the austenitic grain morphology, additional characterization technics, like high temperature treatment in SEM or X-Ray tomography, must be used.

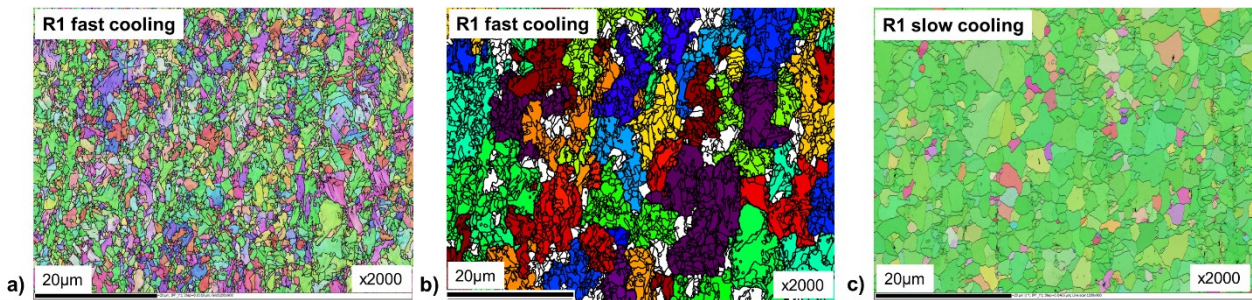


Fig.IV.16 a) Microstructures of martensite structure after fast cooling, b) microstructure of reconstructed austenite from martensite and c) microstructure of ferrite after slow cooling

Another scenario is that the DKS variants that better fulfill DKS conditions than others might have larger selection probability; in other words, DKS variants with smaller misorientation from K-S relation survive more [Hata et al., 2016]. In the present DKS modeling, such a proximity effect to the exact K-S relation is not considered. For instance, if ferrite variants that satisfy DKS at triple junctions with small misorientations to K-S relation with two adjacent austenite grains and grows into the other austenite grain with which K-S relation is not fulfilled at all, the growth would be favored because of smaller interfacial energy of the K-S boundaries and larger mobility of the incoherent non-K-S boundary. They can nucleate earlier and consume less favored DKS nucleation sites during slow cooling. The dispersed oxide particles might contribute to this selective nucleation and growth by inhibiting the growth of nucleus on less favored nucleation sites as well.

One more factor that needs to be considered is that on heating the special boundaries are created within initial ferrite grains [Hutchinson and Kestens, 2008], on which DKS can always be fulfilled for ferrite to precipitate on cooling (see Fig.IV.17). It may lead to stronger variant selection on cooling than heating, although if grain growth of austenite occurs at high temperature, these special boundaries can be wiped out. In ODS steel, however, since the austenite grain growth is inhibited by the oxide particles, it may enhance the texture memory. These mechanisms are most likely mechanisms that operate for the texture memory on slow cooling in this study. A modified DKS modelling for this scenario is still an ongoing subject and should be studied in the perspectives.

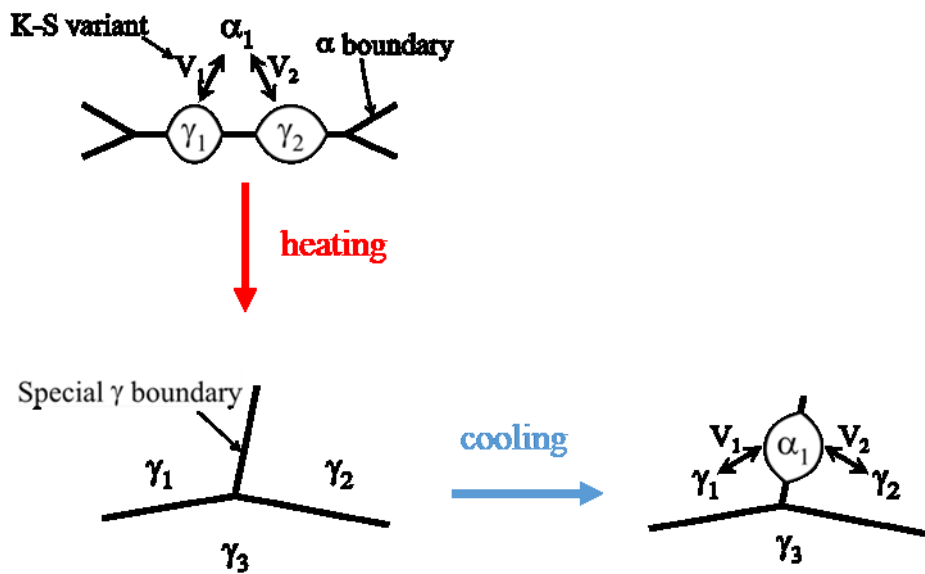


Fig.IV.17 Schematic representation of one of the conventional mechanisms of texture memory due to special boundaries, (upper) two nucleating α particles having the K-S relation to the grain α_1 on an α grain boundary on heating, (bottom left) an γ grain structure with a special boundary after completion of $\alpha \rightarrow \gamma$ transformation, and (bottom right) a nucleating α grain with the original orientation of α_1 having the double K-S relation on the special γ boundary on cooling.

The special boundaries would disappear by the growth of γ grains.

Conclusions for Chapter IV

The evolution of crystallographic texture for 9%Cr ODS tubes was measured using synchrotron X-ray *in-situ* diffraction during heating cycles up to 1050°C and analyzed based on Double Kurdjumov-Sachs modeling. The analysis has led us to the following conclusions:

1. A texture memory effect was observed during ferrite formation particularly at a slow cooling rate where even a texture enhancement was found. Quenching after heat treatment reduced the crystallographic texture and thus reduced this texture memory effect. For manufacturing purposes, this treatment presents as an effective method to reduce the crystallographic anisotropy introduced by cold working.
2. The texture and the diffraction peak widths were measured for the first time in austenitic range for ODS steels. The austenite texture was stable at 1050°C without any indication of recrystallization.
3. Analysis of size and strain by Williamson-Hall method showed that the crystallite size did not evolved during austenitization at high temperatures and after cooling back to room temperature either by slow or rapid cooling. The computed crystallite size is consistent with the average distance between nano-oxides particles. For slow cooling, the lattice distortion of the final ferrite is lower than for the initial ferrite. For rapid cooling the martensitic transformation leads to a significant distortion of both the martensite and of the retained austenite. At high temperature, the lattice distortion of austenite is always low.
4. The higher the cold work strain, the higher the texture index before as well as after heat treatment. The initial microstructure plays a crucial role in the occurrence and intensity of the texture memory effect. This must be considered in the case of highly deformed materials obtained by Mannesmann pilgering conditions.
5. The remarkable thermal stability of the alpha-fiber is likely to be linked to the very dense nano-oxides precipitation that could promote selective growing of specifically oriented variant during $\gamma \rightarrow \alpha$ phase transformation.
6. The texture of parent γ grains can be correctly reconstructed using the harmonic expansion method based on Kurdjumov-Sachs relation without variant selection, indicating that the nucleation of austenite likely does not occur on ferrite grain boundaries but inside of the ferrite grains where nano-oxides could play a role of nucleation centers. It causes the relatively weak texture observed in high temperature austenite.
7. In the case of displacive transformation on cooling, the variant selection model with a Double Kurdjumov-Sachs (DKS) predicts well the martensite texture with a relatively large ω value that indicates an important variant selection intensity. It is probably caused by a small amount of ferrite nucleated on austenite grain boundaries with DKS, along which martensite orientation aligns.
8. For the diffusive ferrite formation, DKS model with a very large ω value reproduces most of the characters of the strong $\langle 110 \rangle // \text{RD}$ fiber and texture memory effect. However, it must be extended to

explain texture enhancement experimentally observed. Then, we suggest a model where nuclei of ferrite with better-fulfilling DKS will nucleate earlier on austenite grain boundaries and grows faster over multiple austenite grains consuming other DKS nucleation.

Chapter V. Influence of heat-treatment parameters on phase transition

Introduction

Based on the obtained investigations on texture evolution in the previous Chapters III and IV, a set of heat treatment experiments was realized in order to identify the particular behavior of ODS steels during phase transition process and to propose an optimized method for intermediate and final heat treatment.

V.1. The objectives for the study of phase transition processes

In this section the microstructures and texture evolution after different thermal cycles applied to sample R1 are studied. On Fig.V.1 the initial microstructure of R1 sample with EBSD and EDX (Ti and Cr) maps are reminded in order to facilitate the reflection through the reading. All results in the following sections are presented on Fig.V.2 - Fig.V.9 that includes the dilatometric curves with the phase transition zones; IPFY maps where the scale bar, the grain size (μm), hardness (HV1) and texture index (TI) are specified; and the EDX maps with Ti and Cr distribution. The relationship between the grain size and hardness for each treatment are summarized on Hall-Petch plot in Annex 2.

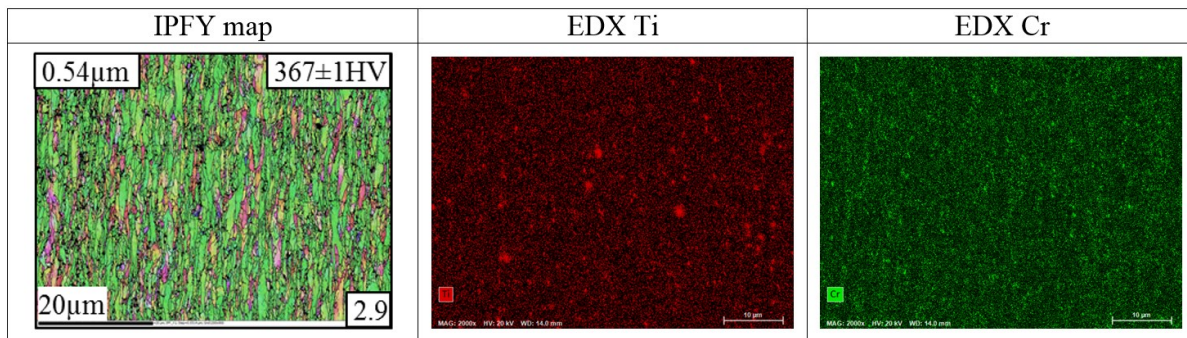


Fig.V.1 The initial microstructure of R1 sample with Ti and Cr EDX maps

The main objectives of this study are to investigate:

1. The influence of holding temperature on the texture formation
2. Mechanism responsible for ferrite nucleation and growth during cooling step
3. The effect of heating rate on the phase transformation kinetics
4. The precipitation distribution under various heat treatment conditions
5. The impact of initial microstructure (textured or isotropic) on the final one
6. Estimation of parent γ grains shape and size

To answer these questions, the different thermal modes are presented in the following sections.

V.2. Influence of holding temperature on texture formation

The role of treatment temperature on the texture evolution is showed on Fig.V.2, where the treatments were realized at 950°C, 1050°C and 1150°C with a **slow cooling rate**.

In all cases the heating was carried out with complete austenitization. The growth of gamma grains is a thermally activated phenomenon. Thus, an increase in treatment temperature will lead to larger grain sizes. It can be noticed that the texture index is also increased. Treatment temperature acts just like holding time at the high temperatures and promotes the enhancement of the fiber intensity. We assume that the phenomenon of texture enhancement is related to the gamma domain size that grows to a bigger size with higher temperature. At the same time, hardness is decreased by bigger grains size.

The final structures are represented by quasi-equiaxed grains arranged into **columns** parallel to the rolling direction, that are continuously disappearing with the temperature increasing. For the sample treated at 950°C the region with the big grains is considered as an artifact (sample preparation or chemical heterogeneities) and it is not taken into account for the analysis.

For all cases Ti oxides precipitates seem to be unaffected by the treatment. Due to the short treatment duration (2s) some columnar boundaries (Prior Particles Boundaries (PPB)) remains even at 1150°C. Re-precipitation of Cr carbides are still observed in ferritic structures.

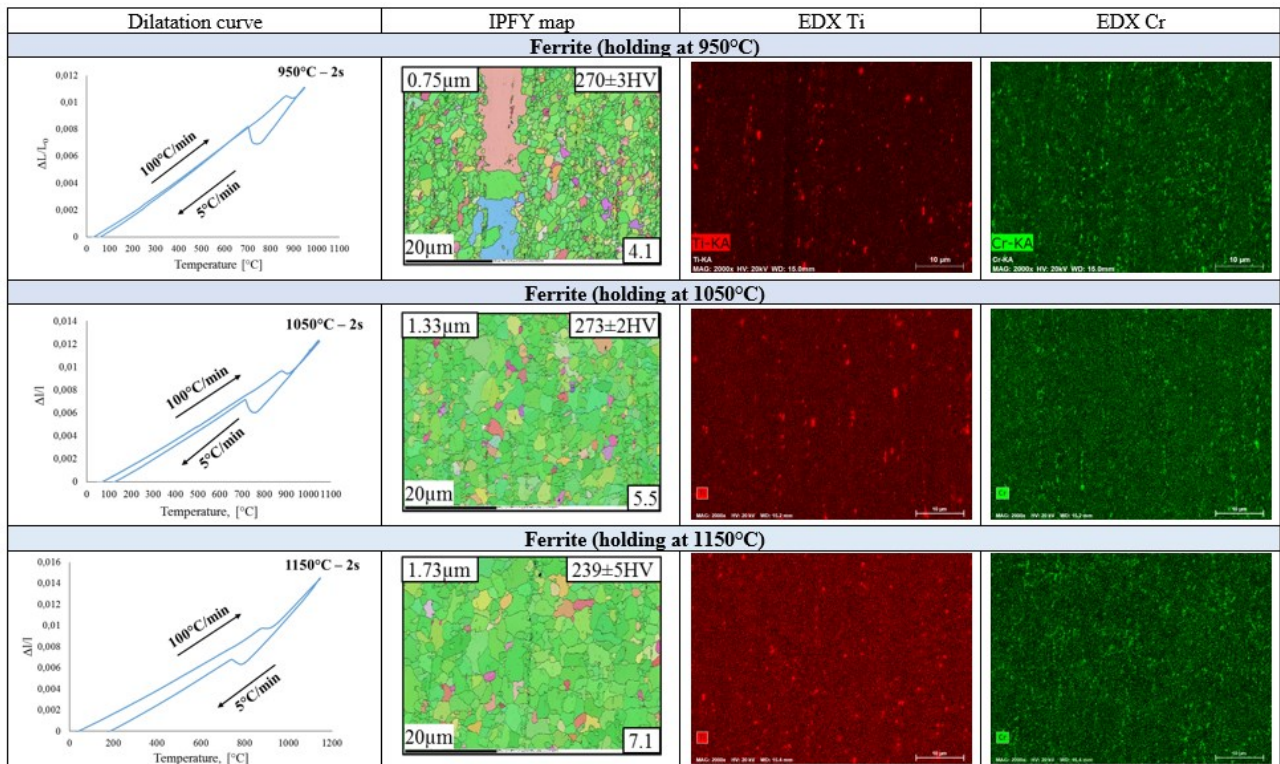


Fig.V.2 Influence of holding temperature (950°C, 1050°C, 1150°C) on texture formation (slow cooling)

The role of treatment temperature was also studied for treatments at 1050°C and 1150°C with a **fast cooling rate**. The same tendency was observed, that the texture index seems to increase with the treatment temperature, this point is consistent with an increased gamma grain size.

On Fig.V.3 it is shown that the microstructure of the samples is not fully restored, but the texture index is low. We also noted that the higher treatment temperature promotes a slightly higher hardness and could be explained by the better dissolution of carbon in the austenite matrix.

Small precipitates of Ti are observed at high temperatures. But chromium carbides, not having time to diffuse in the solid solution, exhibit a homogeneous distribution of Cr maps, even after a tempering at 750°C for 15 min.

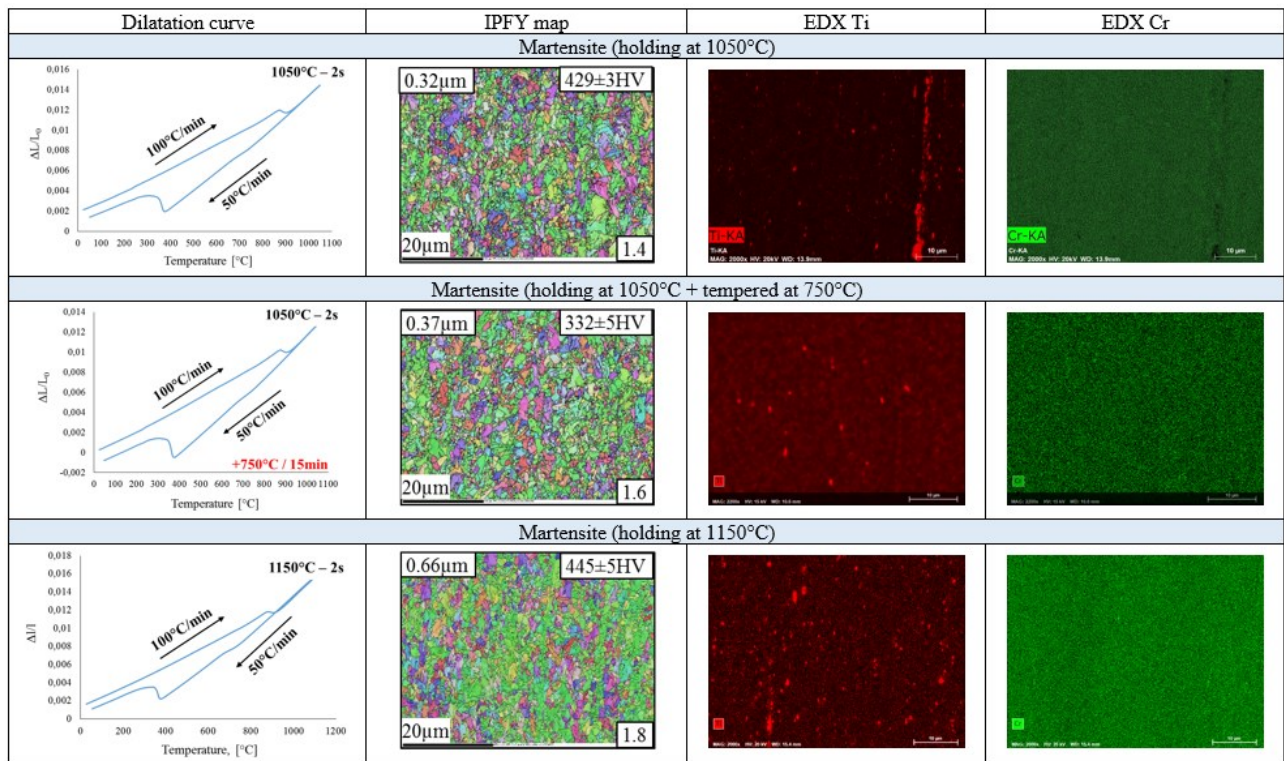


Fig.V.3 Influence of holding temperature (1050°C and 1150°C) on texture formation (fast cooling)

V.2.1. The Sellars model for ferrite grain growth

The experimental results, devoted to the influence of treatment on the ferrite grain growth, inspired us to find a model that allows to link the dependence of the grain size with the temperature and the duration of the treatment at the high temperatures. Sellars model is widely used to predict the average grain sizes of austenite during the growing process [Sellars et al., 1979; Lee et al., 2008].

This model was applied as an approach to predict the ferritic grain size for a given temperature and holding time. Since the hardness is strongly correlated to the grain size, this tool may help to monitor the heat treatment design. In this work we make the assumption that this model can be applied for the determination of ferritic grain size.

Basic calculations of the grain size are based on the equation for ideal grain growth:

$$d^n - d_0^n = A \cdot t \cdot \exp\left(-\frac{Q(T)}{RT}\right)$$

where d is the average grain size (μm), d_0 is the original ferrite grain size (μm), n and A are constants depending on the grain growth kinetics, t is holding time at a given temperature (min), Q is the activation energy necessary for the grain growth (J/mol), R is the gas constant equal to 8.31 J/(mol·K), T is the heating temperature (K).

The grain growth processes for different metals have different constants, such as A , n , and Q . For 9% Cr ODS these values were determined and are presented in Table.V.1. The experimental values (triangle) and calculated values (points) are shown on Fig.V.4 for the sample R1 (after 1st rolling pass) at **different temperatures**.

Table.V.1 Values used in calculation of final grain size at T=1050°C for R1 sample (short time treatment)

T(°C)	d_0 (μm)	A ($\times 10^9$)	n	Q (kJ/mol)
950	0,54	5	6	202
1050				205
1150				207

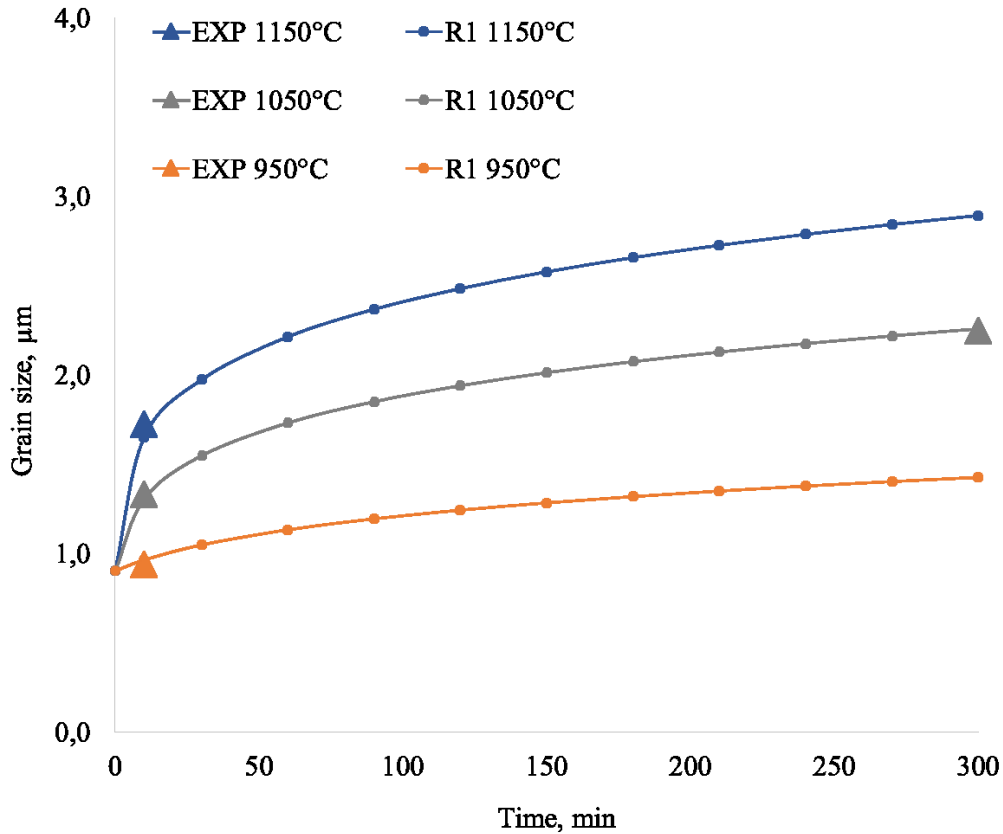


Fig.V.4 Grain size evolution as a function of the temperature and the holding time for R1 sample

Grain size evolution as the function of the **deformation degree** and holding time are presented Fig.V.5 (the experimental values (triangle) and calculated values (points)) for the sample R1 (after 1st rolling pass), R2 (after 2nd rolling pass), R2(HT) (after 2nd rolling pass with intermediate heat treatment). A fitting of calculated values with experimental data is performed to identify the values for the model validation. These values are given in Table.V.2.

Table.V.2 Values used in calculation of final grain size at T=1050°C for HE, R1 and R2(HT) samples

Sample	d0 (µm)	A (×10 ⁹)	n	Q (kJ/mol)
R1	0,54	5	6	205
R2	0,22			200
R2(HT)	0,36			180

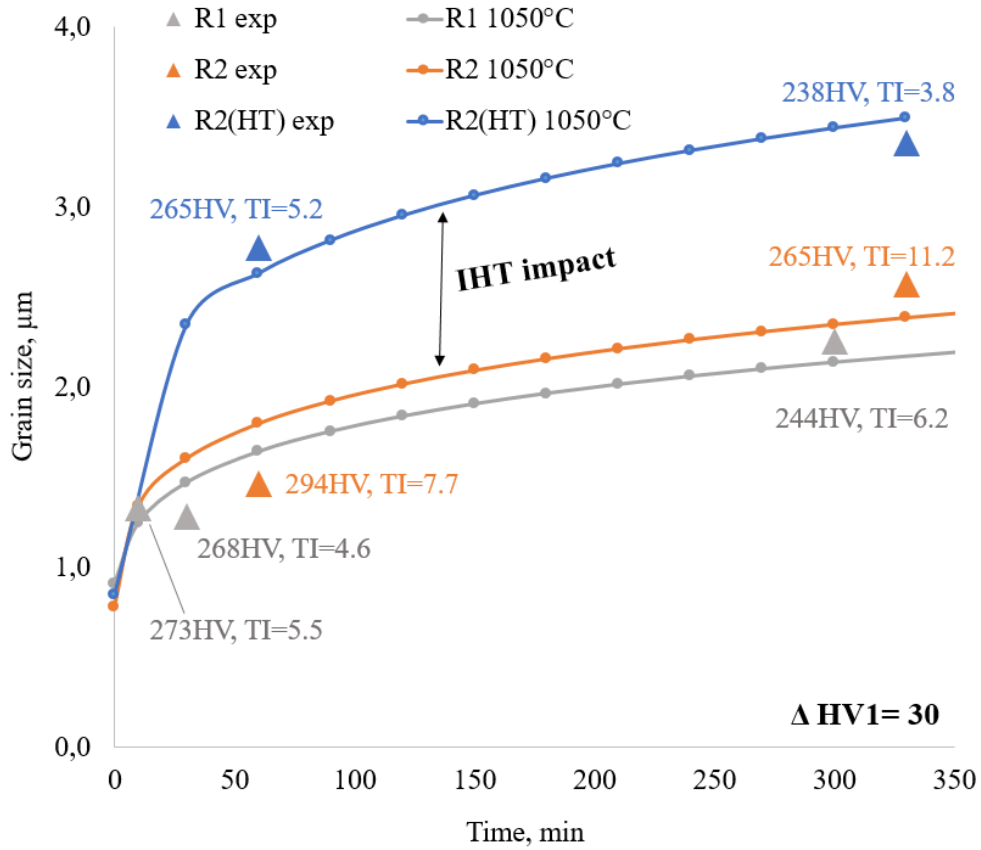


Fig.V.5 Grain size evolution as a function of the deformation degree and the holding time

Those results show that the Sellars model and the identified parameters help in predicting the ferrite grain size after heat treatment. However, the activation energy is strongly dependent on the initial microstructure. If both rolled R1 and R2 samples have more or less the same activation energy, the R2(HT) sample presents a lower activation energy. As proposed by [Yu and Hansen, 2016], this activation energy may evolve during treatment, presenting both recovery and austenitic domain size evolution.

In conclusion, it can be said that the first model application for the ferrite grain size prediction showed a prospective results and for its final validation the missing experimental data should be introduced, including the intermediate states of heat treatment (the points on the lines) and additional rolling step R3, in order to identify the evolution of activation energy and n parameter during processing. This point must be taken in consideration for further cold forming studies.

V.3. Mechanism responsible for ferrite nucleation / growth - Isothermal treatments

Isothermal transformation of austenite to ferrite is studied after interrupted quenching from γ domain (1050°C) until the holding temperature is lower than A_{c1} , but higher than M_s , i.e. between 600°C and 800°C. The cooling rate is equal to 50°C/min that allows to start ferritic transformation not earlier than achieving the holding temperature.

In the work of [Lambard, 1998], similar tests were realized for the ODS material EM10 (9Cr-1Mo-0.5Ni-0.5Mn-0.1C-0.1O-0.024N-0.15Y-0.23Ti) and the fastest transformation kinetics was found at 700°C. Below or above this temperature, the observed morphological evolution was important. Based on this experience, two temperatures are chosen in our work 650° and 710°C and the results of these treatments are presented on Fig.V.6.

- Heat treatment at 650°C: the ferritic structure is finally obtained with small equiaxed grains with an average size of 0.8 μm . The texture Index is relatively low in comparison with the reference ferritic sample. The Cr segregations are very fine and aligned with the RD.
- Heat treatment at 710°C: the shape and size of ferritic grains are not homogeneous, the shape changes from equiaxed to slightly elongated grains. The average grains size is higher than for the treatment at 650°C and equal to 1.06 μm . The segregation of Cr is more frequent and also aligned with the RD. The most important fact is related to the texture index, which is twice higher than in the previous experiment.

The hardness for the experiment at 650°C is 20HV higher than at 750°C, but corresponds well to the hardness of the ferritic structure.

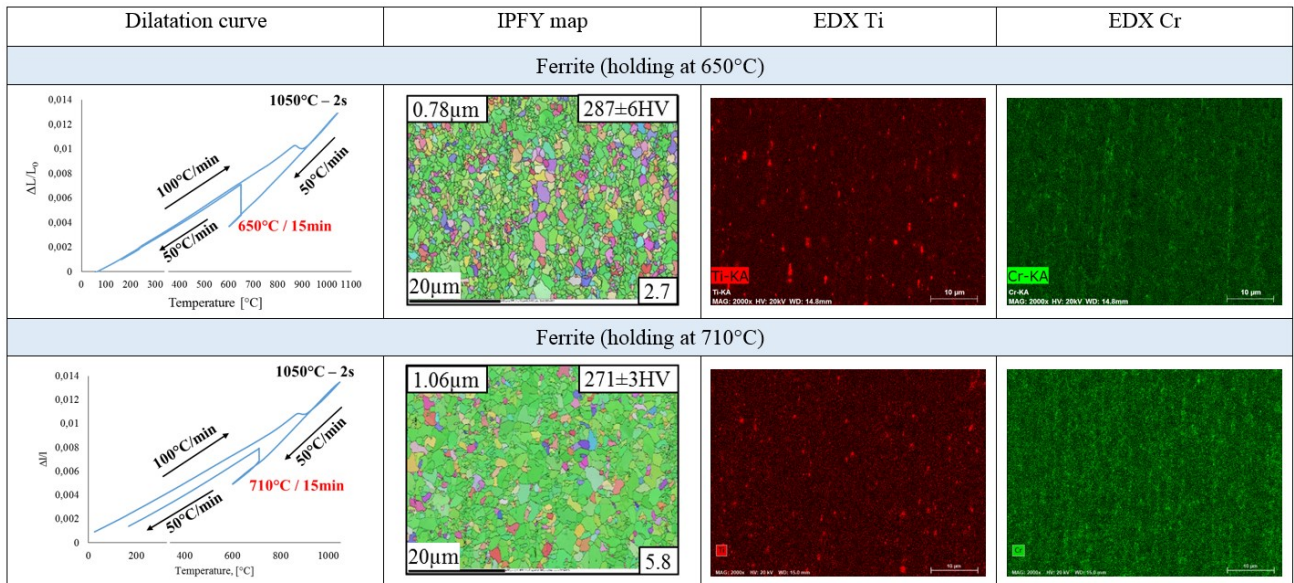


Fig.V.6 Isothermal treatments for identification of mechanism responsible for ferrite nucleation and growth

These tests confirm two mechanisms of ferrite formation observed by [Lambard, 1998]:

- in the case of higher overcooling at the temperatures lower than 700°C, atoms diffusion is very weak, nucleation happens with a high frequency but associated to a slow nuclei growth. The nucleation is initiated at the gamma grains boundaries. Since there is a higher number of new germs, more crystallographic orientations will be presented.
- in the case of lower overcooling at the temperatures higher than 700°C, the diffusion is increasing and new germs will have more capacity to grow rapidly, than to nucleate. This time the nucleation is probably mainly initiated at the triple point of gamma grains. Thus a selective germination of these few nuclei induces a high texture index and bigger grains.

V.4. Impact of initial microstructure on the final one - Double step treatment

For this experience, the sample is heated up to 1050°C in the austenite domain and quenched at 50°C/min to obtain a martensitic structure. Then the sample is reheated again up to 1050°C and cooled down slowly at 5°C/min to form a pure ferritic structure. Such kind of double-step heat treatment allows to identify the contribution of initial microstructure on the texture evolution.

In the previous experiments, it was noted that the high anisotropy in interfacial energy (the energy of elongated grain boundaries) significantly contributes to the texture increasing during cooling. Thus, we suppose that after martensite structure formation, when the carbides particles are dissolved and there is no more the columnar structures, the ferrite formation will happen with a random nuclei orientation. In other words, the martensite transformation will destroy (or reduce) the texture memory effect.

The results of this heat treatment showed on Fig.V.7 that the inherited texture **remains observable** even after passing through the quasi-isotropic martensitic structure. The average grain size is lower than the reference case (*cf. above* 1050°C/2s with $v_c=5^\circ\text{C}/\text{min}$) coupled to a lower texture index tends to prove that the initial microstructure before heat treatment (here martensite) play a role in the final result. This tendency was already evidenced in Chapter III and IV for various strain degrees. This result let us assume that texture enhancement during slow cooling heat treatment needs a strong initial fibre texture to occur.

For the chemical compositions, Ti oxides precipitation remains unchanged by the treatment and chromium carbides appear much finer that in the reference case.

This structure can be interesting to apply as an intermediate heat treatment between passes, because it reduces texture and grain size, but it has the same hardness as after a standard ferritic treatment (< 300HV).

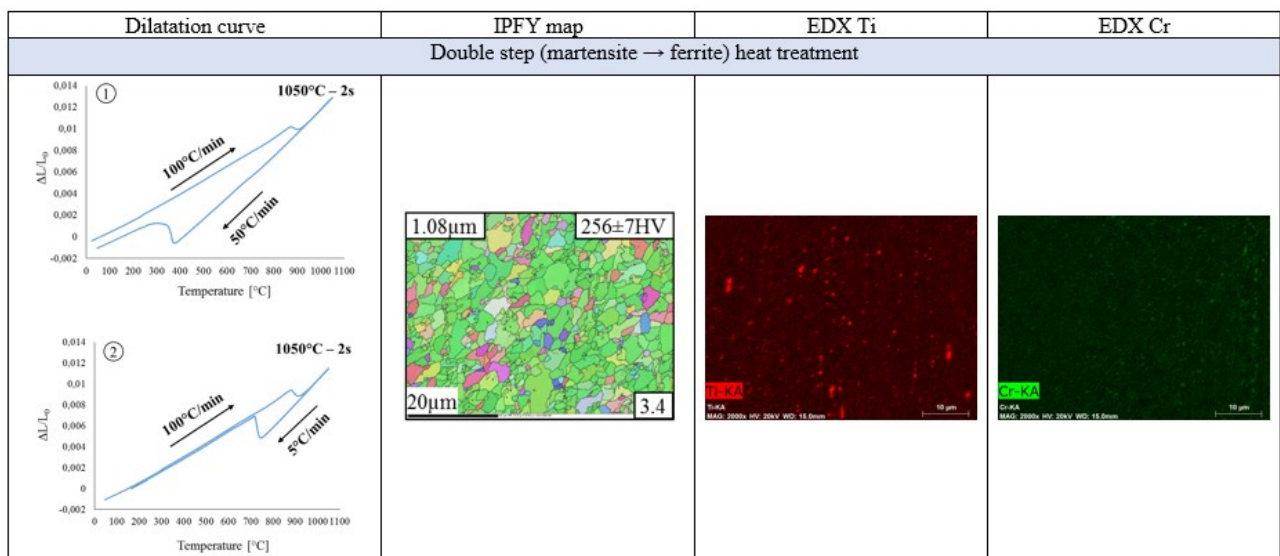


Fig.V.7 Double step treatment for identification of initial microstructure impact on the final one

V.5. Estimation of parent γ grains shape and size – Inter-critical treatments

Thermal treatment at 890°C was carried out with different holding time: 1 and 15 min. Then the samples are cooled down with a cooling rate of 50°C/min.

On the dilatation curve on Fig.V.8 it can be seen that at a temperature of 890°C the steel is in the inter-critical domain: the first γ nuclei already appeared, but there is still some amount of non-transformed ferrite grains.

For a **short holding time** (1min), no martensitic transformation is noticed on calorimetric curves. Some large grains compared to the initial structure are the results of phase transformation $\alpha \rightarrow \gamma \rightarrow \alpha$, while the small grains are non-transformed recovered initial ferritic grains. Observed in non-indexed regions, **chromium** carbides coupled to **Ti** oxides precipitation pins the austenitic transformation and preserve the columnar structure. Since these carbides are not dissolved during short treatment, this leads to purely ferritic structure. Consistently the texture index is rather high which confirms a limited phase transformation for this treatment. Ti oxide precipitation remains unchanged and similar to the initial R1 state. Therefore, we conclude that intercritical treatment has no impact on Ti precipitation.

For a **longer holding time** (15 min), austenitic transformation occurs partially and martensitic transformation is noticed on calorimetric curves. Unfortunately, for this treatment the EDX maps were not done, but we can suppose that the Cr carbides were mainly dissolved and no columnar bands are observed anymore. The texture index is lower in comparison with the previous heat treatment, but higher than for the fully martensite structure. Finally, the hypotheses proposed in DKS section (section IV.5) on the texture increasing due to the first ferrite formation can be considered here.

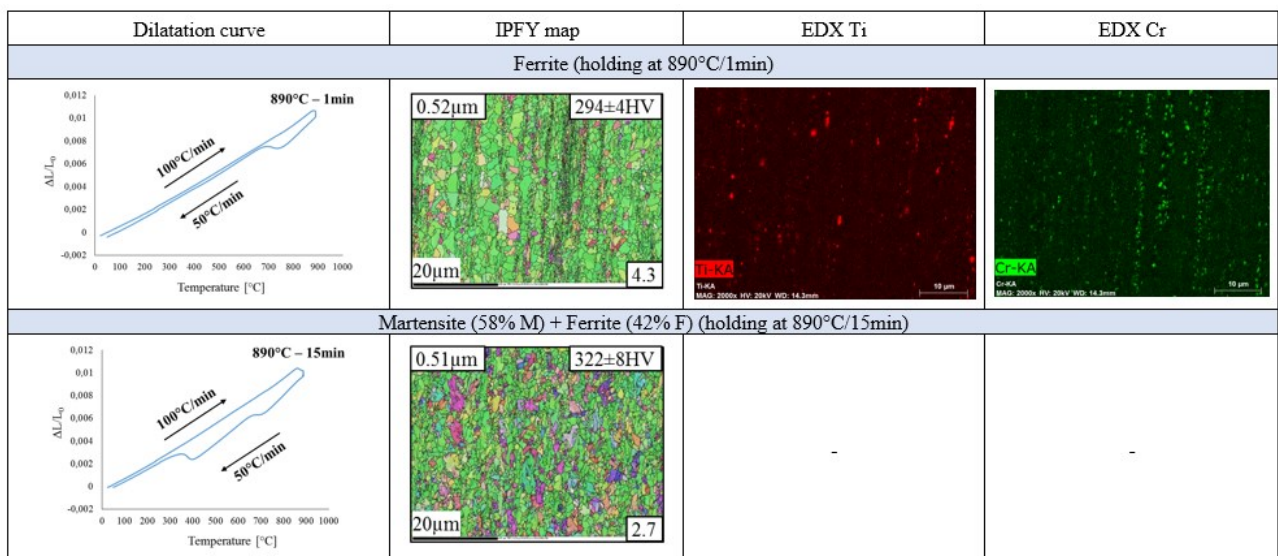


Fig.V.8 Inter-critical treatments carried out with different holding time: 1 and 15 min.

V.6. Effect of heating rate on the phase transformation kinetics

Samples are heated in the inter-critical domain at 880-900°C with different heating rates 100°C/min (standard heating rate in this work) and 600°C/min. Then the samples were cooled down with a slow cooling rate to form a pure ferritic structure.

During the inter-critical treatment **with fast heating**, the structure is constituted of a bimodal grain size distribution, where few large grains are growing rapidly inside the columnar structure (Fig.V.9). For such behavior it can be suggested that the high thermal stability of the small non-transformed ferritic grains is attributable to the high density of second phase particles. Moreover the contribution of high anisotropies in interfacial energy (grain boundary energy) and high chemical nonequilibrium can have an impact. Each of these reasons leads to a very high local rate of gamma grain interface migration, resulting in the strong growth in the columns of few grains compared to the slow growth of the finer matrix grains. For the **standard 100°C/min heating rate**, the phenomenon is less remarkable, since the structure had a longer time to dissolve the precipitates and to reduce the interfacial energy. The addition of 20°C at high temperature may also contributes to this phenomenon.

During slow cooling, phase transition promotes formation of large ferritic grains with a preferential fiber orientation growing inside the columns. It is assumed that those large ferritic grains grow during ferrite formation inside large austenitic domains with a specific orientation relation with previous austenitic domains. This phenomenon enhances the texture index at rather high level. For these two samples carbides precipitates are observed on the grain boundaries. Also in both cases, the columnar structure is preserved showing that even at 900°C the precipitations are pinning the austenitic grain growth quite efficiently. The poor dissolution of chromium carbides may explain the very limited number of ferrite nuclei for inter-critical treatments. Therefore, we can conclude that heating rate has only little consequences on texture evolution.

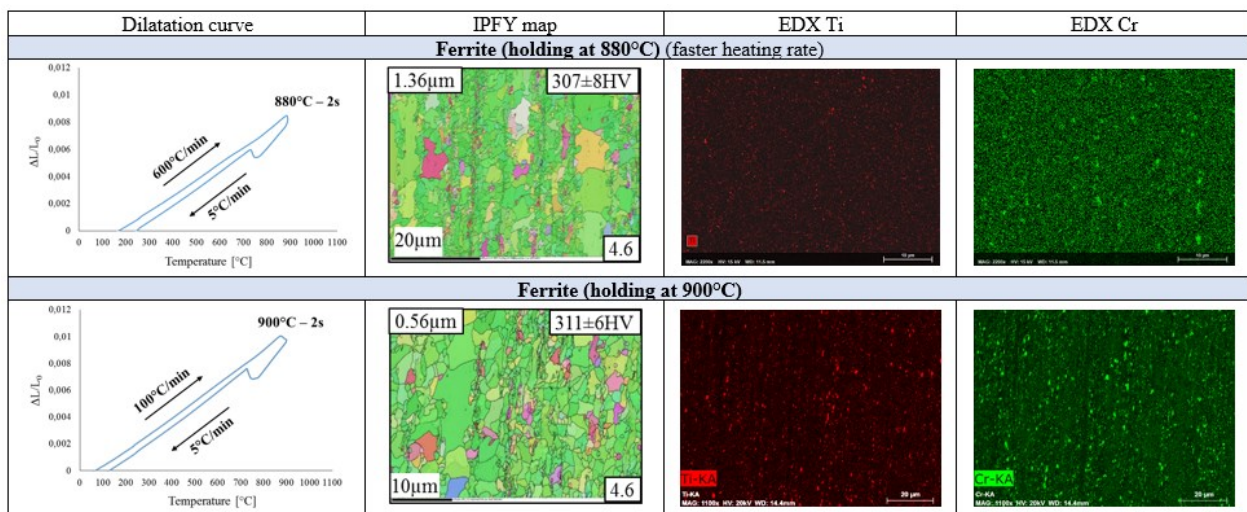


Fig.V.9 Inter-critical treatments with different heating rates 100°C/min and 600°C/ min

V.7. Discussion on the selective nucleation and growth and the role of the particles on the texture formation

Trying to explain the observed phenomenon presented in [Chapter IV](#) and [Chapter V](#) some bibliographic studies are presented below, that includes three aspects: (1) precipitation and phase transition, (2) recrystallization nucleation and texture formation and (3) precipitation and nucleation.

Precipitation and phase transition

Some studies are devoted to the relation between precipitation and phase transition. Those studies reveal that the **orientation relation** between precipitations and matrix may play a crucial role on the phase transition. Ti added bearing steels is an example of this study [[Yen et al., 2010](#)]. In that case, TiC precipitated in the austenitic matrix and presented a specific orientation with transformed ferrite. For those that are formed by interphase precipitation, i.e. nucleating on the moving interface between the two phases, the orientation relation is evidenced and shown to play a crucial role on the phase transition kinetic.

In our material that exhibits a dense precipitation at various scale, orientation relation of nano-phase with the matrix may also have an impact on phase transformation monitoring the kinetic of grain growth.

RX nucleation and texture formation

In this part we are going to draw a parallel between the texture development, observed in this work during the phase transformation, and the cases found in the literature on the recrystallization processes. Even if the driving force in recrystallization is the lattice distortion and in phase transformation - diffusion and solubility of interstitial elements, the process of germination, as itself, should have common points between these two processes.

Two theories can explain the development of a new texture during heat treatment: selective germination and selective growth [[Doherty et al., 1997](#)]. The **first theory** assumes that at the **nucleation** stage the germs prefer a particular orientation to form. The greater number of germs with the same orientation leads to the development of the texture during the grain growth. The **second theory** states that the germs appear in random directions but some will exhibit a selective **growth**. For example, slightly disoriented recrystallized grains will grow less rapidly because of the low mobility of their interface. The texture is then caused by the large grains that have grown in one or more other orientations, it is an effect of grain size [[Jensen, 1995](#)].

Engler also noted that two theories only represent limiting cases that is why a **combination of both theories** in the sense of growth selection out of a limiting spectrum of preferentially formed nucleus orientation must be taken into consideration [[Engler, 1997](#)].

Precipitation and nucleation

Selection of certain orientations can be initiated by particle stimulated nucleation (PSN) in favored sites such as grain boundaries. It has been demonstrated that growth selection from PSN orientations occurs during the annealing in Al alloys [Vatne et al., 1996].

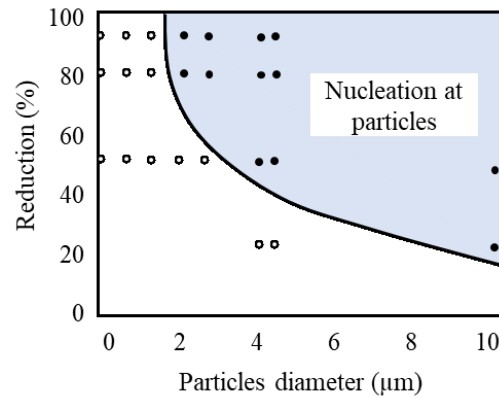


Fig.V.10 The conditions for particle size and strain for PSN to occur at Si particles in cold rolled aluminium [Humphreys, 1977]

Some indications of preferred nuclei orientations appearing in the deformations zones of heavily strained materials have been reported in the works of [Engler et al. , 1989, 1995]. At **low levels of deformation** (50% reduction) they reported a **randomization** of the subgrain orientations within the deformation zones. At **higher strains**, however, a slight **preferred occurrence** of P and ND-rotated Cu subgrains appeared in the regions close to the large particles. Nuclei generated at the particles (investigated after a short time of annealing) also showed this weak preference of P and ND-rotated Cu. Weak recrystallization texture with some preference of P and ND-rotated Cu have been reported in various aluminum alloys where PSN is an assumable important nucleation mechanism [Jensen et al., 1991; Engler aet al., 1992; Vatne et al., 1996; Engler, 1997]. In the sample containing large particles ($>1\mu\text{m}$) nucleation takes place in the deformed zones that form around these large particles during deformation [Humphreys, 1977].

In our ODS material the Cu and P fibers are also noticed in the gamma phase. Even if the two cases differ strongly regarding the driving force of the transformation, precipitation and fibers components shows unexpected similarities.

Conclusions for Chapter V

To understand the mechanism determining the texture increase during ferrite formation in highly deformed material, a set of experiences were realized to study the influence of the heat treatment parameters on the microstructure.

The analysis of texture indexes and grains sizes shows that the texture fiber enhancement is most likely related to the **fast growth** of a limited number of **ferrite nuclei with preferential orientations**. This assumption is confirmed by observation of few large ferritic grains during low temperature inter-critical heat treatment (between A_{c1} and A_{c3}). Those grains confirm the existence of very few ferrite nuclei appearing during the cooling step and their relative fast growth at the beginning of ferritic transformation. Those nuclei should have an orientation relation with the previous austenitic grains to explain the sharp alpha fiber inherited texture. We do not exclude the assumption that, the ferrite nuclei of very small size (fraction), untransformed by heat treatment, initiate the ferrite transformation during cooling. If it is the case, their size and volume proportion is too small to be detected by calorimetric and dilatometric signal.

The higher the treatment temperature and the longer the holding time, the higher is the texture index. This phenomenon is assumed to be related to the austenitic grain growth that promotes fast growing of ferrite nuclei. At the same time, phase transformation kinetic has been shown to be weakly dependent on the heating rate. Therefore, we assume that recovery has no impact on phase transition kinetic.

By isothermal tests (*interrupted quenching from γ domain until the holding temperature between A_{c1} and M_s*) it was observed that overcooling under/above some critical temperature (in the case of ODS $\approx 700^\circ\text{C}$) will strongly determine the morphological and crystallographic evolution.

- In the case of overcooling at temperatures **lower than 700°C** when the atoms diffusion is weak, **nucleation** happens with a high **frequency** associated with a **slow growth** of nuclei. Since there is a **higher number of new germs**, more crystallographic orientations will be presented and a **less pronounced texture** will be measured at the end.
- In the case of overcooling at temperatures **higher than 700°C** , the diffusion is increasing and new germs will have more capacity to **grow** than to nucleate. Thus, a **selective germination and growth** of these few nuclei may induce the **high texture** index and larger grains. These tendency is consistent with the analysis proposed by [Lambard, 1998] and complement it with the data on texture evolution.

In any case the Ti oxides precipitation seems unaffected by the treatments and tend to pin the austenitic grain growth during the transformation. This promotes phase transformation inside the columnar structure defined by Prior Particles Boundaries. Chromium carbides are completely dissolved at 1050°C but still anchored the austenitic grain growth during inter-critical heat treatments.

A summary of the study is proposed on Fig.V.11 that presents a scheme of the $\alpha \rightarrow \gamma \rightarrow \alpha$ transformations mechanism, where the nucleation and growth are linked with texture evolution.

The proposed scheme of phase transformation should be confronted to new experiments. Among them an experiment on the austenization *in-situ* in a SEM with various heating and cooling rates can be proposed as a perspective of this work. Further analysis of coherency of precipitates with ferrite after rolling and after heat treatment may highlight the role of nano-phases on the selective growth of ferrite nuclei.

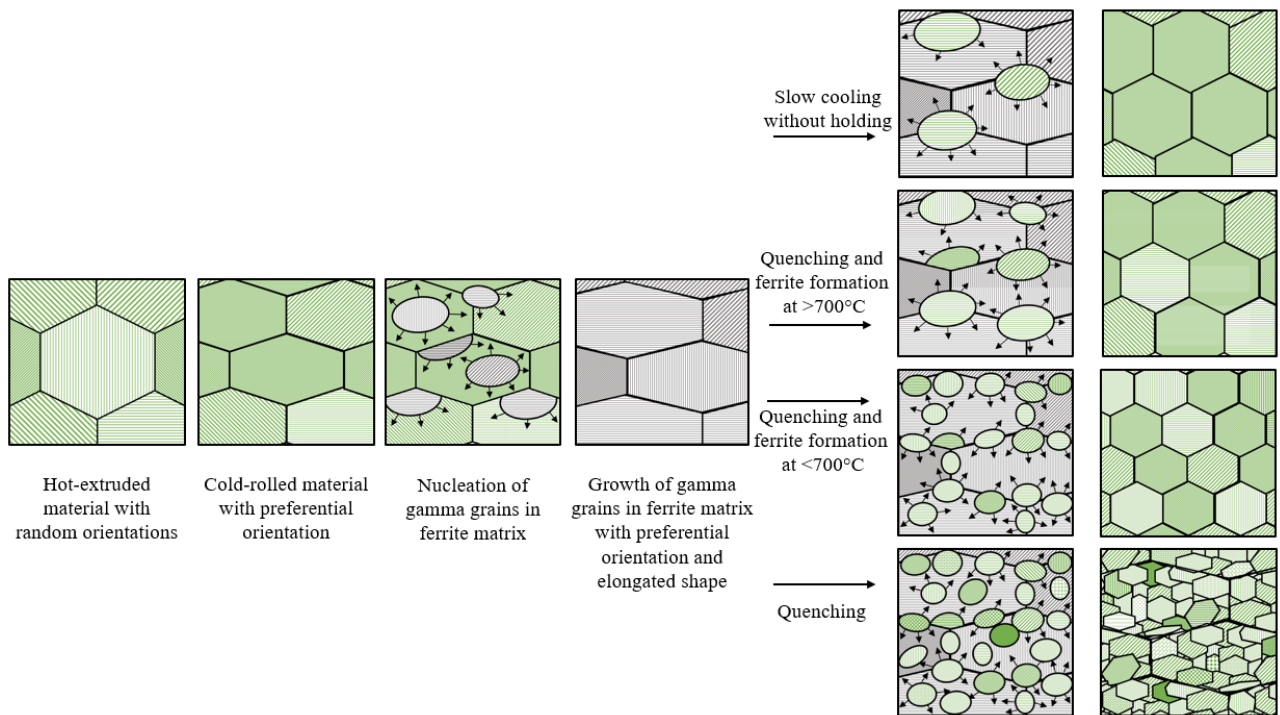


Fig.V.11 Scheme representing the mechanism of $\alpha \rightarrow \gamma \rightarrow \alpha$ transformations and their link with texture memory effect (The colors define the phases: green - ferrite and grey - austenite; the color shades define the orientation spread)

Chapter VI. Modelling of texture and mechanical properties of ODS pilgered tubes

Introduction

In the Chapter III of this thesis, it was shown that the cold-rolled ODS tubes present an anisotropic microstructure and mechanical behavior. The crystallographic texture and the elongated grain shape contributes significantly to this anisotropy. In order to understand the role of grain morphology and crystallographic orientation on the material anisotropy, the modeling of texture and mechanical properties for 9Cr ODS steel is prospected by means of polycrystalline models. It will help to explain the mechanism that leads to increase the texture level during pilgering and the obtained data can be used for further optimization of the manufacturing process.

VI.1. Introduction of texture prediction using polycrystalline models

There are 3 main polycrystalline models that are known by now for the prediction of crystallographic and mechanical anisotropic behavior of crystalline aggregates:

- **Finite Element Models (FEM)**
- **Fast Fourier Transform models (FFT)**
- **Elastoplastic / Viscoplastic Self Consistent models (EPSC / VPSC)**

All this models are generally based on the same principle - the description of the simple crystal behaviour (grain-scale) coupled to a scale transition method that enable to determine the macroscopic behaviour of the aggregate (polycrystal scale).

The comparative [Table.VI.1](#) is given below with the main features of each family of models. In this way, we can see that each model has its advantages and drawbacks. For example, the **FEM** propose a better description of grains morphology and interactions, however the computational costs is quite high. **FFT** models have a big potential for texture prediction, it is less time consuming and quite accurate, but the main disadvantage of this model is restriction to harmonic boundary conditions. Actually, this kind of model are extended to better boundary conditions descriptions. For our application purpose, with large strains, the lack of voxel re-discretization prevents the practical use of actual AMITEX FFT algorithm. In comparison to these two models, the **VPSC** model is the one with the shortest computational time, the prediction results are satisfying and largely discussed in bibliography [[Tomé et al., 1991](#); [Lebensohn et al., 1993](#); [Hu et al., 2012](#); [Saleh et al., 2014](#); [Anglin et al. 2016](#)], nevertheless the description of grain interaction is very limited due to the self-consistent algorithm.

Table.VI.1 The comparative view on the polycrystalline models

VPSC	FFT	FEM
1) Mathematical approach		
Mean-field method (averaging grain environment and assuming constant fields inside the grain)	Full-field method (convolution integrals in discretized microstructure)	Full-field method (microstructure discretized by finite elements)
2) Grain description		
Grain is an ellipsoid in a homogeneous medium (Eshelby scheme)	Grain is a Voronoï cell, Grain rotation have to be implemented, Aggregates can be modeled	Grain is an discretized by Finite Elements, Aggregates can be modeled
3) Grain interaction description		
Interaction with a matrix representing statistically the whole aggregate	Local equilibrium and compatibility constraints (Green's method approach), Grain interaction matrix based on local stress field	Boundary conditions, including friction, shearing gliding or un-bonding
4) Constitutive law		
Elasto / Visco-plastic crystal plasticity (local CRSS/strain tensor, gliding planes)		
5) Hardening model		
Shear threshold on the slip systems, self and latent hardening control (linear or Voce hardening model)		
6) Input data		
Texture information (weighted list of Euler angle orientation)	Crystal orientation for each discretized point within the domain (Voxel or Finite elements)	
7) Computational time		
A few seconds	Minutes / hours	Hours / days

Attempts in the simulation of pilgering process have been done using finite element models and crystal-plasticity finite-element methods. Simplified analytical approaches were considered with investigations based on finite element method by [Montmitonnet et al., 2002]. Another 3D elastic–plastic finite element simulation of cold pilgering of ODS tubes has been carried out by [Mocellin and Vanegas, 2011] to study pilgering process and determine stress, strain and forces that act during pilgering using the theory of plasticity. Due to the cyclic loading involved by pilgering the model should use mixed kinematic and isotropic hardenings. However, in those studies influence of pilgering parameters on the texture formation were investigated.

[Lebensohn et al., 1993,1996; Proust et al., 2007] carried out the first simulation of pilgering process using a **viscoplastic self-consistent model** (VPSC). They showed a strengthening of texture with increase of deformation parameter. [Girard et al., 2001] applying VPSC and experimental measurements with inserts showed that, in the pilgering process, there is an additional shear component to be added to the diagonal strain components with a small effect on deformation texture evolution. [Gloaguen et al., 2006] studied the microstructural evolution during pilgering and the influence of plastic anisotropy on mechanical behaviour. [Raabe et al., 1994, 1995] and [Tóth et al., 1997] devoted their attention in studying the microstructural evolution in BCC materials considering the mechanism of plastic deformation during pilgering and heat treatment.

In this work we carry out the modelling of texture development for ODS materials in pilgering industrial conditions. In the next sections the method of VPSC modeling are explained, as well as the input data and parameters identifications.

VI.2. VPSC formulation

The VPSC developed by Tomé and Lebensohn [Lebensohn and Tomé, 1993] is widely used for modelling deformation textures modelling for various alloys, including materials with BCC structures. In this model the material behavior is the average behavior of all the grains described by their orientations. Each grain is considered as an ellipsoidal inclusion embedded in a matrix whose behavior is the macroscopic behavior (Fig.VI.1). As the Eshelby inclusion scheme [Eshelby, 1957] has no analytical solution in the case of a non-linear behavior, interaction between grains and the average Representative Equivalent Volume (REV) must be solved using various linearization scheme. Among them tangent, a secant or an affine are commonly used. To calculate the strain rate in each grain a rate-dependent visco-plastic law is used. Deformation of a slip system will start when the local stress reaches the critically resolved shear stress (CRSS) according to Schmid law.

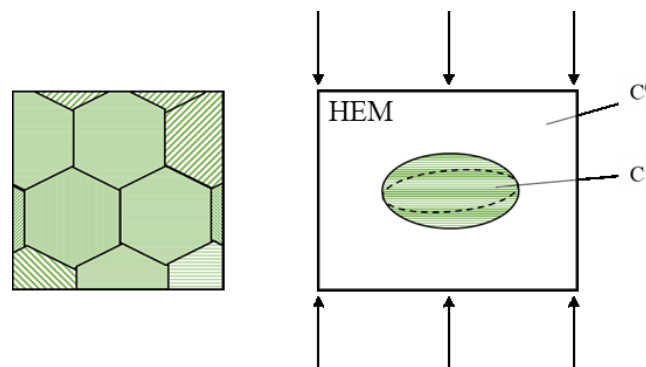


Fig.VI.1 Illustration of Eshelby inclusion (C1) taken from polycrystal and put in the Homogeneous Equivalent Medium (C0) (the properties of HEM is the same as the average properties of the polycrystal)

VI.3. Viscoplastic constitutive law

As mentioned in [Chapter III.7](#) devoted to mechanical properties, ODS steel has a rate-dependent inelastic behavior. It means that it can be characterized by the theory of viscoplasticity. Moreover, BCC structure, due to its high symmetry, leads to undesirable indetermination of gliding plane in some conditions. The choice of viscoelastic modeling overpass this difficulty by splitting the deformation between equivalent gliding planes. The viscoplastic constitutive behavior is described by means of a non-linear rate-sensitive equation:

$$\bar{\sigma} = \lambda(\dot{\bar{\epsilon}})^{1/n}$$

where, λ is the viscosity parameter and n is a power-law type parameter that represents non-linearity. This scheme neglects the elasticity of the material and in particular, the role of elastic anisotropy on grain interactions.

In a given grain the viscoplastic behavior can be described as:

$$\dot{\bar{\epsilon}}_{ij} = \sum_s m_{ij}^s \bar{\gamma}^s = \gamma_0 \sum_s m_{ij}^s \left(\frac{m_{kl}^s \bar{\sigma}_{kl}}{\tau_0^s} \right)^n$$

where τ_0^s and $m_{ij}^s = \frac{1}{2}(n_i^s b_j^s + n_j^s b_i^s)$ are the threshold stress and the symmetric Schmid tensor associated with slip system (s), where n^s and b^s are respectively the normal and Burgers vector of slip systems. $\dot{\bar{\epsilon}}_{ij}$ and $\bar{\sigma}_{kl}$ are the deviatoric strain-rate and stress and $\bar{\gamma}^s$ is the local shear-rate on slip system (s), that can be expressed as:

$$\bar{\gamma}^s = \gamma_0 \left(\frac{m_{kl}^s \bar{\sigma}_{kl}}{\tau_0^s} \right)^n$$

where γ_0 is normalization factor. The threshold stress τ_0^s (CRSS) describes the resistance for activation of deformation modes and it usually increasing with deformation. The VPSC code enables reference hardening functions for each system, described by various law including the Voce law.

After presenting the model context, it is necessary to identify the model parameters and their sensitivity on the results. For model identification, sensitivity analysis of the results are performed for various parameters as following:

- Original grain set (grains number, morphology and orientation)
- Single crystal properties, including active slip systems, their critical resolved shear stresses and the associated hardening parameters
- Boundary conditions (overall velocity gradient components) applied to the aggregate
- Type of interaction between grains (neighbour grains)
- Homogenization scheme (affine, secant, tangent, etc.)

The results of this work on texture prediction will be presented by the following parts:

1. Parameters sensibility analysis based on a traction test for the IHT6 sample (cf. the scheme on Fig.II.2)
2. HE-R1-R2 rolling sequence modelling with an original simplified model
3. Anisotropy of mechanical properties for the R2 state

VI.4. Parameters identifications and sensibility analysis

For parameters identification an interrupted tensile test was realized using the sample R1 **IHT6**. The sample was chosen as the material available in stock, but the best choice for this experience would be the HE state, since it could be more representative in terms of initial microstructure before rolling that does not include the thermal treatment impact. The sample R1 (just after 1st rolling pass) was also used for this traction test, but due to non-indexed zones (mainly linked to high dislocation density and precipitation) and small grain size, the data quality was not sufficient.

The approach consists in an in-situ EBSD measurement of the grains deformation and rotation in a local zone. A carbon micro-grids were applied by FIB for these tests. However, the deposition conditions were not satisfactory and stability under irradiation was too poor to enable further image correlation. For coming campaigns, the deposition of a tungsten grid was proposed, based on the successful results described in the work of [Dadé, 2014].

Nevertheless, the analysis of obtained IPF maps on Fig.VI.2 showed that the grains are not uniformly deformed, with presence of some deformation gradient inside the grain that corresponds to an intragrain misorientation during plastic deformation. Some grains with similar initial orientation, for example grains 1 and 2 on Fig.VI.2, can deform very differently (which is completely ignored in the VPSC model). Some grains are rotated with contribution to alpha fiber increasing (for example, grains 3). But generally, the deformation is homogeneous at the scale of the observed map without the significant gradient between small or big grains zones.

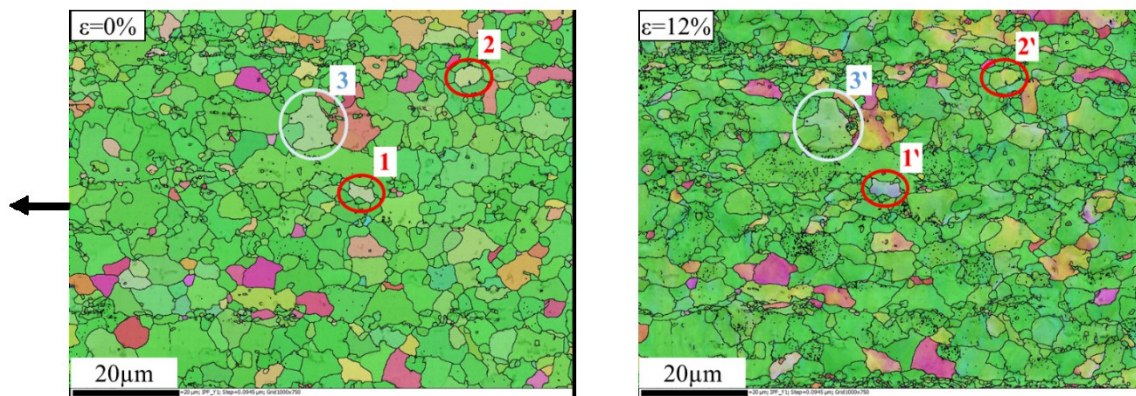
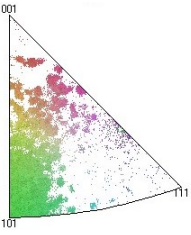
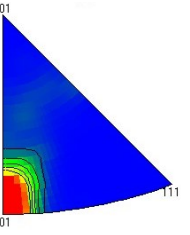
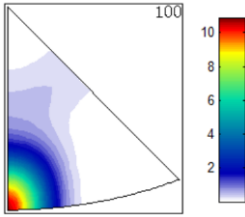
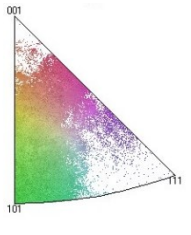
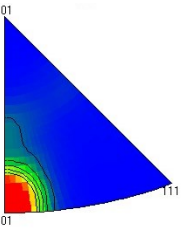
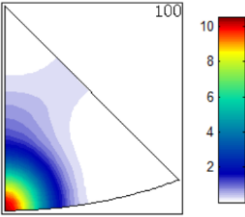


Fig.VI.2 IPF X maps before (0%) and after (12%) plastic deformation at the ambient temperature

The next step for texture modeling is to choose the most suitable parameters for model implementation. In the first order, the impact of the critical angle for grain boundaries (GB) definition, the number of considered grains and the interaction between grains are studied. We are going to compare the results of experiment (before and after deformation) from Table.VI. 2 with the modeling results from Table.VI.4- Table.VI.6.

Table.VI. 2 Grain distribution presented by the means of IPFs for initial and deformed microstructure (experimental data)

HKL (pixels)	HKL (halfwidth=5°)	MTEX (halfwidth=5°)
Initial texture		
		
TI=7.14		TI=6.00
Deformed texture		
		
TI=7.45		TI=6.14

To confirm the best parameters choice, the criteria could be established from the possible variants:

- Texture intensity characterized by Texture Index (TI)
- The distribution of iso-values
- The position of the main poles intensity

The test matrix is presented in Table.VI.3. For the critical angle in grain boundaries definition, the angles of 2°, 3°, 5°, 10° and 15° are taken with the corresponding number of grains on IPF map. For the number of grains, the set of 500, 1000 and 2000 grains are taken with the condition of 5° grain boundaries. And for the interaction between grains, the cases without neighbors (without grain interaction) or 1 and 2 neighbors are studied.

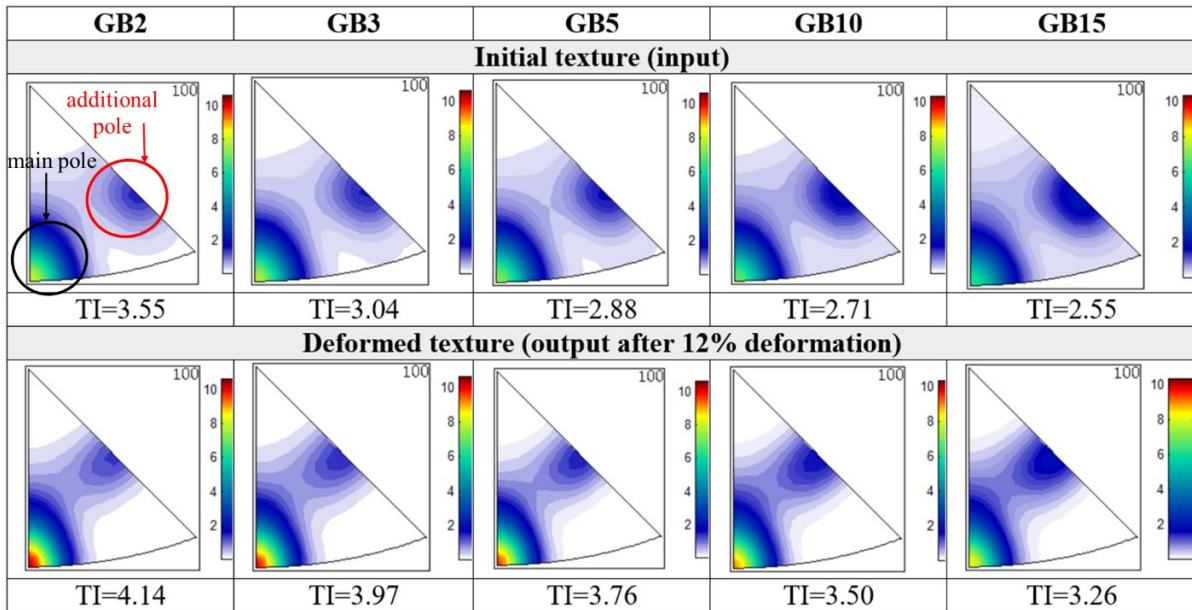
The results are illustrated in the form of inverse pole figures (IPF//RD) and the Texture Index (TI) is specified below.

Table.VI.3 Test matrix for the texture modeling

Input parameter	Values				
	2	3	5	10	15
grain boundaries angle	2	3	5	10	15
grains number	500		1000		2000
homogenization scheme	tangent		affine		secant
active slip system	1		2		3
hardening parameters	with			without	
interaction at the boundaries	with neighbours			without neighbours	

From Table.VI.4, we notice that the input texture (defined by a set of grains orientations taken with a specified critical angles) shows an additional pole (red circle), which was not observed during the experiment. In fact, on Table.VI. 2 the EBSD data is processed as set of pixels representing the whole variety of orientations even intragranular misorientation. For VPSC computation, the structure is represented as a discrete set of crystalline grains. Even, with consideration of grain boundary critical angle or number of grains it is difficult to describe perfectly the true microstructure. Therefore, the slight reinforcement of the main pole (black circle) is associated to this description bias.

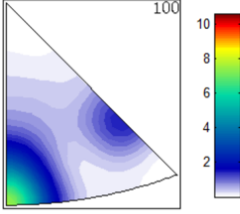
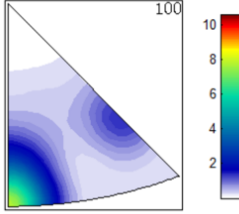
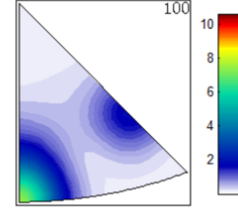
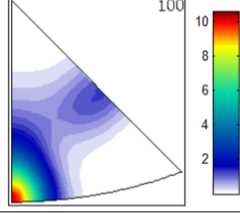
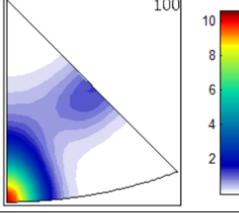
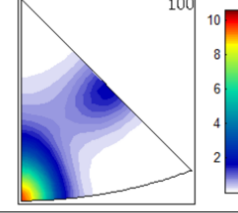
Table.VI.4 Impact of grain boundaries critical angle on texture formation (Secant module, the observed surface is constant)



From this study we conclude that with increasing critical angle of grain boundaries, the texture index value is decreasing. In fact, with increasing critical angle, some areas have to be merged and their new orientation, as a grain, are deviated from the main fibre.

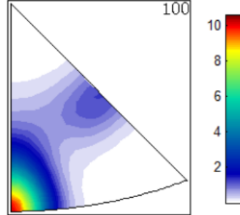
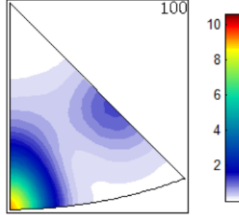
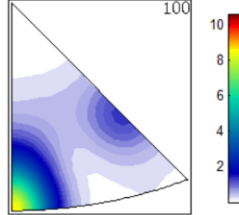
In Table.VI.5 it is showed that the increasing of the grains number used in simulation will increase the number of existing orientation components and this will tend to a reduction in texture intensity.

Table.VI.5 Impact of grains number on texture formation (GB5, Secant module)

500	1000	2000
Initial texture (input)		
 TI=3.26	 TI=3.02	 TI=2.92
Deformed texture (output after 12% deformation)		
 TI=4.33	 TI=4.02	 TI=3.79

The interaction between grains are introduced by the application of neighbours function that couples the reorientation of every grain with the reorientation of neighbours chosen randomly from the discrete texture file during deformation. When neighbouring grains exhibit different reorientation trends, it is expected that they ‘drag’ each other [Tomé et al., 2002]. In result, the grains with the same initial orientation will reorient differently during deformation because each of them will interact with a different neighbour. As it can be seen in Table.VI.6, this coupling is slowing down the evolution of texture during deformation.

Table.VI.6 Impact of neighbours on texture formation (1000 grains, GB5, Secant module)

No neighbours	1 neighbour	2 neighbours
 TI=4.02	 TI=3.48	 TI=3.37

The study on homogenization scheme choice, slip systems activation and hardness parameters was also realized in this work. The next conclusions were made based on this study:

1. The texture evolution is dependent from the choice of the linearization scheme. Texture intensity is increasing in the following order: secant \rightarrow affine \rightarrow tangent $\rightarrow n_{\text{eff}}$.
2. The smaller the number of activated slip systems, the higher is the texture index. The activation of the multiples slip systems leads to a competition (interaction, blocking) between them and retention of the grain to be re-oriented in the fiber direction.
3. The changing in the hardening parameters does not impact the texture evolution, except for the case when the latent hardening is coupled with self-hardening. In this case the texture is decreasing, that could have the same effect than the activated slip systems.

These results allows to study the effect of the model parameters on the texture evolution and the observed dependences will be used in the model construction of the pilgering sequence in the following section.

VI.5. Representative Volume Element for modeling of the pilgering sequence

To model the pilgering sequence, the experimental data is exploited in the code in the form of the initial texture, issued from hot extrusion state (HE) as shown on Fig.VI.3. It is described by 1000 grains (with 5° critical angles for GB) with 3 Euler angles extracted from the EBSD grain file. Three linearization approximations were tested to calculate the localisation tensor. Only one of them will be chosen later on order to obtain the best fit of experimental data. The morphology is assumed equiaxed and therefore no specific file is defined to monitor the grain shape.

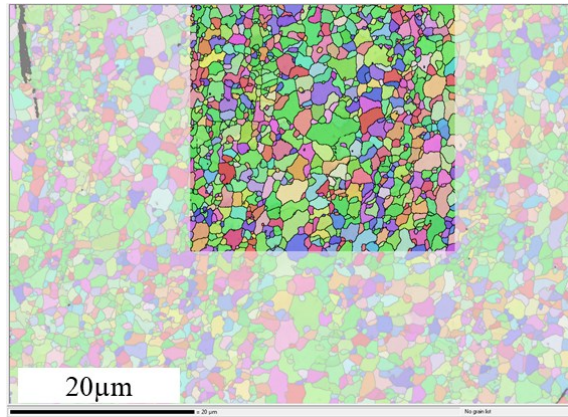


Fig.VI.3 Representative Volume Element taken from HE state for modeling of the pilgering sequence

The deformation mechanisms of BCC materials can be described by 3 main families of slip systems. As there is no dense lattice plane, several slip systems containing $\langle 110 \rangle$ direction can be activated in BCC material. Hardening parameters in Voce law used in simulations are presented in the following expression for each slip system [Tomé et al., 2009]:

$$\tau^s(\Gamma) = \tau_0 + (\tau_1 + \theta_1 \Gamma) \left[1 - \exp\left(\frac{-\theta_1 \Gamma}{\tau_1}\right) \right], \text{ with } \Gamma = \int_0^t \sum_s |\dot{\gamma}^s| dt$$

where Γ is the accumulated shear in the grain; τ_0 , θ_0 , $\theta_1 + (\tau_0 + \tau_1)$ are the initial CRSS, the initial hardening rate, the asymptotic hardening rate and the back-extrapolated CRSS respectively.

The values of threshold stress in Voce hardening law are adjusted to the experimental macroscopic traction curve and shown in Table.VI.7. This strong assumption that identify the crystal law to the experimental aggregate is chosen to avoid more complex iterative identifications of the aggregate itself depending on numerical choices.

Table.VI.7 Voce hardening parameters for 9%Cr ODS steel (MPa)

Slip system	τ_0	τ_1	θ_0	θ_1
$\{110\}\langle 111 \rangle$	405	200	900	2
$\{112\}\langle 111 \rangle$				
$\{123\}\langle 111 \rangle$				

VI.6. VMR modelling

As it was described in [Chapter I](#), the pilgering process is applied in order to simultaneously reduce the diameter and the wall thickness of the tube via incremental rolling sequences. The process consists of several strokes with back-and-forth-moves of the dies (rolls) over the tube and an asymmetric mandrel inside it. At each stroke the tube is rotated around its axis and pushed forward in the dies. Thus, the final deformation history will present a complex loading path which is challenging to identify and simulate.

The calculation of the strain components increments $\Delta\varepsilon_{xx}$, $\Delta\varepsilon_{\theta\theta}$ and $\Delta\varepsilon_{zz}$ proceeds from the tube geometry as the ratio between the initial to final dimensions. The axial and orthoradial strain increments are deduced from [\[Girard et al., 2001\]](#), assuming a constant strain in the thickness and along the circumference of the tube:

$$\Delta\varepsilon_{zz} = -\ln\left(\frac{S_0}{S}\right) \quad \text{and} \quad \Delta\varepsilon_{\theta\theta} = -\ln\left(\frac{D_0}{D}\right)$$

with D – the average tube diameter and S – the tube cross-section (the tube dimensions are given in [Table.II.2, Chapter II](#)). The radial strain increment is deduced by assuming plastic incompressibility:

$$\Delta\varepsilon_{rr} + \Delta\varepsilon_{zz} + \Delta\varepsilon_{\theta\theta} = 0$$

The equivalent plastic strain increment is calculated as: $\Delta\varepsilon_p = \sqrt{\frac{2}{3}(\Delta\varepsilon_{rr}^2 + \Delta\varepsilon_{\theta\theta}^2 + \Delta\varepsilon_{zz}^2)}$

In order to achieve a conditions closer to the real VMR process, a cyclic loading path including an alpha parameter was introduced. This proposed model takes into account the moving position of a material point regarding rolling tools (dies) imposed by the rotative feeding of the tube. This enables to imitate the conditions of pilgering when a material point in the tube is alternatively submitted to the conditions of the Groove Bottom (GB) or the Flange Area (FA) configurations as shown on [Fig.VI.4](#). The proposed loading path applies alternatively two different strain tensors depending on those two positions. In [Table.VI.8](#) the details of this loading path are presented. In a first attempt, the number of cycles N_{cycles} is chosen equal to 8. All shearing components are negligible due to their minor contribution on texture development and also because determination of such shearing is rather complex without available experimental data.

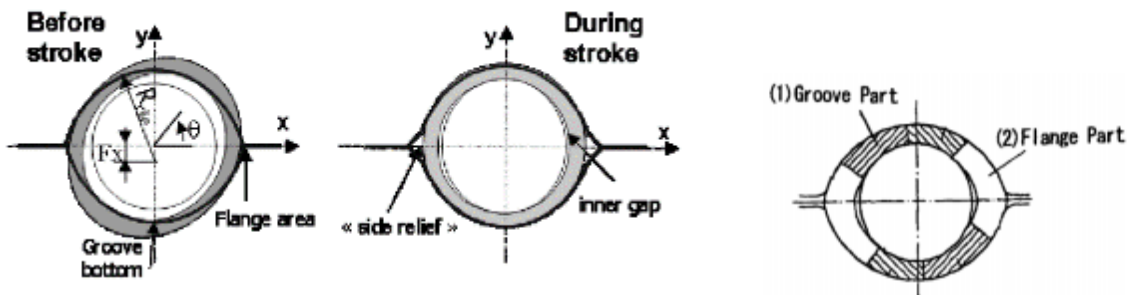


Fig.VI.4 Cross-section of the tube / die / mandrel thin line: mandrel section; thick line: die groove section; grey: section of the tube "transition" [\[Montmitonnet et al., 2002\]](#)

Table.VI.8 Deformation rate between Groove Bottom and Flange Area positions in VMR process

Groove bottom (GB)	$\begin{pmatrix} \frac{\epsilon_{rr} \times (1 + \alpha)}{N_{cycles}} & 0 & 0 \\ 0 & -\frac{\epsilon_{zz}}{N_{cycles}} - \left(\frac{\epsilon_{rr} \times (1 + \alpha)}{N_{cycles}}\right) & 0 \\ 0 & 0 & \frac{\epsilon_{zz}}{N_{cycles}} \end{pmatrix}$
Flange area (FA)	$\begin{pmatrix} \frac{\epsilon_{rr} \times (1 - \alpha)}{N_{cycles}} & 0 & 0 \\ 0 & -\frac{\epsilon_{zz}}{N_{cycles}} - \left(\frac{\epsilon_{rr} \times (1 - \alpha)}{N_{cycles}}\right) & 0 \\ 0 & 0 & \frac{\epsilon_{zz}}{N_{cycles}} \end{pmatrix}$

Thanks to the alpha parameter, the contribution of ϵ_{rr} strain component is alternatively strong and weak depending on the “GB” and “FA” conditions. With alpha equals to 1, ϵ_{rr} is equal 0 in FA conditions. Therefore, only $\epsilon_{\theta\theta}$ and ϵ_{zz} are impacted. When alpha equals 0, ϵ_{rr} and ϵ_{zz} have an equivalent status and the loading path remains monotonic. The increment of axial strain ϵ_{zz} is assumed constant and uniformly distributed between the N cycles. When alpha is greater than 1 a cyclic loading is applied inducing a changing of ϵ_{rr} sign in FA conditions.

In the VPSC7 code, because a large deformation scheme is retained, the loading is specified using the gradient deformation rate. Table.VI.9 presents the introduced values for the case alpha=0.5. The alpha parameter is dependent on pilgering parameters and physically lies between 0.5 and 0.6, according to the simulation results presented in [Montmitonnet, 2007]. However, the real strain distribution is un-known and difficult to be measured on the industrial machine.

Table.VI.9 Deformation rate between Groove Bottom and Flange Area positions with $\alpha=0.5$

Groove bottom (GB)	$\begin{pmatrix} -0.131 & 0 & 0 \\ 0 & 0.006 & 0 \\ 0 & 0 & 0.125 \end{pmatrix}$
Flange area (FA)	$\begin{pmatrix} -0.044 & 0 & 0 \\ 0 & -0.081 & 0 \\ 0 & 0 & 0.125 \end{pmatrix}$
Total = [position1+position2]xN_{cycles}	$\begin{pmatrix} -0.7 & 0 & 0 \\ 0 & -0.3 & 0 \\ 0 & 0 & 1 \end{pmatrix}$

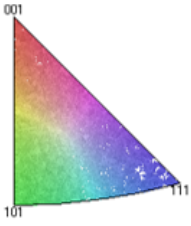
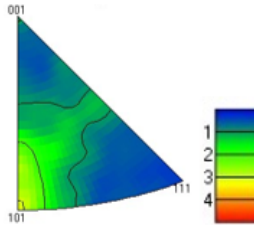
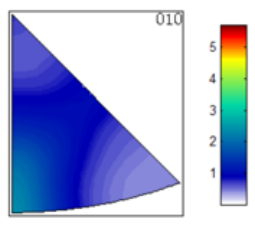
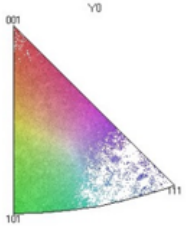
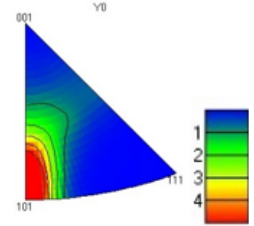
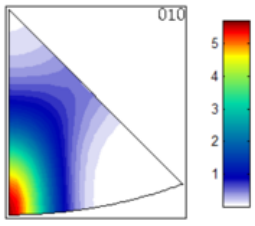
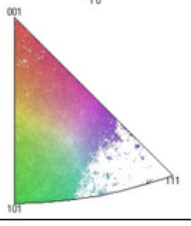
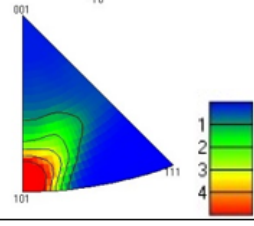
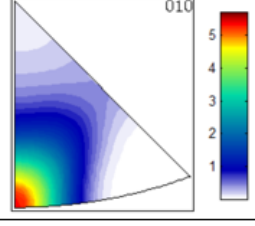
Deformation is simulated imposing successive deformation increments. At each deformation step we impose the boundary conditions velocity gradient components (strain rate) to the aggregate, and calculate the stress and strain-rate in each grain. The shear rates are used to make a forward extrapolation for reorienting the grains (crystallographic texture development), updating the yield stresses in the grains (hardening), and updating the grain shapes (morphologic texture development). The overall (macroscopic) stress and strain tensor components are given by volume averages over the corresponding grain components. Anisotropy of response and properties follows from such averaging procedure over the distribution of orientations.

VI.7. HE-R1-R2 pilgering sequence

VI.7.1. Texture simulation

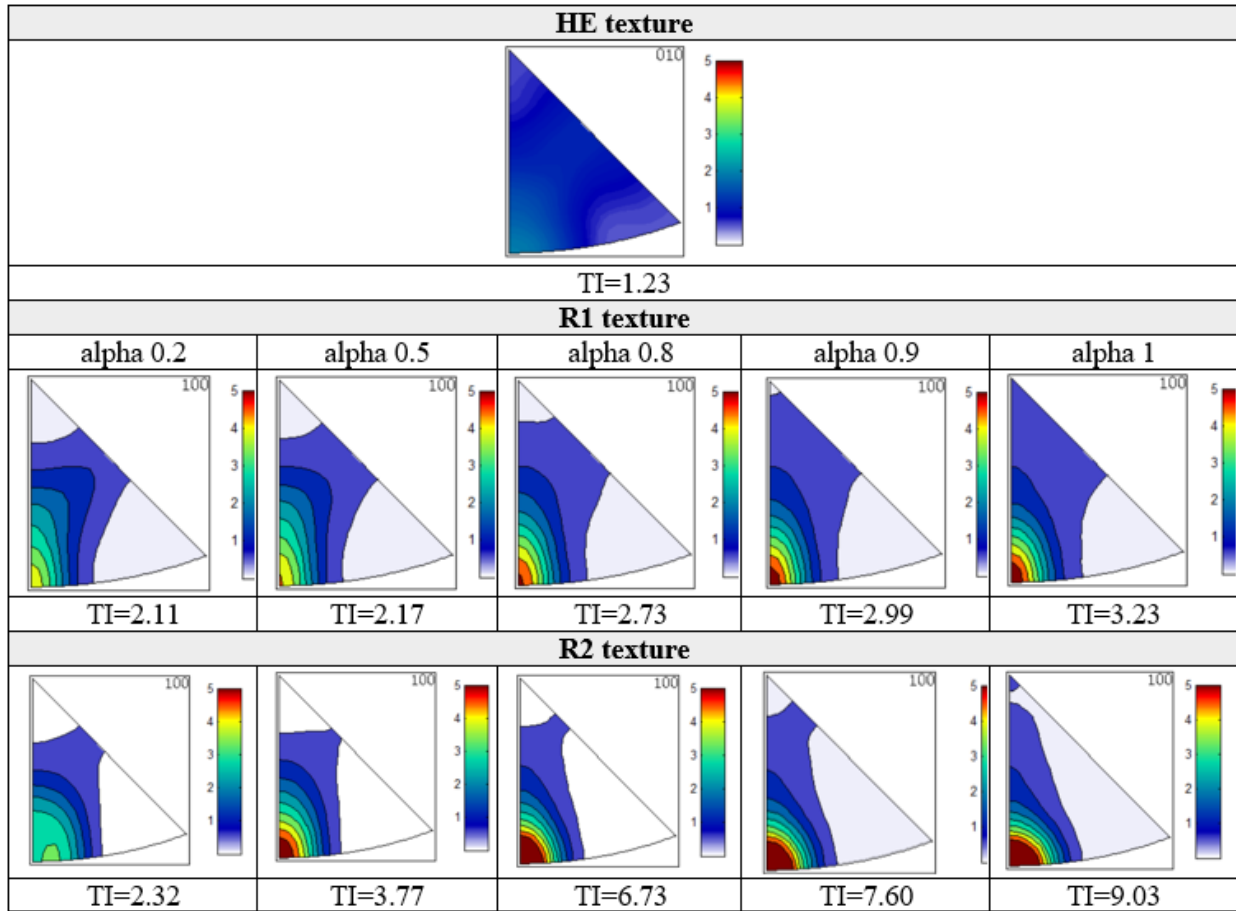
The grains distribution for initial HE and deformed R1 and R2 experimental microstructures are given in Table.VI.10 for further comparison with the results of simulation.

Table.VI.10 Grain distribution presented by the means of IPFs Y//RD for initial and deformed experimental microstructure

HKL pixels	HKL halfwidth=5°	MTEX halfwidth=5°
HE texture		
		
	TI=1.43	TI=1.40
R1 texture		
		
	TI=2.93	TI=2.80
R2 texture		
		
	TI=3.79	TI=3.42

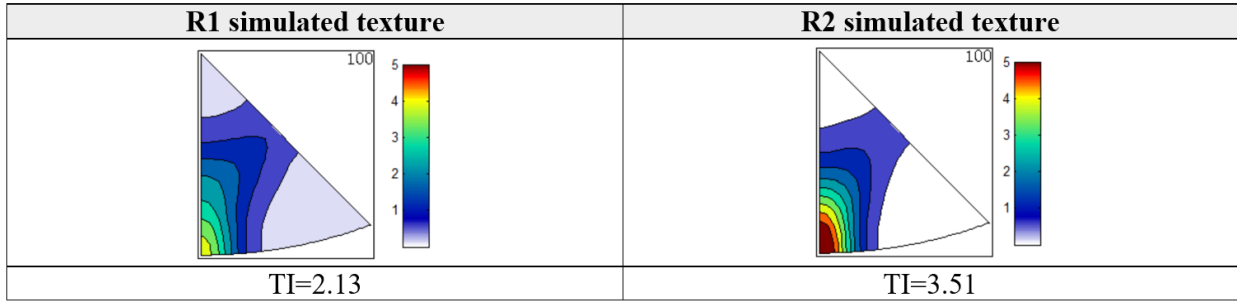
Simulated IPFs with cyclic loading is presented in [Table.VI.11](#), where the alpha parameter is varied in the range [0.2; 1]. The rest of parameters are taken as following: 1000 grains, GB5, 1 neighbour, secant module. The texture intensity tends to increase when the alpha values increase, finally resulting in a hyper-texturized state. A comparison of experimental and simulated IPFs allows to find the conditions closest to the actual VMR process with alpha parameter equal to 0.5. This value represents more an alternative loading than cyclic one.

[Table.VI.11](#) Simulated IPFs for the initial sample HE and deformed R1 and R2 with the cyclic loading path



For the comparison, the test with applied monotonic loading is presented in [Table.VI.12](#). These simulations presents a continuous increase of the deformation that obviously cannot characterize the real pilgering process, but it can be used as a simple model which has a good convergence and is less time consuming.

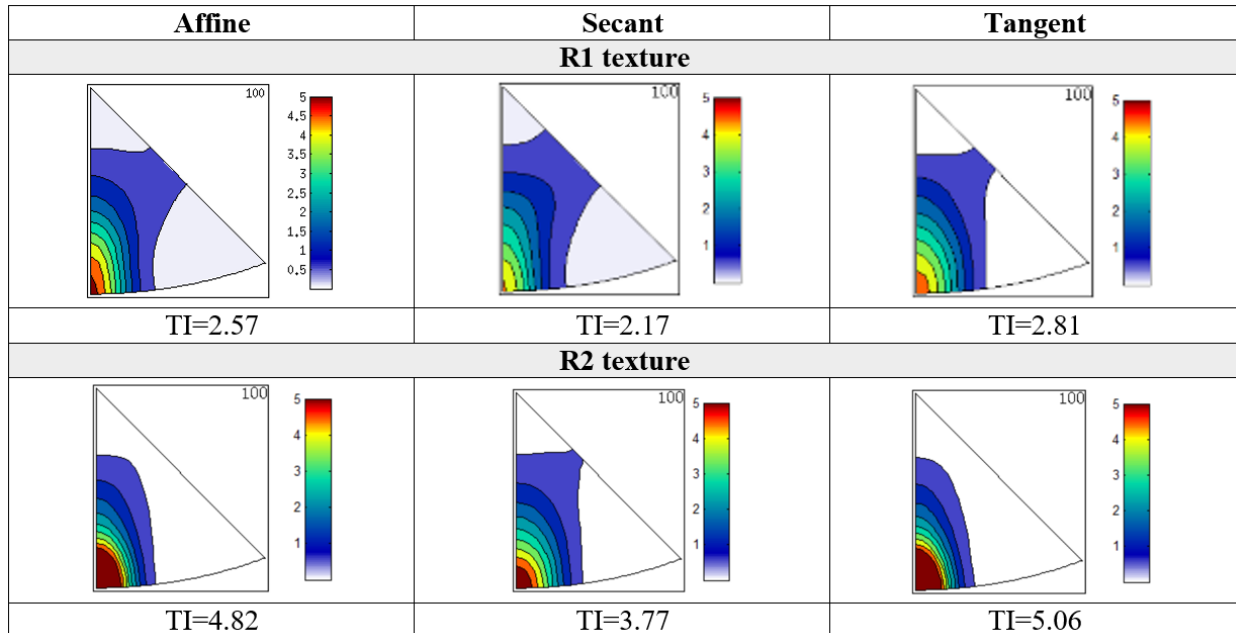
Table.VI.12 Simulated IPFs for deformed R1 and R2 with applied monotonic loading (corresponding to $\alpha=0$)



The comparison of the experimental and simulated IPFs shows that various types of loading path enables to predict the alpha-fibre formation. However, fibre intensity is not at the same level for each simulations. For instance, the main pole presented $\langle 110 \rangle$ is less pronounced for a monotonic loading path than the experimental one, while the cyclic path has a similar pole representation and texture indexes.

To conclude the study on the texture prediction, three linearization schemes were investigated: secant, tangent and affine. The results of simulated IPFs are given in Table.VI.13. As it can be seen the affine and tangent modules increase the texture intensity compared to the secant one. In this case the alpha parameter could be re-identified according to the chosen linearization scheme.

Table.VI.13 Simulated IPFs for deformed R1 and R2 with the cyclic loading path ($\alpha=0.5$) and different linearization schemes (1 neighbour)



VI.7.2. Mechanical anisotropy prediction

The VPSC model is also a good tool to predict the anisotropy of mechanical properties. After simulation of a VMR forming sequence, the obtained grains set, taking into account orientation and morphology is used to simulate a uniaxial tensile test in two different directions, collinear (RD) and normal (TD) to the VMR rolling direction. These two computations highlight the mechanical anisotropy induced by the crystallographic and morphologic texture evolution during rolling. The tensile curves in the rolling and tangential direction are plotted on Fig.VI.5 for various linearization scheme.

For all schemes, the rolling direction (solid line) is stronger than the tangential one (dashed line). Those data can be compared to the experimental data resulting from rings and tiles testing (Fig.VI.6).

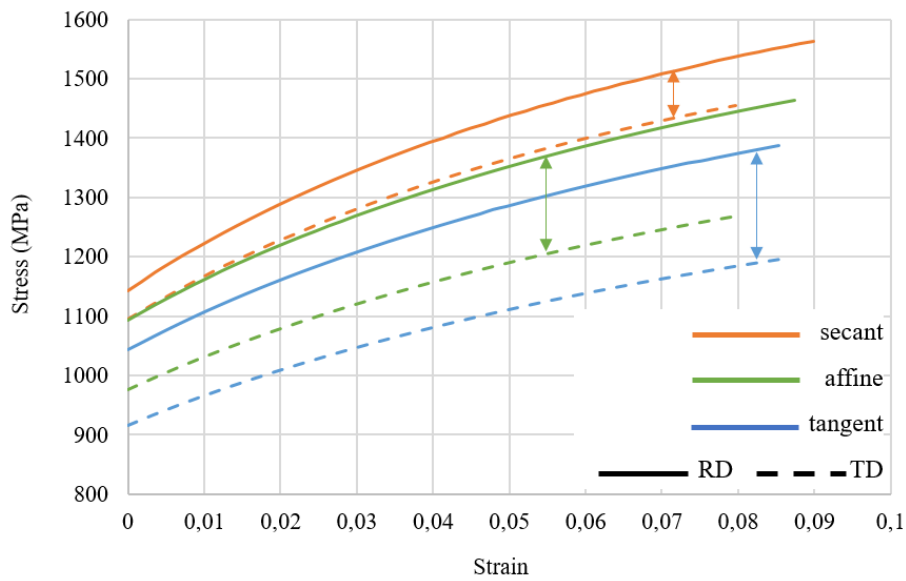


Fig.VI.5 Simulated stress-strain curve for R2 sample with affine, secant and tangent linearization schemes

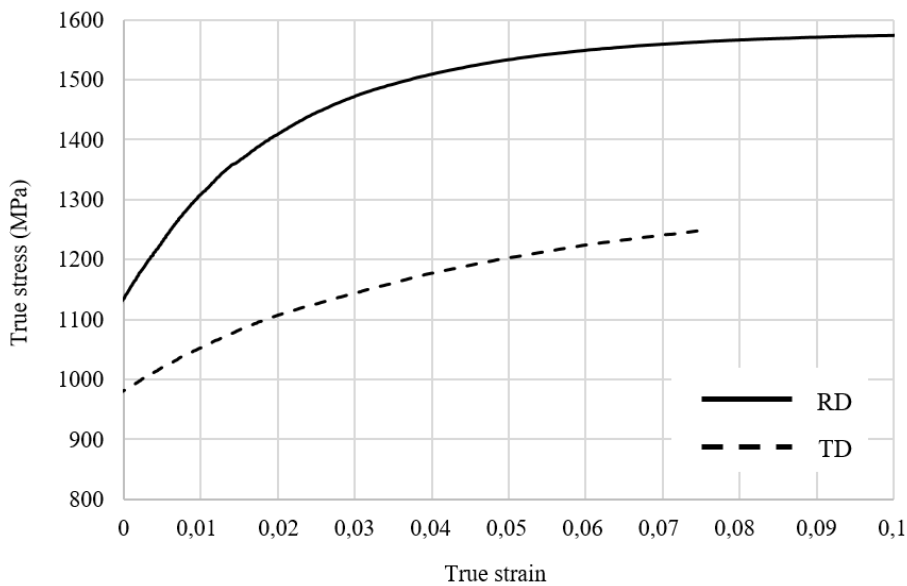


Fig.VI.6 Experimental stress-strain curve for R2 sample in cold-rolled state (strain rate 10^{-2} s^{-1})

It can be concluded, in accordance with the work of [Steckmeyer, 2012], that the experimentally observed anisotropy cannot be explained exclusively by the crystalline and morphological anisotropies.

For this purpose the tangent modulus is there the better way to introduce this mechanical anisotropy [Lebensohn and Tomé, 1993; Eyckens et al., 2012]. Accordingly to this simulation crystallographic anisotropy contributes significantly to the total anisotropy observed.

Contribution of precipitation to anisotropic damage is not taken into account by VPSC modelling. A thorough analysis of the sensitivity of Voce's law parameters should also improve this correlation.

VI.8. Conclusions for Chapter VI

Obtained experimental results allowed to simulate a polycrystalline aggregate with an initial structure derived from the EBSD observations. A representative cyclic loading of industrial rolling VMR was applied to simulate the production sequence. A study of parameters sensitivity was carried out, fitting to the experimental results. The proposed model correctly predicts the evolution of texture due to large plastic deformation if considering a large grain set and rather small grain boundary critical angle.

For a given initial microstructure, the choice of the description parameter of this microstructure may have a critical impact on the overall texture index and the various poles respective intensity. This bias effect of the microstructure description in terms of grains weighted by a volume fraction will still persist whatever the model retained (FEM or FFT).

Mechanical anisotropy between the rolling and tangential directions is semi-qualitatively well predicted but the linearization scheme used for texture simulation is rather poor for this application.

In perspectives, it would be interesting to realize the same study of texture development using FFT and/or FEM models since they can give some advantages in comparison with VPSC model:

- In both cases the stress field is computed and continuously described on the aggregate (and is not constant within a grain, as it should be with a non-linear behaviour)
- This stress field takes by itself into account the grain interactions and grain boundary accommodations. This “true” neighbour grains interaction is a key interest of those simulations.
- Grains behaviour can be discretized as much as needed. For a single crystalline law a large number of voxel can discretize the grain and allows to capture boundary accommodation.
- If process simulation is envisaged, the FFT low cost algorithm can be envisaged to determine material constitutive behaviour at each integration points of a Finite Elements Model.

General Conclusions and Perspectives

For this project the microstructural and mechanical evolution of 9%Cr ODS tubes, manufactured under industrial conditions, were investigated. The tubes were produced by hot extrusion from powder materials to form a seamless tube. Then the tubes were cold pilgered by Mannesmann (VMR) technique. Two processing routes were tested in order to determine the optimal scheme to produce the final product. For the first route, the tubes from Hot Extruded state undergo the first pilgering step R1 and then directly the second pilgering step R2. The second route, in its turn, includes an intermediate heat treatment between R1 and R2 rolling steps. Final heat treatments were applied for the both schemes. It should be noted that heat treatments conditions were based on the recommendations developed in the work of [Toualbi, 2012] on the 9%Cr cold pilgered tubes by laboratory HPTR technique. In this work it was demonstrated that phase transformation $\alpha \rightarrow \gamma \rightarrow \alpha$ enables to restore the anisotropic structure, introduced by pilgering, to isotropic one and to obtain a material with relatively high ductility that is beneficial for further deformation steps.

The evolution of microstructure, crystallographic texture and mechanical properties of industrially produced 9%Cr ODS tubes are studied at each processing step. It was necessary to understand the influence of a strong deformation on the microstructure evolution and the transformation kinetics in order to show the feasibility of the industrial production scheme and to ensure the reliability of obtained tubes in service conditions.

The key results of this study can be summarized in the following way:

- All pilgered samples present elongated grains shape with the size of 0.2 μm -0.5 μm and show a strong texture formation with a preferential α -fiber orientation along the rolling direction. The applied **heat treatment** restores the grain shape to almost equiaxed grains. However, texture intensity is unexpectedly increased and only the **α -fiber** orientation along the rolling direction is preserved. Thus, the textures of heat-treated samples in this study differ from the ODS steel produced by HPTR technology, where the material is almost recovered in term of morphology and grain orientation.
- It was supposed that the remarkable temperature stability of α -fiber is attributed to a **texture memory effect** during phase transformations, when the daughter grains inherited the texture of the parent grains. To understand this phenomenon, texture evolution was analyzed during phase transformation process following a heating-cooling path. The in-situ heat treatment experiment was realized using **synchrotron X-ray diffraction** that allowed to quantify both phase transformation kinetic and crystallographic texture of phases. A **texture** memory effect was observed during ferrite formation particularly at a **slow cooling rate**. **Quenching** after heat treatment **reduced** the crystallographic texture and thus reduced the texture memory effect. Also, by in-situ analysis it was discovered that the austenite texture was stable at 1050°C without any indication of recrystallization.

- Comparing R1 and R2 states, a crucial role of initial microstructure in the occurrence and intensity of the texture memory effect was demonstrated. **The higher the cold work strain, the higher is the texture index after heat treatment.** It can explain the difference of textures observed between highly deformed materials obtained by Mannesmann pilgering conditions and HPTR ones. This also explains why the texture memory effect does not appear in the laboratory produced tubes.
- To explore the mechanism of inherited texture in ODS steel, the transformation texture prediction with a variant selection model based on Double K-S relation (DKS) was carried out. In this model, developed by T. Tomida, the variants having K-S ($\{111\}_\gamma // \{011\}_\alpha$; $\langle 101 \rangle_\gamma // \langle 101 \rangle_\alpha$) or near K-S relations with two or more neighboring parent grains at the same time are preferentially selected.

According to the modelling results, the texture of parent γ grains can be reconstructed using the harmonic expansion method based on KS relation without variant selection, indicating that the **nucleation of austenite** probably does not occur on ferrite grain boundaries but more likely inside the grains in the **highly deformed matrix**.

During cooling, for the **diffusive transformation of ferrite**, the DKS model with a very large ω parameter value has reproduced most of the characters of the strong $\langle 110 \rangle // RD$ fiber and texture memory. This ω parameter determines the strength of the variant selection by DKS and depends on material microstructure. But the peak intensity could not be completely reproduced. It suggests that the strong $\langle 110 \rangle$ fiber texture developed during slow cooling should originate from an enhanced DKS mechanism. Finally, it was suggested that the model should be extended, where the nuclei of ferrite with the better-fulfilling DKS will nucleate earlier on austenite grain boundaries and grows faster over multiple austenite grains consuming other DKS nucleation (combination of selective nucleation and growth).

In the case of **displacive transformation**, the variant selection model with DKS predicts well the martensite texture with a relatively large ω parameter value. The slight texture of martensite is probably caused by a small amount of ferrite nucleated firstly on austenite grain boundaries with DKS, governing the further orientation of martensite.

- To understand the mechanism determining the texture increase during ferrite formation in highly deformed material, a set of experiences were realized studying the influence of the heat treatment parameters on microstructure.

The analysis of texture indexes and grains size exhibits that the texture fiber enhancement is probably related to the **fast growth** of a limited number of **ferrite nucleus with preferential orientations**. This assumption is confirmed by observation of few very big ferritic grains during low temperature inter-critical heat treatment (between A_{c1} and A_{c3}). Those grains confirm the existence of very few ferrite nuclei appeared on the cooling step and their relative fast growing at the beginning of ferritic transformation. Those nuclei should have an orientation relation with the previous austenitic grains and it explains the sharp alpha fiber inherited texture. The **higher the treatment temperature and the longer the holding time, the higher is the texture index**. This phenomenon is assumed to be related to the austenitic grain growth that promotes fast growing of ferrite nuclei. At the same time, phase transformation kinetic has been shown to be weakly dependent on the heating rate.

In addition, by isothermal tests (*interrupted quenching from γ domain down to a holding temperature lower than A_{c1} , but higher than M_s*) it was observed that ferrite formation temperature (in the case of ODS about 700°C) will strongly determine the morphological and crystallographic texture evolutions. In the case of higher overcooling at the temperatures **lower than 700°C**, atoms diffusion is very weak, **nucleation** happens with a high **frequency** associated to a **slow growth** of nuclei. The nucleation is initiated at the gamma grains boundaries. Since there is a **higher number of new germs**, more crystallographic orientations will appear and a **less intense texture** will be measured at the end. In the case of lower overcooling at the temperatures **higher than 700°C**, the diffusion is promoting nuclei **growing** to the detriment of new germs nucleation. This time the nucleation is probably initiated at the triple point of gamma grains promoting variant selection. Thus a **selective germination and growth** of these few nuclei induces a **high texture** index and bigger grains. These results confirm the study of [Lambard, 1998] on ODS EM10 grades, complementing the data on texture evolution.

In any case, the Ti oxides precipitation seems unaffected by the treatments and tends to pin the austenitic grain growth during the transformation. This promotes phase transformation inside the columnar structure defined by Prior Particles Boundaries. Chromium carbides ($M_{23}C_6$) are completely dissolved at 1050°C but still anchor the austenitic grain growth during inter-critical short heat treatments.

- The mechanical properties of the tubes were characterized in cold-rolled and heat treated state. The **as-rolled state** presents extremely high values of mechanical resistance ($R_m=1600\text{ MPa}$ in RD), but at the same time high fragility ($A_{tot}=8\%$). It is also characterized by a high level of anisotropy and makes it obvious the necessity of intermediate heat treatment between the rolling passes to avoid cracking of the material during deformations. In addition the heat treatment demonstrates the decrease of internal stresses introduced by cold working,

Intermediate heat treatment with a slow cooling is recommended at this stage, as it allows to obtain a ductile material which can be easily formed ($R_m=800\text{ MPa}$, $HVI<300$), despite its anisotropy brought by the texture memory effect ($A_{tot}=20\%$ in RD via $A_{tot}=11\%$ in TD). Other modes of intermediate heat treatment can be proposed (for instance, isothermal ferrite formation at 650°C (Fig.V.6) or double step heat treatment(Fig.V.7)), that allow to keep a ferritic structure with a good ductility, but with more isotropic properties

For **final heat treatment** it is necessary to apply a fast cooling, to restore the texture and obtain an isotropic structure; the structure of tempered martensite shows a good compromise between mechanical resistance and ductility.

- Experimental and simulation results were used to characterize the performance of the Mannesmann cold rolling process for the industrial production of ODS steel tubes. A VPSC modeling of pilgering was built and it shows an accurate prediction of the texture evolution due to plastic deformation. This modeling also shows that the mechanical anisotropy depends significantly on the texture and morphological anisotropy generated by pilgering. By this modeling, the understanding of the deformation processes at various scales allows to link microstructure, process and mechanical properties, which will contribute to the optimization of manufacturing sequences.

This work, by a precise analysis of microstructural and mechanical evolutions during Mannesmann pilgering forming, gives fundamental data for further development of ODS steels cold forming sequences. The discovery of an unexpected texture heritage phenomenon during heat treatments highlight the singular effect of nano-phases in the phase transition of ODS 9%Cr stainless steels.

In **perspectives** of this project the following actions can be proposed:

Perspectives for **experimental** observations

- The production route including intermediate heat treatment is recommended as an optimal scheme for industrial tube manufacturing. The mechanical properties of treated tubes with tempered martensite microstructures R2(HT) TM were studied by traction tests at ambient temperature. Thereafter, the behavior of R2(HT) TM tube should be studied with **traction** at high temperatures and also with **creep** tests to confirm the resistance of material in the service conditions.
- The first data about particles size and distributions were obtained using TEM. However, due to the high lattice distortion the obtained signal was very poor. An analysis with more accurately techniques, for instance SAXS or SANS, can be useful for measurements of **particles** size, their evolution on size and chemical composition at different production steps. Moreover, the study on the relation between the orientation of particles and ferrite/austenite matrix can elucidate the origin of variant selection mechanism.
- In this project the hypothesis of selective nucleation and growth during ferrite formation was proposed. To observe the **nucleation** sites and the grain **growth** during phase transition, *in-situ* **SEM heating tests** could be realized in future.
- The first attempt on deformation mechanism study was done by *in-situ* **EBSD traction** tests. It was mentioned that for the strain map construction the adapted grid should be used. The new campaign of tests, ideally for the HE sample, will allow to identify the deformation mechanism and optimize the simulation inputs.

Perspectives for **numerical** studies

- Gamma grains reconstruction was realized in ARPEG software based on the KS orientation relations between martensite and austenite phases. However, some irregularities were observed on the grain boarder lines and martensite orientations distribution. The reconstruction of these structures by **DKS** approach, used for prediction of transformation texture, can be prospective for the following study.
- By now, the VPSC code was used for simulation of pilgering sequence, excluding the heat treatment state. The coupling of VPSC code with DKS approach is proposed to model the whole production scheme.
- VPSC modeling showed a valuable results on texture prediction during cold pilgering process. The application of FFT and/or FEM simulation of aggregates could be realized to compare the accuracy of existing models and try to better describe grain interaction and intragranular stress/strain fields.

Résumé en français

L'énergie nucléaire représente actuellement une part significative de la production électrique. De nombreux pays envisagent une augmentation de leurs capacités de production nucléaire en prenant en compte la réduction des coûts de production et l'objectif d'une sûreté accrue. Les études de matériaux nucléaires se focalisent sur des matériaux capables d'endurer de très forts chargements thermomécaniques sous forte irradiation neutronique. De nombreux programmes internationaux tendent à développer des matériaux de construction pour les réacteurs innovants [ESNII, 2010]. Certains de ces programmes visent à trouver et qualifier de matériaux compatibles avec les conditions d'exploitation de la future génération (GEN IV) de réacteur de fission. Plus spécifiquement, les réacteurs rapides refroidis au sodium (RNR Na) particulièrement soutenus par le Commissariat à l'Énergie Atomique et aux Énergies Alternatives (CEA), suppose une forte augmentation de la résistance à l'irradiation pour des températures bien plus élevées que les réacteurs actuels. Ces conditions sévères et très particulières supposent des matériaux dédiés à ces applications. Les recherches de Kimura & al [Kimura, 2005] montre que les aciers inoxydables ferrite-martensitique ODS sont de bon candidats pour le matériau de gainage combustible des RNR Na. En effet, ils se caractérisent par un faible gonflement sous irradiation et une bonne résistance sous sollicitation de fluage et de corrosion. Ces avantages sont à considérer en regard des meilleurs aciers inoxydables austénitiques (15-15Ti AIM1) qui supportent de plus faibles doses d'irradiation. Il est envisagé d'utiliser les aciers ODS pour des doses de 100 à 200 DPA et des températures maximales de l'ordre de 650°C [Kaito *et al.*, 2003].

Un programme d'étude des aciers ODS ferritiques-martensitiques est actuellement porté par le CEA. Une attention particulière est portée au développement des procédés de fabrication des matériaux et à la détermination de leur comportement sous contraintes thermiques, d'irradiation, mécanique et de corrosion. En raison de sa structure cristalline spécifique et de la présence de nano-renforts d'oxydes d'yttrium, ce matériau présente des performances élevées dans l'application industrielle.

Ce projet vise à déterminer les propriétés métallurgiques et mécaniques des tubes de gainage en acier ODS, envisagés pour l'assemblage de combustible du cœur de réacteur. Leur procédé de fabrication comprend une étape de mécanosynthèse à l'état pulvérulent (attrition de poudre) suivi d'une extrusion à chaud de semi-produits et de laminage à froid. Pour ce projet, la première série de tubes ODS français a été produite par la technologie Vertikaler Massenausgleich Ringwalzei (VMR) de Mannesmann. Durant le processus de laminage VMR, une forte déformation plastique (de l'ordre de plusieurs centaines de pourcents) est appliquée au matériau. Il est donc proposé d'étudier, en détail, les propriétés physiques et mécaniques des tubes ayant subi des taux de déformation élevés et différents traitements thermiques.

Le but final de l'étude étant démontrer la faisabilité de la fabrication industrielle de tubes en acier ODS et de contribuer à l'effort de simulation numérique des procédés. Il en découle plusieurs voies d'optimisation des processus, en prenant notamment en compte le risque de dégradation des propriétés mécaniques et la possibilité de réduire le coût total de production en minimisant le nombre de passes de laminage et la durée des traitements thermiques.

Matériaux et procédures

Le développement de matériaux ODS nécessite un contrôle précis à chaque étape du processus de fabrication pour obtenir la microstructure attendue. La gamme de production de tube en acier ODS est illustrée en [Fig.R.1](#) et elle comprend :

- L'atomisation de la nuance pré-alliée sous atmosphère d'argon
- Le broyage de la poudre d'alliage avec celle d'oxydes
- La consolidation du matériau à haute température par extrusion ou pressage isostatique à chaud
- Le laminage à froid en plusieurs passes jusqu'à obtention des dimensions souhaitées

L'opération de laminage est utilisée pour modifier la géométrie du tube par déformation plastique, où le diamètre et l'épaisseur du tube sont simultanément réduits. Les passes de laminage induisent une augmentation de la dureté, il est donc recommandé d'appliquer une opération de recuit pour restaurer le matériau et éviter les risques d'endommagement.

Les tubes caractérisés dans cette étude ont été produits par extrusion à chaud par CEFIVAL. La poudre métallique pré-alliée Fe-Cr-W-Ni atomisée par AUBERT & DUVAL a été broyée avec de la poudre (0,25wt% Y_2O_3 + 0,3wt% TiH_2) sous atmosphère protectrice d'hydrogène par PLANSEE. La taille moyenne des particules de poudre obtenue était d'environ 80 μm . La poudre broyée a été introduite dans une gaine en acier inoxydable ferritique AISI430. Après une étape de dégazage (2 heures à 400°C), la poudre a été chauffée à la température de 1100°C pendant 2 heures et extrudée à chaud pour former un tube sans soudure.

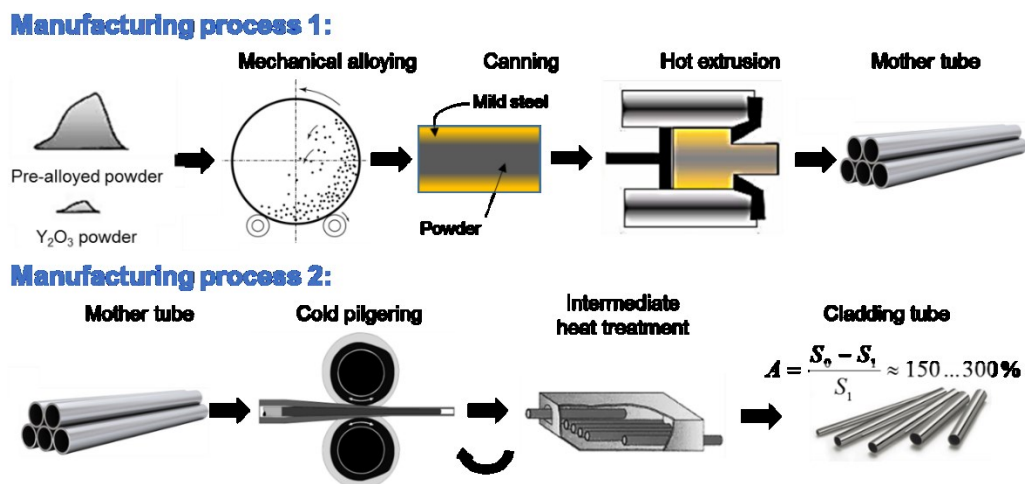


Fig.R.1 Chaîne de production de tubes en acier ODS par extrusion à chaud et laminage à froid, [Inoue et al, 2007]

Le laminage a été réalisé par VALINOX-NUCLEAIRE dans le cadre du projet ANR STRATOTUBE. La fabrication de tubes est réalisée en 2 étapes de laminage. Sur la Fig.R.2, deux schémas de fabrication sont présentées.

- Pour le premier, l'extrusion à chaud (HE) est suivie directement par les 2 passes de laminage R1 et R2 et terminer par un traitement thermique final R2 FHT.
- Pour le deuxième, un traitement thermique intermédiaire (IHT) opéré sous atmosphère d'Ar est effectué entre les 2 passes de laminages.

Cette étude porte sur des aciers ODS ferritiques à 9% de Cr dont la composition chimique est donnée dans le Tableau.R.1. Cette nuance présente une transformation de phase ferrite-austénite ($\alpha \rightarrow \gamma$) à haute température, présentée sur la Fig.R.3.

Tableau.R.1 Composition chimique des aciers ODS à 9% Cr (pourcentage massique)

Cr	W	Ti	Ni	O	Y	C	Fe
9	0.9	0.2	0.2	0.1	0.1	0.08	Balance

Les deux méthodes se terminent par le même traitement thermique. Il est réalisé sous vide à 5.10^{-2} mbar sur de petites sections. Les dimensions du tube après extrusion à chaud, la première et la seconde passe de laminage sont données dans le Tableau.R.2. Le tenseur de déformation générée lors de chaque étape de laminage est obtenu à partir des évolutions dimensionnelles des tubes laminés. Selon [Abe et al., 2012], la déformation et le facteur Q (c'est-à-dire le rapport entre la réduction d'épaisseur et la réduction de diamètre externe) sont estimés pour chaque étape de déformation. Bien que le laminage à froid puisse introduire une composante de cisaillement significative [Girard et al., 2001], il est négligé dans ce travail.

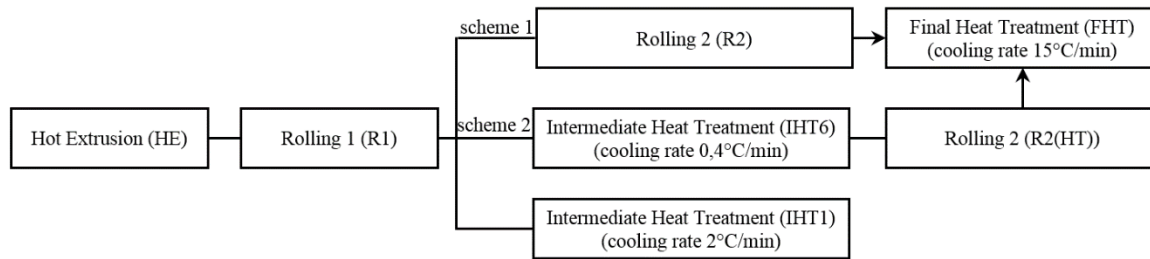


Fig.R.2 Les deux schémas de fabrication des tubes en acier ODS

La restauration par transformation de phase dans le domaine $\alpha + \gamma$ réduit à la fois la dureté et les contraintes résiduelles accumulées lors de la déformation. Deux types de traitement thermique dans un four de laboratoire ont été appliqués aux échantillons R1 afin d'étudier l'influence des conditions de traitement thermique sur la microstructure de l'acier ODS. Les échantillons ont été chauffés sous vide jusqu'à 1050°C avec une vitesse de chauffage de 15°C/min et un temps de maintien de 20 min. Ensuite, les tubes sont soumis à 2 vitesses de refroidissement différentes : une de référence à environ 2°C/min (IHT1) et une seconde qui imite les conditions industrielles à 0,4°C/min (IHT6). Ainsi, le temps de traitement thermique est presque 5 fois plus long dans le cas du traitement industriel. Pour le traitement final, les deux tubes R2 et R2 (HT) ont été exposés à la même vitesse de refroidissement de 15°C/min.

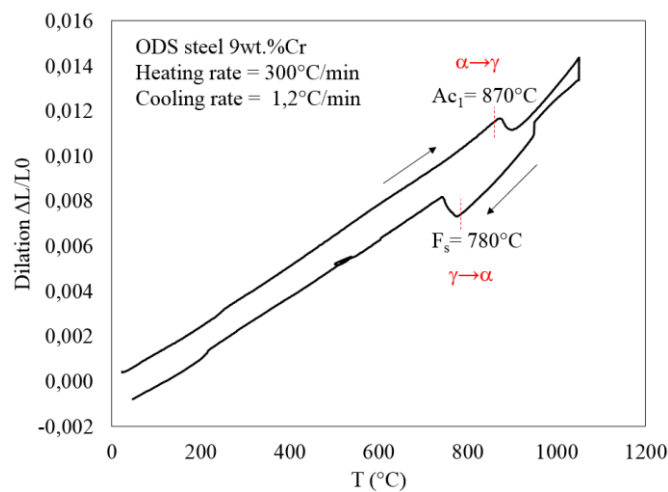


Fig.R.3 Courbe de dilatation de la transformation de phase ferrite austénite pour les aciers ODS à 9% Cr

Tableau.R.2 Evolution de la dimension des tubes pendant le procédé de fabrication (inclus le revêtement en acier AISI430)

Etape	Diamètre (mm)	Epaisseur (mm)	Allongement (%)	Déformation totale ϵ_p (%)	Q facteur
HE	44,3	7,86	-/-	-/-	-/-
R1	28,3	3,98	300	110	1,4
R2	17,6	1,55	385	140	1,6

L'évolution de la microstructure, de la texture cristallographique et des propriétés mécaniques des tubes ODS est étudiée à chaque étape du traitement. Cela nous a permis de comprendre l'influence de l'augmentation du taux de déformation pendant les étapes de laminage sur l'évolution de la microstructure et la cinétique de transformation. Ces éléments étant cruciaux pour assurer la faisabilité de la production industrielle et la fiabilité des tubes obtenus en conditions de service.

Plusieurs techniques expérimentales ont été utilisées pour caractériser la microstructure des tubes ODS à différentes échelles. En commençant par l'étude de nano-précipité au MET et en finissant par des essais en traction pour les propriétés mécaniques macroscopiques. Le MEB, couplé à l'EBSD, et la technique de diffraction des rayons X permettent de suivre les évolutions microstructurales à chaque étape de la production. Les techniques de dilatométrie et de diffraction des rayons X au synchrotron sont complémentaires dans l'étude des transformations de phase des aciers ODS laminés à froid.

L'influence des étapes de laminage sur la microstructure des tubes ODS

Toutes les étapes sont obtenues à partir d'un matériau extrudé à chaud (HE). La structure initiale extrudée à chaud, présentée sur la Fig.R.4, est caractérisée par des grains légèrement allongés avec une isotropie morphologique et sans orientation cristallographique préférentielle. La taille moyenne des grains est de 800 nm.

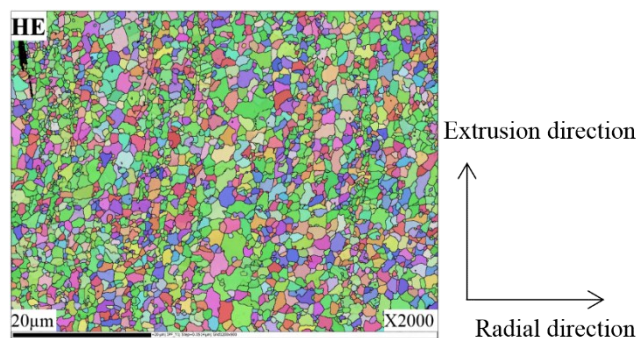


Fig.R.4 Cartographie EBSD d'un échantillon 9% Cr ODS extrudé à chaud

La Fig.R.5 montre des cartographies EBSD des tubes aux différentes étapes du processus de laminage et des traitements thermiques. Ces cartes sont issues de section prélevée dans le sens du laminage. Après la première passe de laminage (R1), les grains présentent des formes allongées avec une texture préférentielle de fibres alpha, parallèles à la direction de laminage. Pendant le traitement thermique intermédiaire (IHT1), la morphologie est transformée en grains presque équiaxes et présentant toujours une intensité de texture élevée. La deuxième étape de laminage (R2 et R2(HT)) retransforme à nouveau la microstructure en grains allongés, jusqu'au traitement thermique final (FHT) qui crée un matériau fortement texturé constitué de grains équiaxes.

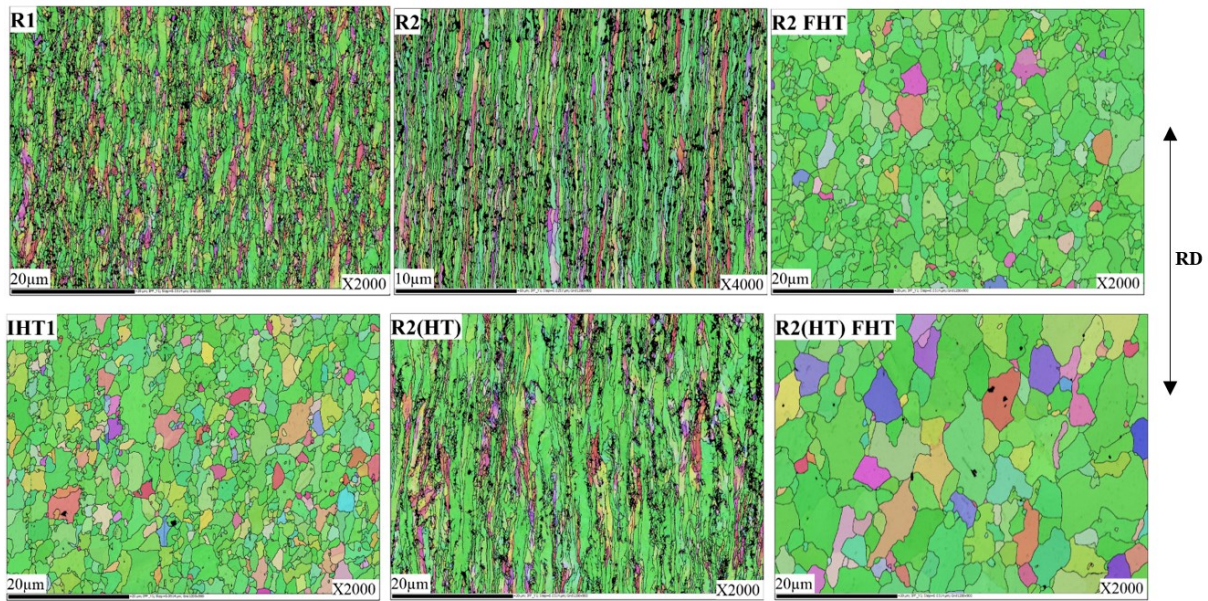


Fig.R.5 Cartographies EBSD avec le réseau des joints de grains à chaque étape de laminage des tubes ODS (cartographies dans le plan formé par la direction de laminage et la direction transversale)

Il est observé une augmentation inattendue de l'intensité de la texture après le traitement thermique des échantillons laminés. Les valeurs de l'index de texture sont données sur la Fig.R.6. Ainsi, la texture des échantillons traités thermiquement dans cette étude diffère de l'acier ODS mis en forme par laminage HPTR en laboratoire [Toualbi, 2012], où le matériau subit uniquement de 20 à 25% de déformation plastique par étape de laminage. Ce faible niveau de déformation permet au matériau de retrouver sa texture et sa morphologie granulaire initiale après le traitement thermique.

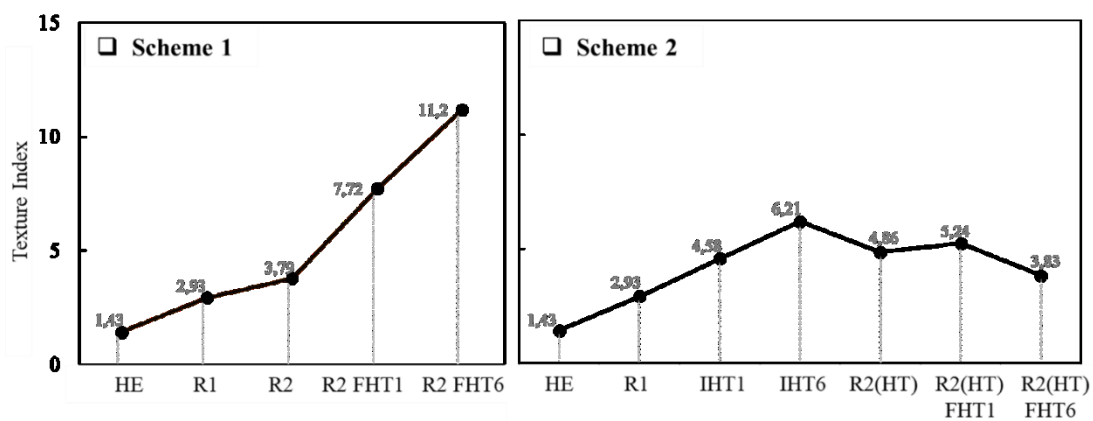


Fig.R.6 Evolution de l'index de texture pendant les étapes de fabrication des tubes ODS

Changement de phase et effet de la mémoire de la texture dans des tubes ODS laminés

Il est supposé que la stabilité remarquable en température de la fibre α est attribuée à un effet de mémoire de la texture lors des transformations de phase, lorsque la phase-fille hérite de la texture des grains de la phase-mère. Pour comprendre ce phénomène, l'évolution de la texture a été analysée pendant la transformation de phase durant un cycle de chauffage-refroidissement. L'expérience de traitement thermique *in situ* a été réalisée en utilisant la diffraction des rayons X au synchrotron qui a permis de quantifier à la fois la cinétique de la transformation de phase et la texture cristallographique des phases.

La sélection des échantillons était basée sur les facteurs pouvant influencer l'évolution de la texture [Wenk and Grigull, 2003; Hutchinson, Ryde and Bate, 2005] : (1) la microstructure initiale; (2) le temps de maintien dans le four à la température d'austénitisation; (3) la vitesse de refroidissement appliquée.

Pour étudier cet effet, il a été décidé d'observer :

- **Pour une transformation martensitique** : deux échantillons avec des taux de déformations différents, un après la première passe de laminage R1 ($\epsilon_p = 110\%$) et le second après la deuxième passe de laminage R2 ($\epsilon_p = 250\%$). Ils ont été chauffés à la vitesse de $100^\circ\text{C}/\text{min}$ jusqu'à 1050°C , avec un temps de maintien de 60 min et refroidi rapidement à la vitesse de $50^\circ\text{C}/\text{min}$, comme indiqué sur la Fig.R.7a.
- **Pour une transformation ferritique** : deux échantillons avec des taux de déformations différents: un après la première passe de laminage R1 ($\epsilon_p = 110\%$) et le second après la deuxième passe de laminage R2 ($\epsilon_p = 250\%$). Ils ont été chauffés à la vitesse de $100^\circ\text{C}/\text{min}$ jusqu'à 1050°C , avec un temps de maintien de 20 min et refroidi à la vitesse de $2^\circ\text{C}/\text{min}$ de Ac3 jusqu'à 500°C , comme indiqué sur la Fig.R.7b. L'influence de l'augmentation du temps de maintien de 20 à 60 min sur les structures austénitiques a également été étudiée avec ces traitements thermiques.

Pour identifier l'effet de mémoire de la texture, la texture cristallographique a été mesurée pour les structures ferritiques déformées initiales, puis les structures ferritiques avant transformation à 850°C , les structures austénitiques à 1050°C et enfin les structures ferritiques/martensitiques finales après refroidissement.

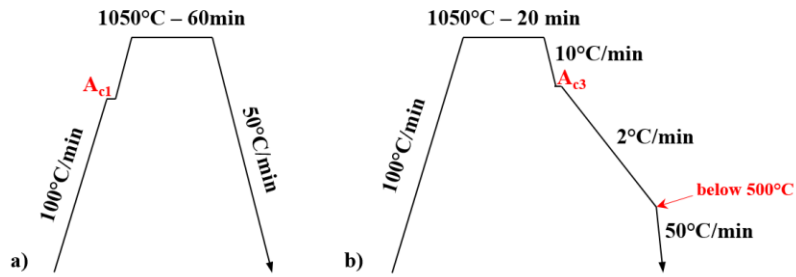


Fig.R.7 Représentation schématique des conditions thermiques expérimentales pour obtenir les transformations $\alpha \rightarrow \gamma \rightarrow \alpha$; a) refroidissement rapide pour obtenir une structure martensitique ; b) refroidissement lent pour obtenir une structure ferritique

L'évolution des textures pendant le traitement thermique pour les échantillons déformés après les refroidissements lent et rapide sont présentées sur la Fig.R.9. Ces textures sont présentées sous forme de sections ODF (Orientation Distribution Function avec des angles d'Euler suivant la convention de Bunge) avec un angle $\phi_2 = 0^\circ$ (Fig.R.9a) et $\phi_2 = 45^\circ$ (Fig.R.9b). L'indice de texture est indiqué dans le coin en bas à droite pour $\phi_2 = 45^\circ$ (Fig.R.9b). Une carte de référence des ODF pour les sections $\phi_2 = 0^\circ$ et 45° identifiant des composantes de texture caractéristiques est donnée en Fig.R.8.

La texture initiale présente une fibre alpha, dont l'intensité diminue légèrement pendant le chauffage. Après la transformation de phase en structure cubique face centrée, la texture consiste en deux pôles proches de la composante Cu (112)[111] et de la composante P (110)[122] [Hutchinson et al., 1998; Saleh, Pereloma and Gazder, 2014; Masoumi et al., 2017]. Lors du maintien à 1050°C, ces fibres conservent leur intensité et ne présentent aucune évolution significative dans le domaine austénitique. L'augmentation du temps de maintien jusqu'à 60 minutes ne change pas non plus l'intensité de la texture.

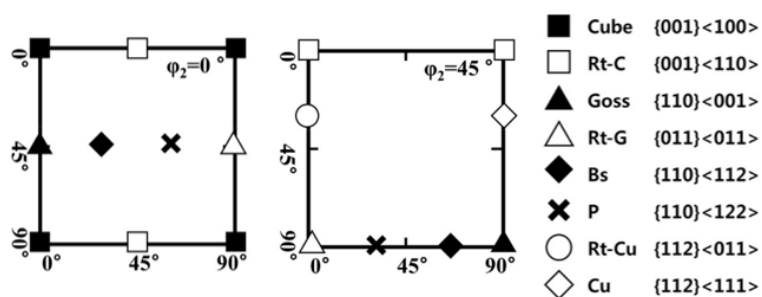


Fig.R.8 Carte de référence pour les sections ODF à $\phi_2 = 0^\circ$ et 45° dans l'espace de Euler avec des éléments de texture connus [Jung et al., 2017]

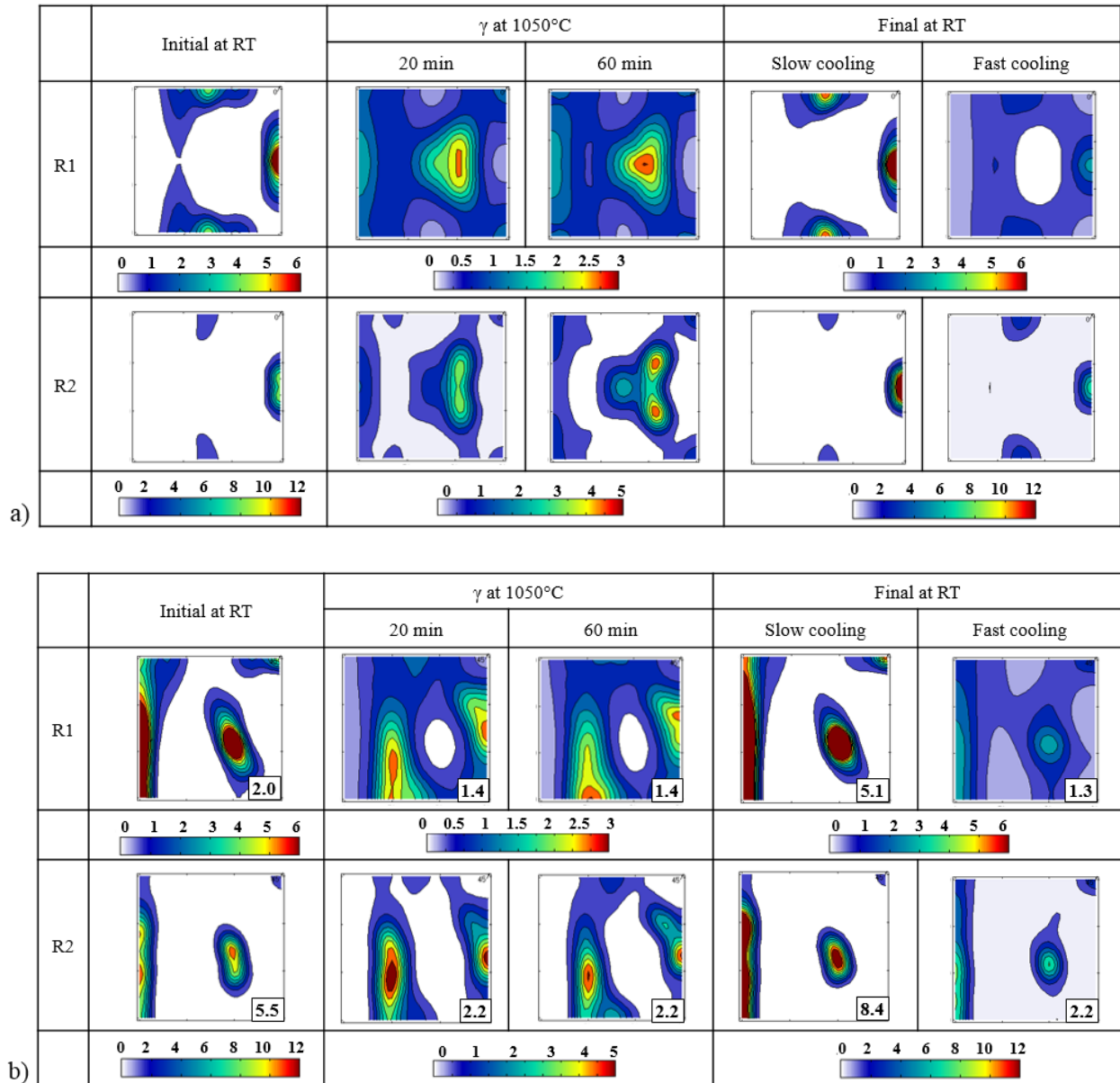


Fig.R.9 Evolution de la texture pendant le cycle thermique pour les échantillons R1 ($\epsilon_p=110\%$) et R2 ($\epsilon_p=250\%$) avec refroidissement lent et rapide a) $\phi_2 = 0^\circ$; b) $\phi_2 = 45^\circ$ (l'index de texture est en bas à droite de chaque section d'ODF)

Sur la Fig.R.10, l'analyse de l'évolution de la texture est présentée en fonction du niveau de texture initial et de la vitesse de refroidissement appliquée. L'échantillon fortement déformé (R2) avec une texture initiale plus élevée, comparé à l'échantillon R1, a montré une texture plus intense dans le domaine austénitique. Pendant le refroidissement lent, on a observé une augmentation de l'intensité de la fibre alpha pour les deux échantillons à structure ferritique: elle est presque deux fois plus élevée que la valeur initiale. Cependant, l'augmentation de la vitesse de refroidissement (trempe) montre que l'indice de texture de la martensite résultant est très faible et peut être caractérisé comme un état presque non-texturé. La trempe de l'échantillon R2 entraîne également un indice de texture faible, mais plus élevé que celui de l'échantillon R1 moins déformé. Ces résultats montrent que, lors de la transformation displacive martensitique, le phénomène de sélection de variants est beaucoup plus faible que lors de la transformation diffusive ferritique dans laquelle un fort effet de mémoire se produit.

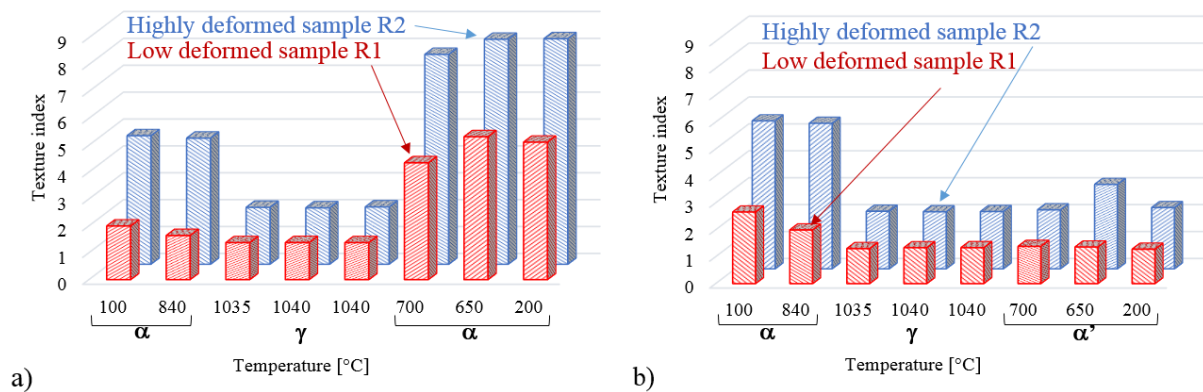


Fig.R.10 Evolution de l'index de texture en fonction de la température pendant les phases de chauffage et refroidissement : a) pour le refroidissement lent ; b) pour le refroidissement rapide

Prédiction de la texture de transformation dans l'acier ODS laminé à froid par la relation Kurdjumov-Sachs Double

Pour étudier le mécanisme d'héritage de texture dans l'acier ODS, la prédiction de la texture de transformation avec un modèle de sélection variant basé sur la relation Kurdjumov-Sachs Double (DKS) a été réalisée. Dans ce modèle, développé par T. Tomida [Tomida, 2018], les variants ayant relation de type K-S ($\{111\}_\gamma // \{011\}_\alpha$; $\langle 101 \rangle_\gamma // \langle 101 \rangle_\alpha$) ou proche de K-S avec deux ou plusieurs grains parents voisins en même temps sont choisis préférentiellement. Les résultats de la modélisation sont présentés sur la Fig.R.11 pour l'échantillon R1 avec un refroidissement rapide.

Selon les résultats, la texture des grains γ parent peut être reconstruite en utilisant la méthode d'expansion harmonique basée sur la relation K-S sans sélection des variants, indiquant ainsi que la nucléation de l'austénite ne se produit pas aux joints de grains de ferrite mais à l'intérieur des grains, dans une matrice hautement déformée.

Dans le cas de la transformation displacive, le modèle de sélection de variants selon DKS prédit bien la texture de la martensite avec une valeur ω relativement grande. Cette valeur détermine la puissance de la sélection de variants par DKS et dépend de la microstructure du matériau. La légère texture de la martensite est probablement causée par une petite quantité de ferrite nucléée tout d'abord sur les joints de grains d'austénite selon DKS, avec lesquels la martensite s'aligne.

Lors du refroidissement avec une transformation ferritique diffusive, le modèle DKS reproduit, avec une très grande valeur de ω , la plupart des caractères forts de la fibre $\langle 110 \rangle // RD$ et l'effet de mémoire de la texture. Mais l'intensité maximale n'a pas pu être reproduite. Cela suggère que la forte évolution de la texture des fibres $\langle 110 \rangle$ au cours du refroidissement lent pourrait également provenir du mécanisme DKS. Finalement, il a été proposé par T. Tomida, une extension du modèle, où les germes de ferrite présentant une relation DKS germeraient plus tôt sur les joints de grains d'austénite et croitraient plus rapidement sur plusieurs grains d'austénite concurrençant alors les autres germes (combinaison de nucléation et croissance sélective).

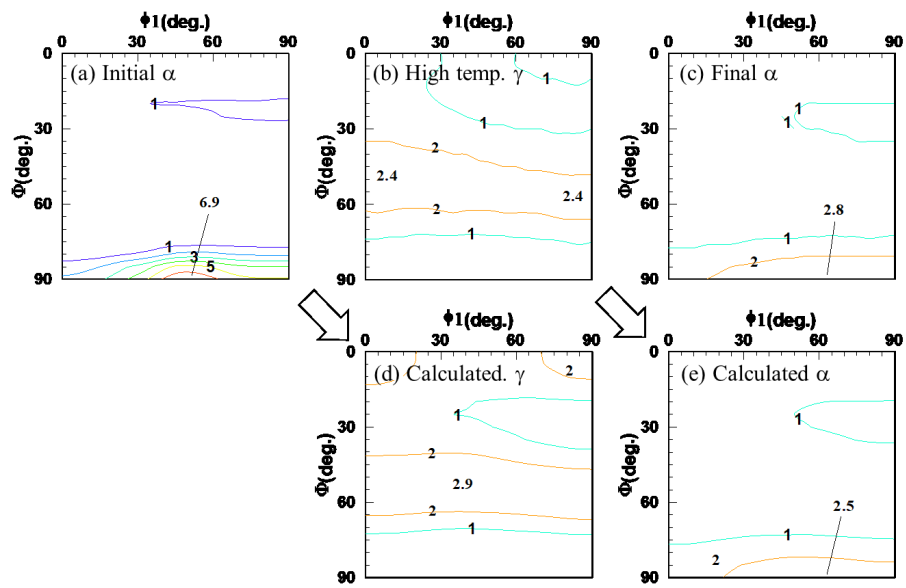


Fig.R.11 Comparaison des textures expérimentales (a à c) et simulées (d et e) pour R1 avec refroidissement rapide ; (d) la texture austénitique est calculée sans sélection de variant ; (e) texture finale martensitique/ferritique est calculée avec DKS à $\omega = 1$, $\phi_2 = 45^\circ$ et les niveaux sont 1,2 et 3

Influence des paramètres de traitement thermique sur les changements de phase

Pour comprendre le mécanisme déterminant l'augmentation de la texture lors de la formation de ferrite dans un matériau fortement déformé, des essais ont été réalisés en étudiant l'influence des paramètres de traitement thermique sur la microstructure.

L'analyse des indices de texture et de la taille des grains montre que la croissance des fibres de la texture de fibre est probablement liée à la croissance rapide d'un nombre limité de germes de ferrite avec des orientations préférentielles. Cette hypothèse est confirmée par l'observation de quelques très gros grains ferritiques lors d'un traitement thermique inter-critique à basse température (entre A_{c1} et A_{c3}). Ces grains confirment l'existence quelques germes de ferrite apparus lors du refroidissement et leur croissance relativement rapide au début de la transformation ferritique. Ces germes pouvant avoir une relation d'orientation avec des anciens grains austénitiques, cela explique l'héritage de texture observé.

Par une expérience, illustrée sur la Fig.R.12, étudiant l'influence de la température de maintien sur la formation de la texture, il a été noté que plus la température de traitement est élevée, plus l'indice de texture est élevé. Ce phénomène est supposé être lié à la croissance des grains austénitiques qui promeut la croissance rapide des germes ferritiques. Dans le même temps, la cinétique de transformation de phase s'est révélée dépendre très peu de la vitesse de chauffage.

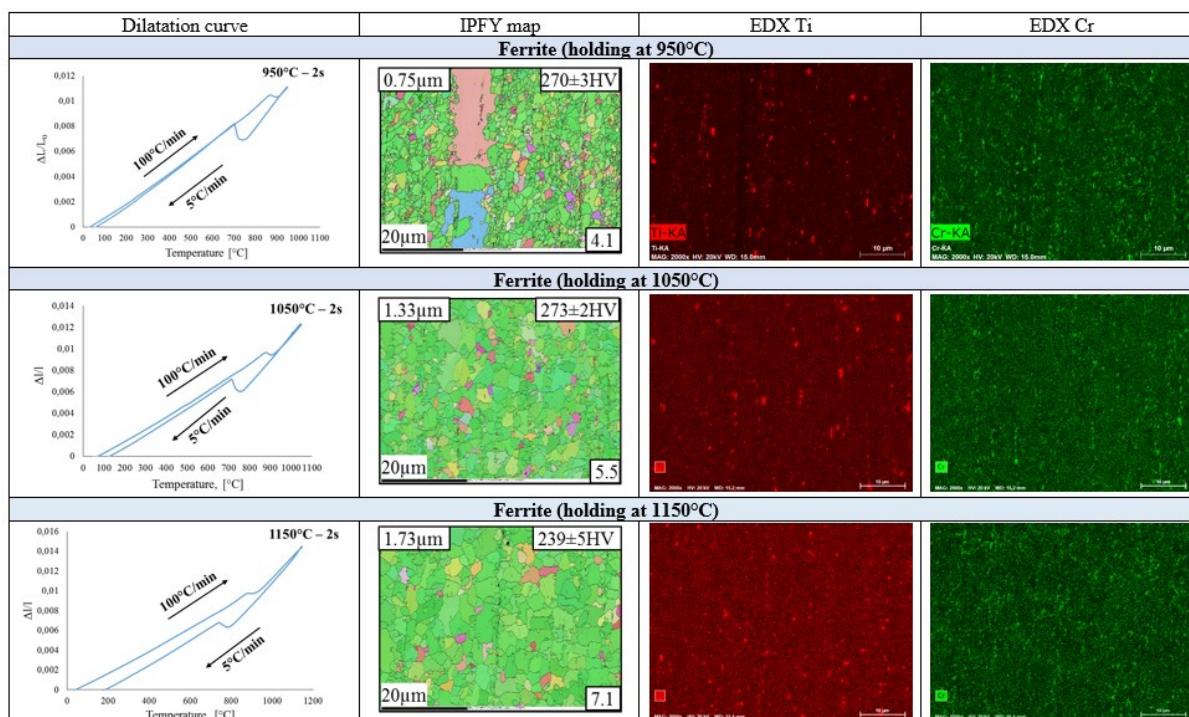


Fig.R.12 Influence de la température de maintien (950, 1050 et 1150°C) sur la formation de texture (refroidissement lent)

Sur la Fig.R.13 des essais isothermes obtenus par une trempe interrompue du domaine γ jusqu'à une température de maintien inférieure à A_{c1} , mais supérieure à M_s , sont présentés. Il a été observé que la température de formation de la ferrite (dans le cas de l'ODS à environ 700°C) déterminera l'évolution de la texture morphologique et cristallographique.

Dans le cas d'un refroidissement à des températures inférieures à 700°C, la diffusion des atomes est plus faible, la nucléation se produit avec une fréquence élevée associée à une croissance des germes lente. La nucléation est initiée aux joints des grains gamma. Comme il y a un plus grand nombre de nouveaux germes, plus d'orientations cristallographiques seront présentées diminuant l'intensité de la texture mesurée.

Dans le cas d'un refroidissement à des températures supérieures à 700°C, la diffusion favorise la croissance des germes existants au détriment de la nucléation de nouveaux germes. Cette fois, la nucléation est probablement initiée au point triple des grains gamma favorisant la sélection de variants. Ainsi, une germination sélective et une croissance de ces quelques grains induisent un indice de texture élevé et des grains plus gros. Ces résultats sont cohérents avec l'étude de [Lambard, 1998] sur les nuances ODS EM10, complétant les données sur l'évolution des textures.

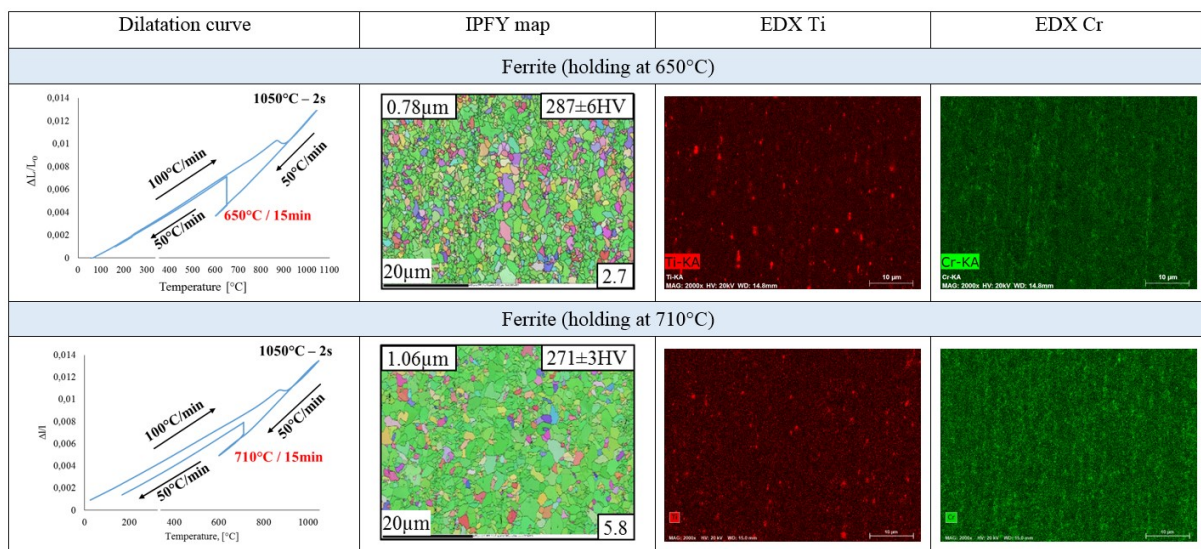


Fig.R.13 Traitements isothermes après trempe caractérisant la formation de la ferrite à différentes températures

Dans tous les cas, la précipitation des oxydes de Ti ne semble pas être affectée par les traitements et tend à épingler la croissance des grains austénitiques pendant la transformation. Cela favorise la transformation de phase à l'intérieur de la structure colonnaire qui est définie par les joints des particules primaires. Les carbures de chrome ($M_{23}C_6$) sont complètement dissous à 1050°C mais ancrent toujours la croissance des grains austénitiques pendant les traitements thermiques courts inter-critiques.

Un résumé de l'étude est proposé sur la Fig.R.14 qui présente un schéma du mécanisme de transformations $\alpha \rightarrow \gamma \rightarrow \alpha$, où la nucléation et la croissance sont liées à l'évolution de la texture.

Le schéma de transformation de phase proposé devrait être confronté à de nouvelles expériences. Notamment, le chauffage *in situ* au MEB avec différentes vitesses de chauffage et de refroidissement peut être proposé comme perspective de ce travail. Une analyse plus approfondie de la cohérence des précipités avec la matrice après le laminage et après le traitement thermique pourrait mettre en évidence le rôle des nanoparticules sur la croissance sélective des grains de ferrite.

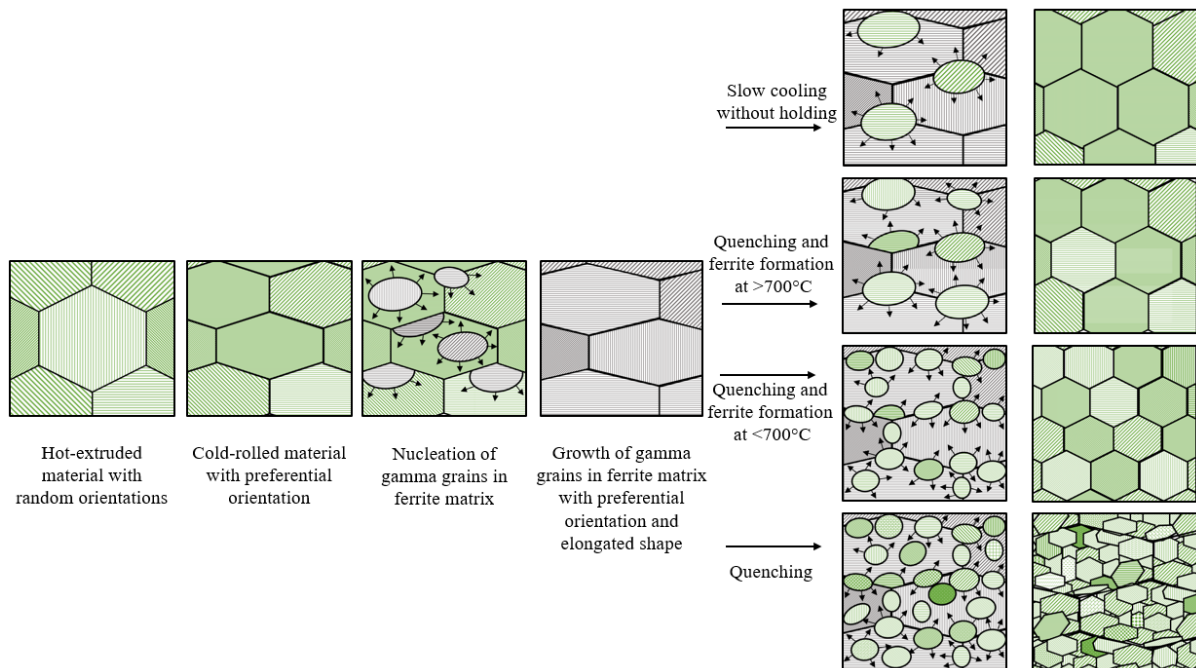


Fig.R.14 Schéma représentant le mécanisme des transformations $\alpha \rightarrow \gamma \rightarrow \alpha$ et leur lien avec l'effet de mémoire de la texture (les couleurs définissent les phases : vert ferrite et gris austénite ; le gradient de couleur définit la misorientation vis à vis de la fibre α)

L'influence des étapes de laminages sur les propriétés mécaniques des tubes ODS

L'augmentation des valeurs de dureté est cohérente avec la relation Hall-Petch, illustrée sur la Fig.R.15. La grande déformation, induite par le laminage à froid VMR, produit une densité de dislocation élevée et une réduction de la taille de grains dans l'acier ODS ce qui améliore ses propriétés mécaniques.

Les données analysées ici concernent simultanément les échantillons d'ODS laminés à froid (déformation de 1.40 par passe) et ceux traités thermiquement décrits dans les chapitres précédents. Les résultats de cette étude sont comparés aux résultats représentatifs d'aciers à grains ultra-fins ou nanocristallisés (UFG / NC). Ces aciers sont obtenus exclusivement par déformation plastique sévère et traitement thermique final : l'acier ODS 12% Cr est produit par extrusion angulaire à canaux égaux (ECAE) (déformation de 1.15 par passe) [Song et al., 2013], l'acier IF (Interstitial Free) après déformation plastique par pression angulaire à canaux égaux (ECAP) (déformation totale comprise entre 1.15 et 9.2) [De Messemaeker et al., 2004] et l'acier IF après laminage à froid (déformation totale comprise entre 0.1 et 0.9) [Li et al., 2003]. On peut voir qu'une fraction plus élevée des joints de grains et une plus forte densité des dislocations, induite par une déformation plastique plus intense, permettra d'augmenter la valeur de la limite d'élasticité conformément à l'effet Hall-Petch.

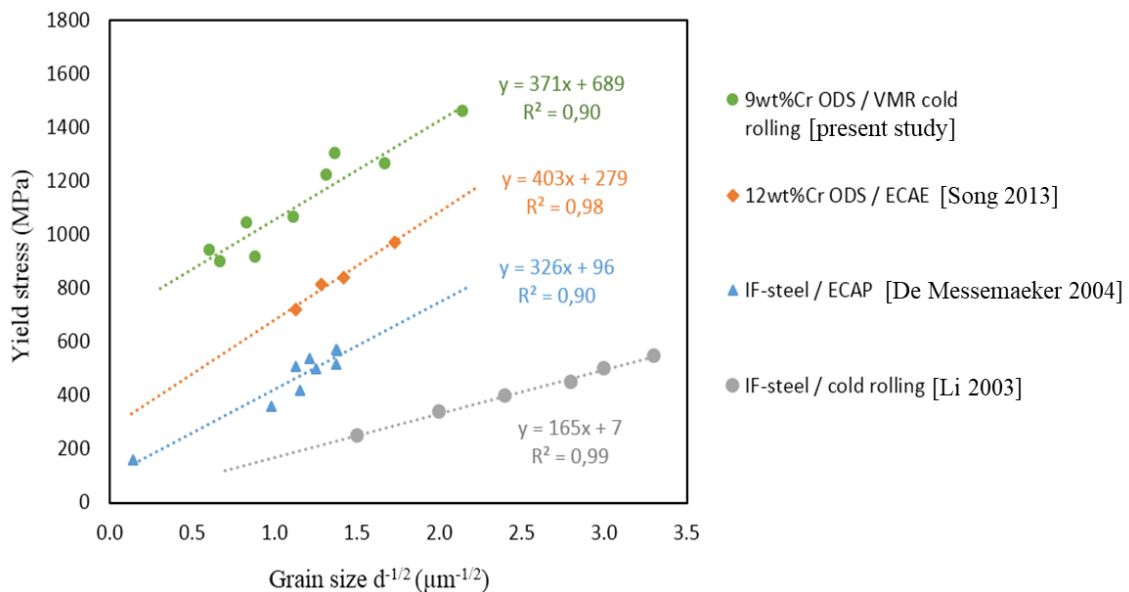


Fig.R.15 Diagramme de Hall Petch pour quelques aciers nanocristallins en comparaison avec les aciers ODS

Il est intéressant de noter que les pentes des deux aciers ODS sont assez similaires, ce qui démontre le raffinement efficace des grains fourni par les deux procédés de déformation sur l'acier ODS. Cela montre également que les mécanismes physiques de durcissement des grains sont les mêmes dans les deux aciers. Cependant, on constate que plus le niveau de déformation est élevé (processus VMR par rapport à ECAE), plus la densité de dislocations produite dans la matrice est élevée et, par conséquent, plus la contrainte de frottement mesurée est élevée. La même tendance a été observée pour les aciers IF produits par ECAP et les procédés de laminage à froid correspondants. L'efficacité de la dispersion d'oxydes est démontrée en comparant l'acier ODS et l'acier IF. En diminuant la mobilité des dislocations, les oxydes améliorent significativement la résistance du matériau [Feaugas et al., 2003].

Les propriétés mécaniques des tubes R2 et R2(HT) laminés et traités (à l'état ferritique et martensitique revenu) ont été caractérisées par des essais de traction uni-axiale sur deux géométries d'échantillons : tuile et anneau. Ces tests ont été réalisés à trois vitesses de déformation 10^{-2} s^{-1} , 10^{-3} s^{-1} et 10^{-4} s^{-1} afin de démontrer la sensibilité à la vitesse de déformation du matériau ODS. Les résultats des essais de traction sont présentés sur la Fig.R.16.

L'état laminé présente des valeurs de résistance mécanique extrêmement élevées ($R_m = 1600 \text{ MPa}$ en RD), mais en même temps une grande fragilité ($A_{\text{tot}} = 8\%$). Il se caractérise également par une anisotropie élevée et met en évidence la nécessité d'un traitement thermique intermédiaire entre les passes de laminage pour éviter la fissuration du matériau lors des déformations. De plus, le traitement thermique contribue à la diminution des contraintes résiduelles introduites par le laminage à froid.

Un traitement thermique intermédiaire avec un refroidissement lent est recommandé à ce stade, car il permet d'obtenir un matériau ductile plus facilement déformable ($R_m = 800 \text{ MPa}$, $HV1 < 300$), malgré l'anisotropie induite par l'effet de mémoire de texture ($A_{\text{tot}} = 20\%$ en RD via $A_{\text{tot}} = 11\%$ en TD). D'autres types de traitement thermique intermédiaires peuvent être proposés qui permettent de conserver une structure ferritique avec une bonne ductilité, mais avec des microstructures plus isotropes.

Pour le traitement thermique final, il est nécessaire d'appliquer un refroidissement rapide, pour restaurer la texture et obtenir une structure isotrope; la structure de la martensite revenue présente un bon compromis entre résistance mécanique et ductilité à la température ambiante et le même comportement que l'état ferritique à 650°C [Chauhan, 2016].

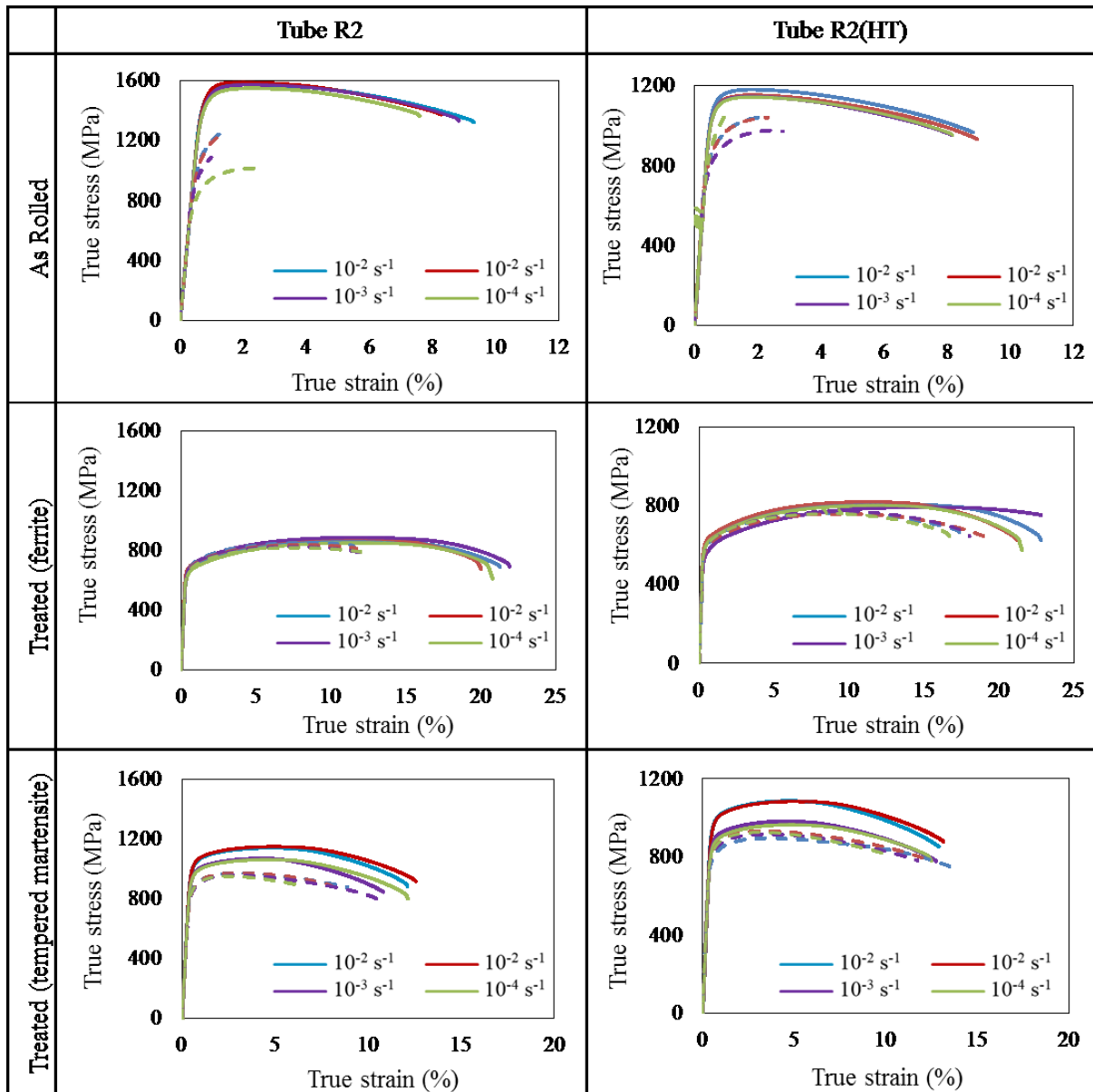


Fig.R.16 Courbes des essais de tractions pour les tubes R2 et R2(HT) et les états traités
 Ligne continue – tuile, ligne pointillée – anneau

Modélisation de la texture et des propriétés mécaniques par un code polycristallin

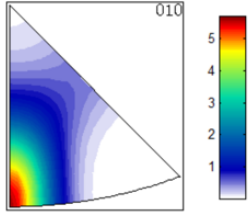
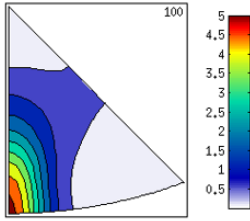
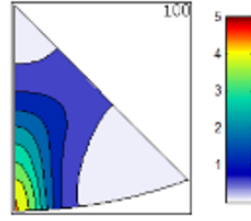
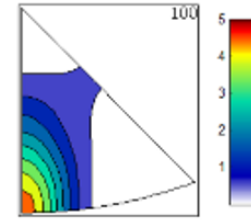
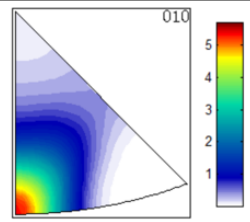
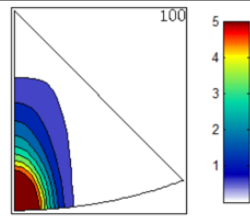
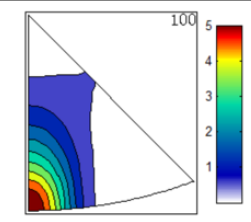
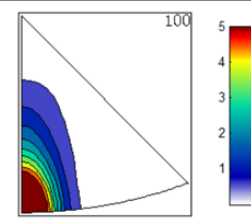
A partir des résultats expérimentaux d'observations EBSD, une simulation d'un agrégat polycristallin avec un code VPSC (ViscoPlastic Self Consistent) est proposée. La liste de grains, leurs orientations cristallographiques et leur fraction surfacique relative étant exploitées comme fichier d'entrée de ces simulations. Un chargement simplifié représentatif du laminage VMR a été appliqué pour simuler la séquence de production. Une étude de la sensibilité des paramètres du modèle a été réalisée, par identification aux résultats expérimentaux. Le modèle proposé prédit correctement l'évolution de la texture induite par les grandes déformations de laminage. Cependant, le matériau présentant de fortes désorientations intra-granulaires il est nécessaire de considérer un grand nombre de grains et un angle critique de joints grains relativement faible.

Pour une microstructure initiale donnée, le choix d'angle critique et du nombre de grains décrivant cette microstructure peut avoir un impact critique sur l'indice de texture global et les intensités respectives des pôles. En effet, la description de la microstructure sous forme de grains monocristallins pondérés par une fraction volumique, retenue par le code VPSC, créer un biais qui persistera toujours quel que soit le modèle retenu (FEM ou FFT).

La comparaison des figures de pôles inverses IPF // direction de laminage (RD) expérimentales et simulées montre que différents types de chemin de chargement permettent de prédire la formation des fibres alpha. Cependant, l'intensité de la fibre n'est pas identique pour chaque simulation. Par exemple, le pôle principal d'orientation $\langle 110 \rangle$ est moins marqué pour le chemin de chargement monotone que pour le chargement cyclique simulant le laminage VMR. Ce dernier chargement donnant des résultats plus proches des pôles et des indices de texture expérimentaux.

Dans une dernière partie, trois schémas de linéarisation ont été étudiés via les modules sécante, tangente et affine. Les IPF simulées sont donnés dans le [Tableau.R.3](#) et montrent que le module sécant donne les indices de texture et les iso-valeurs plus proches des valeurs expérimentales.

Tableau.R.3 Figures de pôles inverse simulées pour les états R1 et R2 avec un chargement cyclique ($\alpha = 0.5$) et différents schémas de linéarisation (1 voisin)

Experimental	Affine	Secant	Tangent
R1 texture			
			
TI=2.80	TI=2.57	TI=2.17	TI=2.81
R2 texture			
			
TI=3.42	TI=4.82	TI=3.77	TI=5.06

Le modèle VPSC est aussi un bon outil pour introduire l'anisotropie des propriétés mécaniques. Après simulation d'une séquence de mise en forme par VMR, les grains obtenus (prenant en compte leur orientation et morphologie) sont utilisés comme données d'entrée pour simuler un test de traction uni-axial dans deux directions différentes, longitudinale (RD) et transversale (TD). Ces deux calculs mettent en évidence l'anisotropie mécanique induite par la texture cristallographique et la morphologie lors du laminage. Les propriétés de traction dans la direction de laminage et dans la direction transversale sont reportées sur la [Fig.R.17](#) pour différents schémas de linéarisation.

Pour tous les schémas, la direction de laminage (ligne continue) présente un seuil d'écoulement plastique plus élevé que la direction transversale ce qui conforme à l'expérience (ligne pointillée [Fig.R.18](#)). En conséquence, l'anisotropie cristallographique contribue de manière significative à l'anisotropie mécanique observée. Cependant, même si la tendance est respectée, l'anisotropie calculée est minorée par rapport à l'expérience.

On peut donc conclure, conformément aux travaux de [[Steckmeyer, 2012](#)], que l'anisotropie observée expérimentalement ne peut pas être exclusivement expliquée par l'anisotropie cristalline.

La contribution de la précipitation à la plasticité et l'endommagement anisotrope n'est pas prise en compte par la modélisation VPSC. Une analyse approfondie de la sensibilité des paramètres de la loi de Voce devrait pouvoir également améliorer la corrélation entre résultats expérimentaux et numériques.

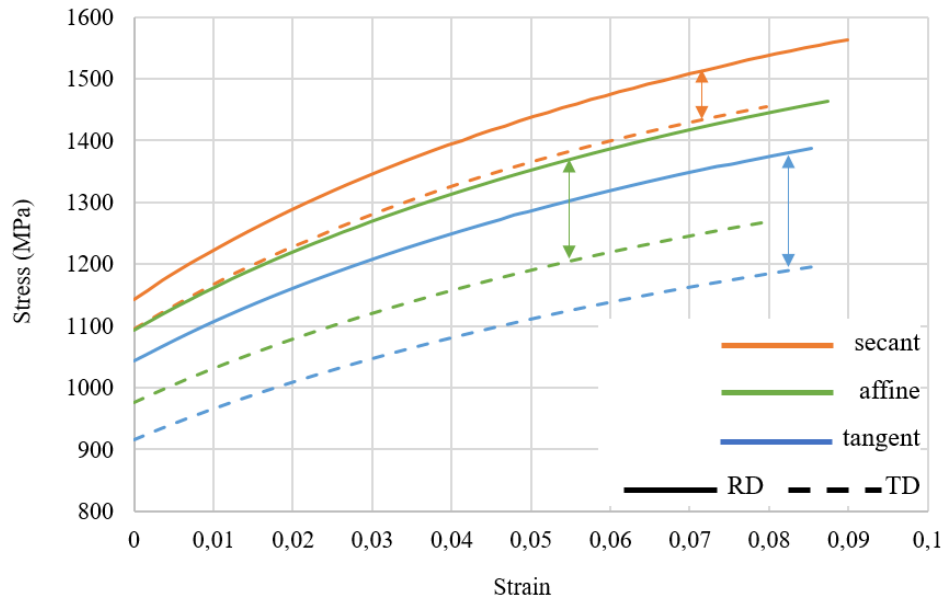


Fig.R.17 Courbes contrainte déformation simulées pour échantillon R2 avec les schémas de linéarisation affine, sécante et tangent

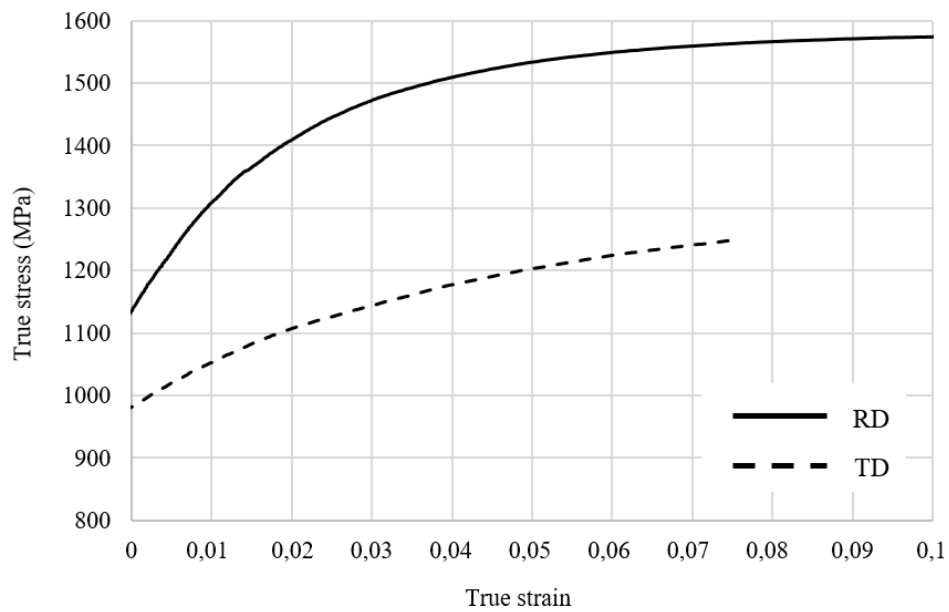


Fig.R.18 Courbes contrainte déformation expérimentales pour échantillon R2, état laminé à froid (taux de déformation 10^{-2} s^{-1})

Conclusions et Perspectives

Ce travail, par une analyse précise des évolutions microstructurales et mécaniques au cours du laminage Mannesmann, donne des données fondamentales pour le développement des séquences de laminage à froid pour les aciers ODS. La découverte d'un phénomène inattendu d'héritage de texture lors de traitements thermiques met en évidence l'effet singulier des nanoparticules sur le changement de phase des aciers inoxydables ODS 9% Cr.

Dans les perspectives de ce projet, les actions suivantes peuvent être proposées :

Sur le plan des observations expérimentales

- Le schéma de production avec un traitement thermique intermédiaire est recommandé comme schéma optimal pour la fabrication de tubes industriels. Les propriétés mécaniques des tubes traités avec des microstructures de martensite revenue R2(HT) MR ont été déjà étudiées par des essais de traction à température ambiante. Par la suite, le comportement du tube R2(HT) MR doit être étudié avec des essais de traction à haute température et également avec des essais de fluage pour confirmer la résistance du matériau dans les conditions d'utilisation.
- Les premières données sur la taille des particules et les distributions ont été obtenues en utilisant les données MET. Cependant, en raison de la forte distorsion du réseau, le signal obtenu était très mauvais. Une analyse avec des techniques plus globales, par exemple la SAXS (Small Angle X-rays Scattering) ou la SANS (Small Angle Neutron Scattering), peut être utile pour mesurer la taille des particules et leur évolution en termes de taille et de composition chimique à différentes étapes de la production. De plus, l'étude de la relation d'orientation de réseaux des particules avec la matrice ferrite / austénite pourrait contribuer à élucider l'origine du mécanisme de sélection de variants.
- Dans cette étude, l'hypothèse de la nucléation et de la croissance sélective lors de la formation de ferrite a été proposée. Pour observer les sites de nucléation et la croissance des germes pendant la transition de phase, des essais de chauffage *in-situ* MEB pourrait être réalisés à l'avenir.
- La première tentative d'étude des mécanismes de déformation à froid a été effectuée par un test de traction *in-situ* MEB (couplé à l'EBS). Il a été mentionné que pour la construction de la carte de déformation, une grille adaptée devrait être utilisée. La nouvelle campagne de tests, idéalement pour l'échantillon extrudé à chaud, permettra d'identifier le mécanisme de formation de la fibre et ainsi d'optimiser les simulations numériques.

Sur le plan des études numériques

- La reconstruction des grains gamma a été réalisée dans un logiciel ARPEG basé sur les relations d'orientation KS entre les phases martensite et austénite. Cependant, certaines irrégularités ont été observées sur les joins de grains et la distribution des orientations de la martensite. La reconstruction de ces structures par une approche DKS, utilisée pour la prédiction de la texture de transformation, peut être une prospective de l'étude.
- Le code VPSC a été utilisé pour la simulation de la séquence de laminage, qui n'inclut pas le traitement thermique. Le couplage du code VPSC avec approche DKS optimisée pourrait être proposé pour modéliser l'ensemble du schéma de production.
- La modélisation VPSC a fournis des résultats précieux pour la prédiction de la texture lors du processus de laminage à froid. L'application de la simulation d'agrégats par des méthodes FFT et/ou FEM pourrait être réalisée pour comparer la précision des modèles sur cette application exigeante.

References

- Abe, H. *et al.* (1994) 'Fabrication process of high nodular corrosion-resistant Zircaloy-2 tubing', *ASTM Special Technical Publication 1245*, pp. 285–306.
- Abe, H. (2000) 'A New Fabrication Process for Zr-Lined Zircaloy-2 Tubing', *ASTM Special Technical Publication*, (1354), pp. 425–459.
- Abe, H. and Furugen, M. (2012) 'Method of evaluating workability in cold pilgering', *Journal of Materials Processing Technology*. Elsevier B.V., 212(8), pp. 1687–1693. doi: 10.1016/j.jmatprotec.2012.03.012.
- Allen, T. *et al.* (2009) 'Advanced structural materials and cladding', *MRS Bulletin*, 34(1), pp. 20–27. doi: 10.1557/mrs2009.8.
- Anglin, B. S., Gockel, B. T. and Rollett, A. D. (2016) 'Developing constitutive model parameters via a multi-scale approach', *Integrating Materials and Manufacturing Innovation*. Integrating Materials and Manufacturing Innovation, 5(1), p. 11. doi: 10.1186/s40192-016-0053-4.
- Arzt, E. (1998) 'Size effects in materials due to microstructural and dimensional constraints: A comparative review', *Acta Materialia*, 46(16), pp. 5611–5626. doi: 10.1016/S1359-6454(98)00231-6.
- Bay, B. and Hansen, N. (1979) 'Initial stages of recrystallization in aluminum of commercial purity', *Metallurgical Transactions A*, 10(279). doi: 10.1007/BF02658335.
- Béchade, J. L. *et al.* (2012) 'Application of synchrotron radiation to analyze the precipitation in ODS materials before irradiation in Fe-9%Cr single grain of powder and consolidated Fe-18%Cr', *Journal of Nuclear Materials*, 428(1–3), pp. 183–191. doi: 10.1016/j.jnucmat.2011.08.025.
- Bhattacharyya, D. *et al.* (2006) 'A study of the mechanism of α to β phase transformation by tracking texture evolution with temperature in Ti-6Al-4V using neutron diffraction', *Scripta Materialia*, 54, pp. 231–236. doi: 10.1016/j.scriptamat.2005.09.026.
- Van Den Bosch, J. *et al.* (2013) 'SANS and TEM of ferritic-martensitic steel T91 irradiated in FFTF up to 184 dpa at 413 °c', *Journal of Nuclear Materials*, 440(1–3), pp. 91–97. doi: 10.1016/j.jnucmat.2013.04.025.
- Brandes, M. C. *et al.* (2012) 'Creep behavior and deformation mechanisms in a nanocluster strengthened ferritic steel.', *Acta. Mater.*, 60, pp. 1827–1839.
- De Bremaecker, A. (2012) 'Past research and fabrication conducted at SCK•CEN on ferritic ODS alloys

References

- used as cladding for FBR's fuel pins', *Journal of Nuclear Materials*, 428(1–3), pp. 13–30. doi: 10.1016/j.jnucmat.2011.11.060.
- Bunge, H. J. and Esling, C. (1982) 'Quantitative Texture Analysis', *Deutsche Gesellschaft für Metallkunde*.
- Bunge, H. J., Humbert, M. and Welch, P. I. (1984) 'Texture transformation', *Textures and Microstructures*, 6(81).
- Carlan, Y. d. *et al.* (2009) 'CEA developments of new ferritic ODS alloys for nuclear applications', *Journal of Nuclear Materials*, 386, pp. 430–432.
- Cayron, C. (2007) 'ARPE: A computer program to automatically reconstruct the parent grains from electron backscatter diffraction data', *Journal of Applied Crystallography*, 40, pp. 1183–1188. doi: 10.1107/S0021889807048777.
- Courtney, T. H. (2000) *Mechanical Behavior of Materials*. 2nd Ed. Mc. Boston, US. doi: 10.1017/CBO9781107415324.004.
- Dadé, M. (2014) 'Plasticité d'alliages nano-renforcés pour le gainage combustible des réacteurs de 4^{ème} génération: compréhension et modélisation de l'influence des paramètres microstructuraux sur le comportement d'alliages modèles', pp. 1–5. doi: 10.1007/s13398-014-0173-7.2.
- Dadé, M. *et al.* (2017) 'Influence of microstructural parameters on the mechanical properties of oxide dispersion strengthened Fe-14Cr steels', *Acta Materialia*. doi: 10.1016/j.actamat.2017.01.026.
- Doherty, R. D. *et al.* (1997) 'Current issues in recrystallization: A review', *Materials Science and Engineering A*. doi: 10.1016/S0921-5093(97)00424-3.
- Dubuisson, P. *et al.* (2012) 'ODS Ferritic/martensitic alloys for Sodium "Y" (no date). Fast Reactor fuel pin cladding', *Journal of Nuclear Materials*, 428(1–3), pp. 6–12.
- Engler, O. (1997) 'Simulation of the Recrystallization Textures of Al-Alloys on the Basis of Nucleation and Growth Probability of the Various Textures Components', pp. 197–209.
- Engler, O., Hirsch, J. and Lücke, K. (1989) 'Texture development in Al 1.8wt% Cu depending on the precipitation state-I. Rolling textures', *Acta Metallurgica*, 37(10), pp. 2743–2753. doi: 10.1016/0001-6160(89)90308-8.
- Engler, O., Hirsch, J. and Lücke, K. (1995) 'Texture development in Al-1.8 wt% Cu depending on the precipitation state-II. Recrystallization textures', *Acta Metallurgica Et Materialia*, 43(1), pp. 121–138. doi: 10.1016/0956-7151(95)90268-6.

- Engler, O. and Luecke, K. (1992) 'Mechanisms of recrystallization texture formation in aluminium alloys', *Scripta Metallurgica et Materialia*, 27(11), pp. 1527–1532.
- Eshelby, J. D. (1957) 'The determination of the elastic field of an ellipsoidal inclusion and related problems', *Source: Proceedings of the Royal Society of London. Series A Mathematical and Physical Sciences*, 241(1226). doi: 10.1098/rspa.1957.0133.
- ESNII (2010) 'A contribution to the EU low carbon energy policy: demonstration program for fast neutron reactors', *Sustainable Nuclear Energy Technology Platform*.
- Eyckens, P. *et al.* (2012) 'Validation of the texture-based ALAMEL and VPSC models by measured anisotropy of plastic yielding', *Materials Science Forum*, 702–703, pp. 233–236. doi: 10.4028/www.scientific.net/MSF.702-703.233.
- Fazio, C. *et al.* (2009) 'Activities performed within the program of Nuclear Safety Research on Structural and Cladding Materials for Innovative Reactor System able to Transmute Nuclear Waste', in *EC-IAEA "Development of New Structural Materials for Advanced Fission and Fusion Reactor Systems*. Barcelona, Spain.
- Feaugas, X. and Haddou, H. (2003) 'Grain-size effects on tensile behavior of nickel and AISI 316L stainless steel', *Metallurgical and Materials Transactions A*, 34(10), pp. 2329–2340. doi: 10.1007/s11661-003-0296-5.
- Fink, C. G. (1910) 'Ductile tungsten and molybdenum', *Trans. Am. Electrochem*, 17, p. 229.
- Fischer, J. J. (1976) 'Dispersion Strengthened Ferritic alloy for use in Liquid-Metal Fast Breeder Reactors', *United States, The International Nickel Company*.
- Gaillac, A. and Ly, C. (2018) 'Optimized manufacture of nuclear fuel cladding tubes by FEA of hot extrusion and cold pilgering processes', *AIP Conference Proceedings*, 1960. doi: 10.1063/1.5034848.
- Girard, E. *et al.* (2001) 'Effect of plastic shearing on damage and texture on Zircaloy-4 cladding tubes: Experimental and numerical study', *Journal of Nuclear Materials*, 294(3), pp. 330–338. doi: 10.1016/S0022-3115(00)00729-7.
- Gloaguen, D. and François, M. (2006) 'Prediction of intragranular strains in metallic polycrystals with a two-level homogenisation approach: Influence of dislocation microstructure on the mechanical behaviour', *Physica Status Solidi (A) Applications and Materials Science*, 203(8), pp. 1950–1953. doi: 10.1002/pssa.200521316.
- Goldstein, J. I. *et al.* (1992) *Scanning electron microscopy and x-ray microanalysis*. Plenum Pre.

References

- Hald, J. (1996) 'Metallurgy and creep properties of new 9-12%Cr steels', *Steel Research*, 67(9), pp. 369–374. doi: 10.1002/srin.199605503.
- Hall, E. O. (1951) 'The deformation and ageing of mild steel: III Discussion of results', *Proceedings of the Physical Society. Section B*, 64(9), pp. 747–753. doi: 10.1088/0370-1301/64/9/303.
- Hamilton, M. L. (2000) 'Fabrication technology for ODS alloy MA957', *Report PNL-13165*.
- Hary, B. (2017) *Compréhension et modélisation de l'influence du taux de renforts et de la texture de déformation sur la recristallisation des aciers ODS ferritiques*. Université Paris-Saclay, France.
- Hata, K. *et al.* (2016) 'In Situ EBSD Analysis on the Crystal Orientation Relationship between Ferrite and Austenite during Reverse Transformation of an Fe-Mn-C Alloy', *Materials Transactions*, 57, pp. 1514–1519. doi: 10.2320/matertrans.MAW201602.
- He, B. B., Preckwinkel, U. and Smith, K. L. (2000) 'Fundamentals of Two-Dimensional X-ray Diffraction (XRD2)', *Advances in X-ray Analysis*, 43. doi: <http://dx.doi.org/10.1154/1.1577355>.
- Hoelzer, D. *et al.* (2012) 'Microstructural Characterization of Friction Stir Welded Oxide Dispersion Strengthened 14YWT Ferritic Alloy and F82H Tempered Martensitic Steel', *Microscopy and Microanalysis*, 18, pp. 1658–1659.
- Hu, L. *et al.* (2012) 'Constitutive relations for AA 5754 based on crystal plasticity', *Metallurgical and Materials Transactions A: Physical Metallurgy and Materials Science*, 43(3), pp. 854–869. doi: 10.1007/s11661-011-0927-1.
- Humphreys, F. J. (1977) 'The nucleation of recrystallization at second phase particles in deformed aluminium', *Acta Metallurgica*, 25, p. 1323. doi: 10.1016/0001-6160(77)90109-2.
- Humphreys, F. J. (1997) 'A unified theory of recovery, recrystallization and grain growth, based on the stability and growth of cellular microstructures - I. The basic model', *Acta Materialia*. doi: 10.1016/S1359-6454(97)00070-0.
- Hutchinson, B. *et al.* (1998) 'Texture in hot rolled austenite and resulting transformation products', *Materials Science and Engineering A*, 257(1), pp. 9–17. doi: 10.1016/S0921-5093(98)00820-X.
- Hutchinson, B. and Kestens, L. A. I. (2008) 'Origins of texture memory in steels', *Ceramic Transactions*, 201, pp. 281–290. doi: 10.1002/9780470444214.ch30.
- Hutchinson, W. B., Ryde, L. and Bate, P. S. (2005) 'Transformation Textures in Steels', *Materials Science Forum*, 495–497, pp. 1141–1150. doi: 10.4028/www.scientific.net/MSF.495-497.1141.

- Inoue, H. and Inakazu, N. (1994) 'Determination of orientation distribution functions from incomplete pole figures by iterative series expansion method', *Nippon Kinzoku Gakkaishi/Journal of the Japan Institute of Metals*, 58, pp. 892–898. doi: 10.2320/jinstmet1952.58.8_892.
- Inoue, H. and Takasugi, T. (2007) 'Texture Control for Improving Deep Drawability in Rolled and Annealed Aluminum Alloy Sheets', *Materials Transactions*, 48(8), pp. 2014–2022. doi: 10.2320/matertrans.L-MRA2007871.
- Inoue, M., Kaito, T. and Ohtsuka, S. (2008) 'Research and development of oxide dispersion strengthened ferritic steels for sodium cooled fast breeder reactor fuels', *Materials Issues for Generation IV Systems Status*, pp. 311–325. doi: 10.1007/978-1-4020-8422-5.
- Jazaeri, H. and Humphreys, F. J. (2004) 'The transition from discontinuous to continuous recrystallization in some aluminium alloys I - The deformed state', *Acta Materialia*. doi: 10.1016/j.actamat.2004.03.030.
- Jensen, D. J., Hansen, N. and Liu, Y. L. (1991) 'Effect of recrystallisation temperature on texture and grain size of Al–SiC composite', *Materials Science and Technology*, 7(4), pp. 369–376. doi: 10.1179/mst.1991.7.4.369.
- Jung, J. *et al.* (2017) 'Numerical analysis on the formation of P-orientation near coarse precipitates in FCC crystals during recrystallization', *Acta Materialia*. Elsevier Ltd, 131, pp. 363–372. doi: 10.1016/j.actamat.2017.04.020.
- Juul Jensen, D. (1995) 'Growth rates and misorientation relationships between growing nuclei/grains and the surrounding deformed matrix during recrystallization', *Acta Metallurgica Et Materialia*. doi: 10.1016/0956-7151(95)00111-8.
- Kaito, T. *et al.* (2003) 'Development of nano-composite 9Cr-ODS martensitic steels by means of a to y phase transformation', in: *Jaeri*, pp. 237–244.
- Kang, C.-Y. *et al.* (1996) 'Effect of Three Kinds of Oxide on the Strength Properties of Mechanically Alloyed 17%Cr Ferritic ODS Materials.', *ISIJ International*, 36(12), pp. 1518–1519. doi: 10.2355/isijinternational.36.1518.
- Kasada, R. *et al.* (2011) 'Anisotropy in tensile and ductile-brittle transition behavior of ODS ferritic steels', *Journal of Nuclear Materials*, 417(1–3), pp. 180–184. doi: 10.1016/j.jnucmat.2010.12.069.
- Kim, I.-S. *et al.* (2003) 'Effect of Ti and W on the Mechanical Properties and Microstructure of 12% Cr Base Mechanical-alloyed Nano-sized ODS Ferritic Alloys', *ISIJ International*, 43(10), pp. 1640–1646. doi: 10.2355/isijinternational.43.1640.

References

- Kimura, A. (2005) 'Current Status of Reduced-Activation Ferritic/Martensitic Steels R&D for Fusion Energy', *Materials Transactions*, 46(3), pp. 394–404. doi: 10.2320/matertrans.46.394.
- Kimura, A. *et al.* (2007) 'High Burnup Fuel Cladding Materials R&D for Advanced Nuclear Systems: Nano-sized oxide dispersion strengthening steels', *Journal of Nuclear Science and Technology*, 44(3), pp. 323–328. doi: 10.1080/18811248.2007.9711289.
- Klimiankou, M., Lindau, R. and Möslang, A. (2003) 'HRTEM study of yttrium oxide particles in ODS steels for fusion reactor application', *Journal of Crystal Growth*, 249(1–2), pp. 381–387. doi: 10.1016/S0022-0248(02)02134-6.
- Kurdjumow, V. G. and Sachs, G. (1930) 'Über den Mechanismus der Stahlhärtung', *Zeitschrift für Physik*, pp. 325–343. Available at: <https://link.springer.com/article/10.1007%2F01397346>.
- Lambard, V. (1998) *Development of ODS ferritic-martensitic steels for application to high temperature and irradiation environment*. Université Paris XI Orsay.
- Laurent-Brocq, M. (2010) *Synthèse et caractérisation d ' un acier ODS préparé par un procédé alternatif inspiré du broyage réactif Etude de l ' influence des conditions de broyage et recuit*. Université Rennes 1, France.
- Lebensohn, R. A. *et al.* (1996) 'Measurement and prediction of texture development during a rolling sequence of Zircaloy-4 tubes', *Journal of Nuclear Materials*, 229, pp. 57–64. doi: 10.1016/0022-3115(95)00210-3.
- Lebensohn, R. A. and Tomé, C. N. (1993) 'A self-consistent anisotropic approach for the simulation of plastic deformation and texture development of polycrystals: Application to zirconium alloys', *Acta Metallurgica Et Materialia*, 41(9), pp. 2611–2624. doi: 10.1016/0956-7151(93)90130-K.
- Lee, S. J. and Lee, Y. K. (2008) 'Prediction of austenite grain growth during austenitization of low alloy steels', *Materials and Design*, 29, pp. 1840–1844. doi: 10.1016/j.matdes.2008.03.009.
- Li, B. L. *et al.* (2003) 'Flow stress and microstructure of the cold-rolled IF steel.pdf', *Materials Science and Engineering A*, 356, pp. 37–42.
- Lutterotti, L. (2006) *MAUD tutorial*. Edited by I. B. Determination.
- Masoumi, M. *et al.* (2017) 'Texture evolution and phase transformation of 25Cr-6Mo-5Ni experimental duplex stainless steel during hot and cold rolling', *Journal of Materials Research and Technology*, 6(3), pp. 232–240. doi: 10.1016/j.jmrt.2017.01.001.

- De Messemaeker, J., Verlinden, B. and Van Humbeeck, J. (2004) ‘On the strength of boundaries in submicron IF steel’, *Materials Letters*, 58(29), pp. 3782–3786. doi: 10.1016/j.matlet.2004.07.026.
- Mocellin, K. and Vanegas, E. (2011) ‘Laminage de tubes ODS’, in, pp. 1–6.
- Montmitonnet, P. *et al.* (2002) ‘3D elastic-plastic finite element simulation of cold pilgering of zircaloy tubes’, *Journal of Materials Processing Technology*, 125–126, pp. 814–820. doi: 10.1016/S0924-0136(02)00379-5.
- Montmitonnet, P. (2007) ‘From steady-state to cyclic metal forming processes’, *AIP Conference Proceedings*, 908, pp. 209–214. doi: 10.1063/1.2740813.
- Mulot, S. *et al.* (1996) ‘A fully 3D finite element simulation of cold pilgering’, *Journal of Materials Processing Technology*, 60, pp. 505–512. doi: [http://dx.doi.org/10.1016/0924-0136\(96\)02378-3](http://dx.doi.org/10.1016/0924-0136(96)02378-3).
- Narita, T. *et al.* (2011) ‘Effect of tungsten addition on microstructure and high temperature strength of 9CrODS ferritic steel’, *Journal of Nuclear Materials*, 417(1–3), pp. 158–161. doi: 10.1016/j.jnucmat.2011.01.060.
- Narita, T. *et al.* (2013) ‘Characterization of recrystallization of 12Cr and 15Cr ODS ferritic steels’, *Journal of Nuclear Science and Technology*, 50(3), pp. 314–320. doi: 10.1080/00223131.2013.772446.
- Note d’essai DMN/SRMA/LTMEx/NE-2013-24, Determination du coefficient de Poisson et du module d’Young d’aciers 9Cr et d’un acier ODS 14Cr à différentes températures* (2013). CEA Saclay, France.
- Ohtsuka, S. *et al.* (2013) ‘Investigation of the cause of peculiar irradiation behavior of 9Cr-ODS steel in BOR-60 irradiation tests’, *Journal of Nuclear Science and Technology*, 50(5), pp. 470–480. doi: 10.1080/00223131.2013.785273.
- Oliveira, V. B. *et al.* (2013) ‘Annealing effects on the microstructure and coercive field of two ferritic-martensitic Eurofer steels: A comparative study’, *Journal of Nuclear Materials*, 435(1–3), pp. 189–195. doi: 10.1016/j.jnucmat.2012.12.017.
- Parmentier, P. (2001) ‘Etude de la mise en forme de différentes nuances d’aciers renforcés par dispersion d’oxydes (ODS)’, *Document Technique, SE2MLETRAM 01-DT-015*,.
- Petch, N. J. (1953) ‘The cleavage strength of polycrystals’, *J. Iron Steel InstInst*, 174(19), pp. 25–28. doi: 10.1007/BF01972547.

References

- Proust, G., Tomé, C. N. and Kaschner, G. C. (2007) 'Modeling texture, twinning and hardening evolution during deformation of hexagonal materials', *Acta Materialia*, 55, pp. 2137–2148. doi: 10.1016/j.actamat.2006.11.017.
- Raabe, D. (1995) 'Simulation of rolling textures of b.c.c. metals considering grain interactions and crystallographic slip on {110}, {112} and {123} planes', *Materials Science and Engineering A*, 197(1), pp. 31–37. doi: 10.1016/0921-5093(94)09770-4.
- Raabe, D. and Lücke, K. (1994) 'Rolling and Annealing Textures of BCC Metals', *Materials Science Forum*, 157–162, pp. 597–610. doi: 10.4028/www.scientific.net/MSF.157-162.597.
- Renzetti, R. A. *et al.* (2011) 'Annealing effects on microstructure and coercive field of ferritic-martensitic ODS Eurofer steel', *Materials Science and Engineering A*. Elsevier B.V., 528(3), pp. 1442–1447. doi: 10.1016/j.msea.2010.10.051.
- Reppich, B. (1998) 'On the attractive particle-dislocation interaction in dispersion-strengthened material', *Acta Materialia*, 46(1), pp. 61–67. doi: 10.1016/S1359-6454(97)00234-6.
- Rich, A. (2015) 'Work Hardening and Annealing'. Mechanical & Aerospace Engineering, West Virginia University.
- Rodriguez, G. (2018) 'ASTRID - LESSONS LEARNED', in *Gen.IV International Forum*. CEA Saclay, France.
- Sakasegawa, H. *et al.* (2007) 'Evaluation of threshold stress of ODS steel', in *ICFRM-13: International Conference on Fusion Reactor Materials*. Nice, France.
- Saleh, A. A., Pereloma, E. V. and Gazder, A. A. (2014) 'Self-consistent modeling of texture evolution in TWIP steel during uniaxial tension', *Steel Research International*, 6, pp. 1120–1127. doi: 10.1002/srin.201300167.
- Savran, V. I., Offerman, S. E. and Sietsma, J. (2010) 'Austenite nucleation and growth observed on the level of individual grains by three-dimensional X-ray diffraction microscopy', *Metallurgical and Materials Transactions A: Physical Metallurgy and Materials Science*. doi: 10.1007/s11661-009-0142-5.
- Sellars, C. M. and Whiteman, J. A. (1979) 'Recrystallization and grain growth in hot rolling', *Metal Science*, 13, pp. 87–194. doi: 10.1179/msc.1979.13.3-4.187.
- Shinozuka, K. *et al.* (2009) 'Creep behavior of oxide dispersion strengthened 8Cr-2WVTa and 8Cr-1W steels', *Journal of Nuclear Materials*, pp. 1–5. doi: 10.1016/j.jnucmat.2008.09.006.

- Song, M. *et al.* (2013) ‘Microstructure refinement and strengthening mechanisms of a 12Cr ODS steel processed by equal channel angular extrusion’, *Journal of Alloys and Compounds*. Elsevier B.V., 577, pp. 247–256. doi: 10.1016/j.jallcom.2013.04.198.
- Steckmeyer, A. (2012) *Experimental study and modelling of the high temperature mechanical behavior of oxide dispersion strengthened ferritic steels*. Ecole Nationale Supérieure des Mines de Paris, France.
- Stoica, G. M. *et al.* (2014) ‘Temperature-dependent elastic anisotropy and mesoscale deformation in a nanostructured ferritic alloy’, *Nature Communications*, 5, pp. 1–8. doi: 10.1038/ncomms6178.
- Tanaka, Y., Tomida, T. and Mohles, V. (2015) ‘Quantitative prediction of deformed austenite and transformed ferrite texture in hot-rolled steel sheet’, in *IOP Conference Series: Materials Science and Engineering*. doi: 10.1088/1757-899X/82/1/012057.
- Thompson, P., Reilly, J. J. and Hastings, J. M. (1987) ‘The accommodation of strain and particle size broadening in rietveld refinement; its application to de-deuterided LaNi₅ alloy’, *Journal of The Less-Common Metals*. doi: 10.1016/0022-5088(87)90037-3.
- Tomé, C. . N. . and Lebensohn, R. A. (2009) *Manual for Code VPSC Version 7c*. Los Alamos.
- Tomé, C. N., Lebensohn, R. A. and Kocks, U. F. (1991) ‘A model for texture development dominated by deformation twinning: Application to zirconium alloys’, *Acta Metallurgica Et Materialia*, 39(11), pp. 2667–2680. doi: 10.1016/0956-7151(91)90083-D.
- Tomé, C. N., Necker, C. T. and Lebensohn, R. A. (2002) ‘Mechanical anisotropy and grain interaction in recrystallized aluminum’, *Metallurgical and Materials Transactions A: Physical Metallurgy and Materials Science*, 33(8), pp. 2635–2648. doi: 10.1007/s11661-002-0385-x.
- Tomida, T. *et al.* (2008) ‘Quantitative Prediction of Transformation Texture in Hot-Rolled Steel Sheets by Multiple KS Relation’, in *Proc. 15th ICOTOM*. Pittsburg, Pennsylvania, p. 325.
- Tomida, T. *et al.* (2010) ‘A Variant Selection Rule in Transformation in Steel and Prediction of Transformation Texture’, *Materials Science Forum*. doi: 10.4028/www.scientific.net/MSF.638-642.2846.
- Tomida, T. *et al.* (2013) ‘Memory effects of transformation textures in steel and its prediction by the double Kurdjumov-Sachs relation’, *Acta Materialia*, 61(8), pp. 2828–2839. doi: 10.1016/j.actamat.2013.01.015.
- Tomida, T. *et al.* (2015) ‘Quantitative prediction of transformation texture in steel by Double Kurdjumov-Sachs relation’, in *IOP Conference Series: Materials Science and Engineering*. doi: 10.1088/1757-899X/82/1/012060.

References

- Tomida, T. (2018) 'Variant selection mechanism by elastic anisotropy and double K-S relation for transformation texture in steel; difference between martensite and ferrite', *Acta Materialia*. Elsevier Ltd, 146, pp. 25–41. doi: 10.1016/j.actamat.2017.12.033.
- Tomida, T. and Wakita, M. (2012) 'Transformation Texture in Hot-rolled Steel Sheets and Its Quantitative Prediction', *ISIJ International*. doi: 10.2355/tetsutohagane.97.230.
- Tóth, L. S. *et al.* (2004) 'Analysis of texture evolution in equal channel angular extrusion of copper using a new flow field', *Acta Materialia*, 52(7), pp. 1885–1898. doi: 10.1016/j.actamat.2003.12.027.
- Tóth, L. S., Molinari, A. and Raabe, D. (1997) 'Modeling of rolling texture development in a ferritic chromium steel', *Metallurgical and Materials Transactions A: Physical Metallurgy and Materials Science*, 28(11), pp. 2343–2351. doi: 10.1007/s11661-997-0191-6.
- Toualbi, L. *et al.* (2012) 'Assessment of a new fabrication route for Fe-9Cr-1W ODS cladding tubes', *Journal of Nuclear Materials*, 428, pp. 47–53. doi: 10.1016/j.jnucmat.2011.12.013.
- Toualbi, L. (2012) *Optimisation de la gamme de fabrication de tubes en acier renforcés par une dispersion nanométrique d'oxydes (ODS) : compréhension des relations microstructure / propriétés mécaniques*. l'École nationale supérieure des mines de Paris, France.
- Toualbi, L. *et al.* (2013) 'Relationships between mechanical behavior and microstructural evolutions in Fe 9Cr-ODS during the fabrication route of SFR cladding tubes', *Journal of Nuclear Materials*. Elsevier B.V., 442(1–3), pp. 410–416. doi: 10.1016/j.jnucmat.2013.04.052.
- Ukai, S. *et al.* (1998) 'development of oxide dispersion strengthened steels for FBR core application, (II): Morphology improvement by martensite transformation', *Journal of Nuclear Science and Technology*, 35(4), pp. 294–300. doi: 10.1080/18811248.1998.9733859.
- Ukai, S. *et al.* (2002) 'Development of 9Cr-ODS Martensitic Steel Claddings for Fuel Pins by means of Ferrite to Austenite Phase Transformation', *Journal of Nuclear Science and Technology*, 39(7), pp. 778–788. doi: 10.1080/18811248.2002.9715260.
- Ukai, S. *et al.* (2004) 'Tube manufacturing trials by different routes in 9CrW-ODS martensitic steels', *Journal of Nuclear Materials*, 329–333(1–3 PART A), pp. 356–361. doi: 10.1016/j.jnucmat.2004.04.082.
- Ukai, S. (2011) 'Microstructure and High-Temperature Strength of 9CrODS Ferritic Steel', *Metal, Ceramic and Polymeric Composites for Various Uses*, 3, pp. 283–302. Available at: <http://www.intechopen.com/books/metal-ceramic-and-polymeric-composites-for-various-uses/microstructure-and-high-temperature-strength-of-9crops-ferritic-steel>.

- Vakhitova, E. *et al.* (2017) 'Texture evolution in Oxide Dispersion Strengthened (ODS) steel tubes during pilgering process', *Journal of Nuclear Materials*. Elsevier B.V, 494, pp. 20–28. doi: 10.1016/j.jnucmat.2017.07.002.
- Vanegas-Marquez, E. (2011) *Numerical modeling of ODS steel tubes pilgering*. École Nationale Supérieure des Mines de Paris.
- Vatne, H. E. *et al.* (1996) 'The effect of particles on recrystallisation textures and microstructures', *Textures and Microstructures*, 26–27, pp. 385–412.
- Vatne, H. E., Shahani, R. and Nes, E. (1996) 'Deformation of cube-oriented grains and formation of recrystallized cube grains in a hot deformed commercial AlMgMn aluminium alloy', *Acta Materialia*, 44(11), pp. 4447–4462. doi: 10.1016/1359-6454(96)00077-8.
- Vaugoude, A. (2016) *Livrable L 2015-310 du projet MACNA, Fabrication et caractérisation de nuances ODS Fe-9Cr et Fe-11Cr consolidées. Rapports de stage de fin d'études*. CEA Saclay, France.
- Wenk, H. R. *et al.* (2009) 'Dauphiné twinning and texture memory in polycrystalline quartz. Part 3: Texture memory during phase transformation', *Physics and Chemistry of Minerals*, 36(10), pp. 567–583. doi: 10.1007/s00269-009-0302-6.
- Wenk, H. R. and Grigull, S. (2003) 'Synchrotron texture analysis with area detectors', *Journal of Applied Crystallography*, 36, pp. 1040–1049. doi: 10.1107/S0021889803010136.
- Wenk, H. R., Huensche, I. and Kestens, L. (2007) 'In-situ observation of texture changes during phase transformations in ultra-low-carbon steel', *Metallurgical and Materials Transactions A: Physical Metallurgy and Materials Science*, 38(2), pp. 261–267. doi: 10.1007/s11661-006-9033-1.
- Williamson, G. K. and Hall, W. H. (1953) 'X-ray line broadening from filed aluminium and wolfram', *Acta Metallurgica*, 1, pp. 24–31. doi: 10.1016/0001-6160(53)90006-6.
- Wronski, S. *et al.* (2017) 'Microstructure evolution of titanium after tensile and recrystallisation', *Materials Science and Engineering A*, 692, pp. 113–126. doi: 10.1016/j.msea.2017.02.100.
- Yamashita, S. *et al.* (2004) 'Formation of nanoscale complex oxide particles in mechanically alloyed ferritic steel', *Philosophical Magazine Letters*, 84(8), pp. 525–529. doi: 10.1080/09500830412331303609.
- Yen, H. W. *et al.* (2010) 'Orientation relationship transition of nanometre sized interphase precipitated TiC carbides in Ti bearing steel', *Materials Science and Technology*, 26(4), pp. 421–430. doi: 10.1179/026708309x12512744154207.

References

- Yoshinaga, N. *et al.* (2007) 'Factors affecting texture memory appearing through alpha-gamma-alpha transformation in IF steels', *Materials Transactions*, 48(8), pp. 2036–2042. doi: 10.2320/matertrans.MA200704.
- Yu, T. and Hansen, N. (2016) 'Coarsening kinetics of fine-scale microstructures in deformed materials', *Acta Materialia*, 120, pp. 40–45. doi: 10.1016/j.actamat.2016.08.032.
- Yvon, P. and Carré, F. (2009) 'Structural materials challenges for advanced reactor systems', *Journal of Nuclear Materials*, 385(2), pp. 217–222. doi: 10.1016/j.jnucmat.2008.11.026.
- Zhang, Z. (2015) *Nanostructures in a ferritic and an oxide dispersion strengthened steel induced by dynamic plastic deformation*. Technical University of Denmark.
- Zhong, S. Y. *et al.* (2012) 'Study of the thermal stability of nanoparticle distributions in an oxide dispersion strengthened (ODS) ferritic alloys', *Journal of Nuclear Materials*, 428(1–3), pp. 154–159. doi: 10.1016/j.jnucmat.2011.12.028.
- Zinkle, S. J. *et al.* (2017) 'Development of next generation tempered and ODS reduced activation ferritic/martensitic steels for fusion energy applications.', in *Nuclear Fusion*. IAEA. Vienna.

Annex 1

Details on the Intermediate Heat Treatment carried out in laboratory conditions (**UC2000 furnace**) and industrial ones (**Valinox furnace**)

The intermediate heat treatment (IHT6) were applied on the tubes after first rolling pass R1 under industrial conditions using Valinox furnaces. Then, the tubes were undergone the second rolling pass R2(HT). Since we did not have the sample, representing the heat treated state, we had to realize this heat treatment under laboratory conditions, using UC2000 furnace. In both cases, the sample was heated, under argon gas, until 1050°C with a rate of 15°C/min and a 20 min holding time. Then, it was submitted to a cooling rate of about 0.4°C/min. The temperature evolution during IHT under industrial and laboratory conditions is presented on Fig. Annex 1.1. An IPF Y map for tube IHT6 treated under laboratory conditions is shown on Fig. Annex 1.2.

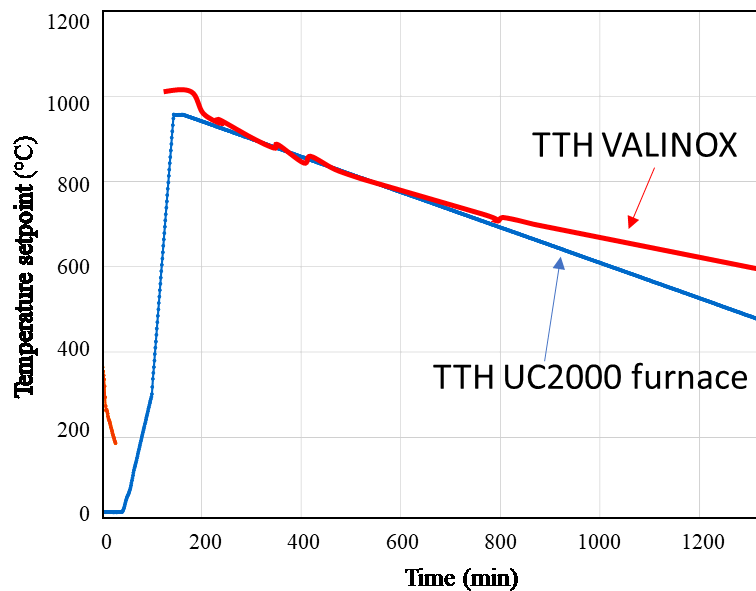


Fig. Annex 1.1 Intermediate Heat Treatment carried out in laboratory conditions (UC2000 furnace) and industrial ones (Valinox furnace)

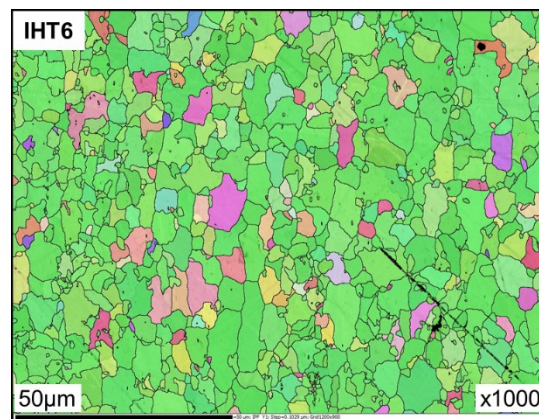


Fig. Annex 1.2 IPF Y map with grain boundaries pattern for tube IHT6 (RD-TD plane)

Annex 2

Hall-Petch plot united all metallurgical states of ODS steel tubes studied in this work

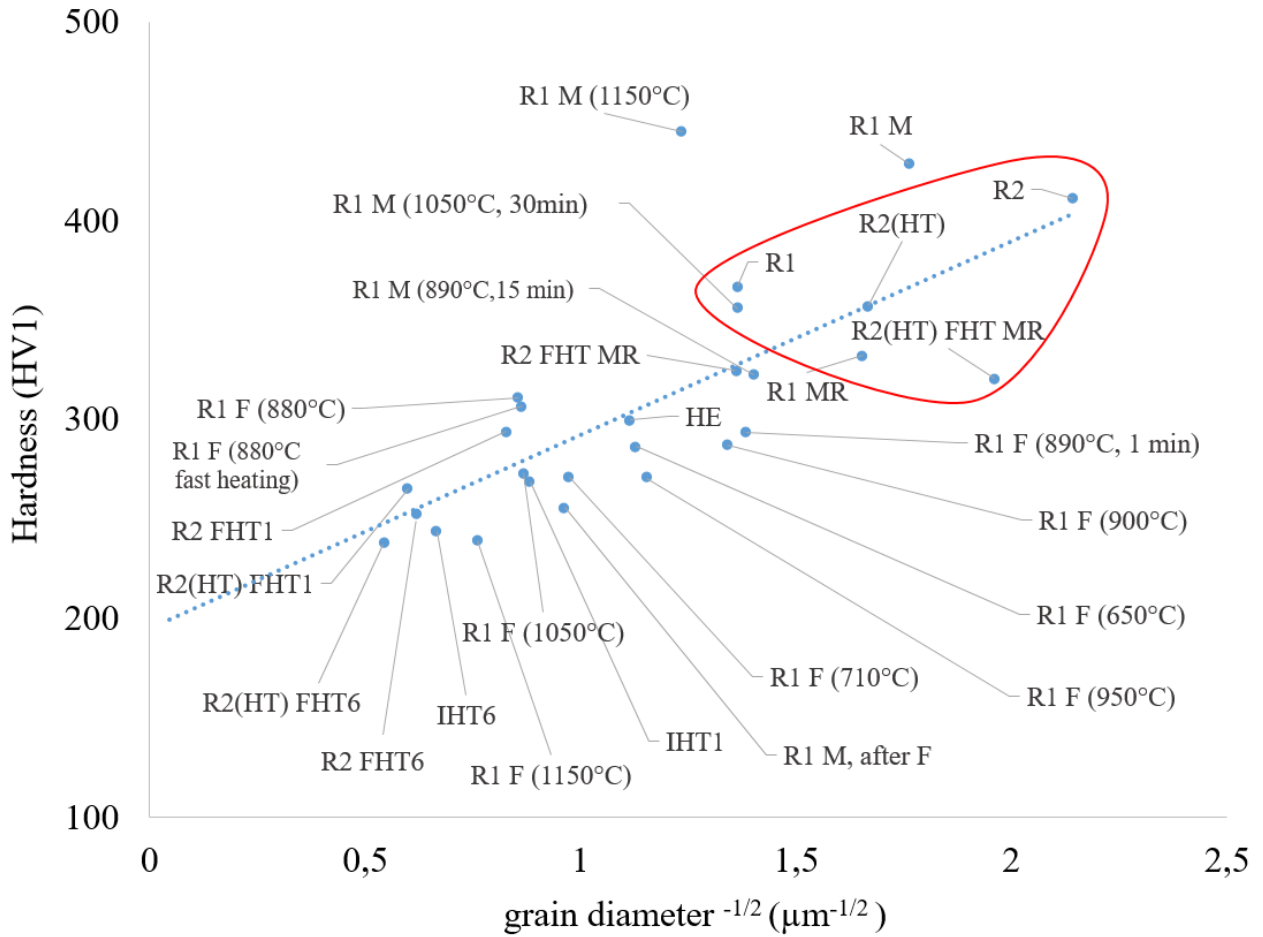


Fig. Annex.2.1 Hall-Petch plots for all ODS steel states studied in this work

Annex 3

Texture evolution during thermal cycle observed by in-situ synchrotron X-ray diffraction analysis

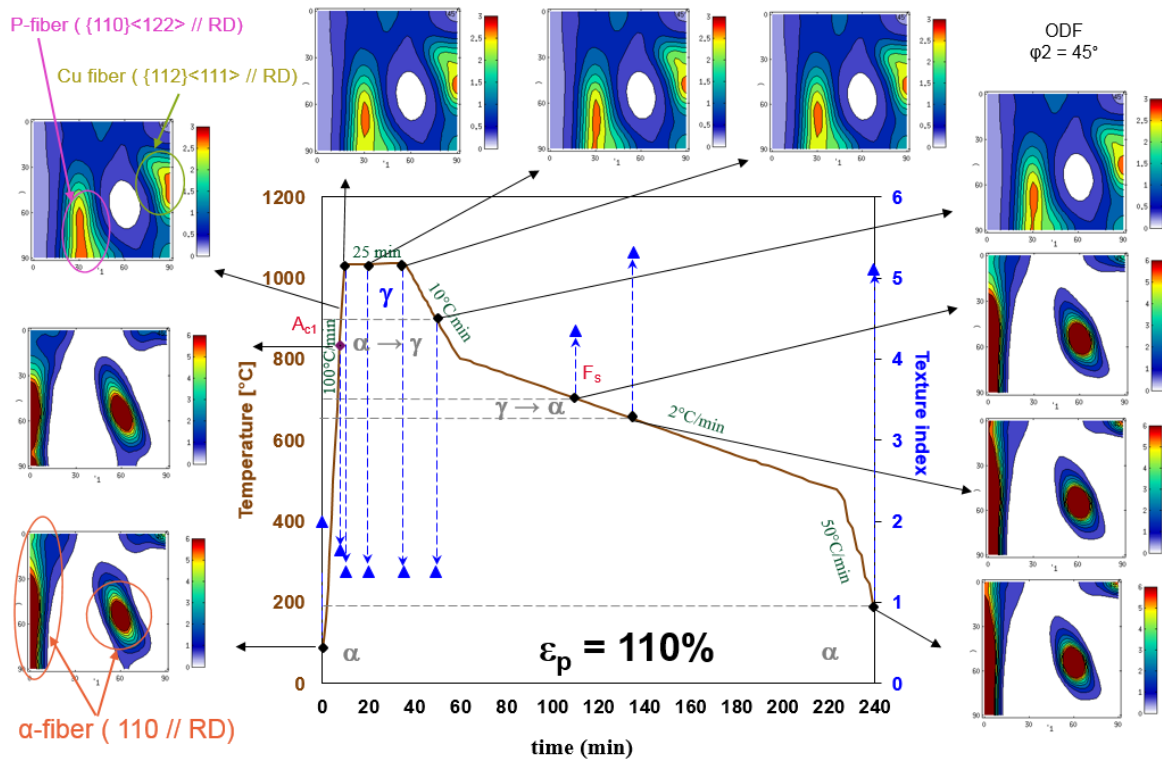


Fig. Annex.3.1 Texture evolution during thermal cycle observed by in-situ synchrotron X-ray diffraction analysis for R1 samples during slow cooling

Elena VAKHITOVA

Doctorat : Matériaux, Mécanique, Optique, Nanotechnologie

Année 2018

Etude microstructurale et micromécanique de tubes en acier ODS transformés par laminage à pas de pèlerin

Ce projet est dédié au développement de matériaux de gainage pour le Réacteur à Neutrons Rapides refroidis au sodium (RNR-Na). L'étude se concentre sur les propriétés mécaniques et microstructurales de tubes en acier ferritique/martensitique 9wt%Cr, renforcé par dispersion d'oxydes (ODS) et mis en forme par laminage à pas de pèlerin. L'objectif de ce projet est d'identifier les relations entre les paramètres thermomécaniques du processus de fabrication industrielle et les propriétés du matériau dans son état final.

L'étude a été effectuée par une approche expérimentale pour analyser l'évolution des propriétés du matériau à chaque étape de sa production : filage à chaud d'une ébauche à partir de l'état de poudre, réduction de la section de tube par plusieurs passes de laminage, traitement thermique intermédiaire entre chaque passe de laminage et traitement thermique final.

Par une analyse précise des évolutions microstructurales et mécaniques au cours du laminage à froid, des données fondamentales ont été obtenues pour le développement des séquences de mis en forme à froid des aciers ODS. La découverte d'un phénomène inattendu d'héritage de texture au cours des traitements thermiques met en évidence l'effet particulier des nano-phases dans le changement de phase des aciers inoxydables ODS 9%Cr.

Le code ViscoPlastique Auto-Cohérent (VPSC) est appliqué pour simuler l'évolution de la texture et des propriétés mécaniques macroscopiques lors du laminage. Ceci permet de relier la microstructure aux paramètres du procédé et de faciliter l'optimisation des paramètres de fabrication.

Mots clés : ODS – laminage à pas de pèlerin – acier, traitement thermique – texture (cristallographie) – analyse EBSD.

Microstructural and Micromechanical Study of ODS Steel Tubes Transformed by Cold Pilgering

This project is dedicated to the development of fuel cladding materials for Gen-IV Sodium-cooled Fast Reactor (SFR). The study focuses on the mechanical and microstructural properties of 9wt%Cr ferritic/martensitic Oxide Dispersion Strengthened (ODS) steel tubes transformed by cold pilgering. The aim of this project is to identify the relationships between the thermomechanical parameters of the industrial manufacturing process and the properties of the material in its final state.

The study was carried out by an experimental approach to analyze the evolution of the properties of the material at each stage of its production: hot extrusion of a tube from the pre-alloyed powder mixture; reduction of the tube section by several rolling passes; intermediate heat treatment between each rolling pass and the final heat treatment.

By a precise analysis of the microstructural and mechanical evolutions during cold rolling, fundamental data were obtained for the development of cold forming sequences of ODS steels. The discovery of an unexpected phenomenon of texture inheritance during thermal treatments highlights the particular effect of the nano-phases in the phase transition of the 9% Cr stainless ODS steels.

The Viscoplastic Self-Consistent code (VPSC) is applied to simulate the evolution of texture and macroscopic mechanical properties during rolling. The link between microstructure and process parameters help the optimization of manufacturing parameters.

Keywords: ODS – cold pilgering – steel, heat treatment – texture (crystallography) – EBSD analysis.

Thèse réalisée en partenariat entre :

